https://ntrs.nasa.gov/search.jsp?R=19920004890 2020-03-17T14:27:44+00:00Z

N92-17121
Unclas
P-84

NASA Technical Paper 3181

December 1991

Limit Cycle Vibrations in Turbomachinery

S. G. Ryan

(NASA-TP-3181) LIMIT CYCLE VIBRATIONS IN TURBOMACHINERY (NASA) 34 p CSCL 13I

Unclas
H1/20 0053070

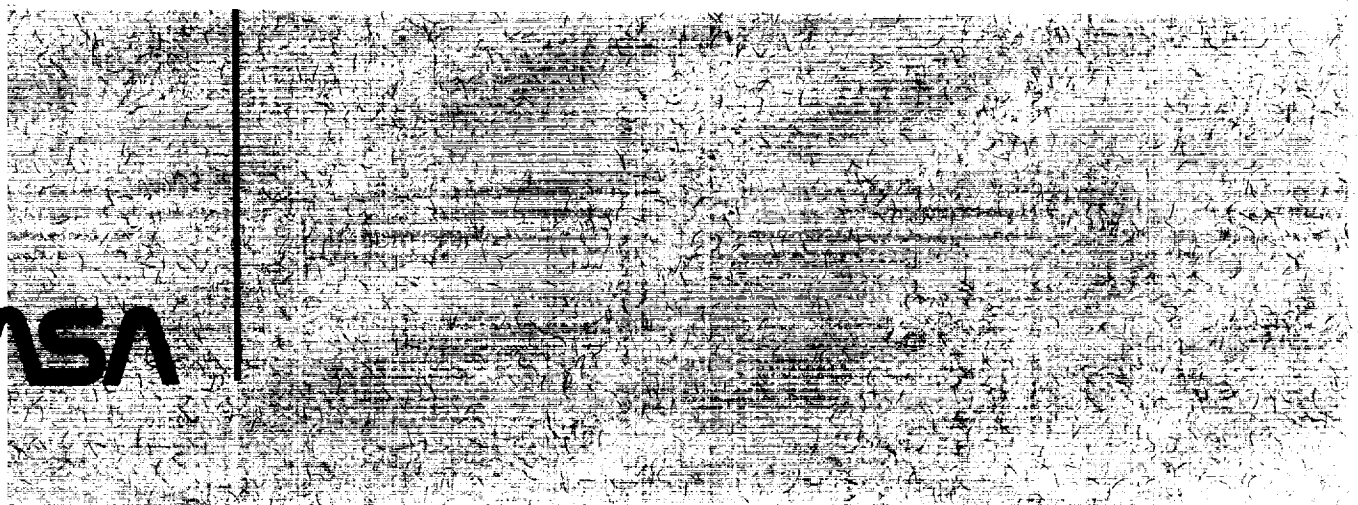

NASA

NASA Technical Paper 3181

1991

Limit Cycle Vibrations in Turbomachinery

S. G. Ryan
George C. Marshall Space Flight Center
Marshall Space Flight Center, Alabama

NASA
National Aeronautics and Space Administration
Office of Management
Scientific and Technical Information Program

TABLE OF CONTENTS

PRECEDING PAGE BLANK NOT FILMED

TABLE OF CONTENTS (Continued)

LIST OF ILLUSTRATIONS

LIST OF ILLUSTRATIONS (Continued)

LIST OF ILLUSTRATIONS (Continued)

LIST OF ILLUSTRATIONS (Continued)

LIST OF ILLUSTRATIONS (Continued)

LIST OF ILLUSTRATIONS (Continued)

LIST OF ILLUSTRATIONS (Continued)

LIST OF ILLUSTRATIONS (Continued)

LIST OF TABLES

LIST OF SYMBOLS

a	dimensionless mass eccentricity
a_r, a_t	acceleration along radial and tangential axes
a_y, a_z	acceleration along Y and Z
a_{y_n}, a_{z_n}	cosine coefficients for Fourier expansion of y and z
b_{y_n}, b_{z_n}	sine coefficients for Fourier expansion of y and z
c	linear damping coefficient
c_{y_n}, c_{z_n}	cosine coefficients for Fourier expansion of f_y and f_z
d_{y_n}, d_{z_n}	sine coefficients for Fourier expansion of f_y and f_z
e	rotor mass eccentricity; also natural exponential function
$\hat{e}_r$, $\hat{e}_t$	radial and tangential unit vectors
F_{ny}, F_{nz}	cartesian components of random noise forces
F_r, F_t	force components along radial and tangential axes
F_{r_n}	nonlinear radial force
F_{r_l}, F_{t_l}	linear radial and tangential support forces
F_{sy}, F_{sz}	cartesian components of constant side forces
F_y, F_z	force components along Y and Z
F_{y_l}, F_{z_l}	cartesian components of linear support forces
F_{y_n}, F_{z_n}	cartesian components of nonlinear radial force
$f_y(y,z)$, $f_z(y,z)$	cartesian components of nonlinear support forces
g_y, g_z	dimensionless side force cartesian components
$\hat{\imath}$, $\hat{\jmath}$	cartesian unit vectors along Y and Z
j	unit imaginary number, $\sqrt{-1}$
k	$k_l + k_n$
k_l	linear stiffness coefficient
k_n	stiffness coefficient in nonlinear force function
m	rotor mass

N	number of subharmonic multiples assumed in harmonic balance
n	summation index
Q	linear cross-coupled stiffness coefficient
q	dimensionless cross-coupled stiffness
R	magnitude of rotor radial displacement
R_{cg}	rotor mass center displacement vector
r	dimensionless polar coordinate
$\bar{r}$	perturbation variable in r
t	time
t^*, $\tilde{t}$	dummy variables of integration representing time
$u(t)$	unit step function starting at time zero
Y, Z	cartesian coordinates defining rotor displacement
$\bar{Y}$, $\bar{Z}$	assumed complex magnitude of homogeneous solution for Y and Z
y, z	dimensionless cartesian coordinates
$\bar{y}$, $\bar{z}$	perturbation variables in y and z
α	angular acceleration of rotor
β	rotation angle of rotor
γ	ratio of nonlinear stiffness to total stiffness, $\frac{k_n}{k}$
δ	deadband in nonlinear support force
ζ	damping ratio of zero deadband linear system
η_y, η_z	cartesian components of dimensionless random noise
$\bar{\eta}$	range scale factor for random number sequence defining η_y and η_z
θ	polar angle coordinate
$\bar{\theta}$	perturbation variable in θ
λ	characteristic root in normalized time
λ^*	characteristic root in unnormalized time
μ	dimensionless rotor angular acceleration
ρ	dimensionless rotor angular velocity
ρ_{gi}	global onset speed of instability
ρ_{lc}	lower speed limit for possible limit cycle instability
ρ_{ue}	stability limit for unbalance equilibrium

σ	cross-coupled stiffness proportionality coefficient, $\frac{q}{2\zeta\rho}$
τ	normalized time
τ^*, $\bar{\tau}$	dummy variables of integration representing normalized time
ω	angular velocity of rotor
ω_n	natural frequency of zero deadband linear system, $\sqrt{\frac{k}{m}}$
$\dot{\xi}$	$\frac{d\xi}{dt}$ where ξ represents any variable
ξ'	$\frac{d\xi}{d\tau}$ where ξ represents any variable
ξ_0	equilibrium value of ξ where ξ represents any variable

LIST OF SYMBOLS FOR APPENDIX A

A_{Py},A_{Pz}	cartesian components of pulse perturbation amplitude
$\mathbf{B}$	rotor damping matrix in body axis, cartesian coordinates
$\mathbf{B}_\eta, \mathbf{B}_\zeta$	partitions of $\mathbf{B}$ corresponding to body axis cartesian coordinates
$\mathbf{B}_{\eta\eta}, \mathbf{B}_{\eta\theta_\zeta}$ $\mathbf{B}_{\theta_\zeta\eta}, \mathbf{B}_{\theta_\zeta\theta_\zeta}$	subpartitions of $\mathbf{B}_\eta$ corresponding to translational and rotational components of the body axis coordinates
$\mathbf{B}_{\zeta\zeta}, \mathbf{B}_{\zeta\theta_\eta}$ $\mathbf{B}_{\theta_\eta\zeta}, \mathbf{B}_{\theta_\eta\theta_\eta}$	subpartitions of $\mathbf{B}_\zeta$ corresponding to translational and rotational components of the body axis coordinates
$\mathbf{B}_i$	i^{th} eigenvector of combined system linear homogeneous solution
c	clearance in rub model
c_x	axial damping coefficient
$c_{y_0}, c_{y_1}, c_{y_2}$ $c_{z_0}, c_{z_1}, c_{z_2}$	cartesian components of the nonlinear damping coefficient for the deadband nonlinear force element
$C_{y0_i}, C_{y1_i}, C_{y2_i}$ $C_{z0_i}, C_{z1_i}, C_{z2_i}$	polynomial coefficients defining the cartesian components of the i^{th} constant side force as functions of speed
$\mathbf{C}$	combined system linear damping matrix
$\mathbf{C_y}, \mathbf{C_z}$	diagonal damping matrix for rotor-housing interaction elements
$\mathbf{C_{Q_y}}, \mathbf{C_{Q_z}}$	diagonal cross-coupled damping matrix for rotor-housing interaction elements
$\hat{e}_{x_i}, \hat{e}_{y_i}, \hat{e}_{z_i}$	cartesian coordinate unit vectors
$\hat{e}_{\bar{x}_i}, \hat{e}_{z'_i}$	unit vectors along Euler angle axes
$\hat{e}_N, \hat{e}_T$	unit vectors along rub contact normal and tangential axes
$\hat{e}_r, \hat{e}_\theta$	unit vectors collinear and normal to radial deflection vector

F_{h_x}	axial interconnection force acting on housing
F_N	rub force component collinear with contact normal vector
$F_{Nh_{y_i}}, F_{Nh_{z_i}}$	cartesian components of i^{th} white noise excitation on housing
$F_{Nr_{y_i}}, F_{Nr_{z_i}}$	cartesian components of i^{th} white noise excitation on rotor
F_{Py}, F_{Pz}	cartesian components of pulse perturbation force
F_R, F_θ	radial and tangential components of rub force using the simple rub model
F_{Sy_i}, F_{Sz_i}	cartesian components of i^{th} side force excitation
F_{Uy_i}, F_{Uz_i}	cartesian components of i^{th} unbalance excitation
$F_{x_i}, F_{y_i}, F_{z_i}$	cartesian components of external forces acting on i^{th} segment of rotor
F_y, F_z	cartesian components of deadband nonlinearity force element
$\mathbf{f(x,t)}$	general vector function representing derivative function of system of first order equations
$\mathbf{F}$	rub force vector
$\mathbf{F_E}$	external excitation force vector (concatenation of $\mathbf{F_{Er_y}}$, $\mathbf{F_{Er_z}}$, $\mathbf{F_{Eh_y}}$, and $\mathbf{F_{Eh_z}}$)
$\mathbf{F_{Eh_y}}$,$\mathbf{F_{Eh_z}}$	cartesian components of external excitation force vector applied to housing
$\mathbf{F_{Er_y}}$,$\mathbf{F_{Er_z}}$	cartesian components of external excitation force vector applied to rotor
$\mathbf{F_{h_y}}, \mathbf{F_{h_z}}$	vectors of cartesian components of rotor-housing interconnection forces and external forces applied to housing
$\mathbf{F_{n_y}}, \mathbf{F_{n_z}}$	vectors of cartesian components of nonlinear rotor-housing interconnection forces
$\mathbf{F_y}, \mathbf{F_z}$	vectors of cartesian components of rotor-housing interconnection forces and external forces applied to rotor
G	rotor Lagrangian dissipation function
h	numerical integration time step
$I_{xx_i}, I_{yy_i}, I_{zz_i}$	moments of inertia of i^{th} rotor segment
$I_{xy_i}, I_{xz_i}, I_{yx_i}$ $I_{yz_i}, I_{zx_i}, I_{zy_i}$	products of inertia of i^{th} rotor segment
$\mathbf{I}$	identity matrix
$\mathbf{I_a}, \mathbf{I_t}$	diagonal matrices of polar and transverse moments of inertia
$\mathbf{I_{h_y}}, \mathbf{I_{h_z}}$	imaginary components of $\mathbf{F_{Eh_y}}$, and $\mathbf{F_{Eh_z}}$

$\mathbf{I_{r_y}}, \mathbf{I_{r_z}}$	imaginary components of $\mathbf{F_{Er_y}}$, and $\mathbf{F_{Er_z}}$
j	$\sqrt{-1}$
k_R	rub contact stiffness coefficient
k_x	axial rotor-housing interaction stiffness coefficient
$k_{y_0}, k_{y_1}, k_{y_2}$ $k_{z_0}, k_{z_1}, k_{z_2}$	piecewise linear stiffness coefficients for deadband nonlinear element
$\mathbf{K}$	combined system linear stiffness matrix
$\mathbf{k_y}, \mathbf{k_z}$	diagonal matrices of rotor-housing interaction linear stiffness coefficients
$\mathbf{k_t}$	diagonal matrix of rotor-housing interaction linear moment stiffness coefficients
m_i	mass of i^{th} rotor segment
M	total mass of rotor
$(ma)_i$	product of mass and eccentricity for i^{th} rotor segment
$\mathbf{m}$	mass matrix for rotor
$\mathbf{m_y}, \mathbf{m_z}$	diagonal matrices of rotor-housing interaction linear inertia coefficients
$\mathbf{M}$	combined system mass matrix
$\mathbf{M_{Q_y}}, \mathbf{M_{Q_z}}$	diagonal matrices of rotor-housing interaction linear cross-coupled inertia coefficients
$\mathbf{N_i}$	displacement component of i^{th} system eigenvector $\mathbf{B_i}$
$\bar{\mathbf{N}}$	complex amplitude vector for harmonic excitation solution
$\mathbf{N_R}, \mathbf{N_I}$	real and imaginary components of $\bar{\mathbf{N}}$
$\mathbf{p}$	generalized coordinate corresponding to housing component modes
$\mathbf{P}$	first order term coefficient matrix for combined system in first order form
q_i	i^{th} generalized coordinate
Q_i	generalized force acting at i^{th} generalized coordinate
$\mathbf{q_y}, \mathbf{q_z}$	generalized coordinates corresponding to rotor component modes in $y-x$ and $z-x$ planes
$\mathbf{Q}$	combined system complex generalized excitation force vector
$\mathbf{Q_R}, \mathbf{Q_I}$	real and imaginary components of $\mathbf{Q}$
$\mathbf{Q_y}, \mathbf{Q_z}$	diagonal matrices of rotor-housing interaction linear cross-coupled stiffness coefficients

r	magnitude of relative deflection vector in deadband nonlinear element
$\mathbf{f}$	magnitude of relative deflection vector in rub nonlinear element
$\mathbf{r}_\eta, \mathbf{r}_\zeta$	vectors of rotor body fixed cartesian coordinates
$\mathbf{R}$	zeroth order term coefficient matrix for combined system in first order form (equation A159) real part of F_E (equation A188)
$\mathbf{R}_{\mathbf{h_y}}, \mathbf{R}_{\mathbf{h_z}}$	real components of $\mathbf{F}_{\mathbf{Eh_y}}$, and $\mathbf{F}_{\mathbf{Eh_z}}$
$\mathbf{R}_{\mathbf{r_y}}, \mathbf{R}_{\mathbf{r_z}}$	real components of $\mathbf{F}_{\mathbf{Er_y}}$, and $\mathbf{F}_{\mathbf{Er_z}}$
$\mathbf{S}$	rub contact surface displacement vector
T_i	kinetic energy if i^{th} rotor segment
$T_{x_i}, T_{y_i}, T_{z_i}$	cartesian components of external torques acting on i^{th} segment of rotor
$\mathbf{T}_{\mathbf{h_y}}, \mathbf{T}_{\mathbf{h_z}}$	vectors of cartesian components of rotor-housing interaction torques acting on housing
$\mathbf{T_x}, \mathbf{T_y}, \mathbf{T_z}$	vectors composed of $T_{x_i}, T_{y_i}, T_{z_i}$
$\mathbf{T}_\mathbf{x}^*$	diagonal matrix formed from elements of T_x
V	rotor potential function
δW	virtual work of external forces acting on rotor
$\mathbf{w}$	vector formed from concatenation of all rotor physical translation and rotation coordinate vectors
$\mathbf{w_y}, \mathbf{w_z}$	cartesian component partitions of $\mathbf{w}$
$\mathbf{w_i}$	complex system transient response vector due to i^{th} eigenvalue and eigenvector
$\mathbf{W_i}$	displacement component of i^{th} eigenvector in physical coordinates
$\mathbf{W_R}, \mathbf{W_I}$	real and imaginary components of $\mathbf{W_i}$
x	rotor axial coordinate
$\bar{x}$	rotor body fixed axial coordinate
x_h	housing axial coordinate at rotor-housing axial interaction point
$\mathbf{x}$	general coordinate vector for first order system of equations
$\mathbf{x}_{\mathbf{n+1}}^{\mathbf{p}}$	predicted value of $\mathbf{x}$ at next time step
$\mathbf{x_{n+1}}$	corrected value of $\mathbf{x}$ at next time step
y, z	rotor lateral cartesian coordinates
$\bar{y}, \bar{z}$	rotor body fixed lateral cartesian coordinates

y_{e_i}, z_{e_i}	cartesian components of relative deflection across i^{th} subelement of deadband nonlinear element
y_h, z_h	housing lateral displacements
y_r, z_r	rotor lateral displacements
y_{rel}, z_{rel}	cartesian components of rotor-housing relative displacement including eccentricities
$Y_{R_k i}, Z_{R_k i}$	cartesian components of $\mathbf{W_{R_i}}$ for k^{th} location
$Y_{I_k i}, Z_{I_k i}$	cartesian components of $\mathbf{W_{I_i}}$ for k^{th} location
α	rotor angular acceleration for unbalance force calculation angle between $\hat{e}_r$ and $\hat{e}_N$ in rub force model
β	coordinate vector for system equations in first order form
γ	angle between $\mathbf{F}$ and $\hat{e}_N$ in rub force model
$\mathbf{\Gamma}$	rotor generalized gyroscopic coupling matrix
$\delta(t)$	unit step function
δ_{ik}	dirac delta function
δ_i	threshold value for i^{th} subelement of deadband nonlinear element $(i = 0, 1, 2)$
$\epsilon_{h_y}, \epsilon_{h_z}$	cartesian components of housing fixed eccentricities
ϵ_r	magnitude of rotating eccentricity
ζ	critical damping ratio for a complex eigenvalue
η	combined system generalized coordinate vector
θ	spin angular position of the rotor
$\theta_x, \theta_y, \theta_z$	euler angles for rotor
$\theta_\mathbf{y}, \theta_\mathbf{z}$	vectors of cartesian components of rotations for all rotor segments (small angle assumption applied to euler angles)
$\theta_\zeta, \theta_\eta$	$\theta_\mathbf{y}, \theta_\mathbf{z}$ transformed to body fixed cartesian axes
$\theta_{\mathbf{y_h}}, \theta_{\mathbf{z_h}}$	vectors of cartesian components of rotations for all housing segments
κ	rotor stiffness matrix
λ	complex eigenvalue $(\lambda_R + j\lambda_I)$
μ	coefficient of friction in rub model
ν	variable introduced to transform system equations to first order form $(\nu = \dot{\eta})$
τ	duration of pulse perturbation

ϕ_i	phase angle of i^{th} mass unbalance excitation
ϕ_r	phase angle of rotating eccentricity
$\mathbf{\Phi}$	displacement component of modal matrix for rotor
$\mathbf{\Phi_{h_x}}, \mathbf{\Phi_{h_y}}, \mathbf{\Phi_{h_z}}$	cartesian displacement components of modal matrix for housing
$\mathbf{\Psi}$	rotation component of modal matrix for rotor
$\mathbf{\Psi_{h_y}}, \mathbf{\Psi_{h_z}}$	cartesian rotation components of modal matrix for housing
ω	rotor spin angular velocity for unbalance excitation force calculation
$\omega_{n_i}^2$	natural frequency of i^{th} rotor component mode
ω_p	frequency of pulse perturbation function
$\omega_{\bar{x}}, \omega_{\bar{y}}, \omega_{\bar{z}}$	body axis angular rates
Ω	rotor spin axis angular velocity
$\mathbf{\Omega}$	vector with all elements equal to Ω
$\omega_{\mathbf{n}}^2$	diagonal matrix of all $\omega_{n_i}^2$
$\omega_{\mathbf{n_h}}^2$	diagonal matrix of housing natural frequencies squared
$2\zeta\omega_{n_i}$	damping coefficient for i^{th} rotor component mode
$\mathbf{2\zeta\omega_n}$	diagonal matrix of all $2\zeta\omega_{n_i}$
$\mathbf{2\zeta_r\omega_{n_r}}$	same as $\mathbf{2\zeta\omega_n}$
$\mathbf{2\zeta_h\omega_{n_h}}$	diagonal matrix of damping coefficients for housing modes
$\delta()$	virtual displacement of ()
$\frac{d}{dt}()$	derivative with respect to time of ()
$\frac{\partial}{\partial q}()$	partial derivative with respect to q of ()
$()^T$	transpose of ()
$\dot{()}$	derivative with respect to time of ()
$\Re()$	real part of ()

TECHNICAL PAPER

LIMIT CYCLE VIBRATIONS IN TURBOMACHINERY

I. INTRODUCTION

High speed turbomachinery is used in many industrial and government applications. These include natural gas compressors, turbines in electric power plants, jet engines, and rocket engine turbopumps. Despite the differences in application, these machines are all susceptible to a variety of common vibration problems. The most common vibration problem encountered with any rotating machinery is rotor unbalance vibration. This problem has received much attention over the last century and is well understood. Another common problem is dynamic instability. This problem is well understood for situations that can be treated using linear analysis techniques; however, the limit cycle instabilities that can occur in nonlinear systems have not received as much attention. A third problem encountered in high speed turbomachinery is subharmonic response to unbalance excitation. This phenomenon requires either nonlinear system characteristics or time varying coefficients. This problem has been studied extensively for simple nonlinear systems. A significant amount of study has been done for turbomachinery experiencing this problem.

These last two problem areas have each received adequate treatment individually. However, situations have occurred where a turbomachine was found to be susceptible to both limit cycle instability and subharmonic response for apparently the same operating conditions. For example, the high pressure fuel turbopump (HPFTP) of NASA's space shuttle main engine (SSME) has a history of exhibiting subsynchronous vibration at frequencies ranging from 47 to 56 percent of shaft rotational speed. This includes many occurrences at exactly 50 percent which could be attributed to a limit cycle instability or a subharmonic response. This appears to be a case of what Hayashi[1] refers to as transition between almost periodic oscillations (limit cycle) and entrained subharmonic oscillations. This makes it difficult to determine whether a (catastrophic) divergent instability is impending or whether the machine is experiencing subharmonic response. An examination of this condition is the focus of this report. Before proceeding with the discussion of the combination of these two phenomena, a review of the prior work for each individual problem is in order.

General discussions of subharmonic resonance can be found in many vibration texts such as the works of Den Hartog[2] and Timoshenko.[3] More detailed analysis can be found in nonlinear vibration texts such as that of Hayashi.[1] These works deal primarily with a single nonlinear second order equation representing 1 degree-of-freedom (DOF). Tondl[4] provides a thorough treatment for 2-DOF models of rotating machinery. Ehrich[5] and Childs[6] have each published analyses of rotating machinery having nonlinearity in the form of a clearance or deadband in the restoring force. Asymmetry in the nonlinear restoring force was required to demonstrate subharmonic response. This asymmetry will occur in the presence of deadband when a static load is present or when rotor-stator misalignment exists. Bently[7] performed an experimental study using a laboratory model rotor. Each of these researchers reached essentially the same conclusions regarding subharmonic response. Namely, the resonance of a nonlinear rotordynamic system can be excited by a frequency that is near an integer multiple of it. The range of excitation

frequencies for which this phenomenon will occur depends on the nature of the nonlinearity and the other system characteristics. The response will be such that the nonlinear resonance frequency is tuned to a fraction of the excitation frequency (e.g., 1/2). Hayashi[1] described this as subharmonic entrainment.

Thorough treatments of the causes of dynamic instability can be found in many references. Vance[8] devotes an entire chapter to the subject and provides an excellent bibliography. Ehrich[9] provides a general survey of the fundamental causes of instability and gives some insight into means for avoiding them. With regard to the type of instabilities considered here, Ehrich states:

> ". . . the unifying generality is the generation of a tangential force, normal to an arbitrary radial deflection of a rotating shaft, whose magnitude is proportional to (or varies monotonically with) that deflection. At some 'onset' rotational speed, such a force system will overcome the stabilizing external damping forces which are generally present, and induce a whirling motion of ever-increasing amplitude, limited only by nonlinearities which ultimately limit deflections."

The tangential force can be generated by a variety of sources. Among these are fluid bearings and seals, turbine aerodynamic forces, and shaft internal damping forces. These tangential forces, as well as the restoring and dissipative forces, are usually represented by linear stiffness and damping coefficients. The coefficients for the tangential force are usually called cross-coupled stiffness and damping, respectively. For fluid bearings and seals, the cross-coupled coefficients are directly related to the direct coefficients due to the fundamental physics involved. Black[10] and Muszynska[11] both point out that the relationship is due to the transformation from the coordinate system which rotates with the fluid average velocity to the inertial system. This fluid average velocity is usually slightly less than half the rotor surface speed. This gives rise to the occurrence of instability at near one-half rotor speed. A similar relationship is true for internal damping except that the coordinate system rotates at the rotor speed. The onset speed of instability is determined by examining the stability for various speeds and observing the value of speed that causes the rotor to be unstable. This can be accomplished using Routh-Hurwitz techniques or by calculating the system eigenvalues. For fluid bearings and seals, it can be shown that the onset speed is approximately equal to the system resonance divided by the ratio of average fluid velocity to rotor surface speed. Hence, for half synchronous (rotor speed) instability, the onset speed is twice the first resonance.

The restoring, dissipative, and tangential forces discussed above are, in general, nonlinear functions of displacement, velocity, and acceleration. Linearizing these functions about an equilibrium point as discussed by Gunter[12] results in the linear coefficients used in the stability analysis. The onset speed of instability determined by the subsequent analysis addresses stability in the small. Due to the nonlinearities, a system may be globally stable when the linearized analysis predicts an instability. A system in this condition could exhibit a limit cycle instability. Sometimes the nonlinearity is in the form of a clearance or deadband in the restoring force. This can occur for example when a seal rotor rubs on the stator or when rolling element bearings are mounted with clearance between the outer race and the support. The nonlinear restoring force can be represented by a piecewise linear function whose value is zero before the clearance is passed and whose slope is equal to the "linear" stiffness of the bearing after it is passed. If all other force elements are linear, the global onset speed of instability can be determined by assuming the value of the clearance to be zero.[13] In this case, limit cycle instabilities can occur at speeds below the global onset speed. The frequency of the limit cycle is determined by the nature of the

tangential force. For a system with linear fluid forces and clearance in the restoring force, if the onset speed of instability is twice the linear resonance, the limit cycle will be at a frequency half the rotor synchronous frequency. This is due to the fluid average velocity being approximately half the rotor surface speed. If the fluid average tangential velocity is increased or decreased, the limit cycle frequency will correspondingly increase or decrease.

Several researchers have demonstrated limit cycle instabilities using numerical simulations. Control Dynamics[13] and Day[14] both modeled a single mass rotor with linear direct damping, cross-coupled stiffness, and deadband type nonlinear direct stiffness. Control Dynamics demonstrated cases that exhibited limit cycles and also cases that did not. They also investigated the stability in the small about an equilibrium point and concluded that global stability is not affected by deadband (clearance). Day also demonstrated cases that exhibited limit cycle instabilities and cases that did not. He searched (unsuccessfully) for analytical expressions defining the transition points between cases with limit cycle instabilities and cases which only exhibit synchronous response to unbalance excitation. Muszynska[15] numerically and experimentally demonstrated limit cycle instability in which more than one mode (resonance) was unstable. As speed was increased, the first mode became unstable. As speed was further increased, the second mode became unstable and the limit cycle of the first mode was suppressed.

The understanding of subharmonic response and limit cycle instability as independent phenomena is important for many problems that occur in practice. However, of equal importance is an understanding of the relationship between each and the response of machinery that is simultaneously susceptible to both. High performance turbomachinery falls into this category. In fact, any rotating machinery that is operating above a critical speed, has nonlinear restoring forces, has static loads and/or misalignments, and has tangential fluid forces can be susceptible to both phenomenon. When the frequency of the limit cycle instability is close to a fraction of rotor speed (e.g., 1/2) it may be confused with subharmonic response. In fact, if the results of Hayashi[1] extend to more complex systems, the limit cycle can become entrained by subharmonic response. A relationship between the two can be intuitively expected. In simple terms, a subharmonic response is caused by the (response amplitude dependent) frequency of a nonlinear system's resonance tuning itself to be at a fraction of the excitation frequency so that it will be reinforced. Likewise, the limit cycle instability is due to the frequency of a nonlinear system's resonance tuning itself so that the (response amplitude dependent) real part of the eigenvalue is zero, yielding a sustained transient.

No other work is known to the author which explores the simultaneous susceptibility to these two phenomena, or the relationship between them in rotordynamic systems. The previous work on subharmonic response generally neglected self-excitation forces that could lead to instability. The previous work on instability did not include the proper conditions to cause subharmonic response. The work by Control Dynamics[13] was contrived to represent fluid forces for a seal with average velocity exactly half the rotor surface velocity. This resulted in a limit cycle at exactly half rotor synchronous frequency. It is impossible to differentiate between the two in this case.

Hayashi[1] examines the behavior of a self-oscillatory second-order system (van der Pol's equation with periodic forcing term) in the transition between almost periodic oscillations (limit cycle whose frequency is not a rational fraction of the excitation frequency) and subharmonic entrainment of these limit cycles. He defines (in terms of the external force parameters) regions

in which entrainment will occur. A similar determination is proposed as part of this work; however, due to the nature of the nonlinearity to be studied here (deadband in the radial restoring force) a purely analytical treatment becomes intractable. A combination of numerical and analytical approaches must be used. In addition, since it will be desirable to investigate complex realistic systems, a comprehensive numerical analysis tool is needed to model and simulate the systems. Such a tool has been developed by the author in order to conduct the proposed research. The tool consists of a package of computer programs to perform linear stability, linear harmonic response, and nonlinear transient analyses of general turbomachinery.

The objective of this research is threefold: (1) to characterize limit cycle instability and subharmonic entrainment and determine interrelationships between them, (2) to determine regions in parameter space for the existence of each and thereby establish criteria for their avoidance, and (3) to attempt to provide guidance for the interpretation of test data with regard to impending divergent instabilities based on observation of subharmonic response or limit cycle instability. The investigation begins using the nondimensionalized equations of a single mass rotor with the appropriate characteristics. This study employs both analytical and numerical techniques. The extension of the single mass model results to a complex, realistic system is demonstrated by examining the HPFTP of the SSME. Available test data are examined and linear analyses and nonlinear simulations performed.

II. MODEL FORMULATION

The initial model used in this study is a greatly simplified representation of a turbopump. The model possesses only 2 DOF and, yet, it contains all the characteristics that are germane to the phenomena being studied. A model which provides a more complex representation of a turbopump is developed in appendix A. The simplified model can be obtained from the more complex one, however, its development will be included here for clarity.

The simplified turbopump model consists of a single mass supported on symmetric supports. The supports represent rolling element bearings or fluid film bearings and seals. They are treated as linear spring and damper elements with the exception of including clearance or deadband in the rolling element bearing force deflection relationship. The shaft flexibility would also be included in the linear support spring. Fluid film bearings or seals require the inclusion of cross-coupled stiffness and damping terms in order to characterize their influence on rotor behavior. The model is excited by three different sources. Rotor mass unbalance provides excitation at the shaft spin frequency (synchronous). Circumferential pressure distributions in a turbopump are represented by fixed direction loads (side loads) at zero frequency. Random noise is used to represent a variety of broadband random excitations that may exist in a turbopump and to serve as a perturbation to investigate the behavior of the nonlinear system. Figure 1 provides a schematic diagram of the system and defines the coordinate systems used in the derivation of the equations of motion.

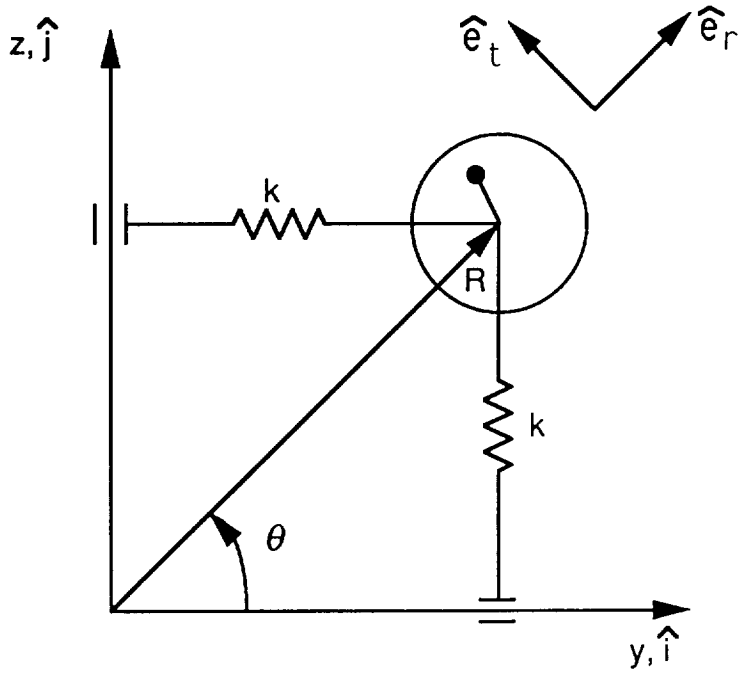

Figure 1. Schematic of simplified rotor model.

The equations of motion are derived from a straightforward application of Newton's second law of motion. Application of this law along the $\hat{i}$ and $\hat{j}$ axes yields

$$ma_y = \sum F_y \ , \tag{1}$$

$$ma_z = \sum F_z \ , \tag{2}$$

and along the $\hat{e}_r$ and $\hat{e}_t$ axes yields

$$ma_r = \sum F_r \ , \tag{3}$$

$$ma_t = \sum F_t \ . \tag{4}$$

The component forces can be categorized as nonlinear support forces, linear support forces, and excitation forces. The force-deflection curve for the nonlinear support force is shown in figure 2. The displacement vector diagram is shown in figure 3a. The force in the direction of radial displacement R can be written directly as

$$F_{r_n} = \begin{cases} -k_n\,(R-\delta) & \text{if } R>\delta \\ 0 & \text{if } R\le\delta \end{cases} \ . \tag{5}$$

This radial force can be resolved into its components along the $\hat{i}$ and $\hat{j}$ axes yielding (for $R>\delta$)

$$F_{y_n} = F_{r_n}\frac{Y}{R} = -k_n\left(1-\frac{\delta}{R}\right)Y \ , \tag{6}$$

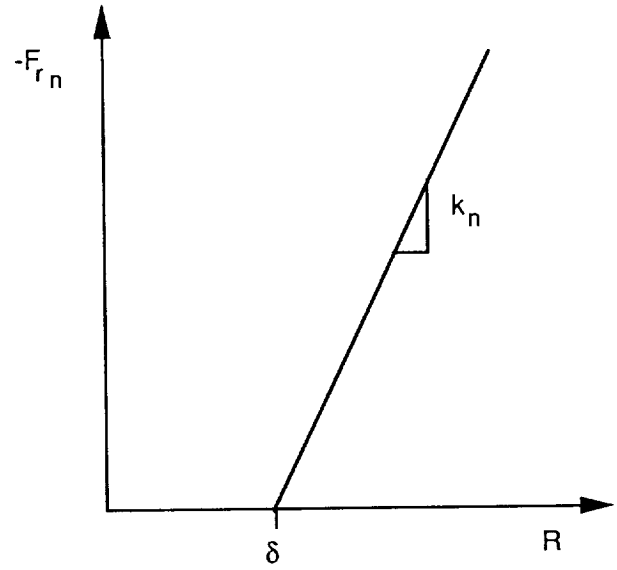

Figure 2. Nonlinear support force deflection curve.

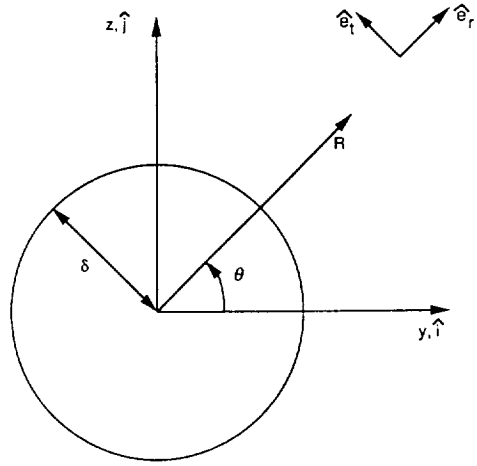

(a) Displacement vectors.

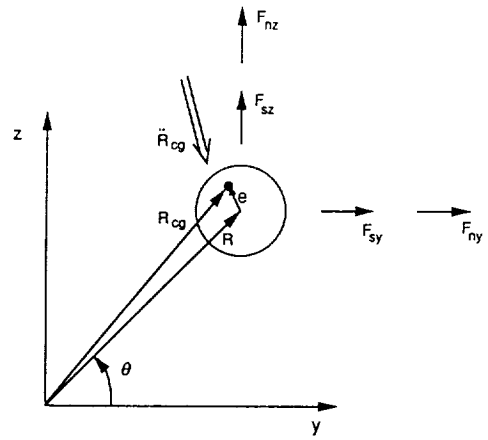

(b) Force vectors.

Figure 3. Vector diagrams for simplified rotor model.

$$F_{z_n} = F_{r_n}\frac{Z}{R} = -k_n\left(1-\frac{\delta}{R}\right)Z \ . \tag{7}$$

The linear support forces can be written in radial and tangential component form as

$$F_{r_l}\hat{e}_r + F_{t_l}\hat{e}_t = (-k_l R - c\dot{R})\,\hat{e}_r + (-cR\dot{\theta} + QR)\,\hat{e}_t \ . \tag{8}$$

Transforming these into cartesian components yields

$$F_{y_l}\hat{i} + F_{z_l}\hat{j} = (-k_l Y - c\dot{Y} - QZ)\,\hat{i} + (-k_l Z - c\dot{Z} + QY)\,\hat{j} \ . \tag{9}$$

The fixed direction side loads and random noise forces are shown in figure 3b. The unbalance excitation force is a natural consequence of the proper differentiation (twice) of the displacement vector of the center of mass. This vector can be written in either cartesian or polar coordinates as the sum of the displacement of the geometric center and the mass eccentricity vector.

$$\begin{aligned} R_{cg} &= (R + e\cos(\beta-\theta))\hat{e}_r + e\sin(\beta-\theta)\hat{e}_t \\ &= (Y + e\cos(\beta))\hat{i} + (Z + e\sin(\beta))\hat{j} \ . \end{aligned} \tag{10}$$

The angle β is defined as the rotation angle of the rotor and can be written as

$$\beta = \int_0^t \int_0^{\tilde{t}} \alpha(t^*)\,dt^*\,d\tilde{t} = \int_0^t \omega(\tilde{t})\,d\tilde{t} \ , \tag{11}$$

where α is the angular acceleration and ω is the angular velocity of the rotor. Differentiating equation (10) twice with respect to time yields

$$\begin{aligned} \frac{d^2}{dt^2}(R_{cg}) &= \left[\ddot{R} - \dot{\theta}^2 R - \dot{\beta}^2 e\cos(\beta-\theta) - \ddot{\beta}e\sin(\beta-\theta)\right]\hat{e}_r \\ &\quad + (R\ddot{\theta} + 2\dot{R}\dot{\theta} - \dot{\beta}^2 e\sin(\beta-\theta) + \ddot{\beta}e\cos(\beta-\theta)]\hat{e}_t \\ &= [\ddot{Y} - \dot{\beta}^2 e\cos(\beta) - \ddot{\beta}e\sin(\beta)]\hat{i} + [\ddot{Z} - \dot{\beta}^2 e\sin(\beta) + \ddot{\beta}e\cos(\beta)]\hat{j} \ . \end{aligned} \tag{12}$$

The appropriate expressions (cartesian or polar) from equations (5) through (12) can be substituted into equations (1) and (2) or equations (3) and (4), respectively, yielding the equations of motion for the system. These equations in cartesian form are

$$m\ddot{Y} + c\dot{Y} + k_l Y + QZ + k_n\left(1-\frac{\delta}{R}\right)u(R-\delta)Y = me\dot{\beta}^2\cos(\beta) + me\ddot{\beta}\sin(\beta) + F_{sy} + F_{ny} \ , \tag{13}$$

$$m\ddot{Z} + c\dot{Z} + k_l Z - QY + k_n\left(1-\frac{\delta}{R}\right)u(R-\delta)Z = me\dot{\beta}^2\sin(\beta) - me\ddot{\beta}\cos(\beta) + F_{sz} + F_{nz} \ , \tag{14}$$

and in polar form are

$$m\ddot{R}+c\dot{R}+k_l R-m\dot{\theta}^2 R+k_n(R-\delta)u(R-\delta) = me\dot{\beta}^2\cos(\beta-\theta)+me\ddot{\beta}\sin(\beta-\theta)$$
$$+(F_{sy}+F_{ny})\cos(\theta)+(F_{sz}+F_{nz})\sin(\theta) \ , \tag{15}$$

$$mR\ddot{\theta}+2m\dot{R}\dot{\theta}+cR\dot{\theta}-QR = me\dot{\beta}^2\sin(\beta-\theta)-me\ddot{\beta}\cos(\beta-\theta)-(F_{sy}+F_{ny})\sin(\theta)$$
$$+(F_{sz}+F_{nz})\cos(\theta) \ , \tag{16}$$

where

$$u(R-\delta) = \begin{cases} 1 & \text{if } R > \delta \\ 0 & \text{if } R \le \delta \end{cases} . \tag{17}$$

Noting from equation (11) that $\dot{\beta} = \omega$ and $\ddot{\beta} = \alpha$ and rearranging the linear and nonlinear stiffness terms yields

$$m\ddot{Y}+c\dot{Y}+k\left[1-\gamma(1-u(R-\delta))-\gamma\frac{\delta}{R}u(R-\delta)\right]Y+QZ = me\omega^2\cos(\beta)$$
$$+me\alpha\sin(\beta)+F_{sy}+F_{ny} \ , \tag{18}$$

$$m\ddot{Z}+c\dot{Z}+k\left[1-\gamma(1-u(R-\delta))-\gamma\frac{\delta}{R}u(R-\delta)\right]Z-QY = me\omega^2\sin(\beta)$$
$$-me\alpha\cos(\beta)+F_{sz}+F_{nz} \ , \tag{19}$$

in cartesian coordinates and

$$m\ddot{R}+c\dot{R}-m\dot{\theta}^2 R+k\left[1-\gamma(1-u(R-\delta))-\gamma\frac{\delta}{R}u(R-\delta)\right]R = me\omega^2\cos(\beta-\theta)+me\alpha\sin(\beta-\theta)$$
$$+(F_{sy}+F_{ny})\cos(\theta)+(F_{sz}+F_{nz})\sin(\theta) \ , \tag{20}$$

$$mR\ddot{\theta}+2m\dot{R}\dot{\theta}+cR\dot{\theta}-QR = me\omega^2\sin(\beta-\theta)-me\alpha\cos(\beta-\theta)$$
$$-(F_{sy}+F_{ny})\sin(\theta)+(F_{sz}+F_{nz})\cos(\theta) \ , \tag{21}$$

in polar coordinates where

$$k = k_l+k_n \ , \tag{22}$$

and

$$\gamma = \frac{k_n}{k} . \tag{23}$$

The bracketed expression multiplying k in equations (18) to (20) is arranged in a way that highlights the two regions of this nonlinear function. For $R \le \delta$, the third term within the brackets is zero and the expression reduces to the linear form $[1-\gamma]$. For $R > \delta$, the second term is zero and the expression reduces to $\left[1-\gamma\frac{\delta}{R}\right]$.

In order to generalize the results from this study, it is advantageous to reduce these equations to a dimensionless form. This also has the benefit of reducing the number of parameters in the problem. The first step is to divide equations (18) through (21) by m. When this is performed, it is convenient to make the following definitions:

$$\frac{k}{m} = \omega_n^2 , \tag{24}$$

$$\frac{c}{m} = 2\zeta\omega_n , \tag{25}$$

ω_n and ζ correspond to the undamped natural frequency and damping ratio for this system with the deadband (δ) and the cross-coupled stiffness (Q) both set to zero. Substituting these definitions yields the cartesian equations

$$\ddot{Y}+2\zeta\omega_n\dot{Y}+\omega_n^2\left[1-\gamma\,(1-u(R-\delta))-\gamma\frac{\delta}{R}\,u(R-\delta)\right]Y+\frac{Q}{m}Z = e\omega^2\cos(\beta)$$

$$+e\alpha\sin(\beta)+\frac{F_{sy}}{m}+\frac{F_{ny}}{m} , \tag{26}$$

$$\ddot{Z}+2\zeta\omega_n\dot{Z}+\omega_n^2\left[1-\gamma\,(1-u(R-\delta))-\gamma\frac{\delta}{R}\,u(R-\delta)\right]Z-\frac{Q}{m}Y = e\omega^2\sin(\beta)$$

$$-e\alpha\cos(\beta)+\frac{F_{sz}}{m}+\frac{F_{nz}}{m} , \tag{27}$$

and the polar equations

$$\ddot{R}+2\zeta\omega_n\dot{R}-\dot{\theta}^2R+\omega_n^2\left[1-\gamma\,(1-u(R-\delta))-\gamma\frac{\delta}{R}\,u(R-\delta)\right]R = e\omega^2\cos(\beta-\theta)+e\alpha\sin(\beta-\theta)$$

$$+\left(\frac{F_{sy}+F_{ny}}{m}\right)\cos(\theta)+\left(\frac{F_{sz}+F_{nz}}{m}\right)\sin(\theta) , \tag{28}$$

$$R\ddot{\theta}+2\dot{R}\dot{\theta}+2\zeta\omega_nR\dot{\theta}-\frac{Q}{m}R = e\omega^2\sin(\beta-\theta)-e\alpha\cos(\beta-\theta)$$

$$-\left(\frac{F_{sy}+F_{ny}}{m}\right)\sin(\theta)+\left(\frac{F_{sz}+F_{nz}}{m}\right)\cos(\theta) . \tag{29}$$

Next, time is normalized by the following substitutions:

$$t = \frac{\tau}{\omega_n} , \tag{30}$$

$$\dot{\xi} = \frac{d\xi}{dt} = \omega_n \frac{d\xi}{d\tau} = \omega_n \xi' \ , \tag{31}$$

$$\ddot{\xi} = \omega_n^2 \xi'' \ . \tag{32}$$

In these expressions, ξ represents any variable which is being differentiated. Performing these substitutions and dividing through each equation by ω_n^2 yields the cartesian equations

$$Y''+2\zeta Y'+\left[1-\gamma\left(1-u(R-\delta)\right)-\gamma\frac{\delta}{R}u(R-\delta)\right]Y+qZ = e\rho^2\cos(\beta)+e\mu\sin(\beta)+\frac{F_{sy}}{k}+\frac{F_{ny}}{k} \ , \tag{33}$$

$$Z''+2\zeta Z'+\left[1-\gamma\left(1-u(R-\delta)\right)-\gamma\frac{\delta}{R}u(R-\delta)\right]Z-qY = e\rho^2\sin(\beta)-e\mu\cos(\beta)+\frac{F_{sz}}{k}+\frac{F_{nz}}{k} \ , \tag{34}$$

and the polar equations

$$R''+2\zeta R'-\theta'^2R+\left[1-\gamma\left(1-u(R-\delta)\right)-\gamma\frac{\delta}{R}u(R-\delta)\right]R = e\rho^2\cos(\beta-\theta)+e\mu\sin(\beta-\theta)$$
$$+\left(\frac{F_{sy}+F_{ny}}{k}\right)\cos(\theta)+\left(\frac{F_{sz}+F_{nz}}{k}\right)\sin(\theta) \ , \tag{35}$$

$$R\theta''+2R'\theta'+2\zeta R\theta'-qR = e\rho^2\sin(\beta-\theta)-e\mu\cos(\beta-\theta)-\left(\frac{F_{sy}+F_{ny}}{k}\right)\sin(\theta)$$
$$+\left(\frac{F_{sz}+F_{nz}}{k}\right)\cos(\theta) \ , \tag{36}$$

where

$$q = \frac{Q}{m\omega_n^2} = \frac{Q}{k} \ , \tag{37}$$

$$\rho = \frac{\omega}{\omega_n} \ , \tag{38}$$

and

$$\mu = \frac{\alpha}{\omega_n^2} \ . \tag{39}$$

The angle β defined by equation (11) can be expressed in terms of τ, ρ, and μ as follows:

$$\beta = \int_0^\tau \int_0^{\bar{\tau}} \omega_n^2 \mu(\tau^*) \frac{d\tau^*}{\omega_n} \frac{d\bar{\tau}}{\omega_n} = \int_0^\tau \int_0^{\bar{\tau}} \mu(\tau^*) d\tau^* d\bar{\tau} = \int_0^\tau \rho(\bar{\tau}) d\bar{\tau} \ . \tag{40}$$

The final step in the nondimensionalization process is to define the following new variables

$$Y = y\delta, \tag{41}$$

$$Z = z\delta, \tag{42}$$

$$R = r\delta. \tag{43}$$

Substituting equations (41) through (43) into equations (33) through (36) and dividing through by δ yields the cartesian equations

$$y''+2\zeta y'+\left[1-\gamma(1-u(r-1))-\frac{\gamma}{r}u(r-1)\right]y+qz = a\rho^2\cos(\beta)+a\mu\sin(\beta)+g_y+\eta_y\ , \tag{44}$$

$$z''+2\zeta z'+\left[1-\gamma(1-u(r-1))-\frac{\gamma}{r}u(r-1)\right]z-qy = a\rho^2\sin(\beta)-a\mu\cos(\beta)+g_z+\eta_z\ , \tag{45}$$

and the polar equations

$$r''+2\zeta r'-\theta'^2 r+\left[1-\gamma(1-u(r-1))-\frac{\gamma}{r}u(r-1)\right]r = a\rho^2\cos(\beta-\theta)+a\mu\sin(\beta-\theta)$$
$$+(g_y+\eta_y)\cos(\theta)+(g_z+\eta_z)\sin(\theta)\ , \tag{46}$$

$$r\theta''+2r'\theta'+2\zeta r\theta'-qr = a\rho^2\sin(\beta-\theta)-a\mu\cos(\beta-\theta)-(g_y+\eta_y)\sin(\theta)$$
$$+(g_z+\eta_z)\cos(\theta)\ , \tag{47}$$

where

$$a = \frac{e}{\delta}, \tag{48}$$

$$g_y = \frac{F_{sy}}{k\delta}\ , \tag{49}$$

$$g_z = \frac{F_{sz}}{k\delta}\ , \tag{50}$$

$$\eta_y = \frac{F_{ny}}{k\delta}\ , \tag{51}$$

$$\eta_z = \frac{F_{nz}}{k\delta}\ . \tag{52}$$

These equations contain a total of 10 dimensionless parameters. The number of parameters can be reduced by making a few assumptions. First, since the system is symmetric, g_z can be assumed to be zero without loss of generality. Second, for the cases to be investigated here,

μ will be very small and can be neglected. Finally, η_y and η_z are assumed to be uniform random number sequences with the same range $(-\overline{\eta},\overline{\eta})$. These assumptions yield a total of seven dimensionless parameters: g_y, a, ρ, ζ, q, γ, and $\overline{\eta}$. A complete parametric study including all seven parameters is not feasible; however, a subset of the most significant will be selected based on the analyses discussed in the next section.

III. ANALYTICAL TREATMENT

The system model defined in the previous section can be analyzed in several ways. The equations can be linearized about various equilibrium conditions in either the cartesian or polar form. This approach is appropriate when examining limit cycle instability. The forced response can be determined for the nonlinear system using a harmonic balance procedure. This is appropriate when examining subharmonic resonance. This method requires a combined analytical/numerical approach in order to determine a solution. Each of the linearizations and the harmonic balance method yield certain insights into the characteristics of the system; however, no single approach is adequate to describe the general case.

A. Linear Stability

The simplest approach to linearization is to neglect the deadband (δ) by assuming it to be zero. For this approach, equations (33) through (36) must be used since equations (44) through (47) are based on nondimensionalizing equations (33) through (36) using δ as the basis. As discussed in reference 13, the stability determined in this manner is the global stability. Working with the cartesian equations, the Routh criterion will be applied to the characteristic equation for the system to determine the stability boundary. Applying the $\delta = 0$ assumption to equations (33) through (34) yields

$$Y''+2\zeta Y'+Y+qZ = e\rho^2 \cos(\beta) + e\mu \sin(\beta) + \frac{F_{sy}}{k} + \frac{F_{ny}}{k} , \tag{53}$$

$$Z''+2\zeta Z'+Z-qY = e\rho^2 \sin(\beta) - e\mu \cos(\beta) + \frac{F_{sz}}{k} + \frac{F_{nz}}{k} . \tag{54}$$

Stability of the system is determined from the homogeneous solution to these equations. Assuming solutions of the form

$$Y = \overline{Y} e^{\lambda t} , \tag{55}$$

$$Z = \overline{Z} e^{\lambda t} , \tag{56}$$

results in the following algebraic equation:

$$\begin{bmatrix} \lambda^2+2\zeta\lambda+1 & q \\ -q & \lambda^2+2\zeta\lambda+1 \end{bmatrix} \begin{Bmatrix} \overline{Y} \\ \overline{Z} \end{Bmatrix} = \begin{Bmatrix} 0 \\ 0 \end{Bmatrix} . \tag{57}$$

This equation has a nontrivial solution only when the determinant of the matrix is zero. Expanding this determinant yields the characteristic equation for the system,

$$\lambda^4+4\zeta\lambda^3+(4\zeta^2+2)\lambda^2+4\zeta\lambda+1+q^2=0 \ . \tag{58}$$

Applying the Routh test to this polynomial yields the following array:

λ^4	1	$4\zeta^2+2$	$1+q^2$
λ^3	4ζ	4ζ	
λ^2	$4\zeta^2+1$	$1+q^2$	
λ^1	$\frac{4\zeta(4\zeta^2-q^2)}{4\zeta^2+1}$		
λ^0	$1+q^2$		

For positive ζ, the only possible sign change in the first column occurs in the λ^1 row. This term will remain positive as long as

$$\frac{q}{2\zeta}<1 \ . \tag{59}$$

Therefore, equation (59) is the stability criterion for the system. In terms of the original system parameters given in equations (18) through (21), this condition becomes

$$\frac{Q}{c}<\sqrt{\frac{k}{m}}=\omega_n \ . \tag{60}$$

As discussed in section I, there is generally a relationship between Q and c (or q and 2ζ) that is determined by the fluid dynamics of the particular system under consideration. This relationship is generally a function of rotor speed. The form of this relationship that is assumed in this study is discussed later.

It is of interest to determine the roots of the characteristic equation (equation (58)) in the marginally stable condition $\left(\frac{q}{2\zeta}=1\right)$. Equation (58) can be expressed in factored form as

$$(\lambda^2+2\zeta\lambda+1+jq)\ (\lambda^2+2\zeta\lambda+1-jq)=0 \ . \tag{61}$$

The roots of this equation can be determined by applying the quadratic formula to each term yielding

$$\lambda_i=-\zeta\pm\sqrt{\zeta^2-1\pm jq} \ . \tag{62}$$

Substituting $q=2\zeta$ into equation (62) yields the four roots

$$\lambda_{1,2}=\pm j1 \ , \tag{63}$$

$$\lambda_{3,4} = -2\zeta \pm j1 \ . \tag{64}$$

These roots can be related back to unnormalized time yielding

$$\lambda^*_{1,2} = \pm j\omega_n \ , \tag{65}$$

$$\lambda^*_{3,4} = -2\zeta\omega_n \pm j\omega_n \ . \tag{66}$$

It can be seen from comparing equations (59) through (66) that the frequency of the instability is equal to ω_n and the instability occurs when the ratio $\frac{Q}{c}$ is equal to ω_n. It will be shown next that for the nonlinear system ($\delta \neq 0$) the frequency of the limit cycle that can occur when $\frac{Q}{c}$ is less than ω_n is equal to $\frac{Q}{c}$ for certain cases.

B. Self-Excited Equilibrium

The approach taken next is to seek an equilibrium solution to the nonlinear, homogeneous equations in polar form. The homogeneous form of equations (46) and (47) is first rewritten for two cases, $r \leq 1$ and $r > 1$. For $r \leq 1$ the result is

$$r'' + 2\zeta r' - \theta'^2 r + (1-\gamma)r = 0 \ , \tag{67}$$

$$r\theta'' + 2r'\theta' + 2\zeta r\theta' - qr = 0 \ . \tag{68}$$

For $r > 1$ the $\hat{e}_t$ equation is identical to equation (68) and the $\hat{e}_r$ equation is given by

$$r'' + 2\zeta r' - \theta'^2 r + r - \gamma = 0 \ . \tag{69}$$

For an equilibrium solution, the quantities r'', r', and θ'' are all zero. Eliminating these terms from equation (68) yields the equation governing the equilibrium angular velocity

$$2\zeta r_0 \theta'_0 - q r_0 = 0 \ , \tag{70}$$

or expressed explicitly

$$\theta'_0 = \frac{q}{2\zeta} \ . \tag{71}$$

This applies for all values of r. It should be noted that this is the ratio that governs the system global stability as shown in the preceding paragraphs. For the case where $r \leq 1$, eliminating the same quantities as before in equation (67) yields the equation governing the equilibrium radius

$$(1 - \gamma - \theta'^2_0)\, r_0 = 0 \ . \tag{72}$$

The only equilibrium solution to this equation is $r = 0$ which was expected since, for this range of r, the system is linear. For the case where $r > 1$, the same quantities are eliminated from equation (69) yielding

$$(1-\theta'^2_0)\, r_0-\gamma=0 \ , \tag{73}$$

or explicitly

$$r_0=\frac{\gamma}{1-\theta'^2_0}=\frac{\gamma}{1-\left(\frac{q}{2\zeta}\right)^2} \ . \tag{74}$$

In order for a nonzero solution to exist for r_0, r_0 must have a value greater than 1. Examination of equation (74) shows that to meet this condition, $\frac{q}{2\zeta}$ must be greater than $\sqrt{1-\gamma}$. This can be recognized as the instability criterion for the linear system obtained for the case $r \leq 1$. In other words, if the linear system defined for the case of the radial deflection being less than the dead-band is stable, no equilibrium solution (other than $r_0 = 0$) is possible. If the linear system is unstable, the equilibrium radius is governed by equation (74). This equilibrium motion represents a limit cycle instability. It can also be seen from equation (74) that at the global stability boundary, $\frac{q}{2\zeta} = 1$, the solution is unbounded, as would be expected.

C. Mass Unbalance Equilibrium

The self-excited equilibrium determined in the above paragraph gives insight into the behavior of the system; however, it does not represent a very practical case since it is completely unforced. Another case of interest is the equilibrium solution to the system when excited only by mass unbalance. The solution is assumed to be harmonic with frequency equal to the excitation frequency (synchronous response), i.e., $\theta'_0 = \rho$.The equilibrium assumptions are applied to equations (46) and (47) (assuming $\mu = 0$). The result for $r \leq 1$ is

$$(1-\gamma-\rho^2)\, r_0 = a\rho^2 \cos\,(\beta-\theta) \ , \tag{75}$$

$$(2\zeta\rho-q)\, r_0 = a\rho^2 \sin\,(\beta-\theta) \ . \tag{76}$$

For $r > 1$ the $\hat{e}_t$ equation is identical to equation (76) and the $\hat{e}_r$ equation is

$$(1-\rho^2)\, r_0-\gamma= a\rho^2 \cos\,(\beta-\theta) \ . \tag{77}$$

Equations (75) and (76) can be solved simultaneously for r_0 yielding

$$r_0=\frac{a\rho^2}{\sqrt{(1-\gamma-\rho^2)^2+(2\zeta\rho-q)^2}} \ , \tag{78}$$

for $r \leq 1$. Equations (77) and (76) can be solved simultaneously for r_0 yielding

$$r_0=\frac{(1-\rho^2)\gamma\pm\sqrt{a^2\rho^4(1-\rho^2)^2+a^2\rho^4(2\zeta\rho-q)^2-\gamma^2(2\zeta\rho-q)^2}}{(1-\rho^2)^2+(2\zeta\rho-q)^2} \ , \tag{79}$$

for $r > 1$. Equation (78) is valid for all values of the parameters for which the linear system defined for the case of $r \leq 1$ is stable. Three conditions must be met for equation (79) to be valid. First, the quantity under the radical must be greater than zero since r must be real valued. Second, one of the differential equations from which equation (79) was derived (equation (69)) is only valid for $r > 1$; therefore, the predicted value of r must be greater than 1. Third, the equilibrium must be stable (determined in a following section).

D. Side-Force Equilibrium

A third equilibrium point of interest is the case with fixed direction side forces and no unbalance. The solution is assumed to be static, i.e., all time derivatives are equal to zero. Applying these assumptions to equations (46) and (47) (and recalling that g_z was assumed to be zero in section II) yields

$$(1-\gamma)r_0 = g_y \cos(\theta_0) \ , \tag{80}$$

$$qr_0 = g_y \sin(\theta_0) \ , \tag{81}$$

for $r \leq 1$. For $r > 1$, the $\hat{e}_t$ equation is identical to equation (81) and the $\hat{e}_r$ equation is

$$r_0 - \gamma = g_y \cos(\theta_0) \ . \tag{82}$$

Solving equations (80) and (81) for the case of $r \leq 1$ yields

$$r_0 = \frac{g_y}{\sqrt{(1-\gamma)^2+q^2}} \ , \tag{83}$$

$$\theta_0 = \tan^{-1}\left(\frac{q}{1-\gamma}\right) \ . \tag{84}$$

This solution can easily be expressed in terms of cartesian coordinates as

$$y_0 = \frac{g_y(1-\gamma)}{(1-\gamma)^2+q^2} \ , \tag{85}$$

$$z_0 = \frac{g_y q}{(1-\gamma)^2+q^2} \ . \tag{86}$$

For the case of $r > 1$, equations (81) and (82) yield the following quadratic equation in r_0,

$$(1+q^2)r_0^2 - 2\gamma r_0 + \gamma^2 - g_y^2 = 0 \ . \tag{87}$$

The solution of this equation is found to be

$$r_0 = \frac{\gamma + \sqrt{g_y^2(1+q^2) - q^2\gamma^2}}{1+q^2} \quad . \tag{88}$$

It can be shown that for all cases where r_0 predicted by equation (83) is greater than 1, the quantity under the radical in equation (88) is greater than zero. The corresponding solution for θ_0 is

$$\theta_0 = \tan^{-1}\left(\frac{qr_0}{r_0 - \gamma}\right) \quad . \tag{89}$$

Equations (88) and (89) can be transformed into cartesian coordinates yielding

$$y_0 = r_0 \cos(\theta_0) \quad , \tag{90}$$

$$z_0 = r_0 \sin(\theta_0) \quad . \tag{91}$$

E. Linearization About Self-Excited Equilibrium

Equilibrium solutions have now been determined for three specific cases of interest. These cases are the self-excited system (equations (71) and (74)), the synchronous response to unbalance excitation (equations (78) and (79)), and the static response to side forces (equations (83) through (91)). Linearizations of the equations of motion can be determined for each of these cases. The polar form of the equations will be used for the first two cases and the cartesian form for the last.

Linearization of the equations of motion is only necessary for $r > 1$ since the system is already linear for $r \leq 1$. The linearized form of the equations of motion for the first two cases can be developed together. The appropriate excitation terms can be dropped in order to obtain the equations for the self-excited case. Equations (46) and (47) are used with only the unbalance excitation forces retained. Also, as in the determination of the equilibrium solution, the angular acceleration μ is assumed to be zero. The resulting equations are

$$r'' + 2\zeta r' - \theta'^2 r + r - \gamma = a\rho^2 \cos(\beta - \theta) \quad , \tag{92}$$

$$r\theta'' + 2r'\theta' + 2\zeta r\theta' - qr = a\rho^2 \sin(\beta - \theta) \quad . \tag{93}$$

The linear equations will be obtained by examining perturbations about the equilibrium solutions. This is achieved by making the following substitutions into equations (92) and (93):

$$r = r_0 + \bar{r} \quad , \tag{94}$$

$$\theta' = \theta'_0 + \bar{\theta}' \quad . \tag{95}$$

The variables $\bar{r}$ and $\bar{\theta}'$ are the perturbation variables. The linearization is accomplished by making the substitutions and neglecting terms of second order or greater in the perturbation variables.

For the self-excited case the resulting equations are

$$\bar{r}''+2\zeta\bar{r}'+(1-\theta'^2_0)\bar{r}-2\theta'_0 r_0\bar{\theta}' = r_0(\theta'^2_0-1)+\gamma \ , \tag{96}$$

$$r_0\bar{\theta}''+2\theta'_0\bar{r}'+(2\zeta\theta'_0-q)\bar{r}+2\zeta r_0\bar{\theta}' = (q-2\zeta\theta'_0)r_0 \ . \tag{97}$$

The equilibrium conditions are obtained by setting the perturbation terms to zero. The results are identical to those obtained previously (equations (71) and (74)). The stability of this equilibrium is determined from the homogeneous solution of equations (96) and (97). The characteristic equation for this system (with the substitution $\theta'_0 = q/2\zeta$) can be written as

$$\lambda^3+4\zeta\lambda^2+\left(\frac{16\zeta^4+4\zeta^2+3q^2}{4\zeta^2}\right)\lambda+\left(\frac{4\zeta^2-q^2}{2\zeta}\right)=0 \ . \tag{98}$$

It can be shown that the Routh test applied to equation (98) yields the same stability criterion as the global stability criterion given in equation (59).

F. Linearization About Mass Unbalance Equilibrium

For the synchronous response case, the linearized equations are (with the substitution $\theta'_0 = \rho$)

$$\bar{r}''+2\zeta\bar{r}'+(1-\rho^2)\bar{r}-2\rho r_0\bar{\theta}' = r_0(\rho^2-1)+\gamma+a\rho^2\cos(\beta-\theta) \ , \tag{99}$$

$$r_0\bar{\theta}''+2\rho\bar{r}'+(2\zeta\rho-q)\bar{r}+2\zeta r_0\bar{\theta}' = (q-2\zeta\rho)r_0+a\rho^2\sin(\beta-\theta) \ . \tag{100}$$

Before proceeding with the perturbation analysis, the sine and cosine terms must be expressed in terms of the perturbation variables. For the constant speed condition under consideration, it can be seen from equation (40) that $\beta = \rho\tau+\beta_0$. θ can be written in terms of the perturbation variable as

$$\theta = \int_0^\tau (\theta'_0+\bar{\theta}')d\bar{\tau} = \rho\tau+\theta_0+\int_0^\tau \bar{\theta}'d\bar{\tau} = \rho\tau+\theta_0+\bar{\theta} \ . \tag{101}$$

The resulting argument of the sine and cosine terms in equations (99) and (100) is $\beta_0-\theta_0-\bar{\theta}$. The equilibrium solution for r_0 obtained by setting the perturbation terms to zero is identical to that given in equation (79). The equilibrium solution for the phase angle $\beta_0-\theta_0$ can be expressed implicitly by

$$\cos(\beta_0-\theta_0) = \frac{(1-\rho^2)r_0-\gamma}{a\rho^2} , \tag{102}$$

$$\sin(\beta_0-\theta_0) = \frac{(2\zeta\rho-q)r_0}{a\rho^2} . \tag{103}$$

The terms $\cos(\beta_0-\theta_0-\bar{\theta})$ and $\sin(\beta_0-\theta_0-\bar{\theta})$ can be expanded using elementary trigonometric addition identities into the form

$$\cos(\beta_0-\theta_0-\bar{\theta}) = \cos(\beta_0-\theta_0)+\sin(\beta_0-\theta_0)\bar{\theta} , \tag{104}$$

$$\sin(\beta_0-\theta_0-\bar{\theta}) = \sin(\beta_0-\theta_0)-\cos(\beta_0-\theta_0)\bar{\theta} . \tag{105}$$

The small angle assumptions $\cos(\bar{\theta}) = 1$ and $\sin(\bar{\theta}) = \bar{\theta}$ have already been incorporated into these equations. Equations (102) and (103) are now substituted into equations (104) and (105). The resulting expressions are substituted into equations (99) and (100). Retaining only those terms involving the perturbation variables yields

$$\bar{r}''+2\zeta\bar{r}'+(1-\rho^2)\bar{r}-2\rho r_0\bar{\theta}'-(2\zeta\rho-q)r_0\bar{\theta} = 0 , \tag{106}$$

$$r_0\bar{\theta}''+2\rho\bar{r}'+(2\zeta\rho-q)\bar{r}+2\zeta r_0\bar{\theta}'+((1-\rho^2)r_0-\gamma)\bar{\theta} = 0 . \tag{107}$$

The characteristic equation which results from these homogeneous equations is

$$\lambda^4+4\zeta\lambda^3+\left(4\zeta^2+2\rho^2+2-\frac{\gamma}{r_0}\right)\lambda^2+2\left[2\zeta(1-\rho^2)-\frac{\zeta\gamma}{r_0}+2\rho(2\zeta\rho-q)\right]\lambda$$

$$+(2\zeta\rho-q)^2+(1-\rho^2)\left(1-\rho^2-\frac{\gamma}{r_0}\right) = 0 . \tag{108}$$

This equation involves the equilibrium solution r_0 and, hence, a stability criterion cannot be easily expressed analytically. The stability of this equilibrium will be determined numerically for various values of the system parameters and presented in section IV.

G. Linearization About Side-Force Equilibrium

The side-force equilibrium case will now be treated using the cartesian form of the equations of motion. The equations of motion (equations (44) and (45)) with only side-force excitation can be written as

$$y''+2\zeta y'+qz-g_y = -\left(1-\frac{\gamma}{\sqrt{y^2+z^2}}\right)y , \tag{109}$$

$$z''+2\zeta z'-qy-g_z = -\left(1-\frac{\gamma}{\sqrt{y^2+z^2}}\right)z , \tag{110}$$

where the nonlinear restoring force has been isolated on the right-hand side and r has been expressed explicitly in terms of y and z. The right-hand sides of equations (109) and (110) can be linearized using their Taylor's series expansions about the equilibrium points y_0, z_0. Retaining only the first-order terms and rearranging the equations results in the homogeneous equations

$$\bar{y}''+2\zeta\bar{y}'+\left(1-\frac{\gamma}{\sqrt{y_0^2+z_0^2}}+\frac{y_0^2\gamma}{(y_0^2+z_0^2)^{\frac{3}{2}}}\right)\bar{y}+\left(\frac{y_0z_0\gamma}{(y_0^2+z_0^2)^{\frac{3}{2}}}\right)\bar{z}+q\bar{z}=0\ , \tag{111}$$

$$\bar{z}''+2\zeta\bar{z}'+\left(1-\frac{\gamma}{\sqrt{y_0^2+z_0^2}}+\frac{z_0^2\gamma}{(y_0^2+z_0^2)^{\frac{3}{2}}}\right)\bar{z}+\left(\frac{y_0z_0\gamma}{(y_0^2+z_0^2)^{\frac{3}{2}}}\right)\bar{y}-q\bar{y}=0\ . \tag{112}$$

The equilibrium points (given in equations (90) and (91)) were derived for the case where $g_z = 0$. In examining equations (111) and (112), it would be convenient to be able to consider an equilibrium point on one of the coordinate axes, such as $z_0 = 0$. This can be accomplished without loss of generality by considering the load to be applied at an angle of $-\theta_0$ with respect to the y axis where θ_0 is given by equation (89). In this condition, y_0 will be equal to r_0 as defined by equation (88) and z_0 will be zero. Since the system is symmetric, the stability of this equilibrium point will be identical to the original point. For this case, equations (111) and (112) become

$$\bar{y}''+2\zeta\bar{y}'+\bar{y}+q\bar{z}=0\ , \tag{113}$$

$$\bar{z}''+2\zeta\bar{z}'+\left(1-\frac{\gamma}{r_0}\right)\bar{z}-q\bar{y}=0\ . \tag{114}$$

The corresponding characteristic equation is

$$\lambda^4+4\zeta\lambda^3+\left(2-\frac{\gamma}{r_0}+4\zeta^2\right)\lambda^2+2\zeta\left(2-\frac{\gamma}{r_0}\right)\lambda+1-\frac{\gamma}{r_0}+q^2=0\ . \tag{115}$$

Application of the Routh test to this equation yields the following stability criterion:

$$\frac{q}{2\zeta}<\sqrt{1+\frac{\gamma}{2r_0}\left(\frac{\gamma}{8\zeta^2r_0}-1\right)}\ . \tag{116}$$

Since this relation involves the equilibrium solution r_0. A general conclusion about the stability cannot be drawn. However, for cases where the quantity within the parentheses is positive, this requirement is less restrictive than the global stability criterion (equation (59)). This implies that over some range, the addition of side forces to a system with deadband in the restoring force has a stabilizing influence (in the small). More general results will be presented in section IV by evaluating the roots for various values of the system parameters.

H. Subharmonic Response Analysis

The stability of the system model has been examined for various equilibrium conditions. The solutions obtained provide insight into the characteristics of the limit cycle instability. An understanding of the characteristics of the subharmonic response will now be sought using a

harmonic balance method. The dimensionless cartesian equations (equations (44) and (45)) will be used. The assumptions made previously ($g_z = 0$ and $\mu = 0$) will be made here, and the random noise excitation (η_y and η_z) will be neglected.

The nonlinear restoring forces in equations (44) and (45) can be rewritten to facilitate the development of the harmonic balance equations. The modified equations are

$$y''+2\zeta y'+(1-\gamma)y+qz+f_y(y,z) = a\rho^2 \cos(\rho\tau)+g_y \ , \tag{117}$$

$$z''+2\zeta z'+(1-\gamma)z-qy+f_z(y,z) = a\rho^2 \sin(\rho\tau) \ , \tag{118}$$

where

$$f_y(y,z) = \begin{cases} \gamma\left(1-\dfrac{1}{\sqrt{y^2+z^2}}\right)y & \text{if } \sqrt{y^2+z^2} > 1 \\ 0 & \text{if } \sqrt{y^2+z^2} \le 1 \end{cases} , \tag{119}$$

and

$$f_z(y,z) = \begin{cases} \gamma\left(1-\dfrac{1}{\sqrt{y^2+z^2}}\right)z & \text{if } \sqrt{y^2+z^2} > 1 \\ 0 & \text{if } \sqrt{y^2+z^2} \le 1 \end{cases} . \tag{120}$$

The method used here is essentially the same as that used by Noah.[16] This investigation will be limited to subharmonics of order 2 (one-half synchronous). The solutions for y and z are assumed to be superpositions of a fundamental sinusoidal component and N of its harmonics. The fundamental in this case is the one-half synchronous subharmonic. These solutions are given by

$$y = a_{y_0} + \sum_{n=1}^{N}\left(a_{y_n}\cos\left(n\frac{\rho}{2}\tau\right) - b_{y_n}\sin\left(n\frac{\rho}{2}\tau\right)\right) , \tag{121}$$

$$z = a_{z_0} + \sum_{n=1}^{N}\left(a_{z_n}\cos\left(n\frac{\rho}{2}\tau\right) - b_{z_n}\sin\left(n\frac{\rho}{2}\tau\right)\right) . \tag{122}$$

The nonlinear restoring forces f_y and f_z are approximated by similar harmonic expansions given by

$$f_y = c_{y_0} + \sum_{n=1}^{N}\left(c_{y_n}\cos\left(n\frac{\rho}{2}\tau\right) - d_{y_n}\sin\left(n\frac{\rho}{2}\tau\right)\right) , \tag{123}$$

$$f_z = c_{z_0} + \sum_{n=1}^{N}\left(c_{z_n}\cos\left(n\frac{\rho}{2}\tau\right) - d_{z_n}\sin\left(n\frac{\rho}{2}\tau\right)\right) . \tag{124}$$

Substituting equations (121) through (124) into equations (117) and (118) and performing a harmonic balance yields a set of $4N+2$ linear equations in $8N+4$ unknowns (a_{y_o}, a_{z_o}, c_{y_o}, c_{z_o}, a_{y_i}, a_{z_i}, b_{y_i}, b_{z_i}, c_{y_i}, c_{z_i}, d_{y_i}, d_{z_i}, ..., i = 1,N). The additional $4N+2$ equations needed for a solution are determined from the relationship between f_y and f_z and the solutions y and z given by equations (119) and (120). These equations can be solved using an iterative numerical procedure. The results will provide insight into the effects of the various system parameters on the subharmonic response.

Analytical solutions have been developed for the model formulated in section II. These solutions are expressed in terms of the model parameters. In section IV, numerical values (or ranges of values) will be specified to define the model. The numerical values of the analytical solutions will then be presented for various values of the model variables.

IV. MODEL DEFINITION AND ANALYSIS RESULTS

A simplified single mass model of a turbopump rotor has been formulated in section II. Analytical expressions for various equilibria and linearized stability conditions were obtained in section III. In this section, numerical values and ranges of values will be specified in order to define the model. Using these values, numerical results will be presented for the solutions developed in section III.

A. Model Definition

The model consists of seven dimensionless parameters (g_y, a, ρ, ζ, q, γ, and $\overline{\eta}$). These parameters are defined at the end of section II. The values to be chosen for these parameters will be based in part on the author's experience and in part on the analytical expressions obtained in section III. Initially, the random noise parameter $\overline{\eta}$ will be neglected. This assumption was made in the developments of section III. Parametric studies of the effects of $\overline{\eta}$ will be performed later using simulations.

The nonlinear stiffness to total stiffness ratio (γ) is restricted by its definition to range from zero to one. Typically, in rocket engine turbomachinery, rolling element bearings provide a significant, if not the majority, of the rotor support stiffness. These bearings frequently are mounted with clearance between the outer race and the bearing support. This clearance provides the deadband δ discussed in section II. A value for γ of 0.75 has been selected to represent a typical rotor support situation where clearance mounted bearings provide a majority of the rotor support stiffness.

The dimensionless side load g_y and dimensionless unbalance a were normalized by the deadband δ. Hence, they should have values on the order of unity to represent cases where the rotor is operating in a highly nonlinear fashion. Values much greater than unity will tend to obscure the deadband. Values much less will cause operation in the linear range of the function defining the rotor support (equation (5)). Nominal values of 1.0 and 0.5 have been assigned to g_y and a, respectively.

The shaft angular velocity ρ is a primary parameter in any investigation of rotating machinery, and a wide variety of values will be examined. However, the upper limit of interest is the maximum of the global onset speed, the unbalance stability threshold, and the side-force stability threshold.

As discussed in sections I and III, the dimensionless cross-coupled stiffness q is generally related to the fluid damping 2ζ. This relationship is due to the fluid average tangential velocity being a function of rotor surface velocity. If a fixed ratio is assumed, q can be expressed in terms of this ratio, the rotor speed, and the damping. This ratio is typically slightly less than one half. If the configuration is such that the fluid is entering the fluid seal or bearing with a tangential velocity greater than the rotor surface speed, the ratio can be greater than one half. Designating this ratio as σ, the cross-coupled stiffness can be expressed as

$$q = 2\zeta\rho\sigma \ . \tag{125}$$

Since a primary objective of this study is to examine systems which are simultaneously susceptible to limit cycle instability (governed by σ) and subharmonic resonance, the value of σ has been selected to be 0.48 (close to but slightly less than one half). This ratio has frequently been observed in SSME test data. Values greater than one half will also be examined. The damping ratio ζ is typically low in rocket engine turbomachinery. A nominal value of 0.10 has been assigned to this study. This value is representative of the damping in the HPFTP of the SSME.

Nominal values have been assigned for all parameters of the model. These values are summarized in table 1. The results of the analyses of section III will be presented for these nominal values.

Table 1. Nominal model parameters.

Parameter	Value
g_y	1.0
a	0.5
ρ	0.-4.0
ζ	0.1
σ	0.48
γ	0.75

B. Analysis Results

The first result developed in section III was the stability criterion for the case of zero deadband (equation (59)). Substituting equation (125) into equation (59) results in the criterion

$$\rho < \frac{1}{\sigma} = \frac{1}{0.48} = 2.08 \ . \tag{126}$$

As discussed in section III, this is the global onset speed of instability for the system. It will be designated by ρ_{gi}. The roots of the characteristic equation (equation (58)) are shown in figure 4 for various values of ζ and σ as ρ is varied from 0.0 to 4.0. The plot for variations in ζ shows the roots in the complex plane. As σ is varied, the roots follow identical loci except that the speed correspondence is different. For this reason, the critical damping ratio is displayed for the roots as σ is varied. As expected, the imaginary axis crossing is determined by equation (126).

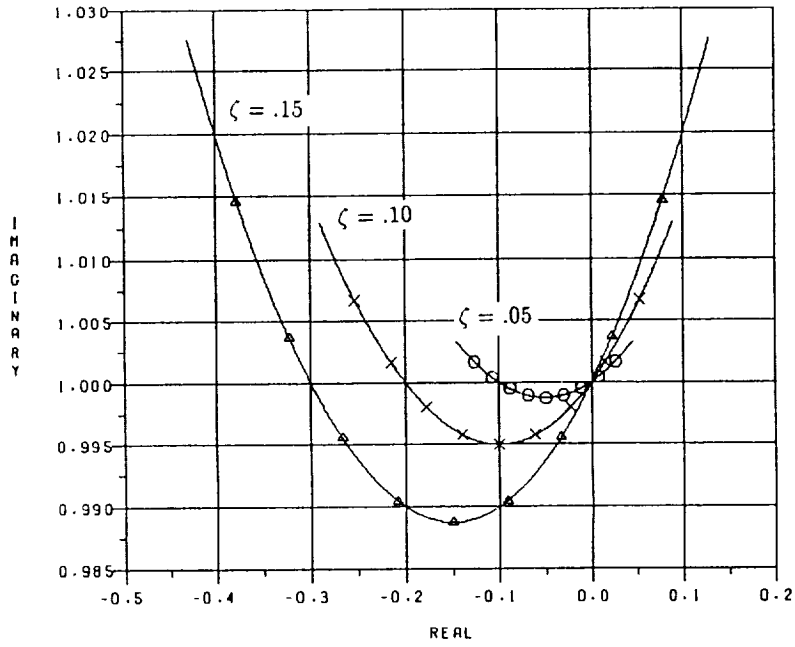

(a) Effects of ζ on roots in complex plane.

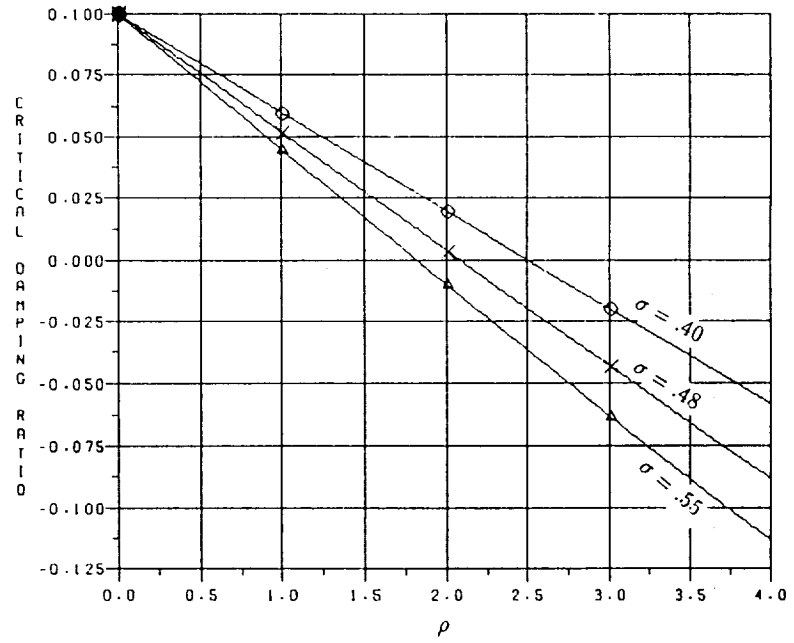

(b) Effects of σ on critical damping ratio of roots.

Figure 4. Roots of characteristic equation (equation (58)) as ρ is varied from 0.0 to 4.0.

The next result developed was for the equilibrium solution to the homogeneous polar equations. The results showed the possibility of a limit cycle instability with a frequency given by equation (71) and radius given by equation (74). Substituting equation (125) into these equations and applying nominal values for the parameters yields

$$\theta'_0 = \sigma\rho = 0.48\rho \ , \tag{127}$$

and

$$r_0 = \frac{0.75}{(1-0.48^2\,\rho^2)} \ . \tag{128}$$

As discussed in section III, this equation is valid only when r_0 is greater than 1. This will be true whenever $q/2\zeta$ is greater than $\sqrt{1-\gamma}$. Expressing this in terms of the parameter values yields

$$\rho \geq \frac{\sqrt{1-\gamma}}{\sigma} = \frac{\sqrt{0.25}}{0.48} = 1.04 \ . \tag{129}$$

Since this is the initial value for which a limit cycle is possible, it will be designated by ρ_{lc}. Equation (128) is plotted in figures 5 and 6 for a range of ρ from zero to the global stability limit. Figure 5 presents the solution for various values of γ and figure 6 for various values of σ. The primary effect of each parameter is to change the range of values of ρ over which the homogeneous equilibrium is possible. γ does not alter the upper limit (ρ_{gi}) but it has a strong effect on the lower limit (ρ_{lc}). For $\gamma = 0$ (the linear problem), no homogeneous equilibrium is possible. For $\gamma = 1$, the equilibrium is possible for all values of ρ from zero to the global onset speed of instability. σ affects the lower and the upper limit since both are inversely proportional to σ. As would be expected from examination of equation (128), the amplitudes increase dramatically as the value of ρ approaches the upper limit.

The equilibrium solutions for the unbalance mass excitation case are given by equations (78) and (79) for values of $r_0 \leq 1$ and $r_0 > 1$, respectively. The equations are subject to the validity conditions discussed in section III. Stability of the equilibrium is governed by the roots of the characteristic equation (equation (108)). The solutions are plotted in figures 7 through 10. The absence of a portion of a curve indicates that the solution is not valid or is unstable in that region. The stability condition for the linear case of $r_0 < 1$ (ρ_{lc}) and the global stability condition (ρ_{gi}) are indicated on the figures. The stability threshold for the equilibrium solution is also indicated. This value was determined by examining the real parts of the roots of equation (108) as the parameters were varied. This threshold is designated by ρ_{ue}.

Figures 7 through 10 present the solutions for various values of γ, a, ζ, and σ, respectively. These curves contain regions where dual solutions are possible for the same value of all parameters. One solution is for $r_0 < 1$ and the other for $r_0 > 1$. There are also regions where no mass unbalance equilibrium solutions are possible. These are the regions where the equilibrium would reside in the linear range $r_0 < 1$, but the system is unstable in this range ($\rho > \rho_{lc}$), or the solution would reside in the range $r_0 > 1$ and the solution is unstable in that range ($\rho > \rho_{ue}$). In these ranges, some combination of the homogeneous limit cycle solution given in figures 5 and 6 and the unbalance might be expected. γ has a strong influence on the limits of these ranges. As γ is increased, both ρ_{lc} and ρ_{ue} (when $r_0 > 1$) decrease. It also causes an

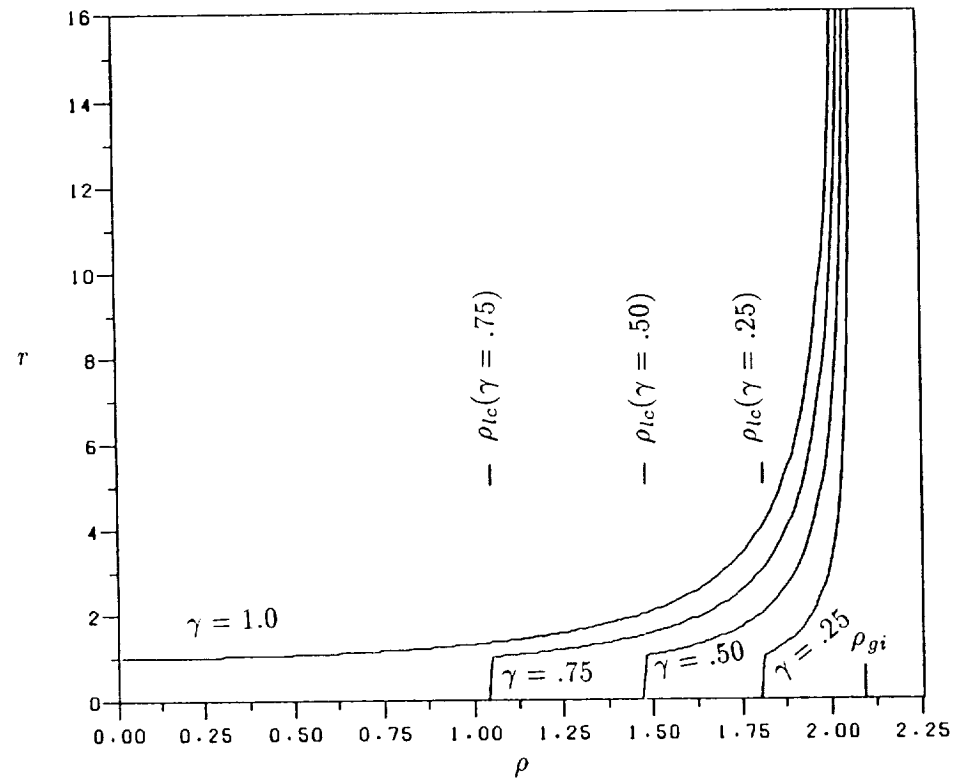

Figure 5. Homogeneous equilibrium solution versus ρ. Effects of γ on solution amplitude and ρ_{lc}.

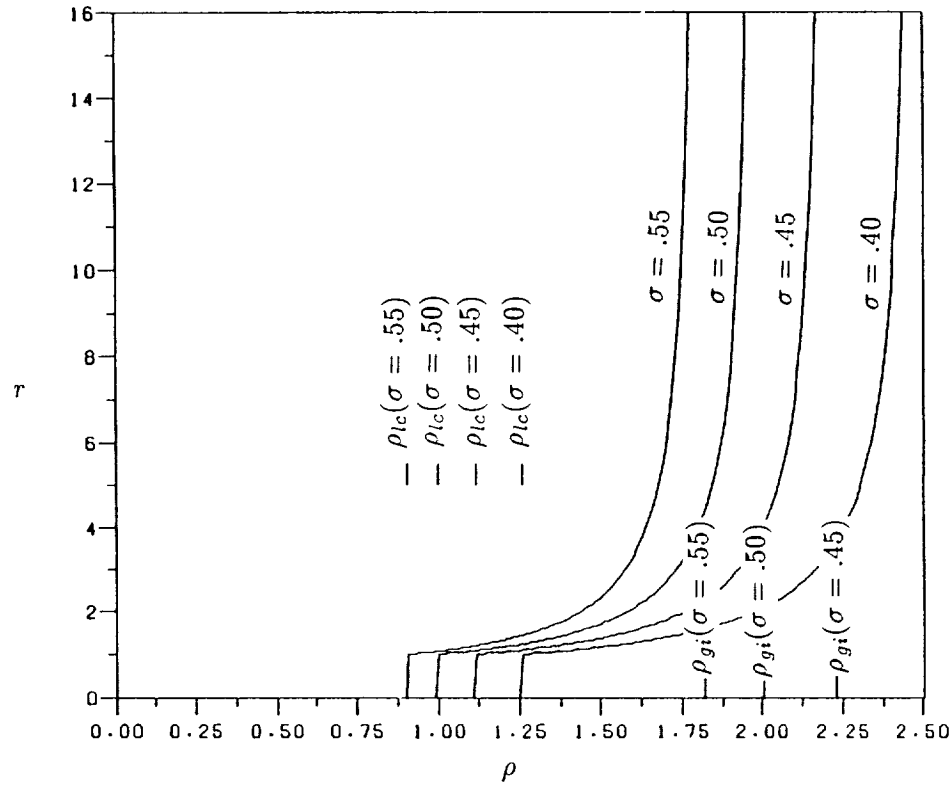

Figure 6. Homogeneous equilibrium solution versus ρ. Effects of σ on solution amplitude, ρ_{lc}, and ρ_{gi}.

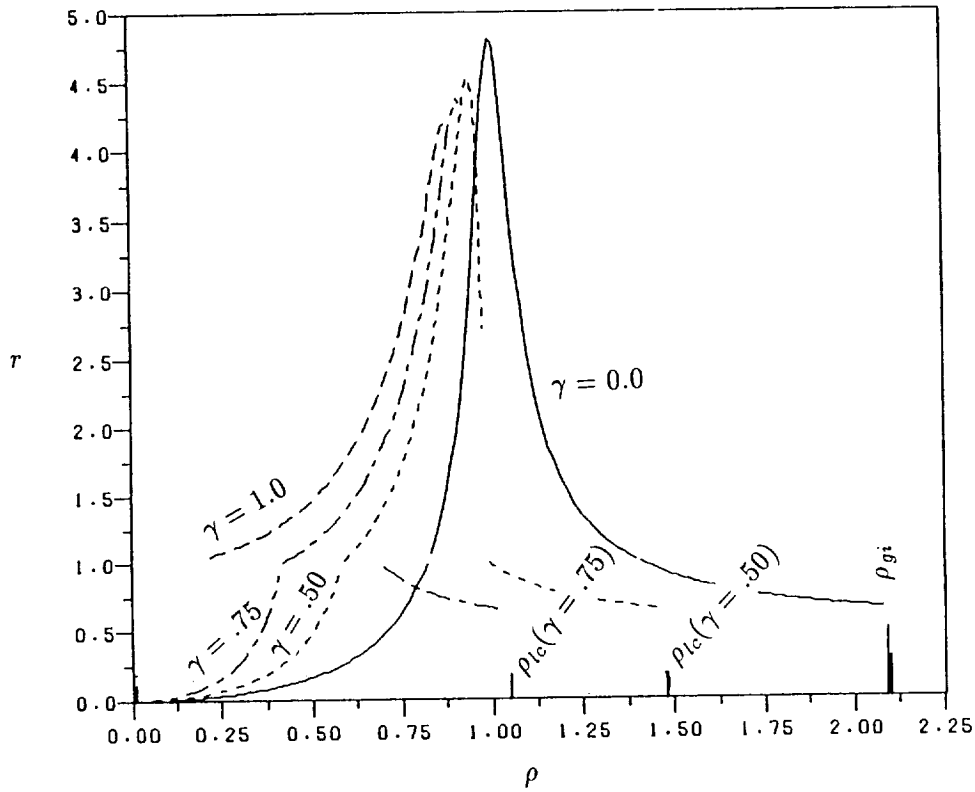

Figure 7. Mass unbalance equilibrium solution versus ρ. Effects of γ on solution amplitude and ρ_{lc}.

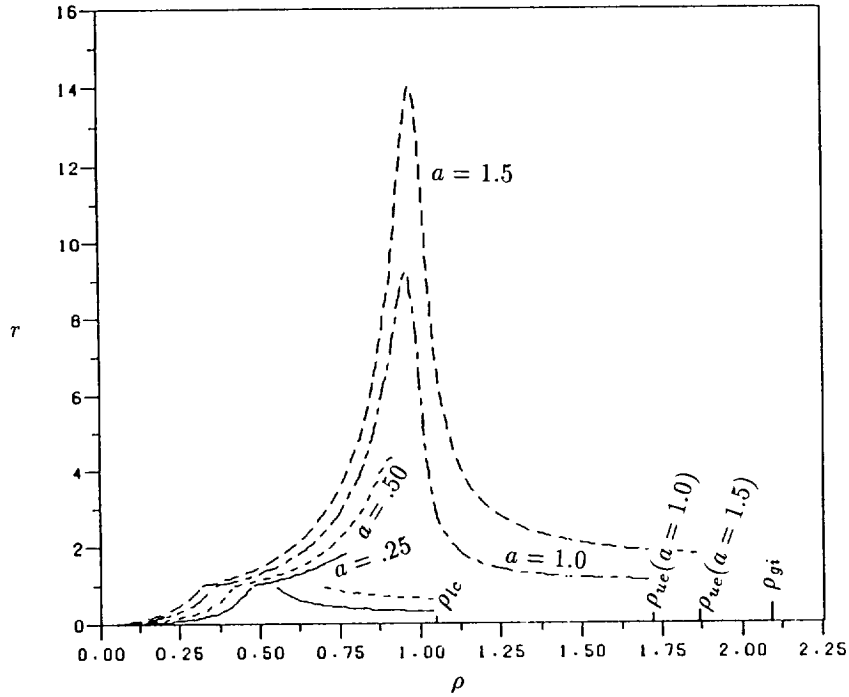

Figure 8. Mass unbalance equilibrium solution versus ρ. Effects of a on solution amplitude and ρ_{ue}.

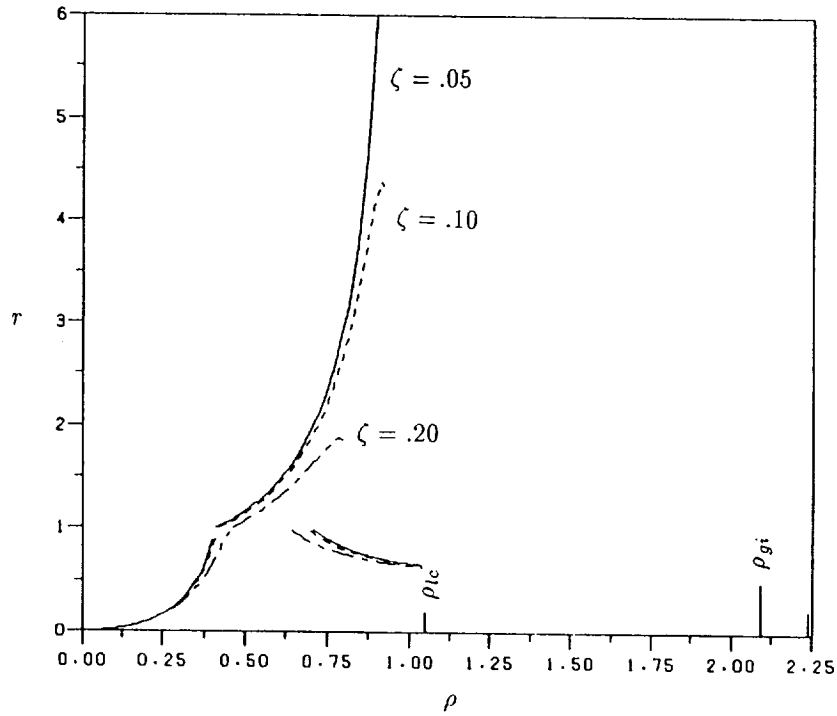

Figure 9. Mass unbalance equilibrium solution versus ρ. Effects of ζ on solution amplitude.

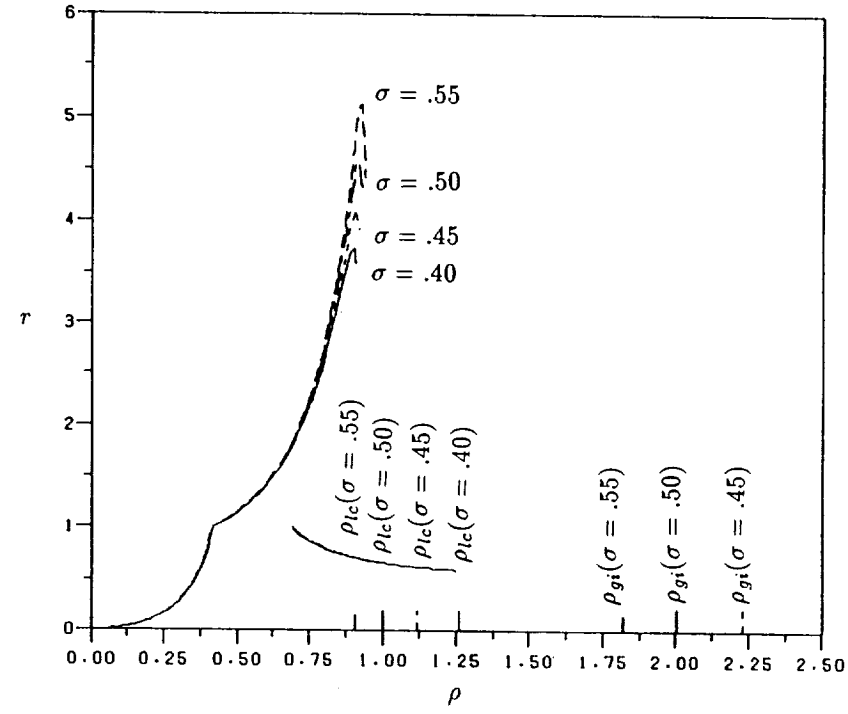

Figure 10. Mass unbalance equilibrium solution versus ρ. Effects of σ on solution amplitude, ρ_{lc}, and ρ_{gi}.

effective lowering of the system resonance frequency. This would be expected since γ softens the support in a nonlinear way. The unbalance parameter a does not affect the limits ρ_{lc} or ρ_{gi}. However, for the larger values, the solution never drops below 1.0 and, therefore, it exists for all values of ρ up the equilibrium stability threshold ρ_{ue} . ζ has little effect on the speed ranges where unbalance equilibrium is impossible. Its primary effect is on the amplitude of the solution at resonance (as with linear systems). σ directly affects both ρ_{lc} and the global stability limit ρ_{gi} (each is inversely proportional to σ). It affects the equilibrium solution stability threshold ρ_{ue} in a manner similar to its effect on ρ_{gi}.

The equilibrium solutions for the fixed-direction side forces are given by equations (83) through (86) for $r_0 \leq 1.0$ and equations (88) through (91) for $r_0 > 1.0$. These equations are in terms of q which should be replaced with its definition given by equation (125). The stability of the solution for $r_0 > 1.0$ is determined by equation (116) or direct evaluation of the roots of equation (115). Again, the definition of q given by equation (125) should be substituted into these equations. The roots of equation (115) are plotted in figure 11 for various values of ζ and σ and in figure 12 for various values of γ and g_y. In both figures, ρ is varied from 0.0 to 4.0. As in figure 4, the roots for variations in σ and g_y are presented as critical damping ratios. The results for all cases have certain similar characteristics. For $\rho = 0.0$, the y and z axis equations are uncoupled due to the special form assumed for q (equation (125)). The roots occur in complex conjugate pairs with all real parts equal to ζ. One pair of roots has an imaginary part equal to $\sqrt{1.0-\zeta^2}$ (corresponding to equation (113)) and the other has an imaginary part equal to $\sqrt{1.0-\gamma/r_0-\zeta^2}$ (corresponding to equation (114)). As ρ increases from zero, the equations become coupled and the roots approach each other along the line defined by the real part equal to ζ. When the roots meet, they branch symmetrically away from the vertical line given by the real part equal to ζ. One branch becomes more stable while the other moves toward the right half plane.

The parameter ζ affects the roots primarily in two ways. First, it defines the real part of the roots for values of ρ prior to the intersection of the roots. Second, since q is a linear function of ζ, increasing it causes the root intersection and imaginary axis crossing to occur for lower values of ρ. Increasing σ has a similar effect without shifting the value of the real parts for small ρ. For some small values of σ, the roots never intersect for the range of ρ examined here. γ affects the imaginary part of the lower root for $\rho = 0$. For smaller γ, this root moves closer to the higher root. For $\gamma = 0$ (the linear system), the roots are identical. Since the roots are closer together their intersection and the imaginary axis crossing occurs for smaller values of ρ. The effect of g_y is similar to that of γ, only inverted. This would be expected from examination of equation (115). γ and r_0 always appear as $\frac{\gamma}{r_0}$ in this equation and, from equation (88), it can be seen that r_0 is almost a linear function of g_y. For large values of g_y or small values of γ, equation (116) indicates that the side force equilibrium is less stable than the global stability of the linear system. However, for increasing values of g_y, the stability condition approaches the global stability condition. This result was previously shown by Control Dynamics.[12]

The subharmonic resonance solution was developed in section III using a harmonic balance procedure. This procedure was implemented using the Newton-Raphson method as presented by Noah.[16] The primary interest here is in the values of the subharmonic components of the series solution (a_{y1}, b_{y1}, a_{z1}, b_{z1}). The magnitudes of the y axis components $\left(\sqrt{a_{y_1}^2+b_{y_1}^2}\right)$ are plotted in figures 13 through 17 for various values of g_y, a, γ, ζ, and σ, respectively. The z axis components behave similarly. The absence of a portion of a curve in these figures indicates a

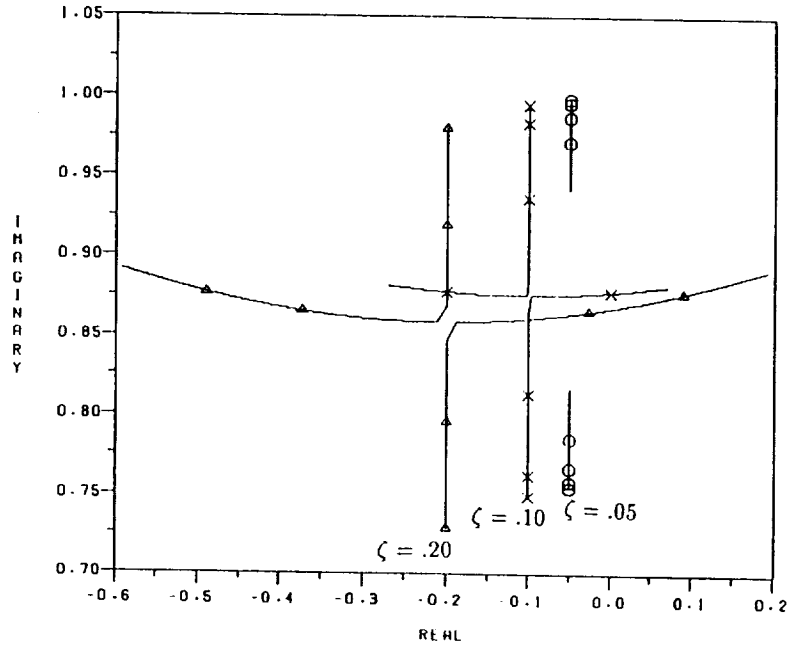

(a) Effects of ζ on roots in complex plane.

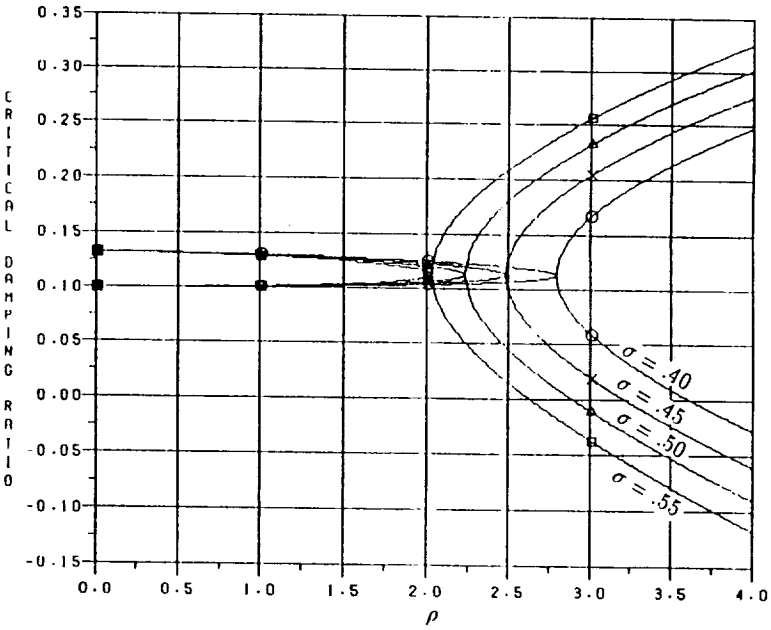

(b) Effects of σ on critical damping ratio of roots.

Figure 11. Roots of side-force equilibrium characteristic equation (equation (115)) as ρ is varied from 0.0 to 4.0.

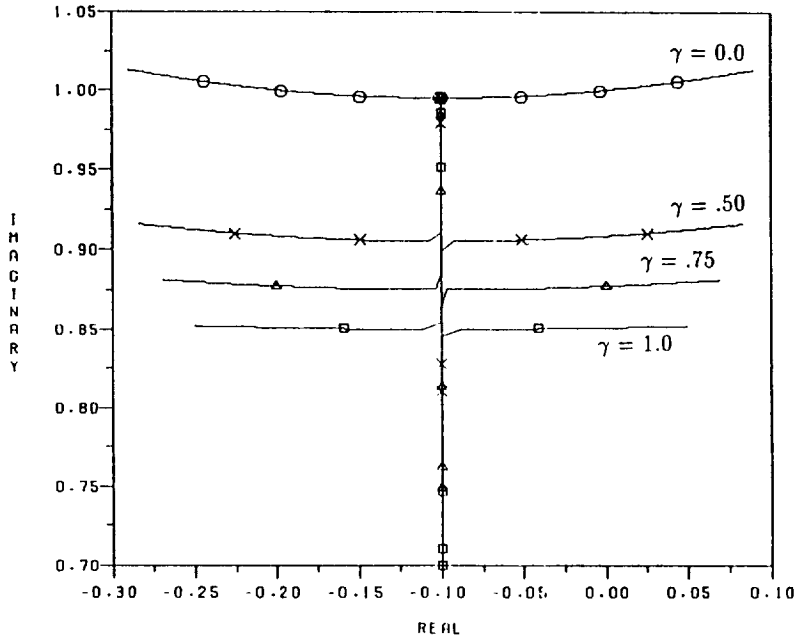

(a) Effects of γ on roots in complex plane.

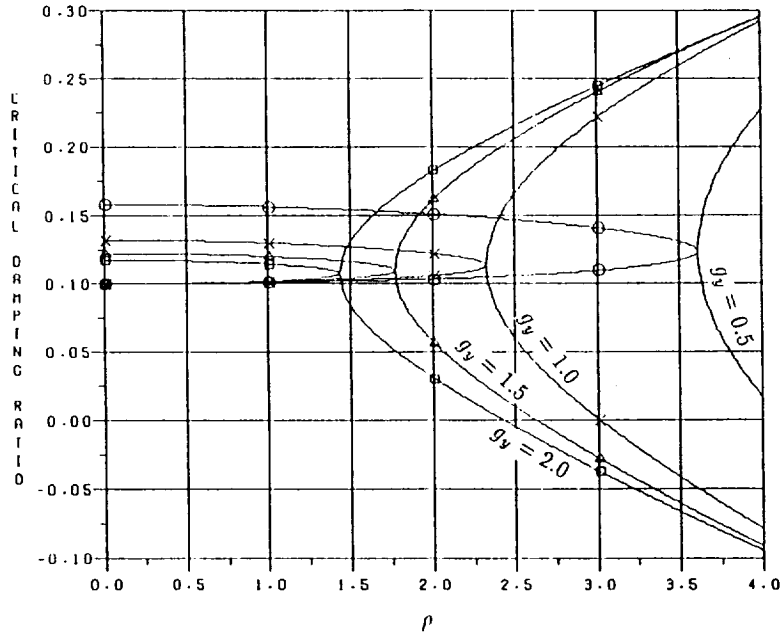

(b) Effects of g_y on critical damping ratio of roots.

Figure 12. Roots of side-force equilibrium characteristic equation (equation (115)) as ρ is varied from 0.0 to 4.0.

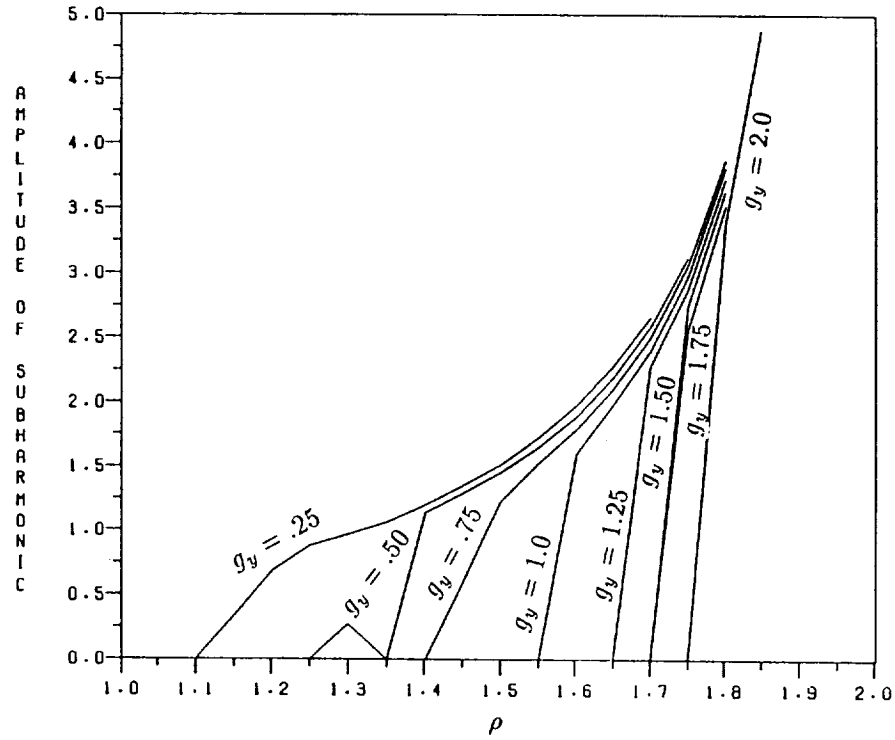

Figure 13. Subharmonic response solution versus ρ. Effects of g_y on magnitude of y-axis component.

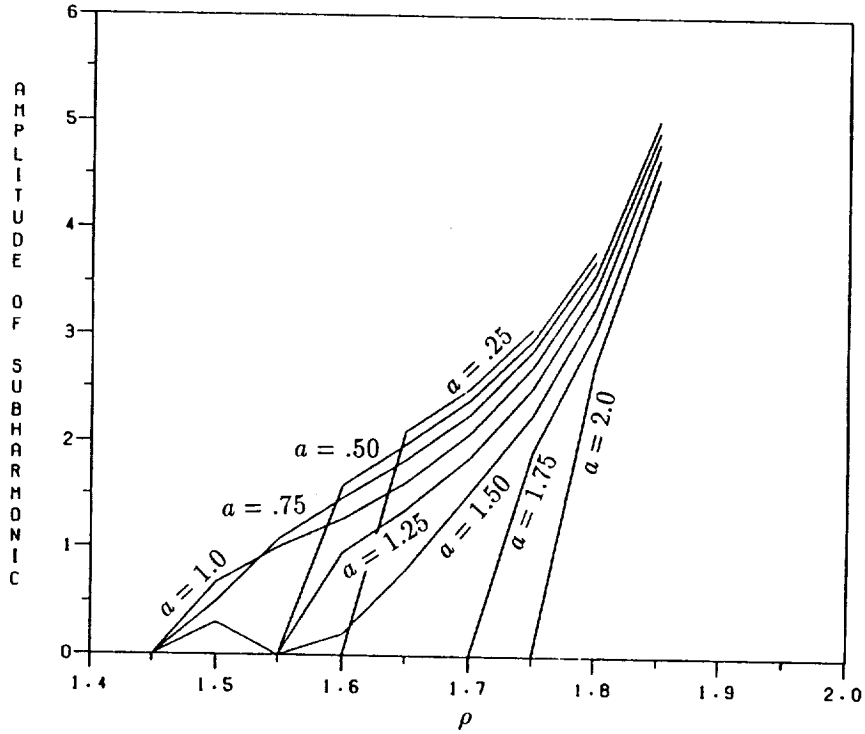

Figure 14. Subharmonic response solution versus ρ. Effects of a on magnitude of y-axis component.

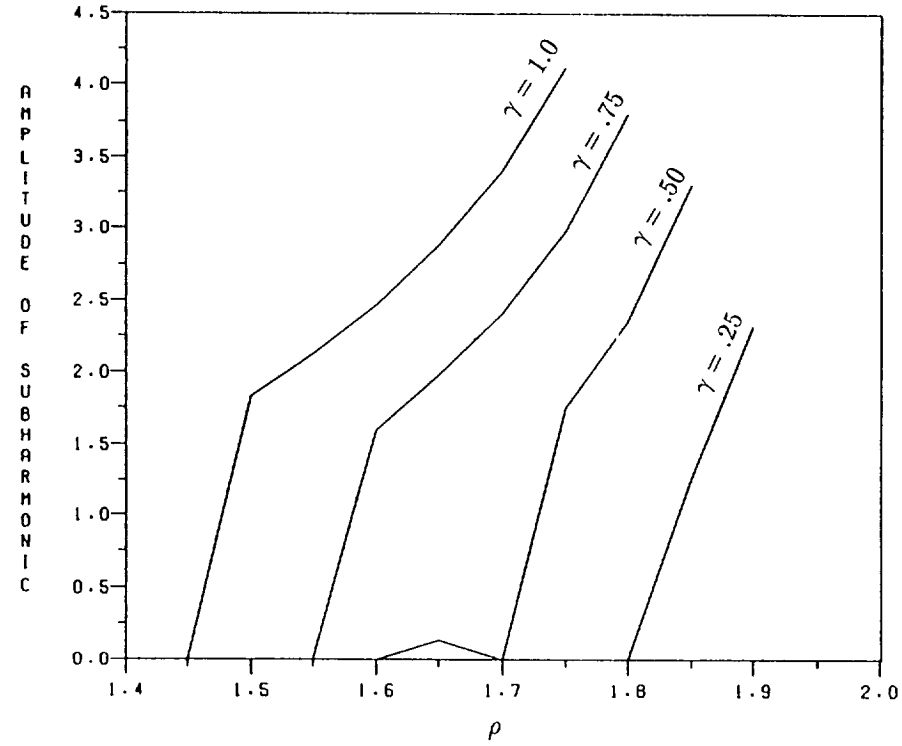

Figure 15. Subharmonic response solution versus ρ. Effects of γ on magnitude of y-axis component.

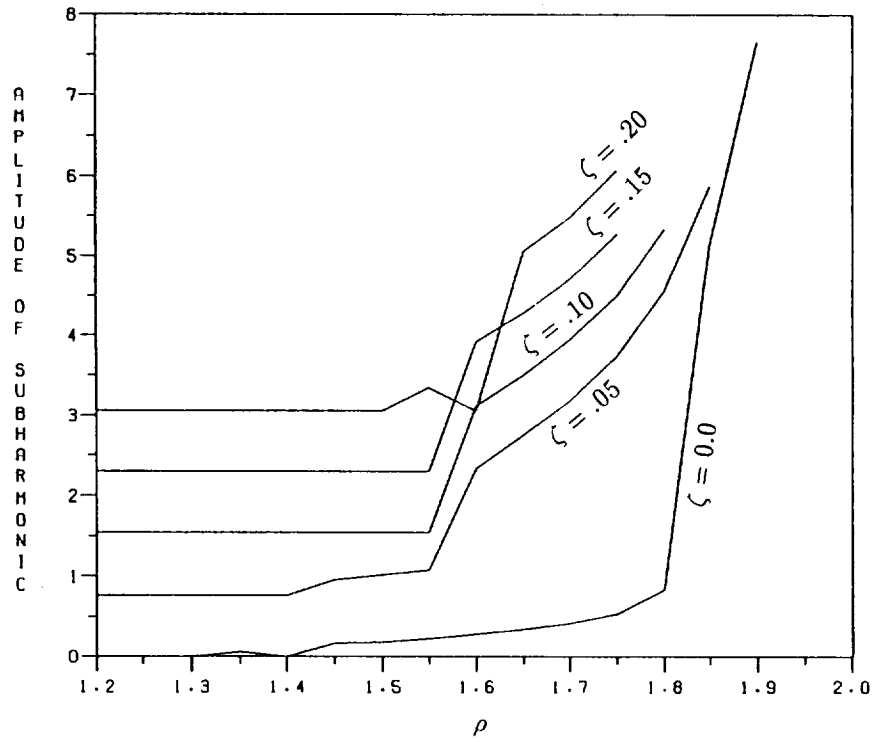

Figure 16. Subharmonic response solution versus ρ. Effects of ζ on magnitude of y-axis component.

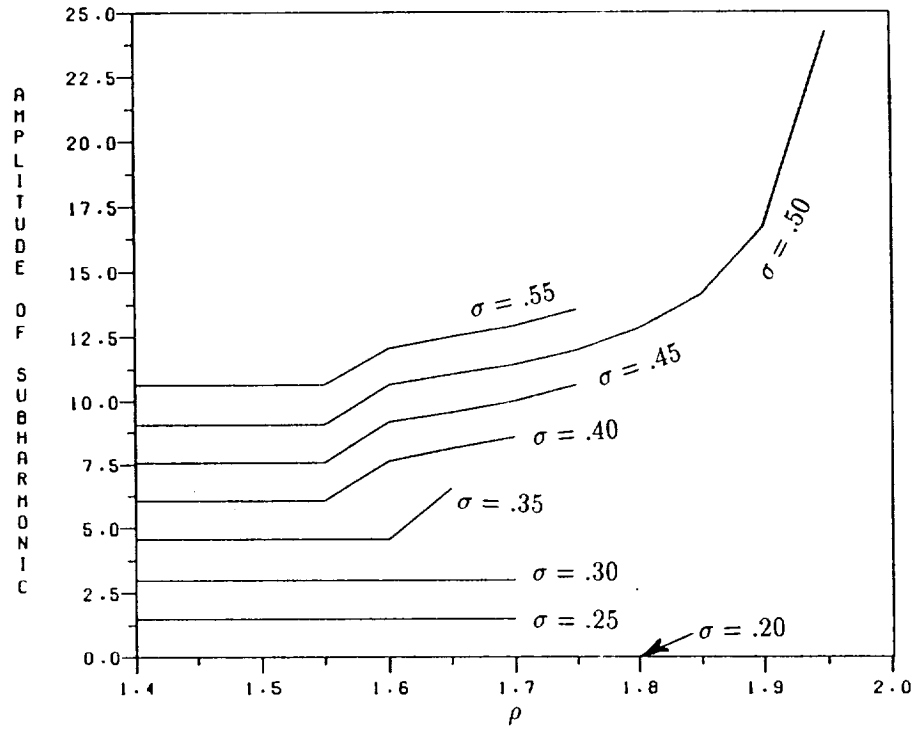

Figure 17. Subharmonic response solution versus ρ. Effects of σ on magnitude of y-axis component.

failure to converge to a solution. This failure most likely indicates that the assumed form of the solution does not represent a solution that can actually exist for the given set of parameters. On the other hand, the achievement of convergence for another set of parameters does not guarantee that the solution will take the prescribed form, only that it is possible. This is important to note when examining results from simulations which exhibit nonfractional subsynchronous response (e.g., limit cycle instability), since these motions cannot be represented by the subharmonic solution form.

The effect of g_y on the subharmonic response can be seen from figure 13. As g_y is increased, the range of occurrence of the subharmonic narrows. The upper limit moves upward slightly. The amplitude of the response is not significantly affected at a given value of ρ as long as the value is within the range of occurrence. Within the range of occurrence of the subharmonic, the response increases with increasing ρ.

The unbalance parameter a affects the subharmonic response in much the same way as g_y. This can be seen in figure 14. One difference to note is that the range of occurrence initially broadens and subsequently narrows as a is increased. Also, the amplitude at a given value of ρ varies a little more with a than with g_y.

The most significant influence comes from the parameter γ. This is not surprising since this parameter gives a measure of the degree of nonlinearity in the system. The effects of γ can be seen in figure 15. For $\gamma = 0$, no subharmonic is developed since the system is linear. As γ increases to 1 (its maximum), the amplitude and the range of occurrence of the subharmonic response increase. The upper limit of the range drops somewhat.

The damping parameter ζ has much less influence than the parameters discussed previously. The primary effect is to increase the upper limit of the range of occurrence of the subharmonic. This effect is shown in figure 16. Since ζ has little effect on the amplitudes, the curves for each successive value of ζ have been shifted vertically for clarity. The cross-coupled stiffness parameter σ also primarily affects the upper limit. Figure 17 shows its effect on the subharmonic response. These curves are shifted as in figure 16. For very small values, no subharmonic response occurs. After a certain value is exceeded, the range begins to broaden. Both the lower limit and the upper limit are affected. The largest change comes as σ approaches a value of 0.5. As this value is approached, the upper limit of the range of occurrence and the amplitude of the response at the upper limit increase dramatically. This is due to the coalescence of the limit cycle instability frequency with the subharmonic response frequency. The upper limit and the amplitude decrease as σ increases beyond 0.5. These effects are indications of the inherent relationship between limit cycle instability and subharmonic response that was postulated to exist in section I.

C. Preliminary Observations

The results developed in section III and presented in this section apply for certain restricted, sometimes nonrealistic conditions. For example, the homogeneous equilibrium solution is of little value for predicting actual system response since any real system will possess some amount of excitation. Similar statements could be made about the other solutions developed. However, each yields some insight into the characteristics of the behavior of the system and some general conclusions can be drawn. The conclusions drawn for the restricted cases can be extended to apply for cases where one parameter is dominant. For example, if the unbalance is much larger than the side force, the characteristics observed for the unbalance excitation case would be expected to hold. When this is not the case, other conclusions can be drawn based on the results of the restricted cases.

The homogeneous solution to the polar equations yielded a range of occurrence, a frequency, and an amplitude for the limit cycle instability. The analysis of the unbalance response equilibrium determined the possibility of a solution in regions where the limit cycle equilibrium is also possible. The stability analysis of the side-force equilibrium demonstrated that this excitation increased the stability of the system (in the small). It is reasonable to expect that both of these effects would tend to reduce the range of occurrence of the limit cycle. The limit cycle instability is induced by the circulatory force represented by the cross-coupled stiffness. The nature of this force for this system is expressed by the relationship $q = 2\zeta\rho\sigma$. The value of σ determines the frequency of the limit cycle in the homogeneous case. Since the fundamental driving mechanism for the instability is the same even when excitation is present, it is expected that the frequency of a limit cycle under these conditions would remain close to that predicted for the homogeneous case. The amplitudes predicted for the homogeneous case would most likely be significantly changed by the addition of the unbalance and side-force excitations. However, the general trend of increasing amplitude as the global stability limit is approached would be expected to hold.

The unbalance response equilibrium solution demonstrated certain regions in which a synchronous sinusoidal response could not exist. In these regions, a combination of synchronous response and either limit-cycle instability or subharmonic response might be expected. The addition of a side-force excitation would alter the specific range of occurrence and amplitudes of

this behavior; however, for some values of side force this behavior might still be expected to occur. The stabilizing capacity of the side force has already been discussed. The side force has an additional effect of making the system behave like a linear system. This is true for relatively large values of side force (compared to deadband and unbalance).

The subharmonic response analysis already includes the combination of unbalance excitation and side-force excitation. However, the form of solution assumed in the procedure does not allow for the occurrence of limit-cycle instability. The ranges of possible subharmonic response should be valid; however, the existence of this form of solution is not guaranteed. Limit-cycle instability may also occur in regions where subharmonic response is possible. The results still show the effects that various model parameters will have on the subharmonic if it occurs. This is typical of certain types of nonlinear systems where multiple solutions are possible. In fact, for a given set of parameters, the initial conditions may determine which solution is obtained. Other perturbations, such as the random noise, may also play a strong part in the determination.

The results presented in this section provide general characteristics of the responses of the nonlinear rotor system. They provide insights into the effects that the various parameters will have and give direction for the simulation studies to be presented in the next section. The various behaviors postulated in this section for the general system will be investigated using simulations.

V. SIMULATION RESULTS FOR SIMPLIFIED MODEL

Numerical results were presented in the previous section for the analytical expressions developed in section III. These results consisted of equilibrium response amplitudes, stability conditions, and subharmonic response amplitudes. The analyses were developed for specific excitation cases (homogeneous, unbalance, and side force) and a specific assumed form of solution (subharmonic response). None of the analyses are fully applicable for a system under general excitation and one whose solution form is not known a priori to be a superposition of subharmonics. However, some general conclusions were drawn for the system in the previous section for both the restricted cases for which the analyses apply and for the general case. In this section, simulation will be used to demonstrate the validity of the results presented and the conclusions drawn in the previous section. In addition, results which can only be determined through simulation will be presented. These results were obtained using the general turbopump model developed in appendix A. The numerical integration method used for the simulation solution is discussed in this appendix.

A. Demonstrations of Equilibria and Stability of Restricted Cases

The first result developed was the stability condition for the zero deadband case. For nominal parameters, this condition was shown to be $\rho < 2.08$. This is illustrated (fig. 18) by slowly ramping the simulation through this value and observing the divergent growth of the response beyond this value of ρ. A very low level of random noise was used to initiate the instability. Fast Fourier transform (FFT) analysis of the response (fig. 19) shows that the frequency of the instability is equal to the normalized natural frequency of the system (1 radian/second).

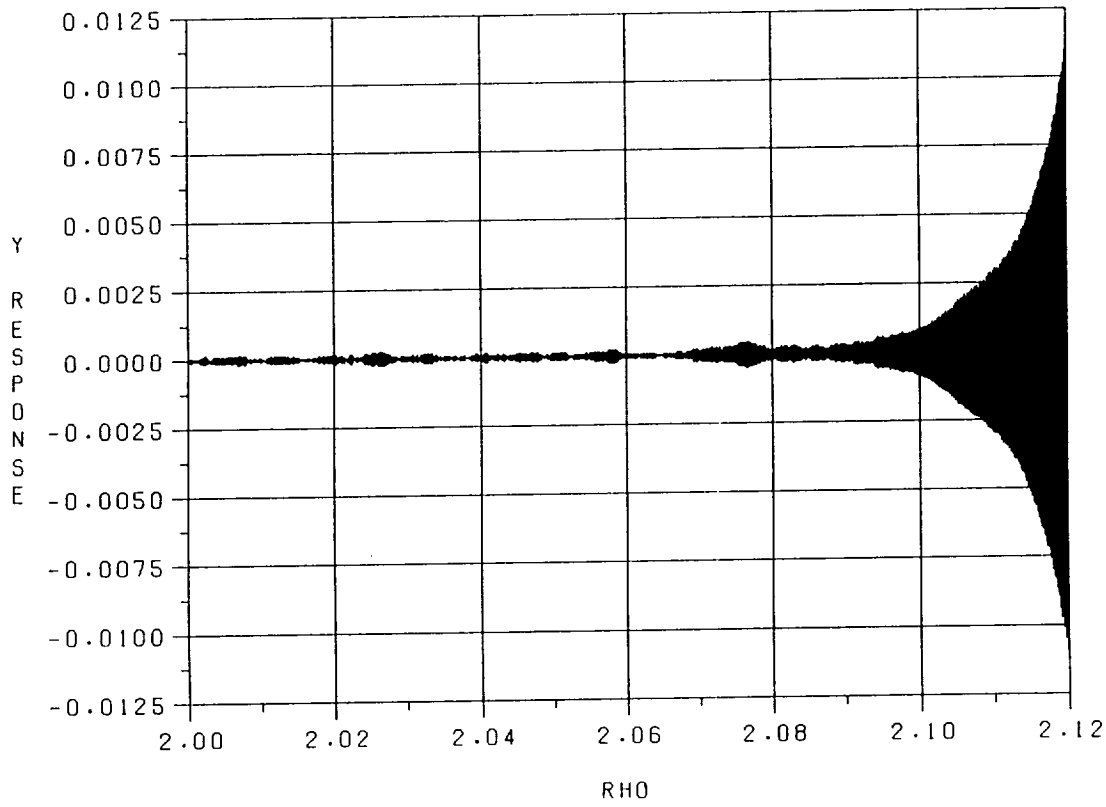

Figure 18. Demonstration of stability threshold for zero deadband linear model.

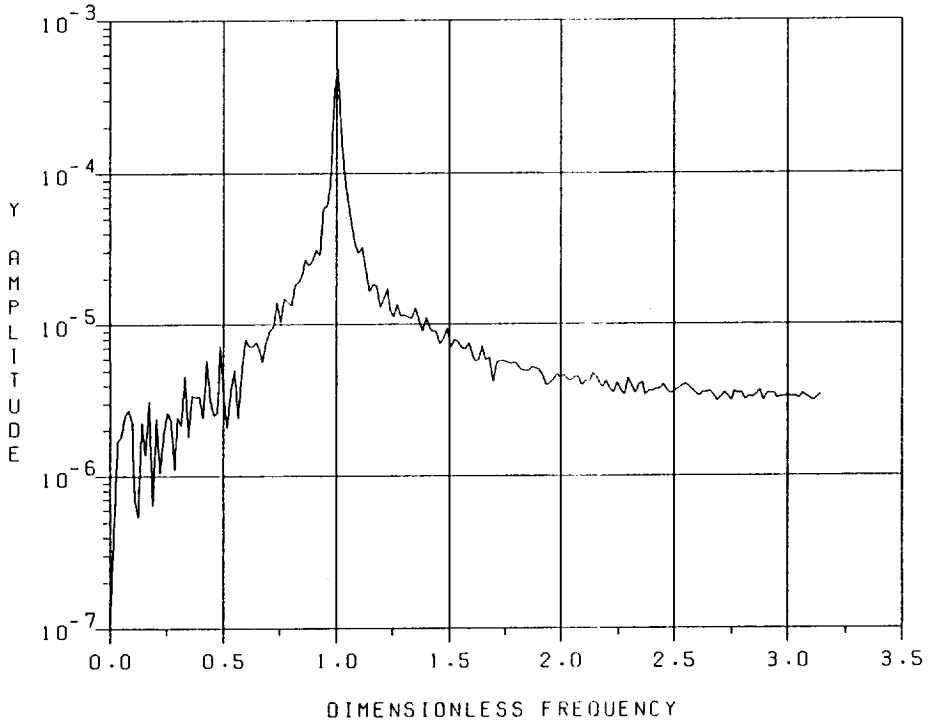

Figure 19. Magnitude spectrum of y response of figure 18. Spectrum taken at $\rho \approx 2.1$.

The limit-cycle equilibrium radius given by equation (128) is shown in figure 20 for nominal values of all parameters. Simulation results are shown on this plot for certain values of ρ. FFT analyses for the various values of ρ show that the frequency of the limit cycle is 0.48ρ as predicted by equation (121). These spectra are shown in figure 21.

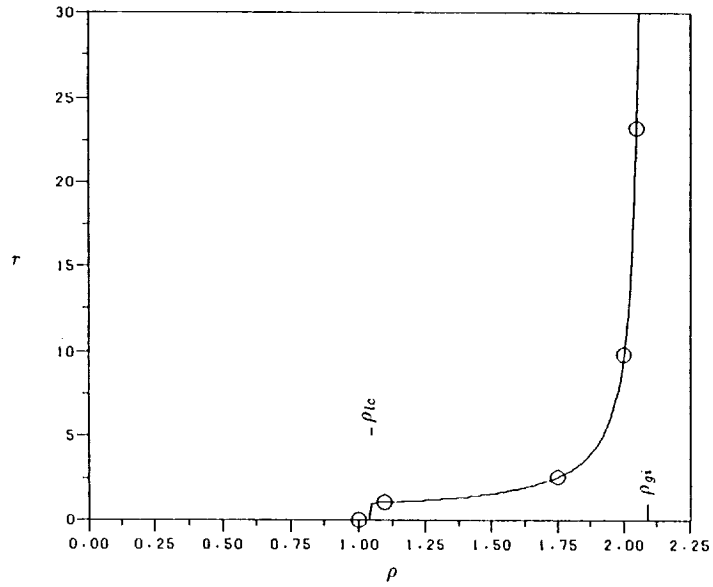

Figure 20. Homogeneous equilibrium solution amplitude as ρ is varied. All parameters are nominal. Solid line represents analytical solution, circles represent simulation results.

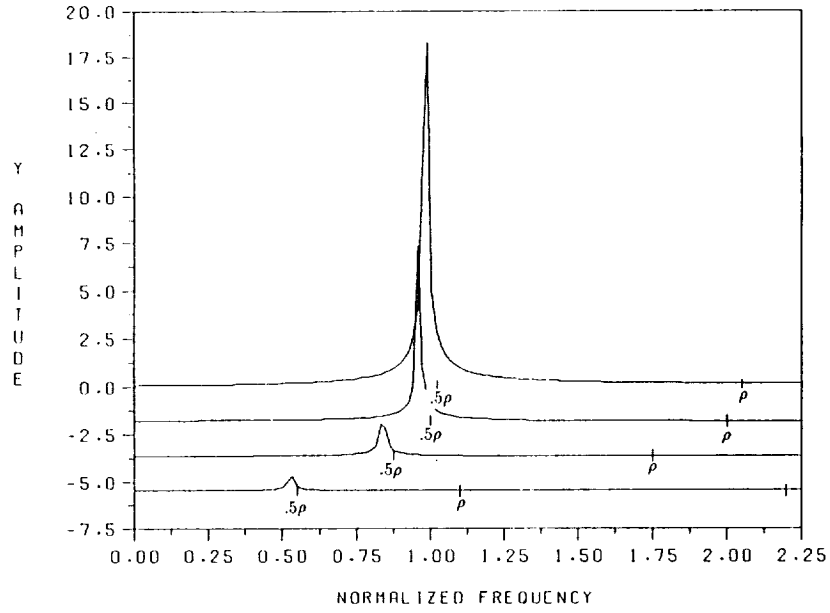

Figure 21. Cascade spectral plot of simulation of homogeneous equilibrium. Spectra taken at dwells in ρ profile.

The mass unbalance equilibrium radius given by equations (78) and (79) is shown in figure 22 for nominal values of all parameters. Simulation results are shown for a ramp up to $\rho = \rho_{lc}$. Above this value, the mass unbalance equilibrium results are not valid since $r_0 < 1$ and the solution is unstable. Simulation results are also presented for the ramp down from this speed, illustrating the multivalued solution which exists in a small range near the resonance. In order to explore the stability threshold of the unbalance equilibrium (ρ_{ue}), a larger unbalance case was simulated. This was necessary to generate an equilibrium solution whose value exceeds 1.0. Simulation results are presented in figure 23 for the model operating at a steady speed ($\rho = 1.7$) just below the stability threshold ($\rho_{ue} = 1.72$) and then ramping to and holding at a speed ($\rho = 1.73$) just above the threshold. A very low level of noise excitation ($\overline{\eta} = 0.0001$) was used to perturb the equilibrium. At the lower speed, the equilibrium is maintained. At the higher speed, the amplitude appears to diverge and then limits at a higher level than the equilibrium. FFT analysis of the response (fig. 24) shows that the limit cycle instability has emerged along with the mass unbalance response. This result shows that at speeds above this stability threshold the unbalance response equilibrium cannot be maintained, and a combination of unbalance response and limit-cycle instability results; however, it does not show the converse, i.e., it does not show that below this threshold the combination response cannot be maintained. It only shows that below the threshold the unbalance equilibrium without the limit-cycle instability is possible.

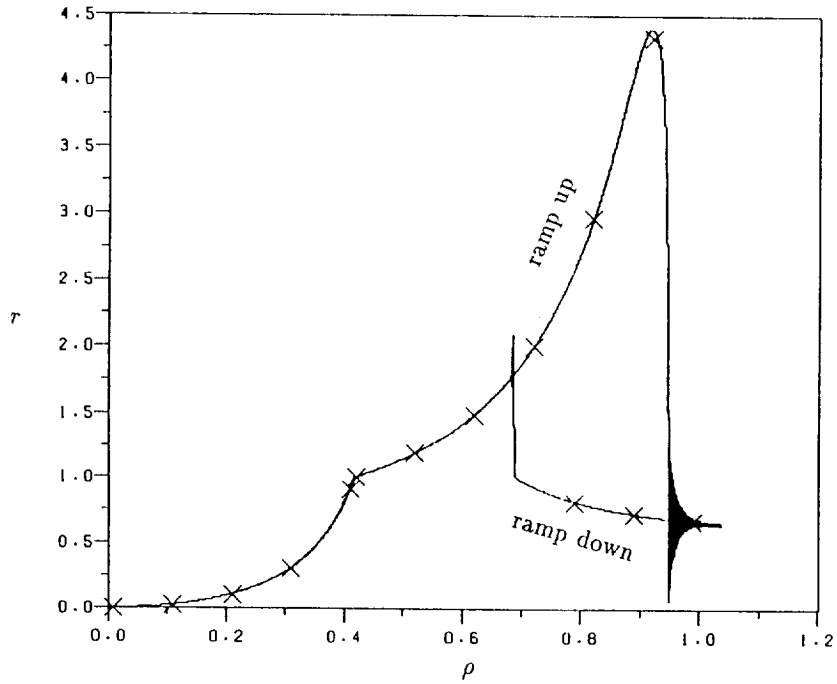

Figure 22. Mass unbalance equilibrium solution amplitude as ρ is varied. All parameters nominal. Solid line represents simulation solution, X symbols represent analytical results.

The stability analysis of the side-force equilibrium showed that this equilibrium was stable for speeds beyond the global stability threshold. This is demonstrated for a nominal case (with no unbalance) in figure 25. This case has a low level of noise excitation ($\overline{\eta} = 0.001$) to perturb the system. The predicted stability threshold for this case (equation (116)) is $\rho = 3.0$. The system clearly remains stable for speeds below this threshold and diverges beyond it. Since the analysis only addressed stability in the small, it is of interest to determine how sensitive the

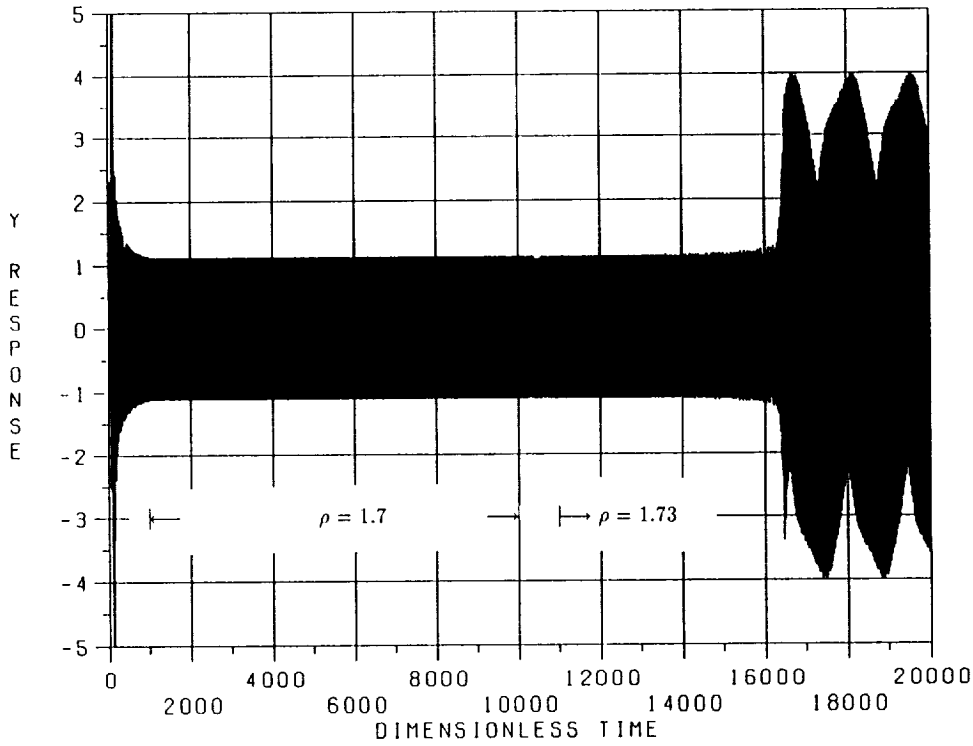

Figure 23. Demonstration of mass unbalance equilibrium stability threshold. $\overline{\eta} = 0.0001$, all other parameters nominal.

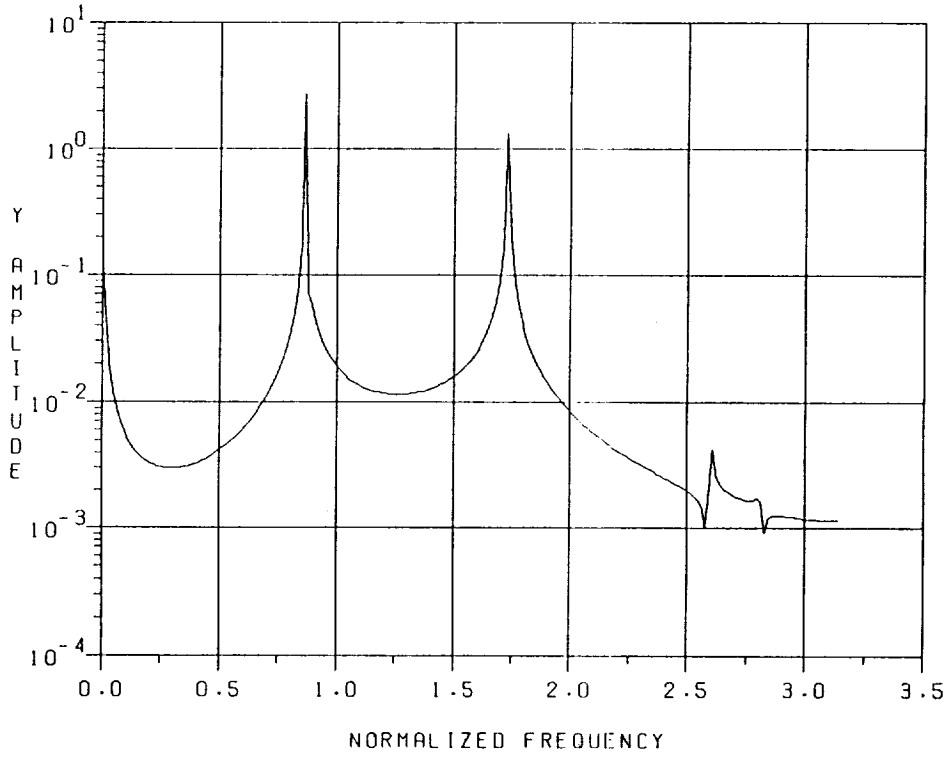

Figure 24. Magnitude spectrum of y response of figure 23. Spectrum taken at dimensionless time equal 18,000.

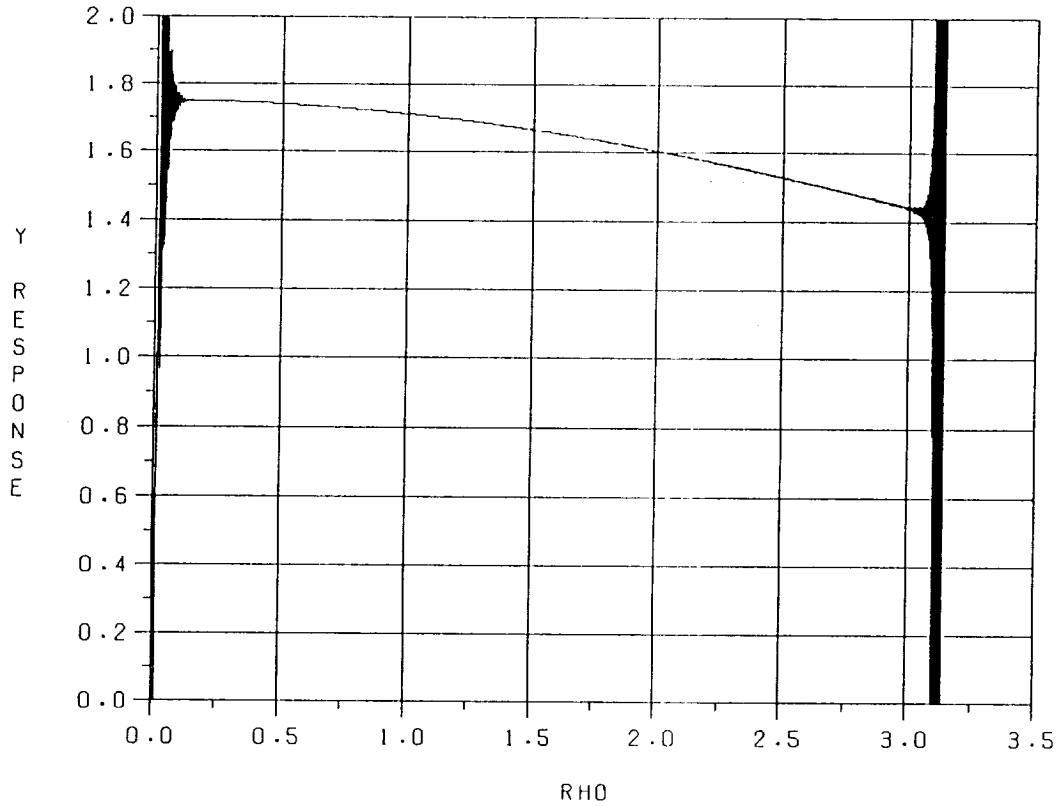

Figure 25. Demonstration of side-force equilibrium stability threshold. $\overline{\eta} = 0.001$, $a = 0.0$, $g_y = 1.0$. Predicted stability threshold is $\rho = 3$.

stability is to perturbation. This was examined by simulating the system at a constant speed of $\rho = 2.7$ and increasing the amplitude of the noise perturbation $(\overline{\eta})$. Results from this simulation are shown in figure 26 and show that a value of $\overline{\eta} \approx 0.47$ was required to perturb the system beyond the range of stability. This is not an exact value due to the random nature of the noise excitation and the fact that the value was steadily increasing. An even more interesting result is shown in figure 27. This figure presents two cases, one in which the noise is only applied along the y axis and the other only along the z axis. The amplitude is increased as before. For the y-axis perturbation, the system remains stable for all values of η_y up to 1.0. However, the z-axis perturbation behaves just like the dual-axis perturbation. The system becomes unstable above $\eta_z \approx 0.4$. In hindsight, this should not be a surprising result. The fundamental driving force for the instability is a tangential force. The side-force equilibrium point is primarily along the y axis and, hence, a z-axis perturbation would impart a tangential velocity to the rotor. One might hypothesize then that an unbalance excitation superimposed on the side-force excitation might rather easily perturb the system beyond its range of stability. This might be expected since the unbalance provides a large, regularly occurring tangential perturbation to the rotor. This will be explored in a later section.

The analytical results presented in section IV showed that the stability threshold for the side-force equilibrium increases as the magnitude of the side force decreases. This is true as long as the side force is sufficient to cause the displacement to exceed the deadband ($r_0 > 1.0$). This can be understood by realizing that the greatest asymmetry occurs in the linearized stiffness coefficients when the deflection is the smallest. Gunter,[12] among others, has shown the stabilizing capacity of asymmetry. However, due to the smaller magnitude of the side force and

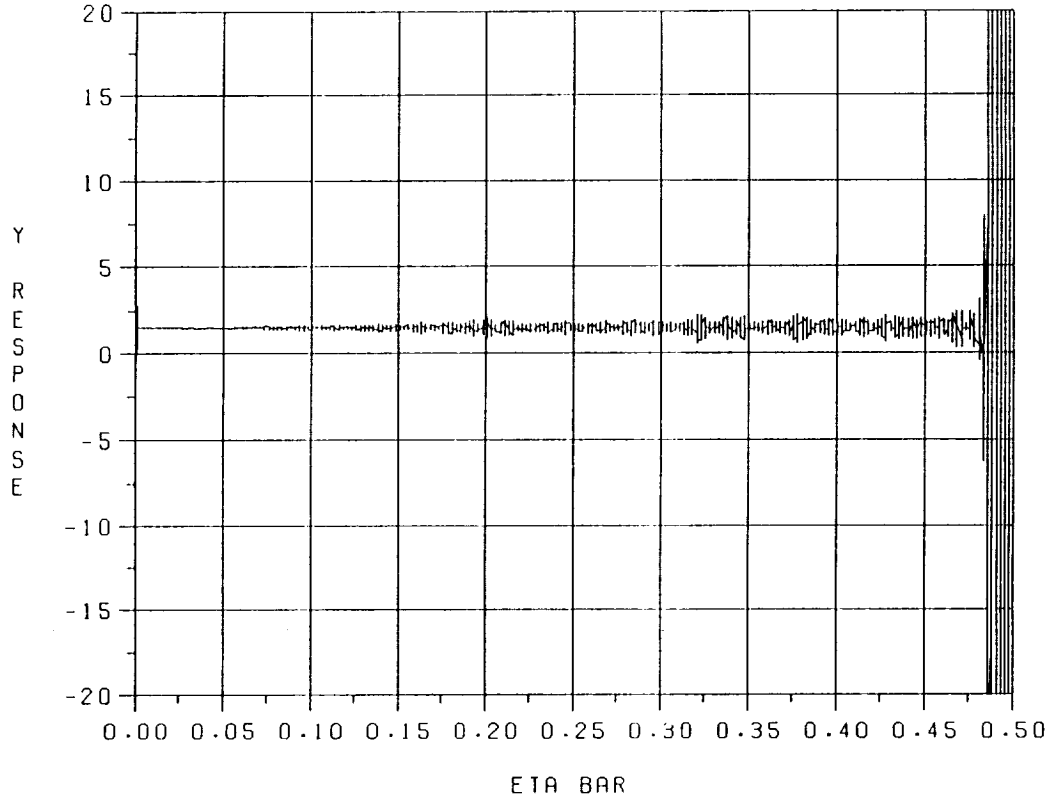

Figure 26. Sensitivity of side-force equilibrium stability to perturbation. $\rho = 2.7$, $g_y = 1.0$, $\eta_y = \eta_z = \overline{\eta}$.

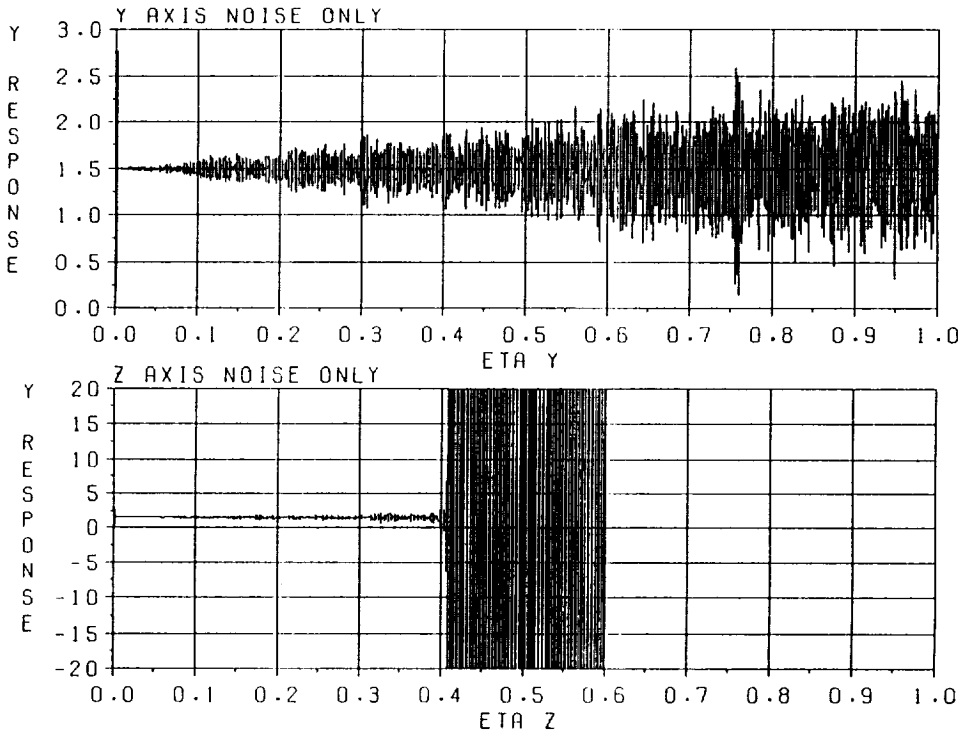

Figure 27. Sensitivity of side-force equilibrium stability to uniaxial perturbation. $\rho = 2.7$, $g_y = 1.0$.

the deflection for this case, this highly stable (in the small) equilibrium might be expected to be more sensitive to perturbation than a more highly loaded case. This is shown to be the case in figure 28. The result is for a case of side force $g_y = 0.5$ instead of 1.0 as was the case in figure 26. The side-force equilibrium stability threshold for this case is $\rho \approx 4.25$. All other conditions are the same and the system becomes unstable when $\overline{\eta} \approx 0.25$. For increasing side force, although the sensitivity of the stability to disturbance will decrease somewhat, the stability threshold will also decrease and, in the limit, will approach the global stability threshold (ρ_{gi}).

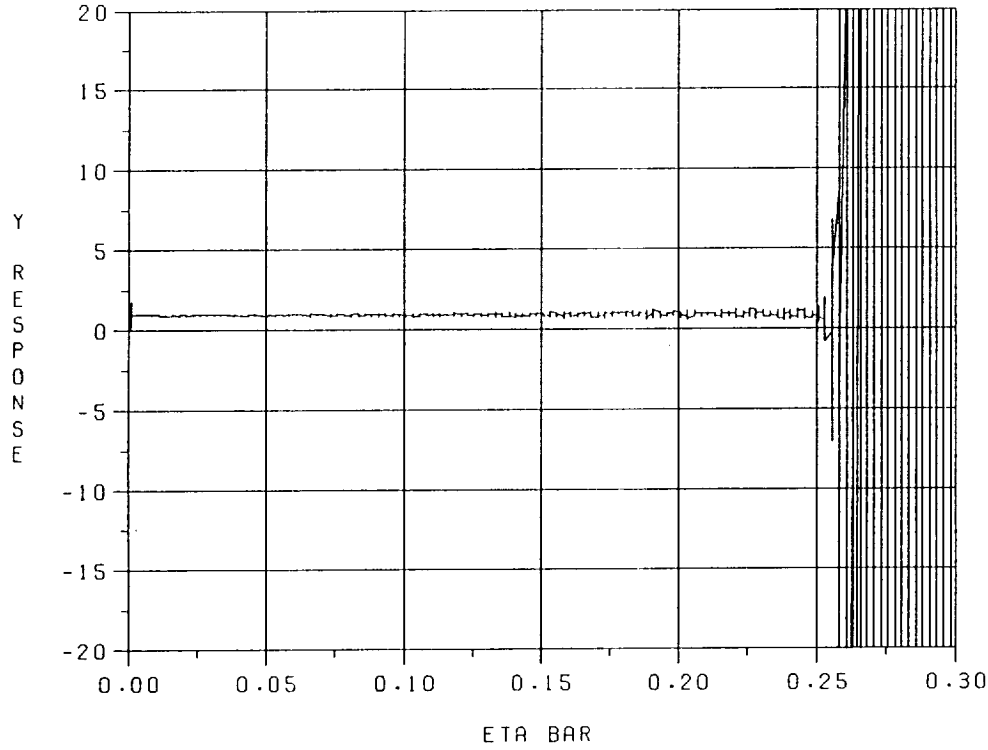

Figure 28. Sensitivity of side-force equilibrium stability to perturbation.
$\rho = 2.7$, $g_y = 0.5$, $\eta_y = \eta_z = \overline{\eta}$.

Subharmonic response harmonic balance results were presented in section IV for nominal values of the model parameters and several variations of each parameter. These results give the amplitudes of a subharmonic if it occurs, but they do not address any perturbations or initial conditions which may be required to initiate the response. In order to more easily obtain the subharmonic response in a simulation, a case with a damping of $\zeta = 0.01$ will be demonstrated. In addition, the destabilizing force parameter σ will be set to zero to avoid potential interaction between the subharmonic response and limit cycle instability. The harmonic balance results are shown for this case in figure 29. The z-axis component has a much larger amplitude than the y-axis component for this case. The maximum value of ρ for which convergence was attained is 1.775. The simulation results are shown in figure 30. The transient data in figure 30b has been bandpass filtered between the normalized frequencies 0.3 and 1.26 in order to illustrate the amplitude of the subharmonic component. The response matches the prediction quite well up to $\rho = 1.775$. The frequency is exactly one half the excitation frequency, and the amplitudes match for both axes. As the speed continues to increase beyond this point, the response begins a transition phase where it appears to be seeking a new equilibrium. A new equilibrium is then achieved, one for which the harmonic balance procedure failed to converge. Simulation of the

same case with noise perturbation added ($\overline{\eta}$ = 0.05) yields a very interesting result (fig. 31). The response below ρ = 1.775 is similar to the previous case. Above this value, however, when the response enters the transition phase it does not arrive at the same equilibrium that it did previously. Instead, a harmonic equilibrium (i.e., no subharmonic response) is obtained. This result suggests that the subharmonic solution above ρ = 1.775 is not very stable. This might explain why the harmonic balance procedure fails to converge to a solution in this speed range.

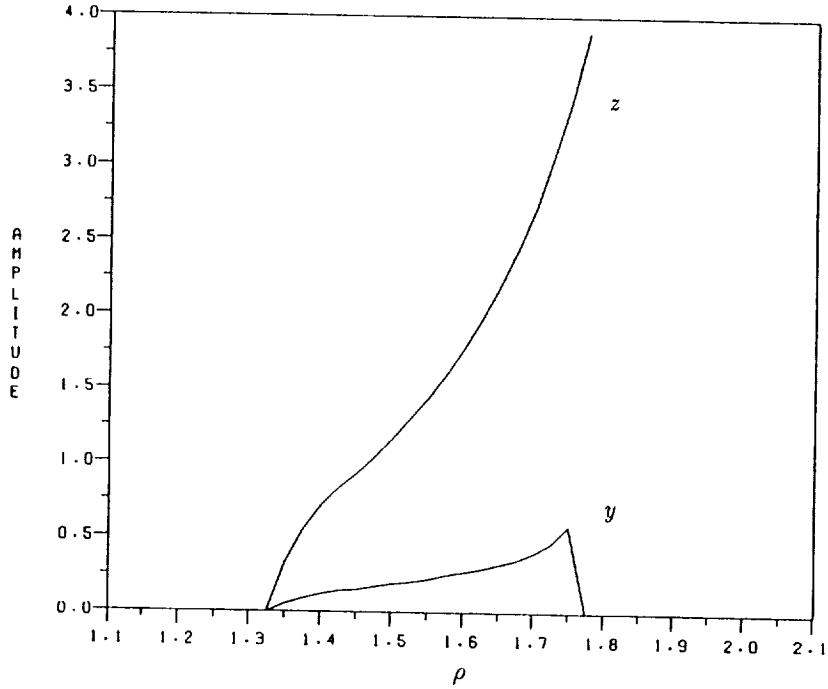

Figure 29. Subharmonic response solution versus ρ. σ = 0.0, ζ = 0.01. Magnitudes of y- and z-axis components.

B. Interaction Between Limit Cycle and Mass Unbalance Response

The previous section dealt with the restricted cases for which equilibria and stability have been determined analytically. These cases assume a specific excitation form and/or a specific form for the solution. This section and those that follow will deal with cases for which the assumptions do not apply.

The mass unbalance equilibrium simulation was presented in figure 22. This case was restricted to speeds below ρ_{lc} since this equilibrium (r_0 > 1.0) would be unstable beyond that point. Proceeding beyond this point results in a combination of unbalance response and limit cycle instability. This is shown for the same model parameters in figure 32. The initiation of the limit cycle is most clearly evident from the cascade spectral plot. The frequency of the limit cycle is seen to be approximately equal to $\sigma\rho$; however, the unbalance excitation does alter it somewhat. Modulation frequencies of the excitation frequency and the limit cycle frequency can also be observed in the spectral data. As predicted by Day,[14] these frequencies can occur at all multiples of the difference between the two, plus or minus the limit cycle frequency. The system in this case possesses a unique solution. For $\rho < \rho_{lc}$, the only possible solution is the unbalance equilibrium. For $\rho > \rho_{lc}$, the only possible solution is the combination solution.

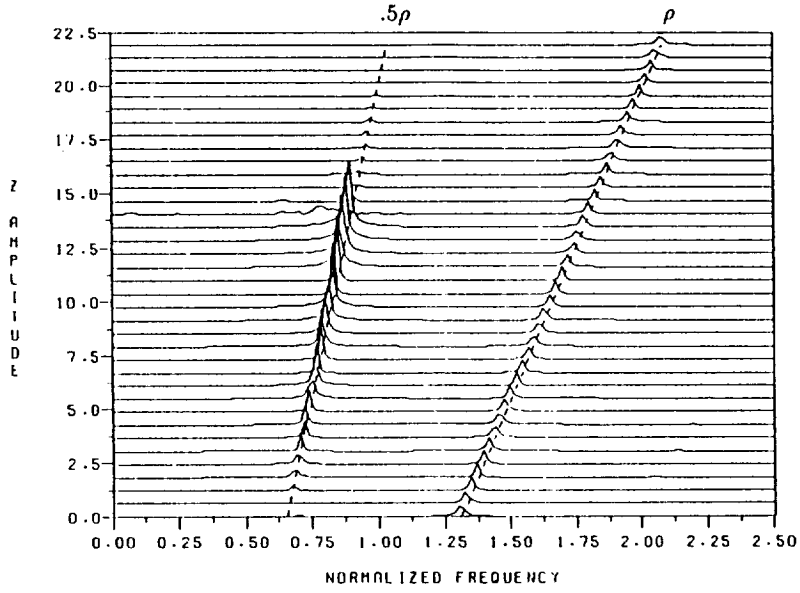

(a) Cascade spectral plot.

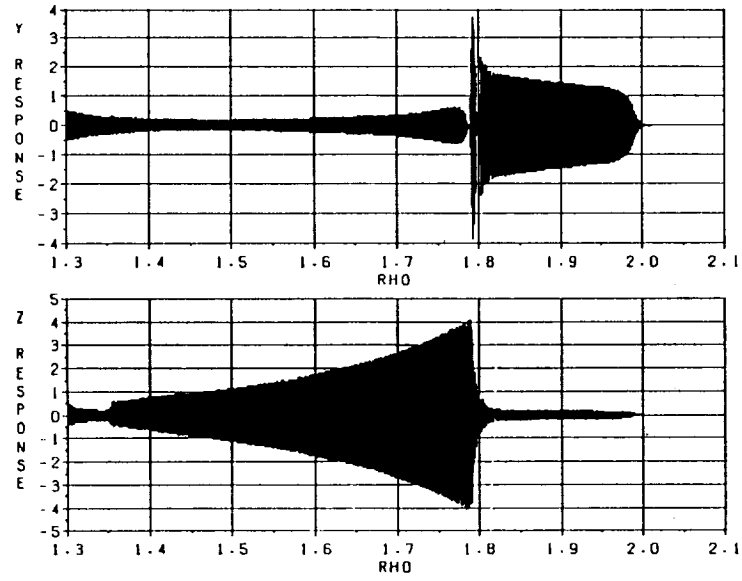

(b) Response versus ρ.

Figure 30. Simulation of subharmonic response corresponding to figure 29.

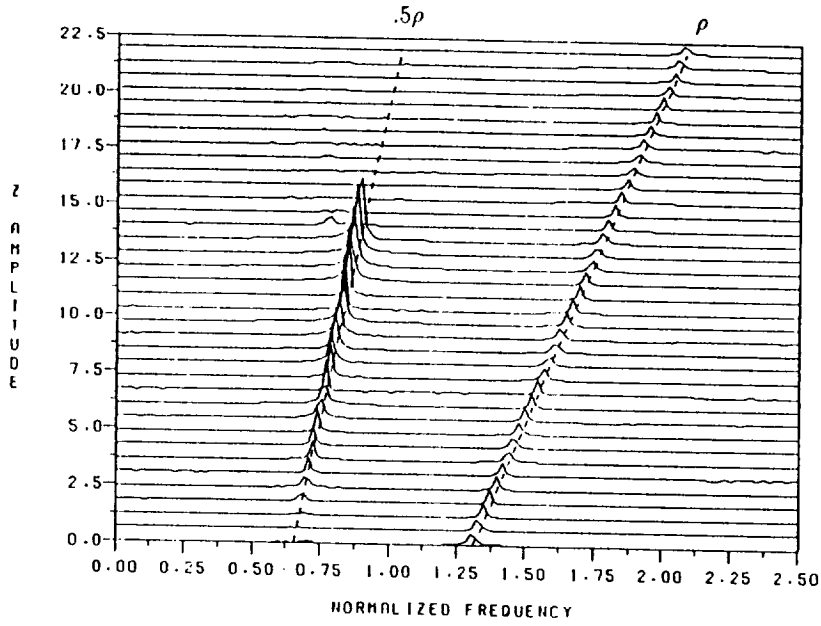

(a) Cascade spectral plot.

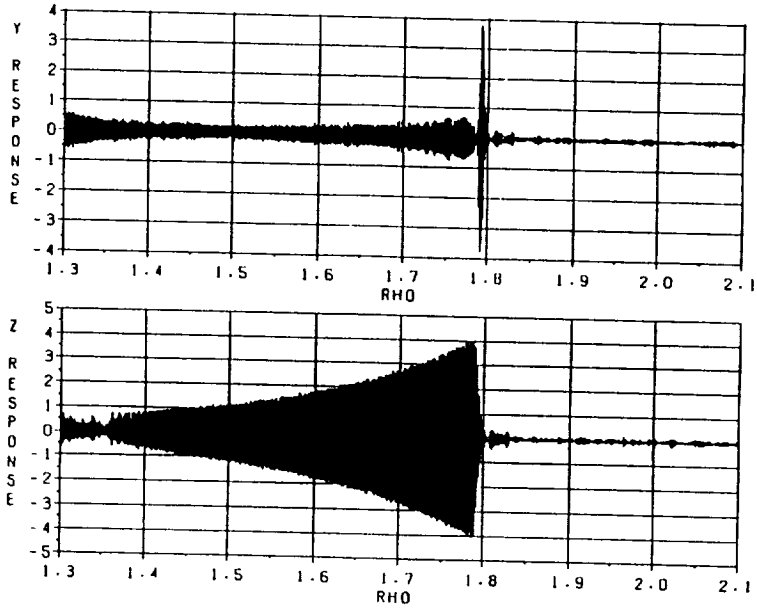

(b) Response versus ρ.

Figure 31. Simulation of subharmonic response corresponding to figure 29 with noise excitation added ($\overline{\eta}$ = 0.05).

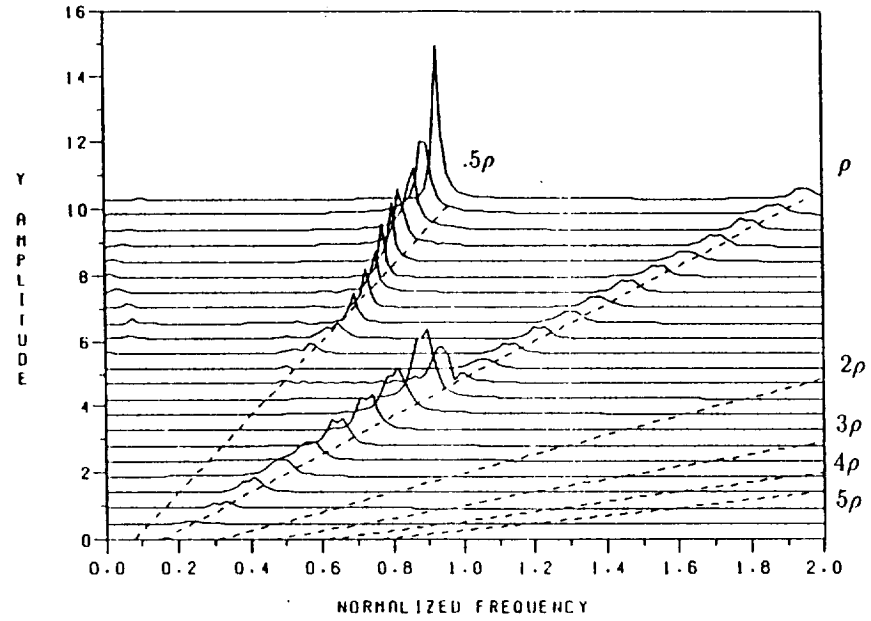

(a) Cascade spectral plot.

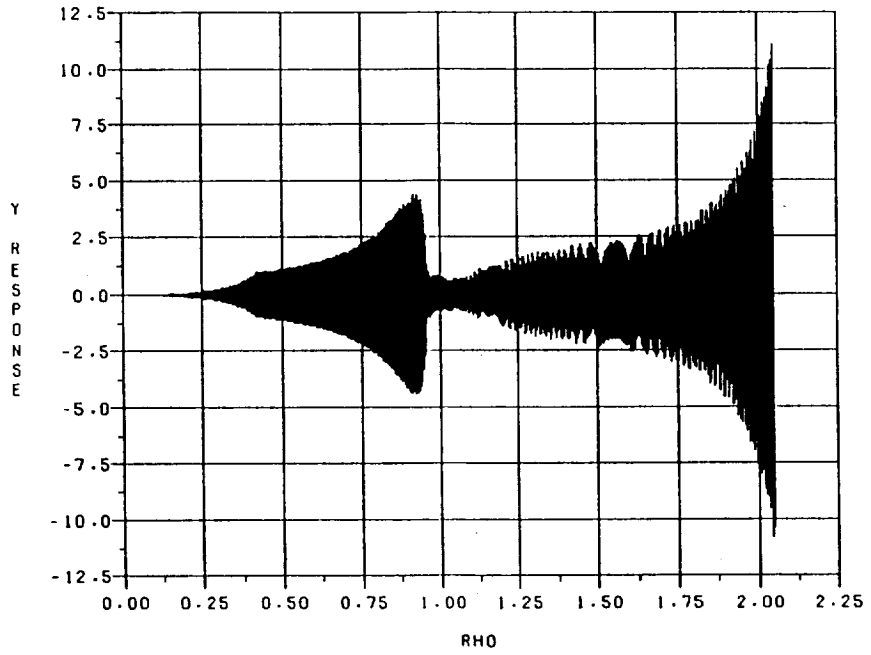

(b) Response versus ρ.

Figure 32. Interaction between limit cycle and mass unbalance response. Simulation results for $a = 0.5$.

Another mass unbalance equilibrium was presented in figure 23. This solution is for a case of increased unbalance (a = 1.0). For this case, the equilibrium radius exceeds the deadband (r_0 > 1.0). This allows for a stable equilibrium beyond the previous limit of $\rho = \rho_{lc}$. The stable equilibrium is possible for speeds up to the equilibrium stability limit ρ_{ue} = 1.72. This was demonstrated in figure 23. Although the stable equilibrium is possible up to $\rho = \rho_{ue}$, it is not guaranteed to be a unique solution. For values of ρ greater than ρ_{lc}, a combination of unbalance response and limit cycle instability is possible even though a stable equilibrium is also possible. This is illustrated in figure 33 by beginning where the simulation of figure 23 ended and ramping back down into the potentially stable region. The limit cycle is maintained in this region down to $\rho \approx 1.45$. To verify that the response is not merely the transient decay of an unstable response at higher speeds, the ramp down is stopped at ρ = 1.5 and the limit cycle continues (fig. 34). The absence of the limit cycle below ρ = 1.45 suggests that the unbalance excitation introduces a threshold between ρ_{lc} and ρ_{ue} below which the combination response is not possible. The limit cycle can also be obtained in this region by perturbation. Figure 35 shows a case where random noise excitation is used to perturb the system ($\overline{\eta}$ = 0.1). The limit cycle response is initiated in this case at about ρ = 1.6 which is below ρ_{ue}. As speed continues to increase to ρ = 2.0, the limit cycle instability increasingly dominates the response. The amplitude grows as predicted by the homogeneous analysis and the frequency becomes equal to $\sigma\rho$.

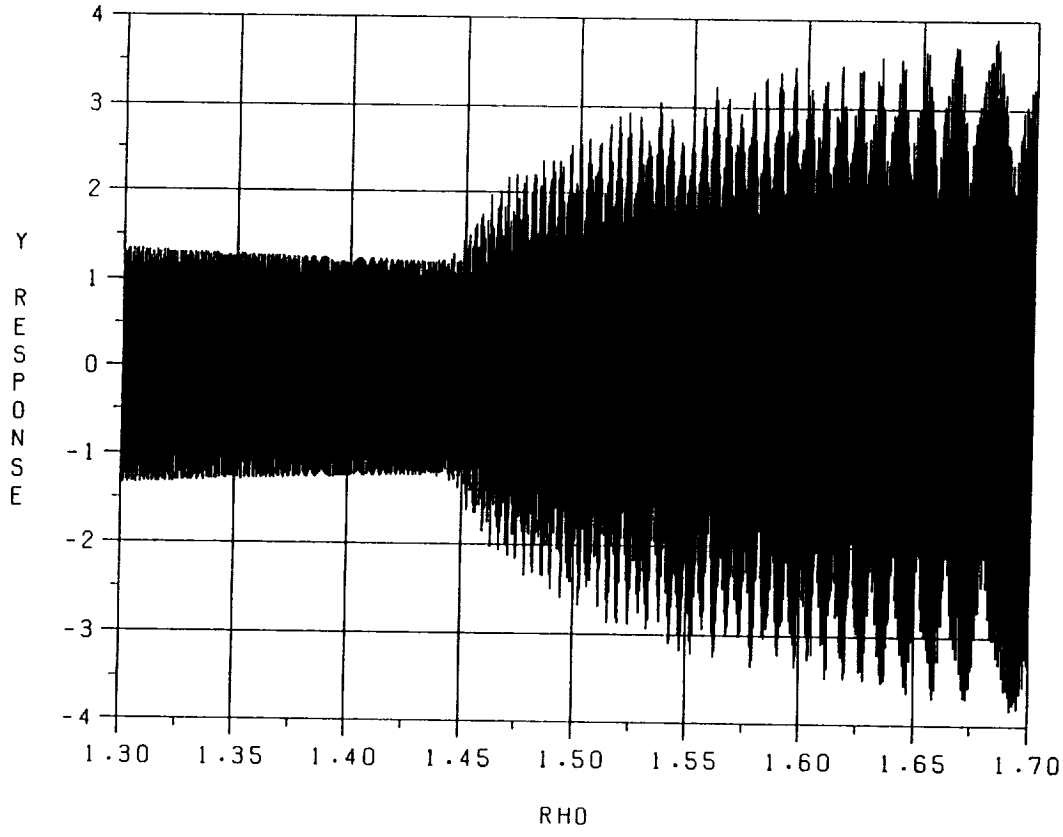

Figure 33. Nonuniqueness of unbalance equilibrium solution. Ramp down from ρ = 1.73. ρ_{lc} = 1.04, ρ_{ue} = 1.72, $\overline{\eta}$ = 0.0001.

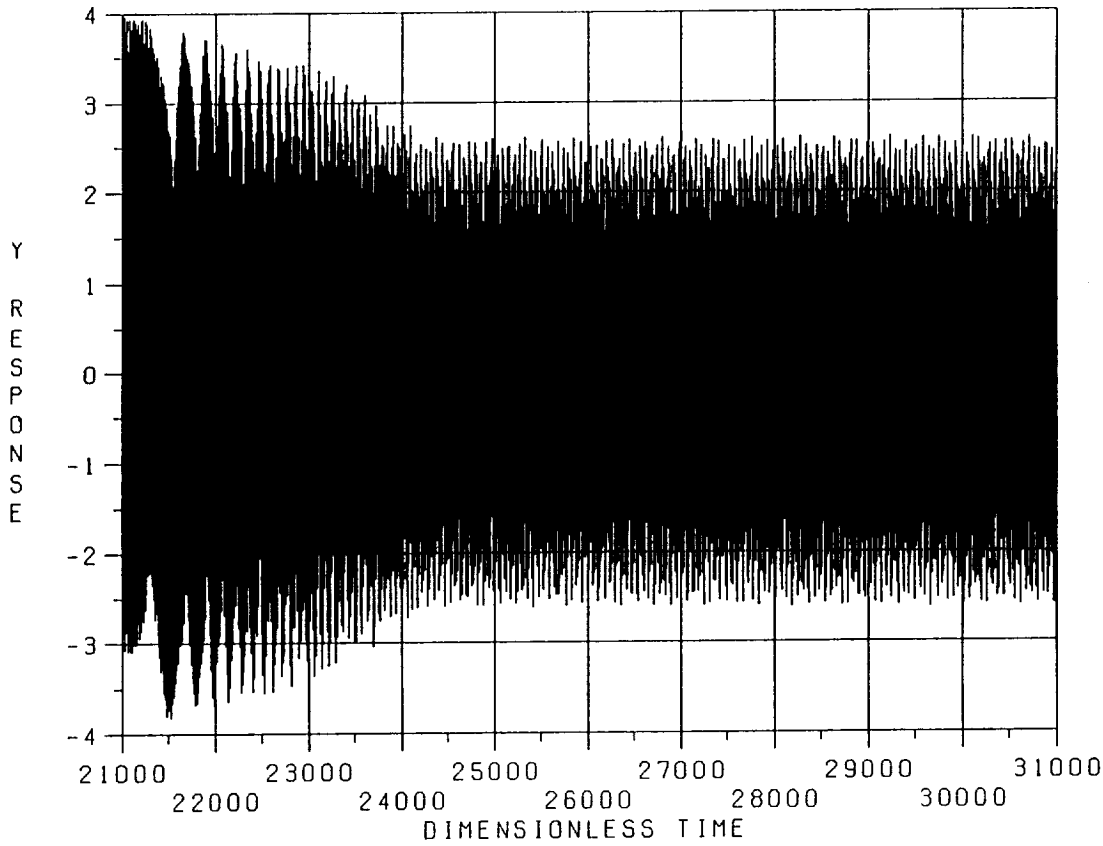

Figure 34. Repeat of simulation of figure 33 with dwell on ramp down at $\rho = 1.5$ (dimensionless time equal 24,150).

C. Interaction Between Limit Cycle and Side-Force Response

The stabilizing capacity of the side force was explored in an earlier section. The effects of side force on limit cycle instability will be addressed here. Since the side force can stabilize the system at speeds greater than the global stability threshold, one might speculate that it could also suppress the limit cycle instability that can occur at speeds below this threshold. Examples of this are presented in figures 36 through 40. For each of these figures, the simulation has no unbalance excitation. The side force is initially zero and is slowly ramped up to a maximum and then back down to zero at the same rate.

Figures 36 through 38 represent three different values of ρ: 1.25, 1.75, and 2.0, respectively. The maximum side force for each is 3.0. The simulation was initiated by quickly ramping to the operating speed and allowing the limit cycle to achieve steady-state conditions before the side force was applied. For the first two cases, the response exhibited a hysteretic behavior. While increasing the side force, a value was reached which caused the limit cycle to cease. While decreasing the side force, the limit cycle remained suppressed until a lower value of side force was reached. The more unstable case ($\rho = 1.75$) required more side force to suppress the limit cycle on the up ramp than did the case with $\rho = 1.25$. For the third case ($\rho = 2.0$), the maximum side force ($g_y = 3.0$) was not sufficient to suppress the limit cycle. This case was suppressed for a side force of approximately 6.0. With the larger maximum side force, the system exhibited the same hysteretic behavior as in the other cases. It is interesting to note that the limit cycle reinitiates at about the same value of side force on the down ramp for all three cases. This corresponds to the value for which the side force is insufficient to displace the rotor beyond

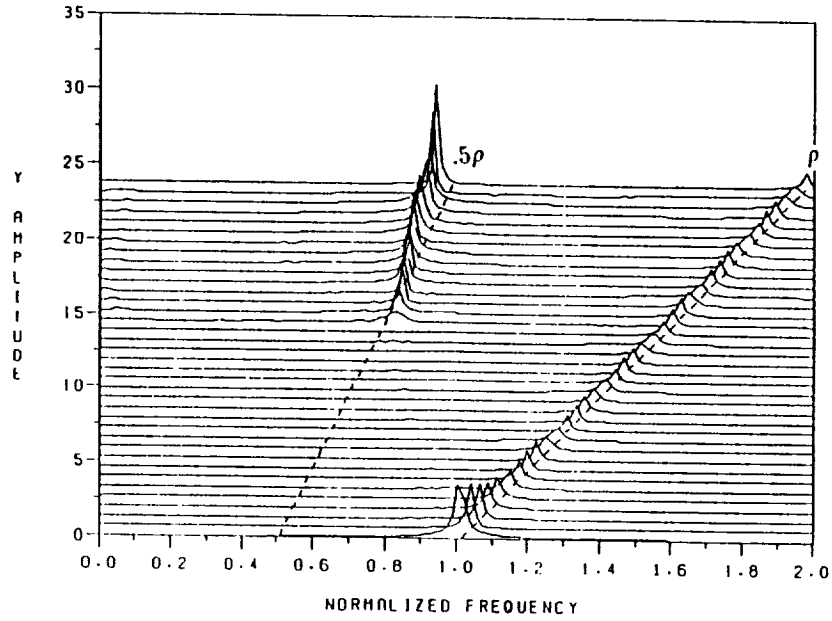

(a) Cascade spectral plot.

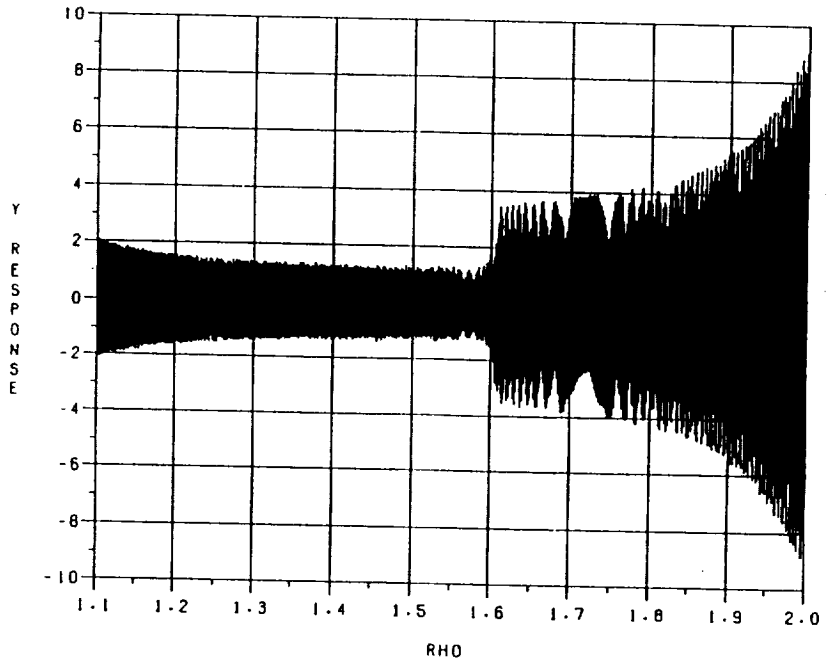

(b) Response versus ρ.

Figure 35. Interaction between limit cycle and mass unbalance response. Simulation results for $a = 1.0$ with noise excitation added ($\overline{\eta} = 0.10$).

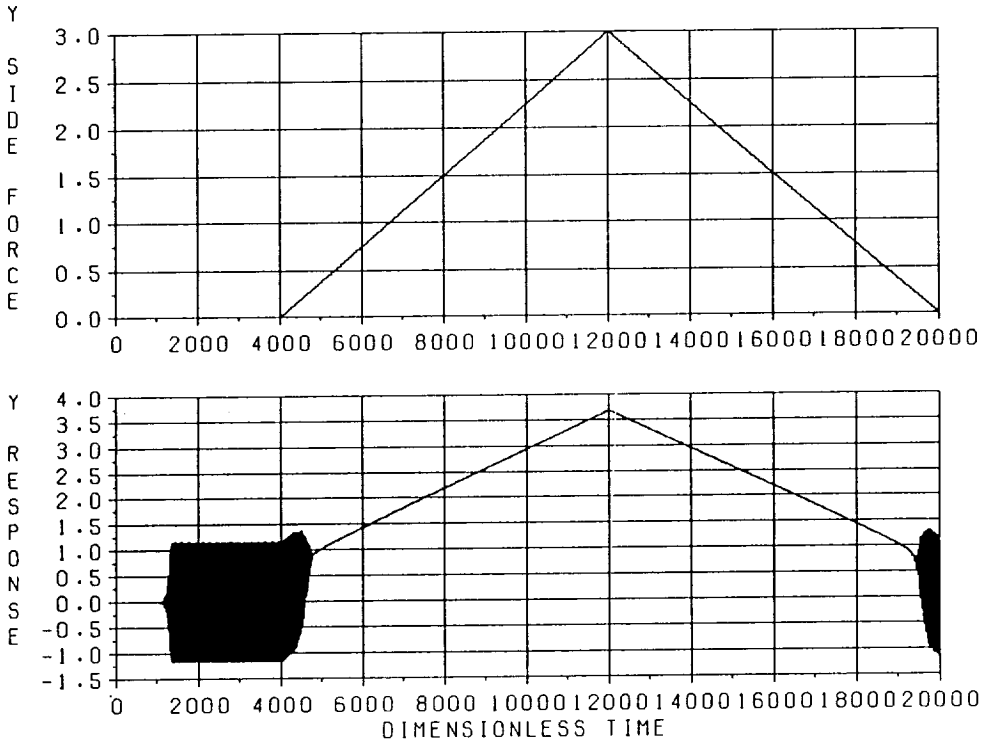

Figure 36. Limit cycle suppression by side force. Maximum $g_y = 3.0$, $\rho = 1.25$, $a = 0.0$, $\overline{\eta} = 0.0001$.

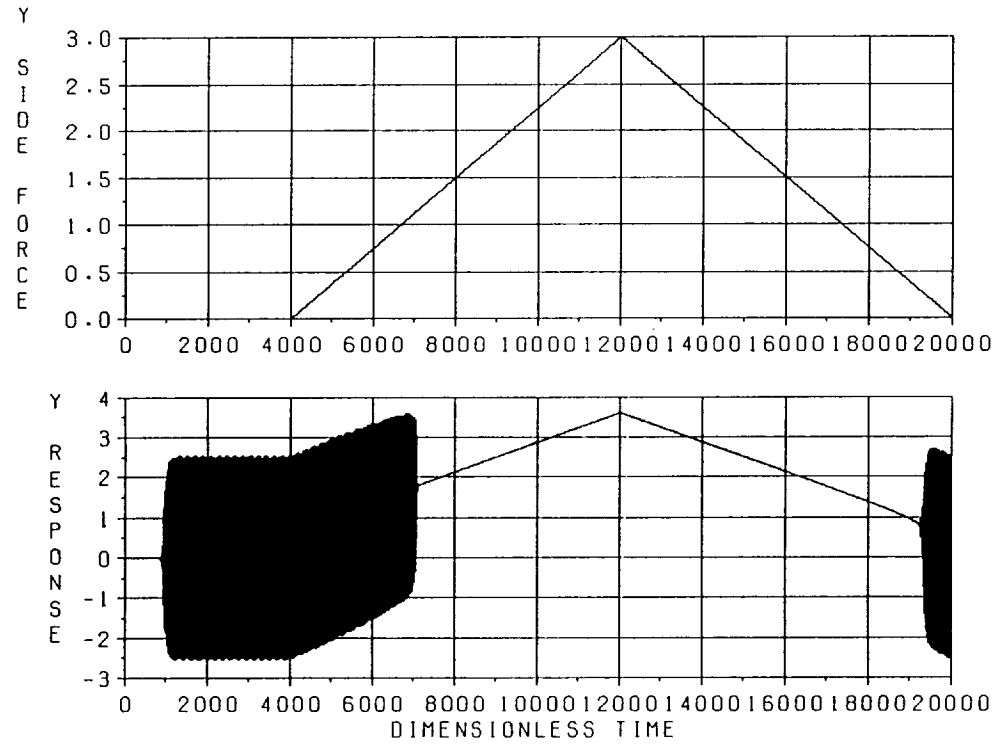

Figure 37. Limit cycle suppression by side force. Maximum $g_y = 3.0$, $\rho = 1.75$, $a = 0.0$, $\overline{\eta} = 0.0001$.

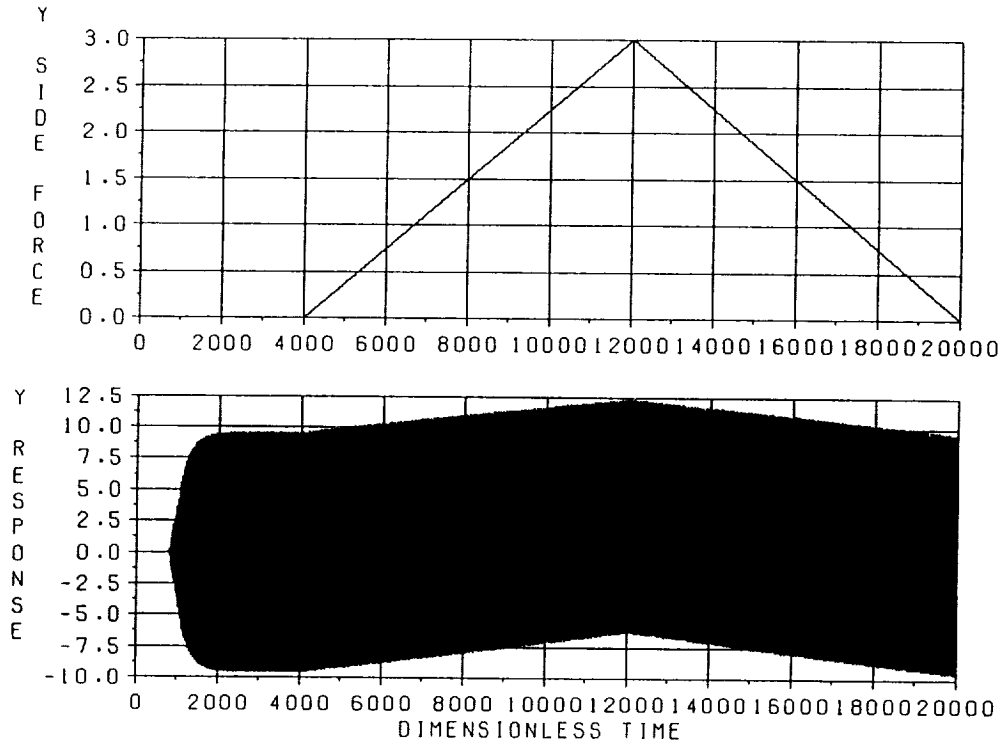

Figure 38. Limit cycle suppression by side force. Maximum $g_y = 3.0$, $\rho = 2.00$, $a = 0.0$, $\overline{\eta} = 0.0001$.

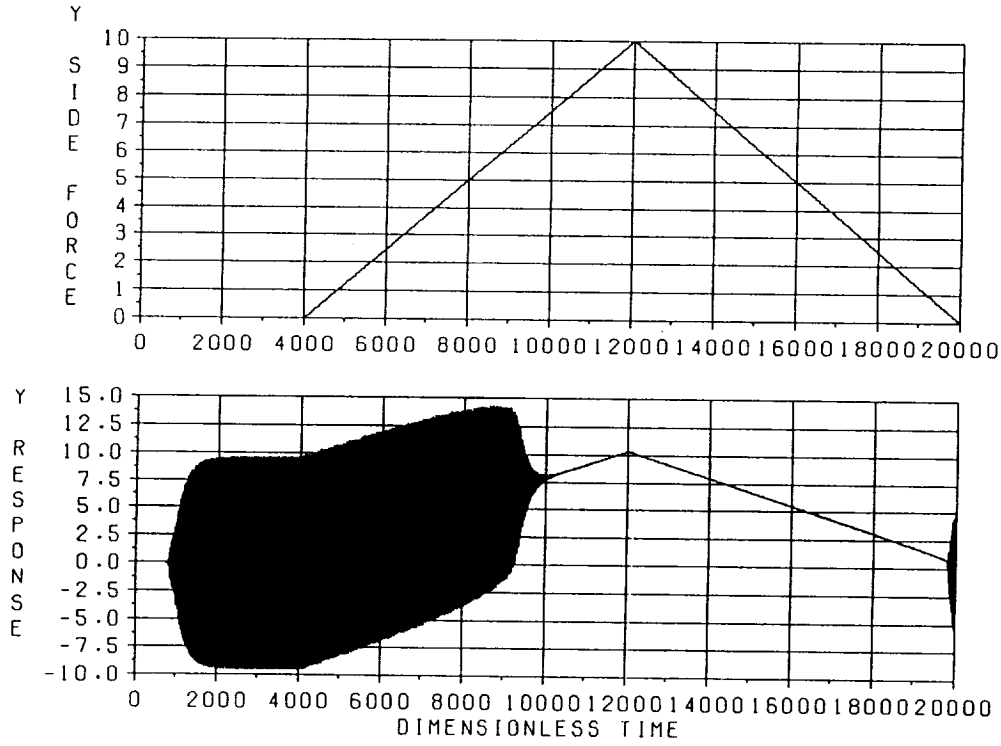

Figure 39. Limit cycle suppression by side force. Maximum $g_y = 10.0$, $\rho = 2.00$, $a = 0.0$, $\overline{\eta} = 0.0001$.

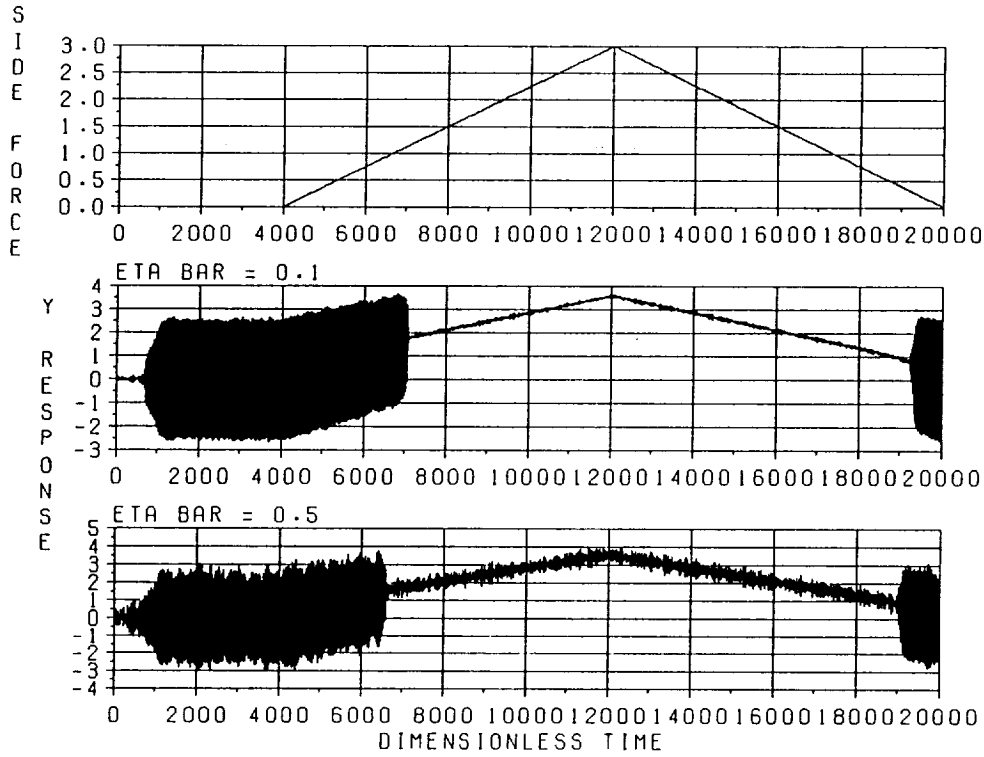

Figure 40. Effects of noise perturbation on limit cycle suppression by side force. Maximum $g_y = 3.0$, $\rho = 1.75$, $a = 0.0$, $\overline{\eta} = 0.1$, and $\overline{\eta} = 0.5$.

the deadband. Although the limit cycle suppression occurs at different values of side force, in each case it occurs approximately at the value where the rotor trajectory passes within the deadband zone. In other words, if the magnitude of the deflection vector falls below 1.0 during a portion of each period of the limit cycle, suppression of the limit cycle is imminent. The sensitivity of the suppression and reinitiation thresholds to noise perturbation is also of interest. Figure 40 shows the same system as figure 37 for two cases of noise excitation, $\overline{\eta} = 0.1$ and $\overline{\eta} = 0.5$. The first case shows little effect from the noise. The second shows a small reduction in the side force required to suppress the limit cycle (from $\approx$1.15 to $\approx$0.95). It also shows a small increase in the reinitiation threshold (from $\approx$0.3 to $\approx$0.4). One final observation that should be made for these cases is that the frequency of the limit cycle is relatively unaffected by the magnitude of the side force. This can be seen from the cascade spectral plot of the $\rho = 1.75$ case shown in figure 41.

D. Interaction Between Limit Cycle and Subharmonic Response

The capacity of mass unbalance and side-force excitation to inhibit limit cycle instability has been explored for each excitation individually. The effect of these excitations applied simultaneously will now be explored. One effect that is anticipated is the entrainment of the limit cycle frequency by the subharmonic response frequency. This is only possible for this system when both excitations are present since both are required to produce the subharmonic response phenomenon.

The approach now taken is to repeat the previous numerical experiments (figs. 36 through 39) with mass unbalance added. This will be done for two values of the unbalance parameter, a = 0.5 and a = 1.0. The effects of noise will also be explored. Figures 42 through 44 present the

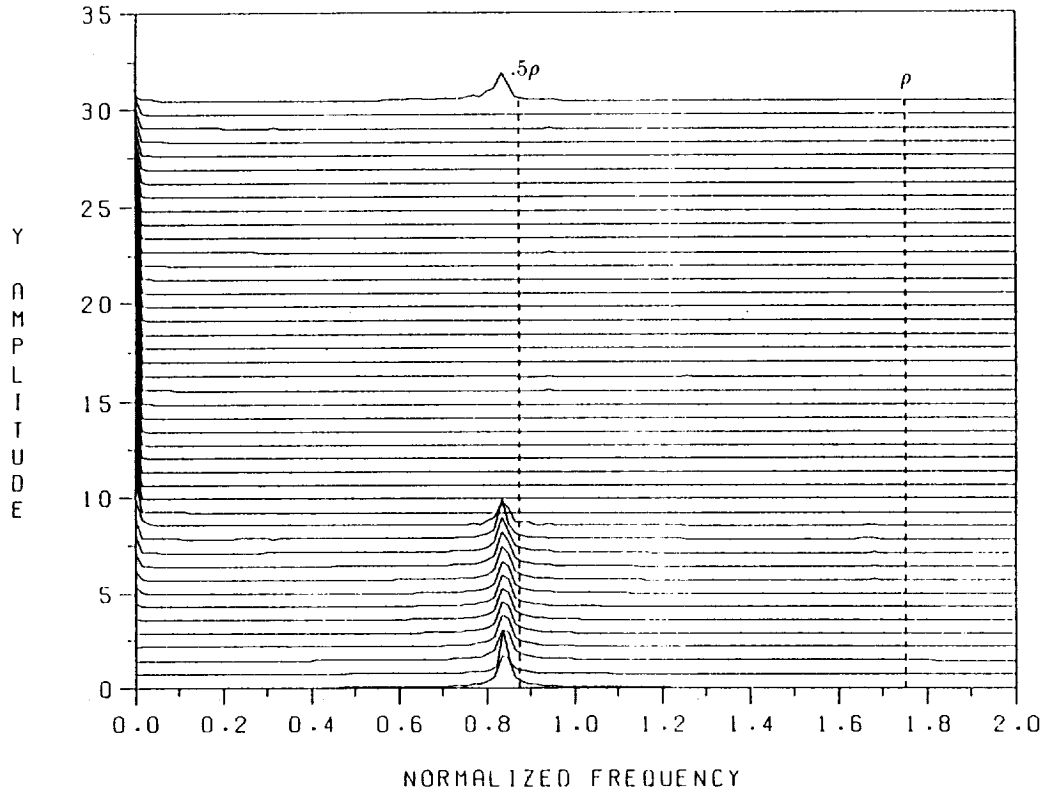

Figure 41. Cascade spectral plot of response of figure 37. Spectra taken in dimensionless time increments of 400. $\rho = 1.75$.

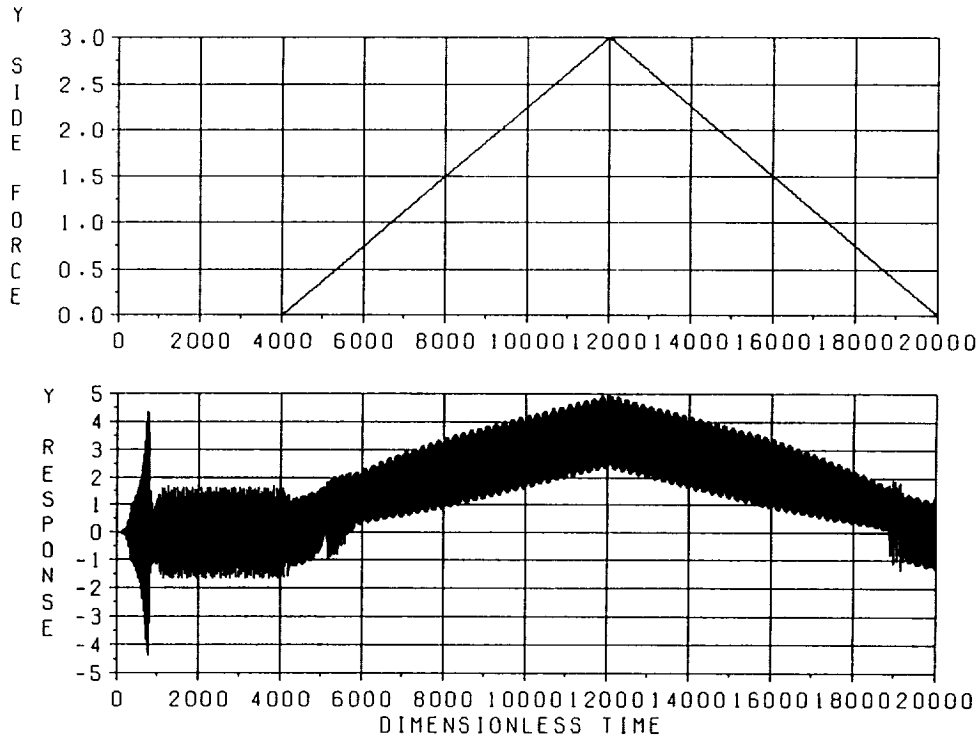

Figure 42. Interaction between limit cycle and subharmonic response. Maximum $g_y = 3.0$, $\rho = 1.25$, $a = 0.5$, and $\overline{\eta} = 0.0001$.

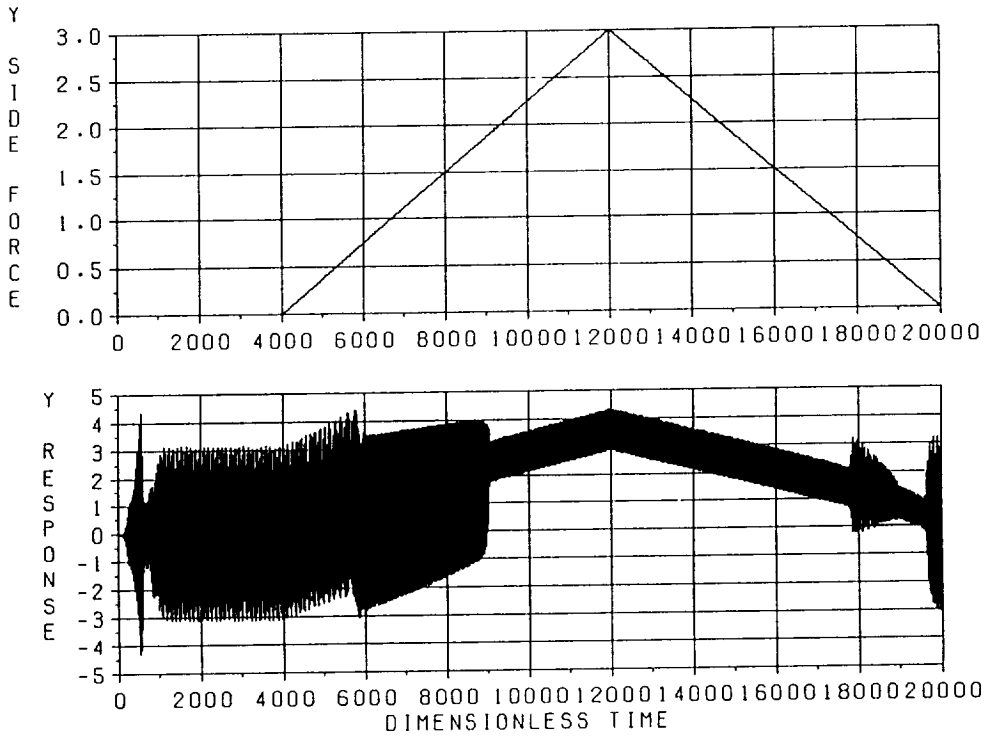

Figure 43. Interaction between limit cycle and subharmonic response. Maximum $g_y = 3.0$, $\rho = 1.75$, $a = 0.5$, and $\overline{\eta} = 0.0001$.

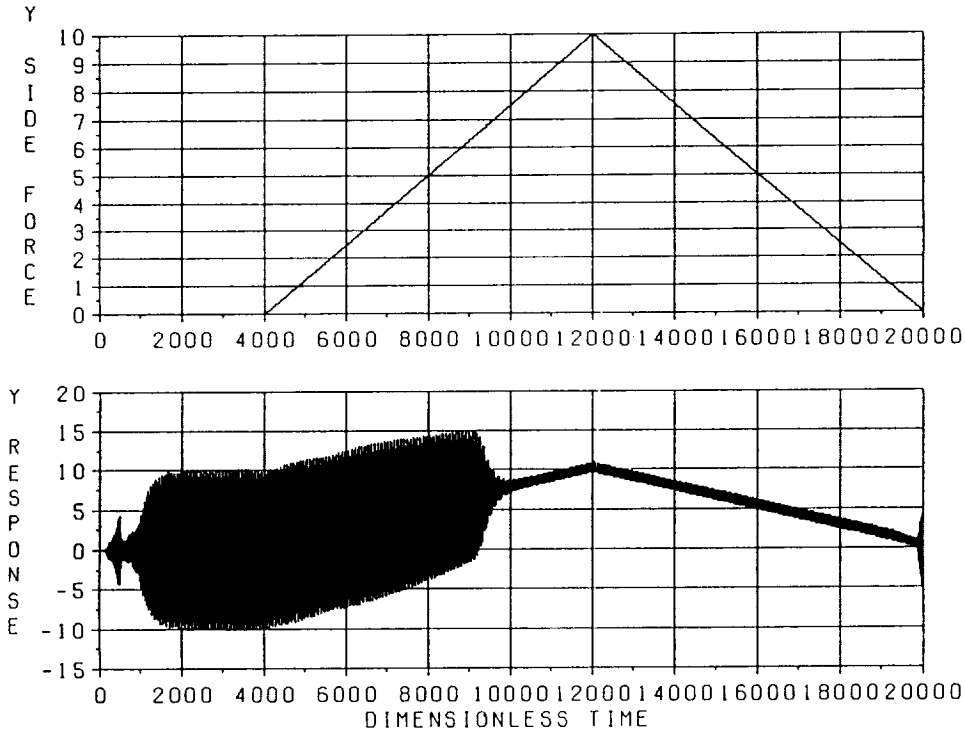

Figure 44. Interaction between limit cycle and subharmonic response. Maximum $g_y = 10.0$, $\rho = 2.0$, $a = 0.5$, and $\overline{\eta} = 0.0001$.

results for a = 0.5. In figures 42 and 43, ρ has values of 1.25 and 1.75, respectively, and g_y has a maximum value of 3.0 as before. In figure 44, ρ has a value of 2.0 and g_y has a maximum value of 10.0. The results for these cases are similar to the side force only cases. One major difference is the entrainment of the limit cycle by the subharmonic response. In figure 42, this occurs almost instantly as the side force is applied. Comparing figure 43 with the corresponding case with no unbalance (fig. 37), it is clear that the limit cycle transitions to subharmonic at a value of g_y which is less than the value which suppressed the limit cycle in figure 37 ($\approx$0.75 versus $\approx$1.25). In addition, the subharmonic response is maintained beyond the limit cycle suppression value (up to $g_y \approx$ 1.75). Upon decreasing the side force, the subharmonic and limit cycle remain suppressed until a lower value of side force is reached. Adding noise affects this behavior as shown in figure 45 ($\overline{\eta}$ = 0.5). The reinitiation occurs for larger values of side force than without the noise. The cascade spectral plot for this case (fig. 46) shows the distinct frequency shift that occurs when the limit cycle becomes entrained. The case with ρ = 2.0 (fig. 44) does not demonstrate the entrainment. This case behaves almost identically to the corresponding case without unbalance (fig. 39) with a small harmonic component superimposed due to the unbalance excitation. The absence of the subharmonic is due to the fact that ρ = 2.0 is above the range of possible existence of the subharmonic, as shown in figure 13.

The results for the same cases with increased unbalance (a = 1.0) exhibit somewhat different behavior. The low speed case (ρ = 1.25) does not exhibit any limit cycle instability. This is due to the existence of a stable unbalance equilibrium for this speed. The lack of a one-half subharmonic is due to the fact that ρ = 1.25 is below the range of possible existence. As the side force increases, a low amplitude two-thirds subharmonic develops for a small range of side force when noise excitation is present ($\overline{\eta}$ = 0.5). The results are shown in the cascade spectral plot in figure 47. The intermediate speed case (ρ = 1.75) exhibits subharmonic response almost

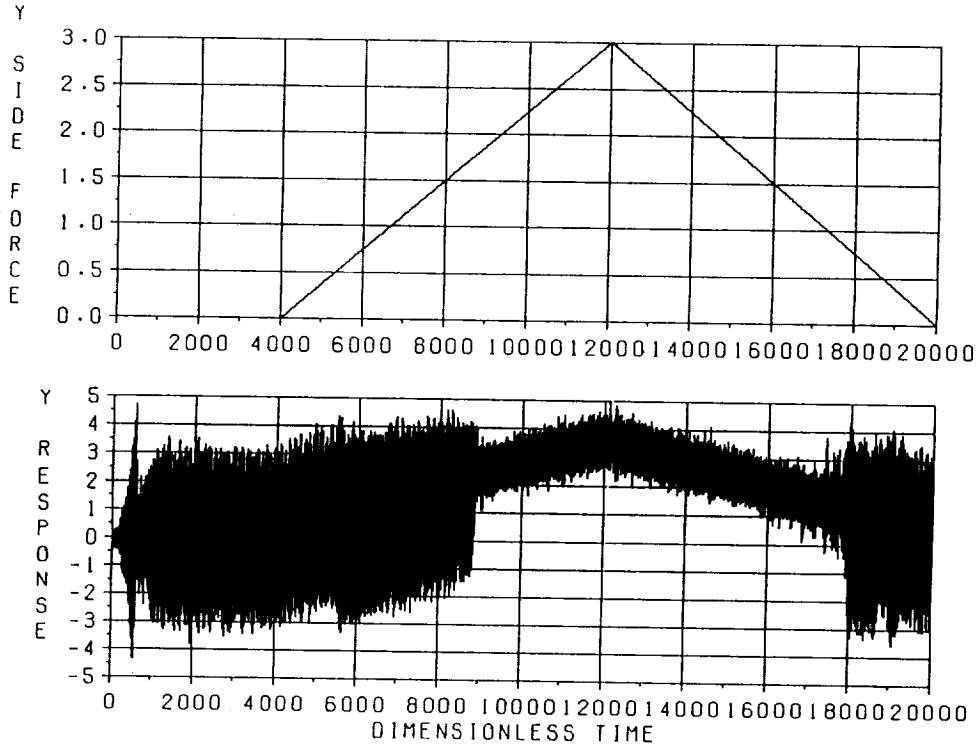

Figure 45. Interaction between limit cycle and subharmonic response. Maximum g_y = 3.0, ρ = 1.75, a = 0.5, and $\overline{\eta}$ = 0.5.

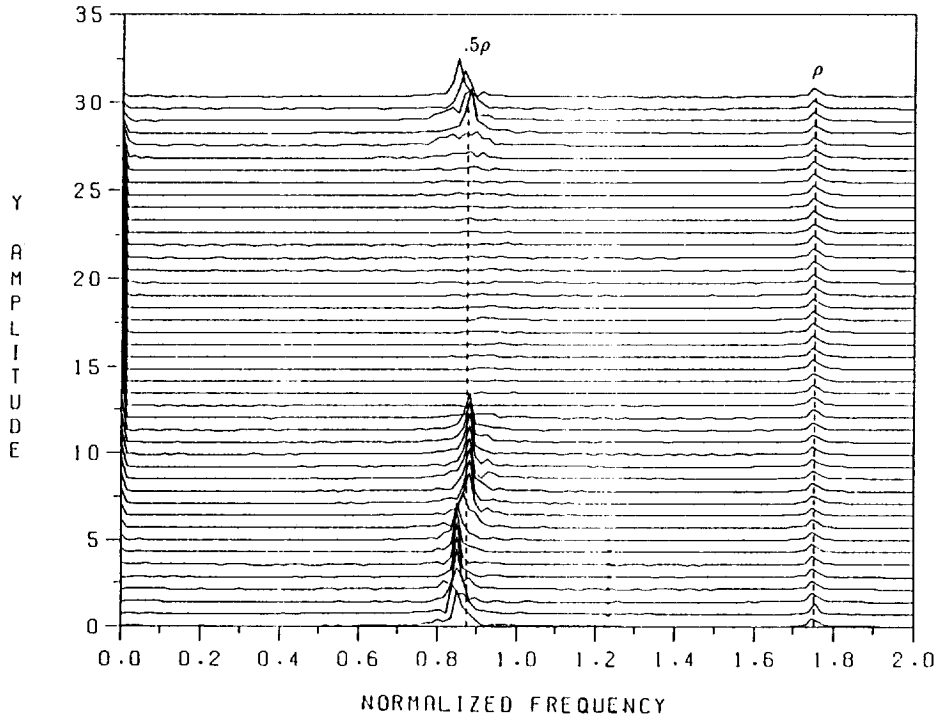

Figure 46. Cascade spectral plot of response of figure 45. Spectra taken in dimensionless time increments of 400. ρ 1.75, $a = 0.5$, and $\overline{\eta} = 0.5$.

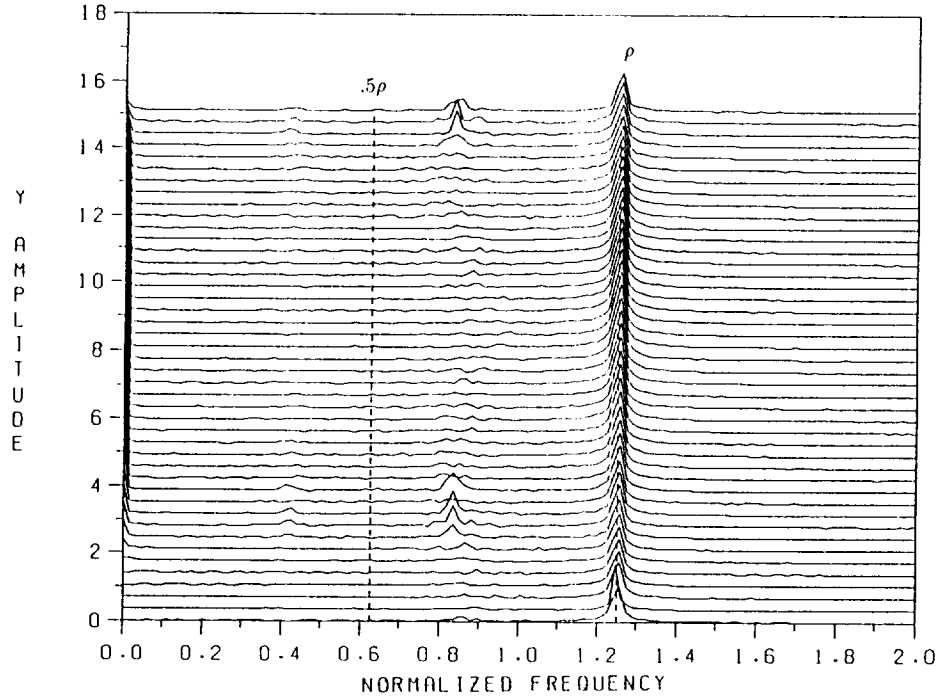

Figure 47. Interaction between limit cycle and subharmonic response. Cascade spectral plot of response. Spectra taken in dimensionless time increments of 400. Maximum $g_y = 3.0$, $\rho = 1.25$, $a = 1.0$, and $\overline{\eta} = 0.5$.

immediately after the initiation of the side-force ramp. Due to unbalance excitation effects, the limit cycle frequency ratio is very near 0.5 for this case. The subharmonic is suppressed when the side force exceeds the value for which existence is possible. The subharmonic reinitiates at a lower value when the side force is decreased. These results are shown in figure 48. The high speed case (ρ = 2.0) again exhibits only limit cycle instability since it falls beyond the range of possible subharmonic. The results are very similar to the previous cases (a = 0.0 and a = 0.5) and are shown in figure 49.

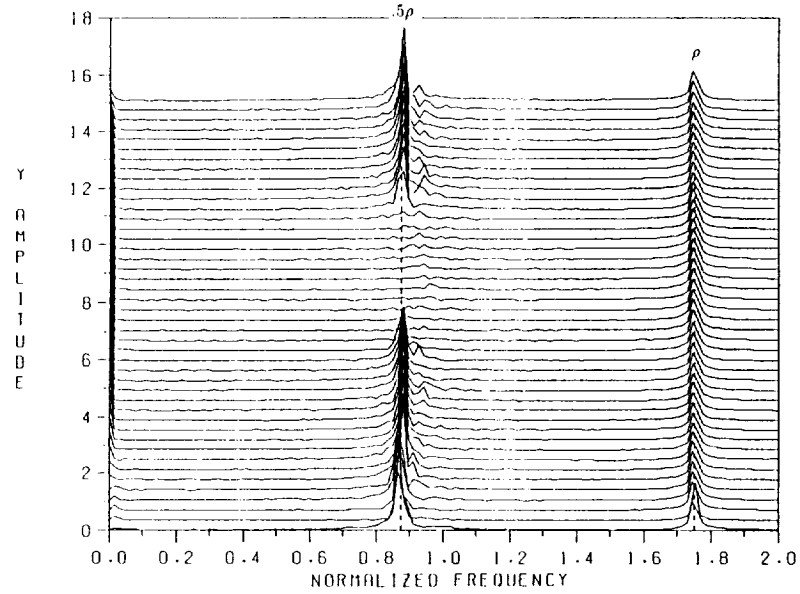

Figure 48. Interaction between limit cycle and subharmonic response. Cascade spectral plot of response. Spectra taken in dimensionless time increments of 400. Maximum g_y = 3.0, ρ = 1.75, a = 1.0, and $\overline{\eta}$ = 0.5.

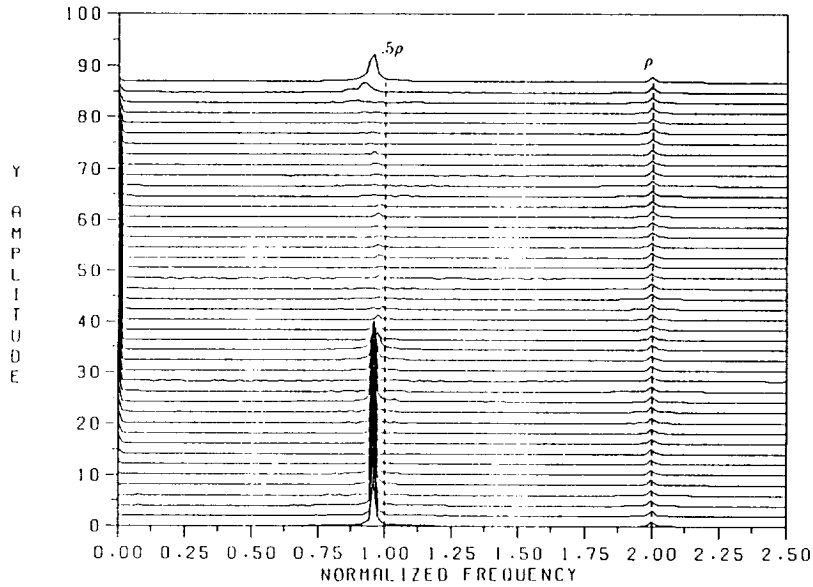

Figure 49. Interaction between limit cycle and subharmonic response. Cascade spectral plot of response. Spectra taken in dimensionless time increments of 400. Maximum g_y = 10.0, ρ = 2.00, a = 1.0, and $\overline{\eta}$ = 0.5.

E. Effects of Operating Profile on Interacting Responses

The effects of the unbalance, side force, and combined unbalance and side force on the limit cycle instability have been demonstrated. The results have shown a strong dependence on initial conditions and perturbations. This is indicated by the hysteretic behavior during the side-force ramp up and back down, for example, and by the sensitivity to noise perturbation. These results were obtained using certain numerical experiments where parameters were intentionally varied in order to gain insight into the response of the system. These variations were not necessarily representative of actual operating profiles of a turbomachine. Due to the sensitivity of the system to initial conditions, it is important to consider realistic operating profiles to assess the potential for the occurrence of limit cycle behavior or subharmonic response. This will be accomplished using a series of simulations where speed is ramped up and back down while the other system parameters are held fixed. The simulations are initialized by rapidly ramping speed from zero to a value of $\rho = 1.0$. Speed is then held constant for a period of time. The side force begins at zero initially and ramps to its steady value somewhat slower than speed. It reaches its maximum at the end of the steady hold time for speed. Speed is then ramped up to $\rho = 2.0$ and back to $\rho = 1.0$ while the side force remains constant. These profiles are shown in figure 50. This approach allows the system to achieve a steady-state initial condition at a speed which is outside the range of limit cycle or subharmonic response. The maximum value of the side force, the unbalance, and the random noise parameter are the model parameters that will be varied in this series of experiments.

The first three cases examined all have unbalance magnitudes of $a = 0.5$. The first has a side force magnitude of $g_y = 1.5$. For the second $g_y = 1.0$ and for the third $g_y = 0.5$. Results for the first case are shown in figure 51. This case also has random noise perturbation ($\overline{\eta} = 0.5$). No limit cycle or subharmonic occurs for this case. A low-level response of the system resonance to the noise excitation is visible in the plot. Without the noise excitation this case exhibited only synchronous harmonic response to the unbalance excitation. This case represents a case similar to that of figures 43 and 45. In the earlier simulations, speed was held fixed and the side force was varied while the converse is true in the current simulation. Examining the response in figure 45 at a value of $g_y = 1.5$ shows that a subharmonic existed on the up ramp but only the synchronous harmonic existed at this value on the down ramp. These results indicate that the initial conditions and/or the perturbation used in the current simulation were not suitable for initiating the subharmonic response. The second case ($g_y = 1.0$) also failed to exhibit any nonsynchronous response in the absence of noise. With noise excitation ($\overline{\eta} = 0.5$) however, both subharmonic response and limit cycle instability are observed. These results are shown in figures 52 and 53. The subharmonic initiates at $\rho \approx 1.6$. The response transitions to limit cycle instability above $\rho \approx 1.8$. This is approximately the upper limit of possible subharmonic response for this case. For the case of low damping and no cross-coupled stiffness examined previously (figs. 29 and 30), the response in this region appeared to be seeking a subharmonic equilibrium that was not predicted by the harmonic balance procedure. When noise excitation was added (fig. 31) this did not occur. The current results suggest that for a system which has cross-coupled stiffness of the type addressed here (σ near 0.5), the response will transition to the limit cycle instability in this region and not arrive at the weakly stable subharmonic solution. This would be expected since the system is moving very close to the global onset speed of instability ρ_{gi}. The third case ($g_y = 0.5$) behaves very similarly to the second. The results are shown in figures 54 and 55. One significant difference is that noise excitation was not necessary to initiate the subharmonic response. The lower value of side force causes the displacement to fall within the deadband ($r < 1.0$) which perturbs the system to such an extent that the subharmonic is initiated. Once the

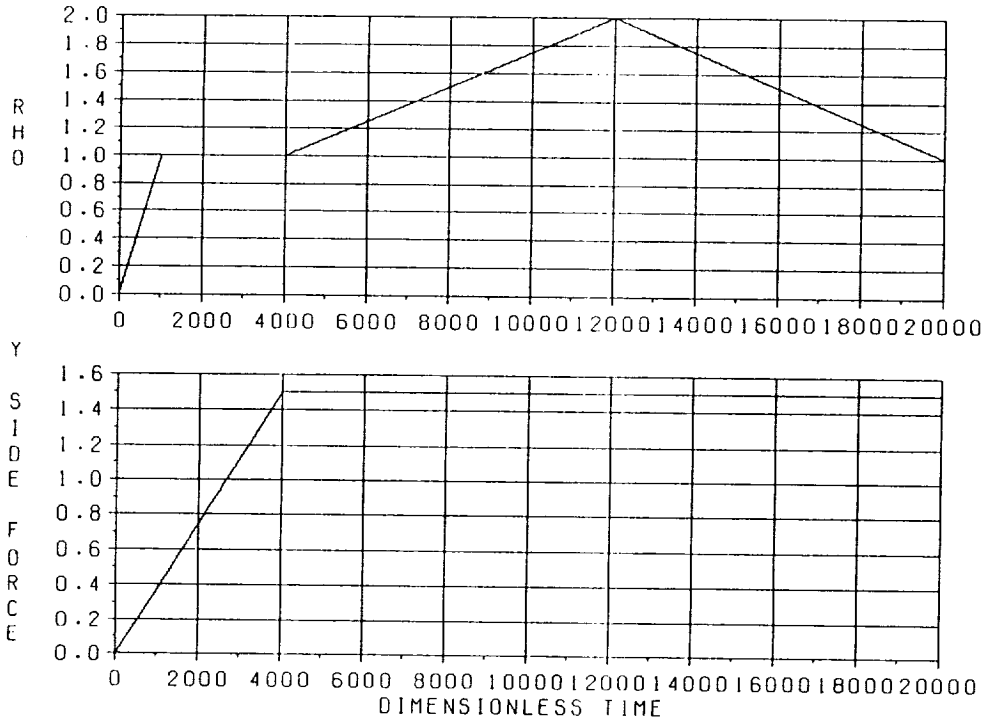

Figure 50. Effects of operating profile on interacting responses. Typical profiles for ρ and g_y.

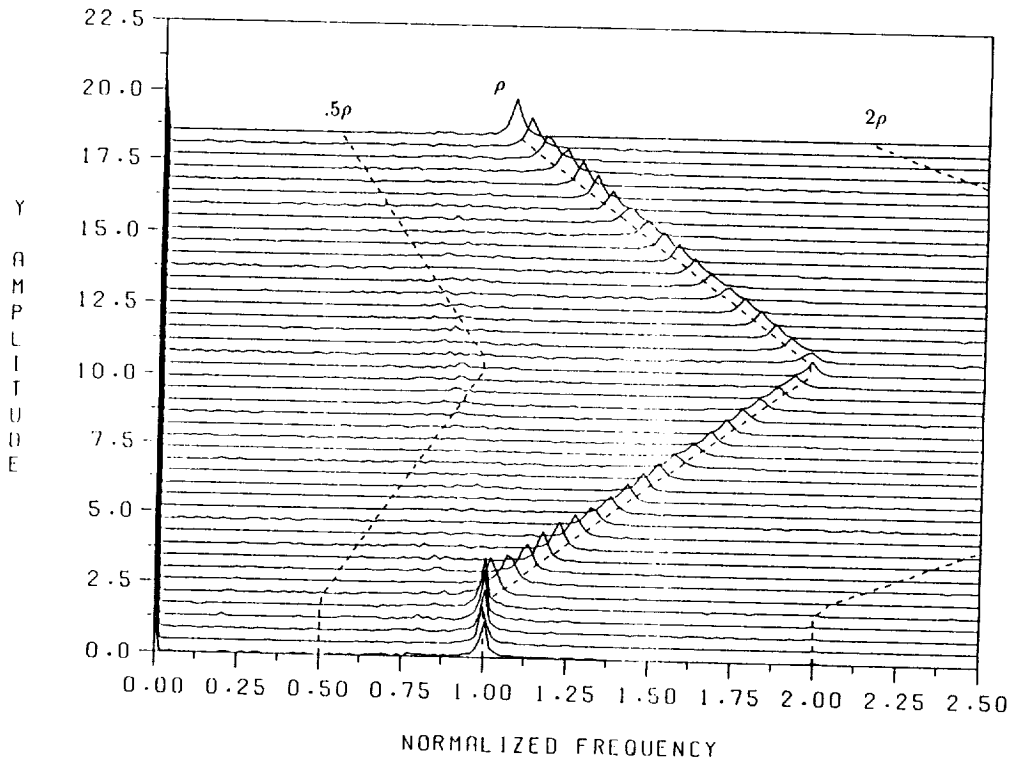

Figure 51. Effects of operating profile on interacting responses. Cascade spectral plot of response. Spectra taken in dimensionless time increments of 400.
$g_y = 1.5, a = 0.5, \overline{\eta} = 0.5.$

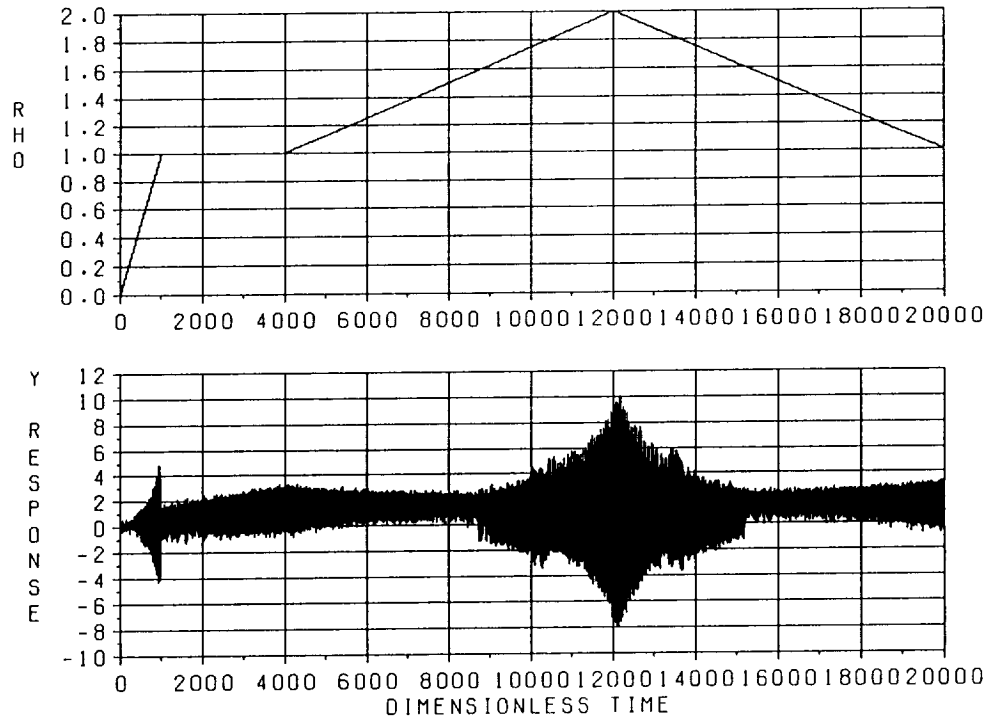

Figure 52. Effects of operating profile on interacting responses. $g_y = 1.0$, $a = 0.5$, and $\overline{\eta} = 0.5$.

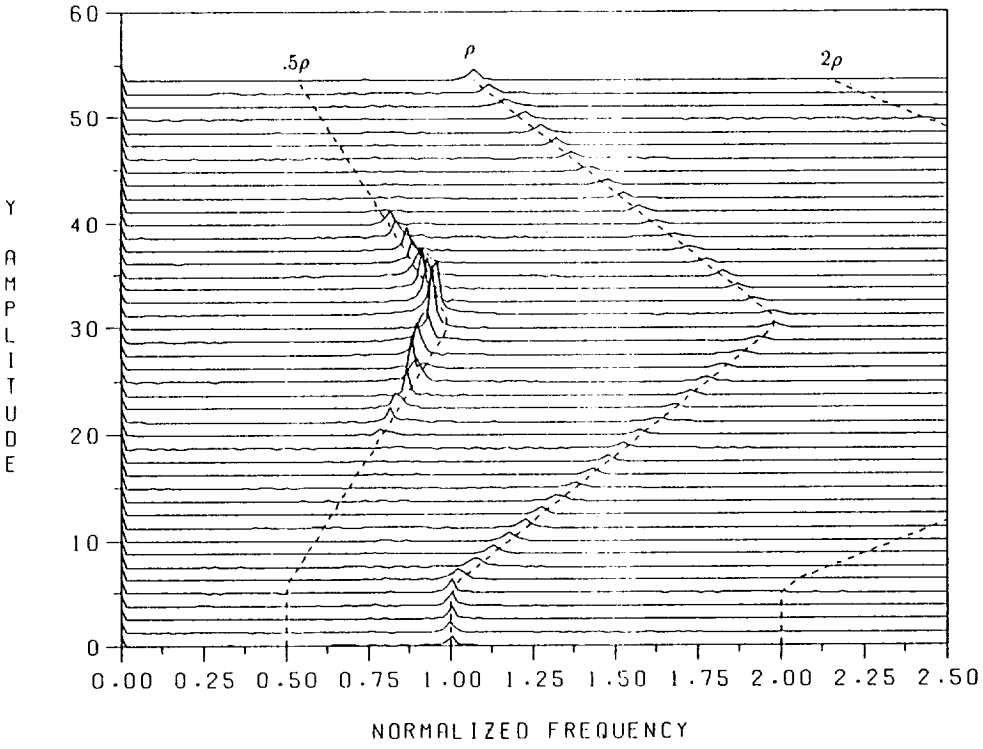

Figure 53. Cascade spectral plot of figure 52. Spectra taken in dimensionless time increments of 400. $g_y = 1.0$, $a = 0.5$, and $\overline{\eta} = 0.5$.

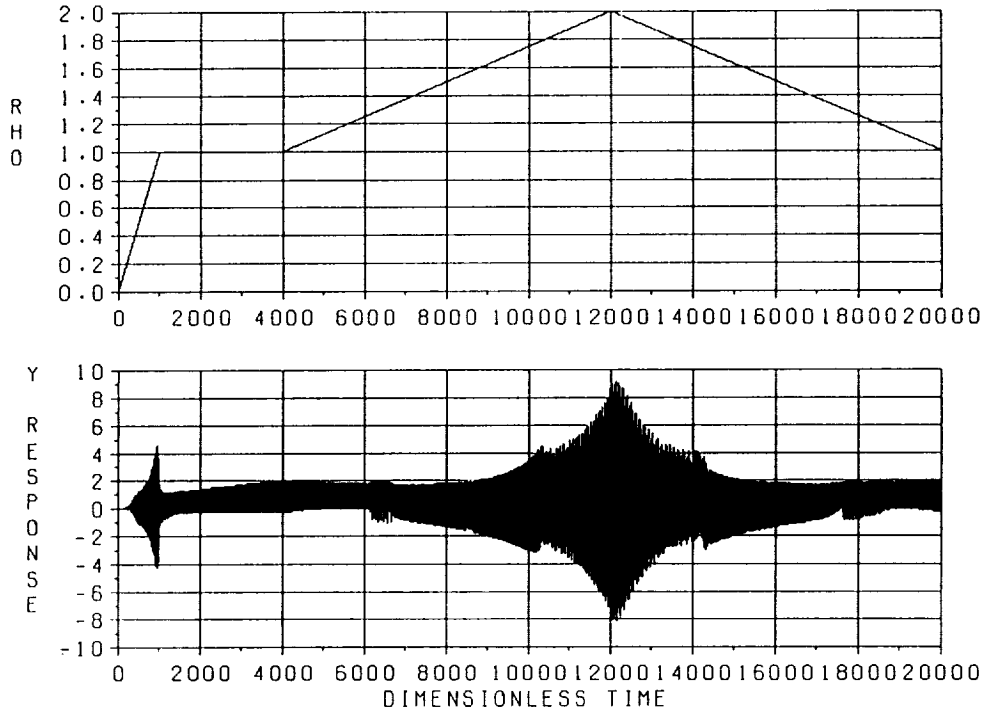

Figure 54. Effects of operating profile on interacting responses. $g_y = 0.5$, $a = 0.5$, and $\overline{\eta} = 0.0001$.

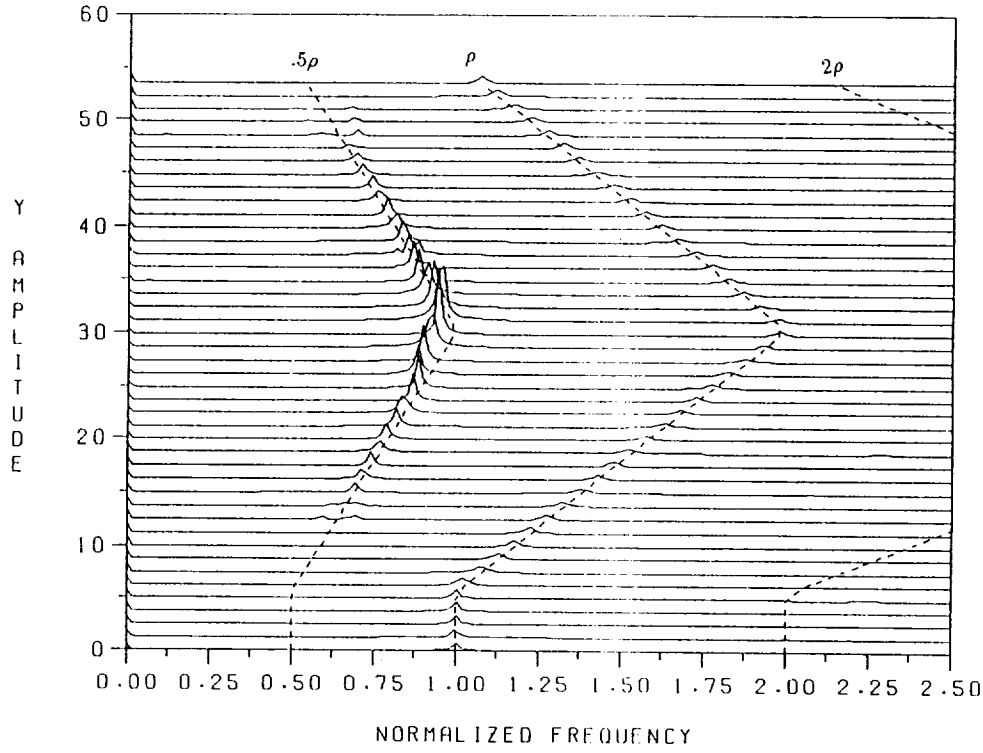

Figure 55. Cascade spectral plot of figure 54. Spectra taken in dimensionless time increments of 400. $g_y = 0.5$, $a = 0.5$, and $\overline{\eta} = 0.0001$.

subharmonic is initiated, it transitions to the limit cycle when ρ exceeds the range of possible subharmonic. The only other difference noted is in the specific values of ρ at which transition occurred.

The three cases just examined were repeated with an unbalance value of a = 1.0 instead of a = 0.5. The results are shown in figures 56 through 61. For each of these cases, the subharmonic was initiated and transitioned to limit cycle instability without the noise perturbation. When the side force is increased to g_y = 2.0, noise is necessary to cause the subharmonic response to initiate (figs. 62 and 63).

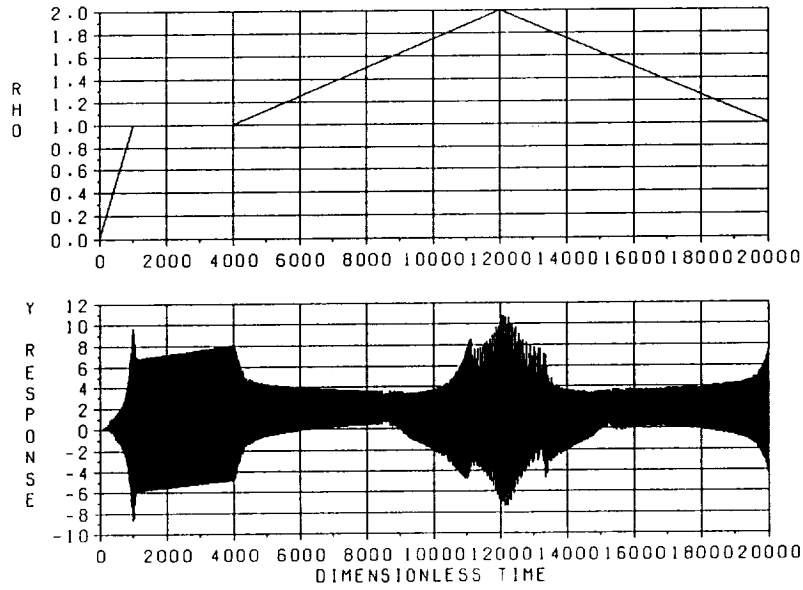

Figure 56. Effects of operating profile on interacting responses. g_y = 1.5, a = 1.0, and $\overline{\eta}$ = 0.0001.

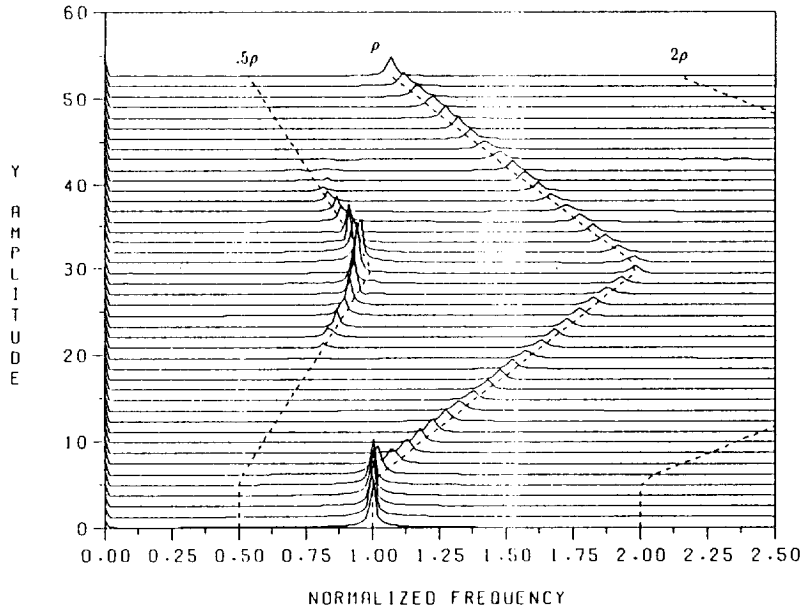

Figure 57. Cascade spectral plot of figure 56. Spectra taken in dimensionless time increments of 400. g_y = 1.5, a = 1.0, and $\overline{\eta}$ = 0.0001.

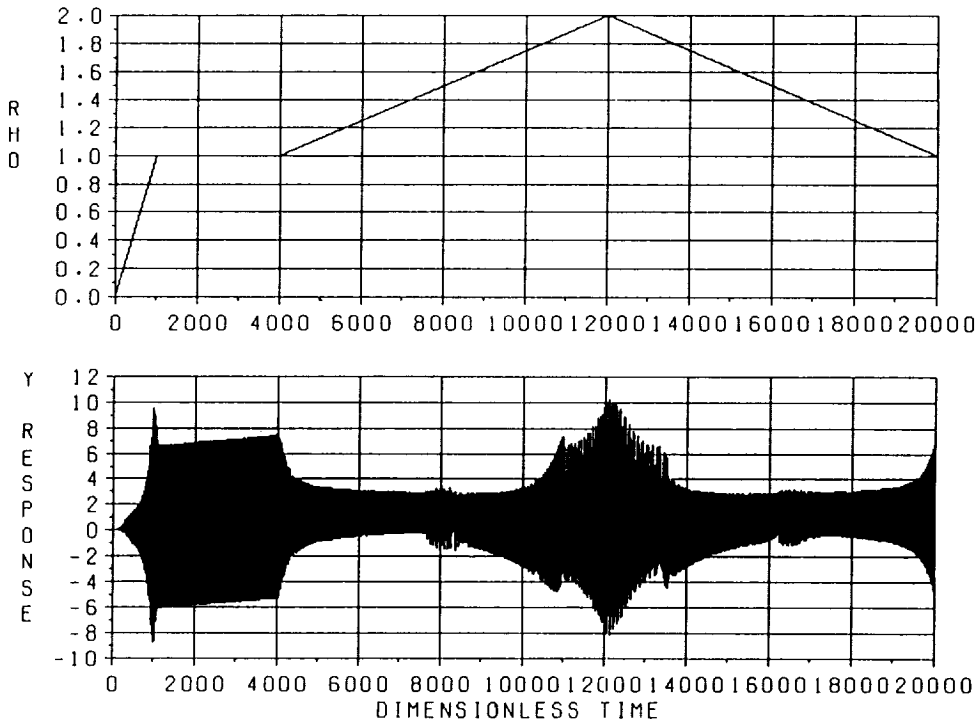

Figure 58. Effects of operating profile on interacting responses. $g_y = 1.0$, $a = 1.0$, and $\overline{\eta} = 0.0001$.

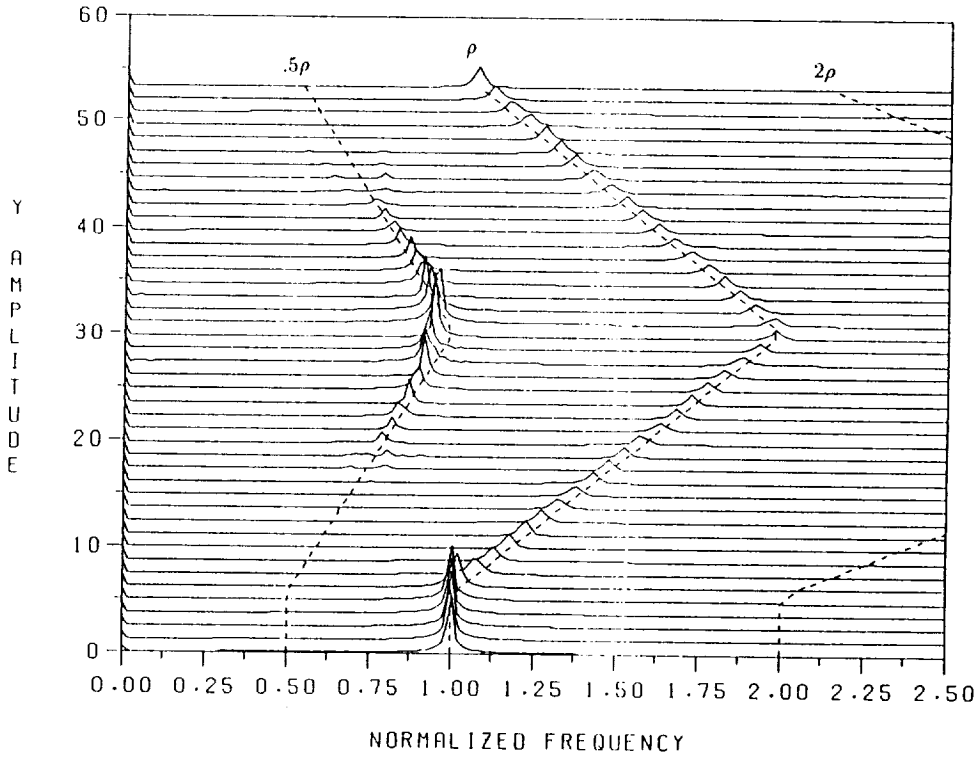

Figure 59. Cascade spectral plot of figure 58. Spectra taken in dimensionless time increments of 400. $g_y = 1.0$, $a = 1.0$, and $\overline{\eta} = 0.0001$.

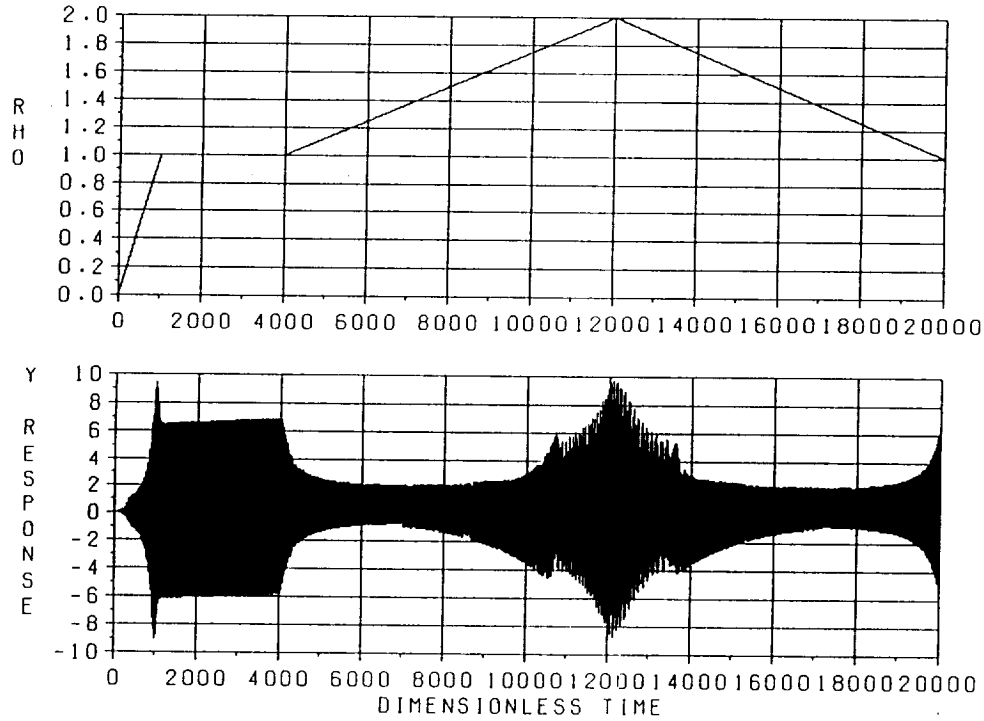

Figure 60. Effects of operating profile on interacting responses. $g_y = 0.5$, $a = 1.0$, and $\overline{\eta} = 0.0001$.

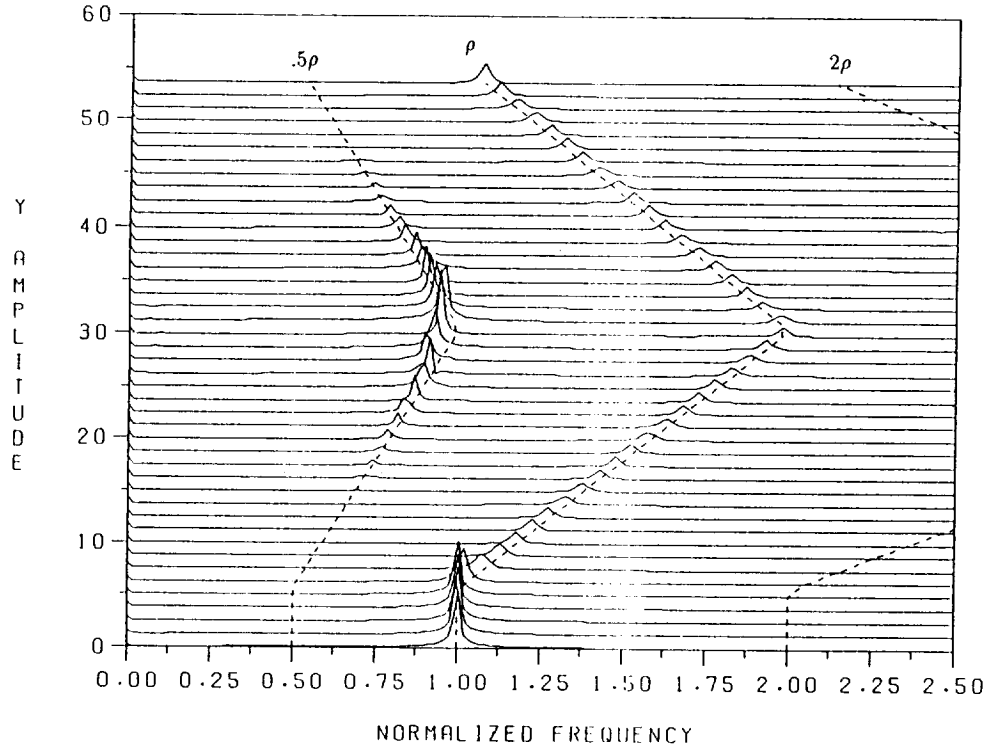

Figure 61. Cascade spectral plot of figure 60. Spectra taken in dimensionless time increments of 400. $g_y = 0.5$, $a = 1.0$, and $\overline{\eta} = 0.0001$.

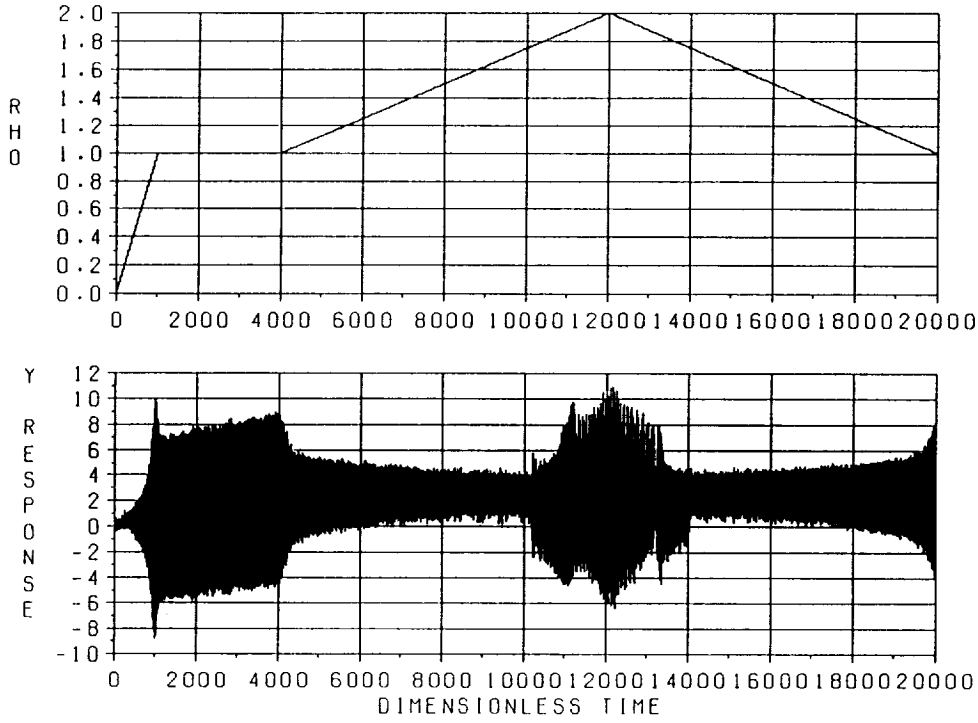

Figure 62. Effects of operating profile on interacting responses. $g_y = 2.0$, $a = 1.0$, and $\overline{\eta} = 0.5$.

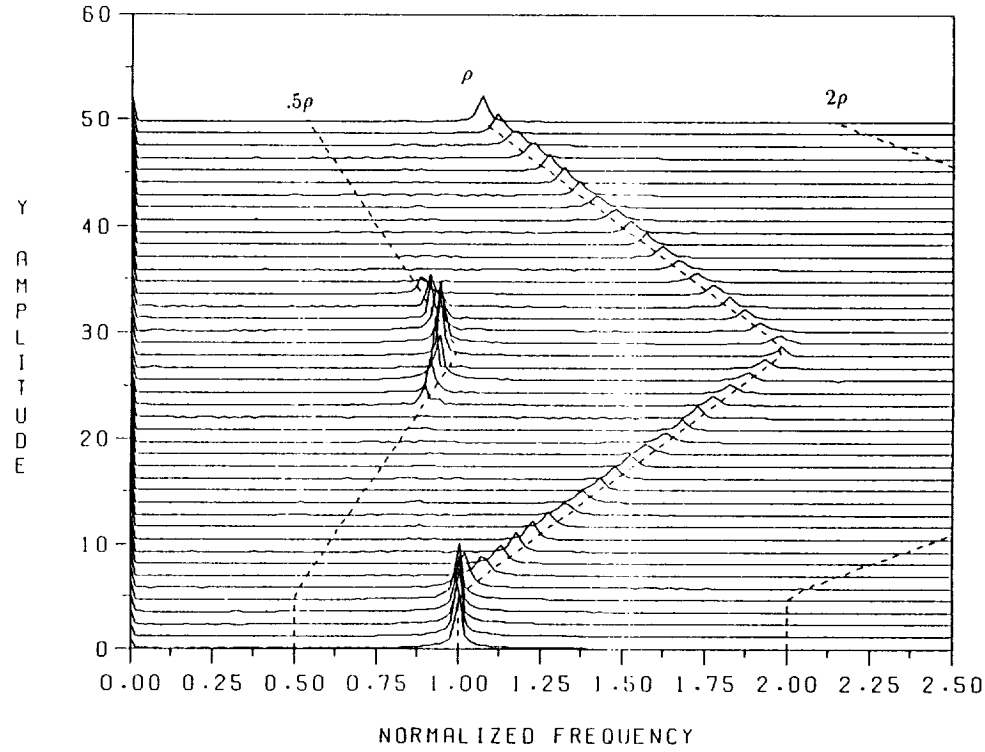

Figure 63. Cascade spectral plot of figure 62. Spectra taken in dimensionless time increments of 400. $g_y = 2.0$, $a = 1.0$, and $\overline{\eta} = 0.5$.

F. Effects of Other System Parameters on Interacting Responses

The effects of speed, side force, mass unbalance, and random noise on the interacting limit cycle and subharmonic response have been explored. The effects of the cross-coupled stiffness parameter σ, the nonlinear stiffness parameter γ, and the damping parameter ζ are also of interest. The previous case with $g_y = 1.0$ and $a = 1.0$ (figs. 58 and 59) will be used as the basis for making variations in these other system parameters.

The effects of σ were examined by changing its value from the nominal of 0.48 to 0.40 and 0.52. Results of the first case are shown in figures 64 and 65. The maximum speed was increased to $\rho = 2.5$ for this case since that is the value of the global instability threshold. Random noise was used to increase the probability of initiation of potential subharmonic response or limit cycle. A subharmonic response occurs for this case in the speed range where it can exist. When this range is exceeded, the subharmonic disappears and no limit cycle appears. This is in contrast to the previous cases where the subharmonic transitioned to a limit cycle. For this value of σ however, the destabilizing force is insufficient to overcome the stabilizing capacity of the side force. As speed is increased and the system becomes less stable, the limit cycle initiates at a frequency of $\approx\sigma\rho$. This occurs at a higher speed than in the cases with the nominal value of σ. There are, therefore, two distinct regions of speed where subharmonic response and limit cycle instability individually occur when $\sigma = 0.40$. The case with $\sigma = 0.52$ is shown in figures 66 and 67. The behavior here is similar to the baseline case except for the obvious difference in the limit cycle frequency ($\approx 0.52\rho$). One other difference is that the global instability limit ($\rho_{gi} = 1.92$) is just slightly above the upper limit of possible subharmonic response. This causes the transition from subharmonic to limit cycle to occur just before the onset of divergence. This simulation was executed with a ramp rate half that of the previous cases in order to identify the transition. Another difference is that the transition back to subharmonic response on the ramp down exhibits considerably more hysteresis than the previous cases. In other words, the range of speed for which either response can occur is greater.

The effects of γ were examined by changing its value from the nominal of 0.75 to 0.50 and 0.25. These values represent progressively more linear cases. The results for $\gamma = 0.50$ are shown in figures 68 and 69. The general characteristics of the response are the same as the nominal case. As predicted by the subharmonic response analysis, the subharmonic remains for higher speeds and has a lower amplitude. As predicted by the homogeneous limit cycle analysis, the limit cycle has a lower amplitude also. The results for $\gamma = 0.25$ are shown in figures 70 and 71. This case did not develop either subharmonic response or limit cycle. This is due to the very narrow range of speed and low amplitude for potential subharmonic and the low amplitude for potential limit cycle. Since this system is nearly linear, this might also have been intuitively expected.

The effects of ζ were examined by changing its value from the nominal of 0.10 to 0.05 and 0.20. It should be noted that when ζ is changed the cross-coupled stiffness is also changed proportionately according to equation (125). The results for $\zeta = 0.05$ are shown in figures 72 and 73. The only difference noted is that the transition from subharmonic to limit cycle occurs at a higher speed than in the nominal case. This is due to the fact that the upper limit of potential subharmonic is higher for this case (fig. 16). The results for $\zeta = 0.20$ are shown in figures 74 and 75. As might be expected, the transition occurs at a lower value of speed for this case.

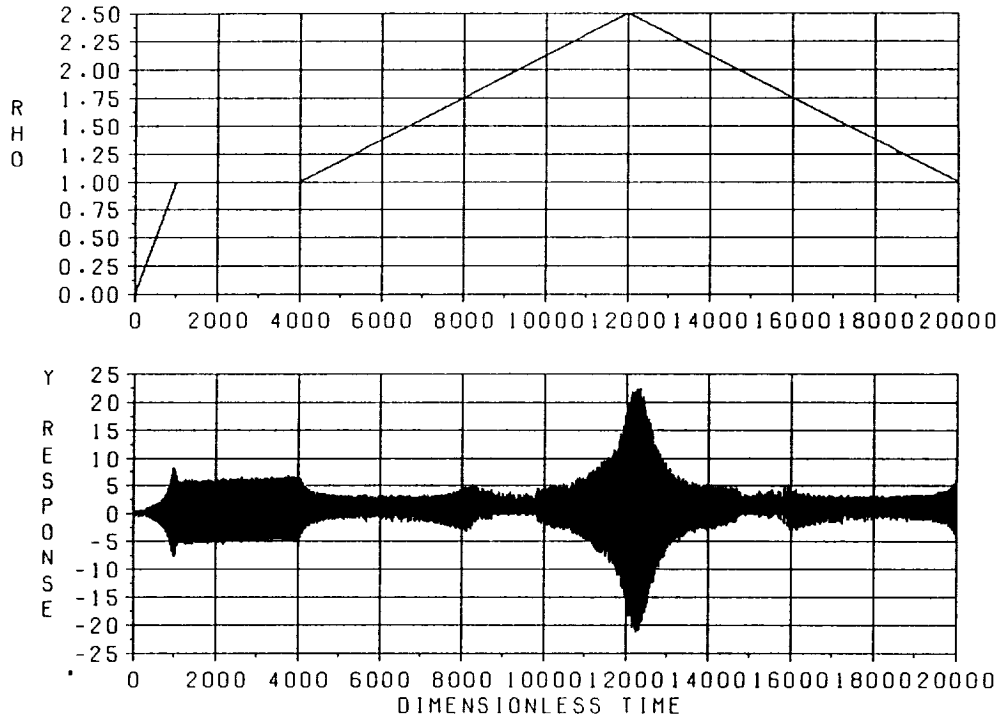

Figure 64. Effects of other system parameters on interacting responses. $\sigma = 0.40$, $g_y = 1.0$, $a = 1.0$, and $\overline{\eta} = 0.5$.

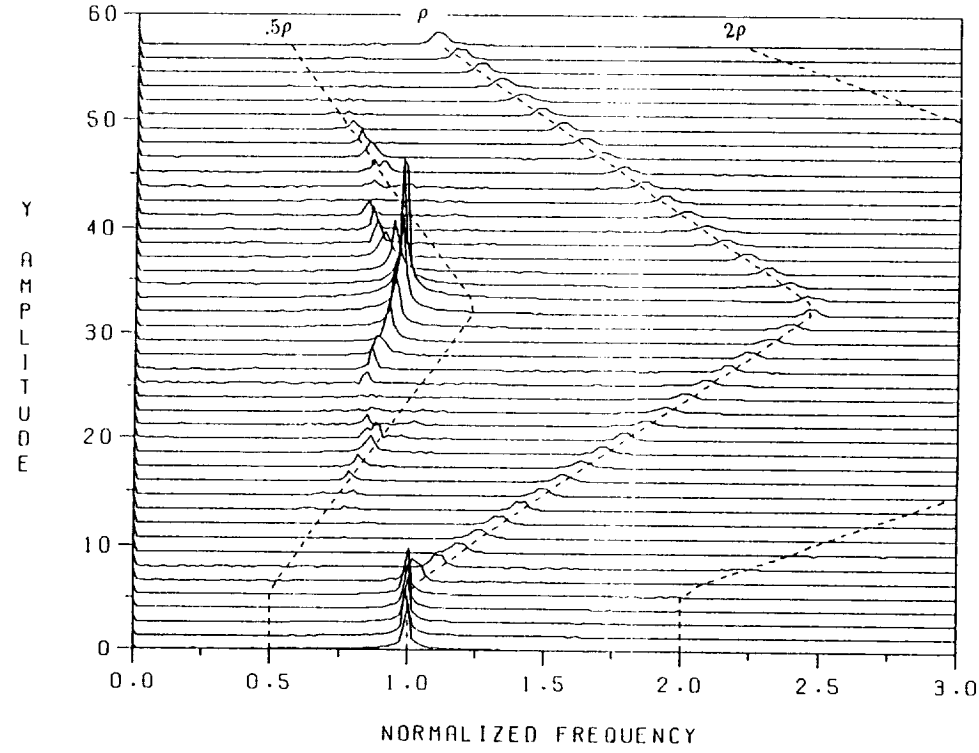

Figure 65. Cascade spectral plot of figure 64. Spectra taken in dimensionless time increments of 400. $\sigma = 0.40$, $g_y = 1.0$, $a = 1.0$, and $\overline{\eta} = 0.5$.

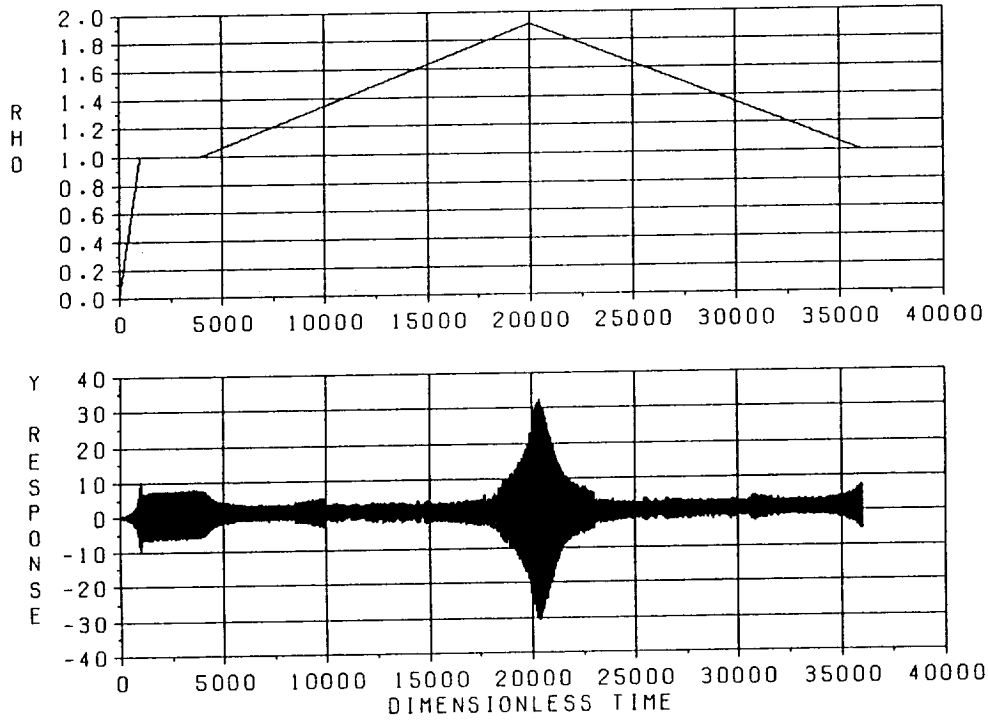

Figure 66. Effects of other system parameters on interacting responses. $\sigma = 0.52$, $g_y = 1.0$, $a = 1.0$, and $\overline{\eta} = 0.5$.

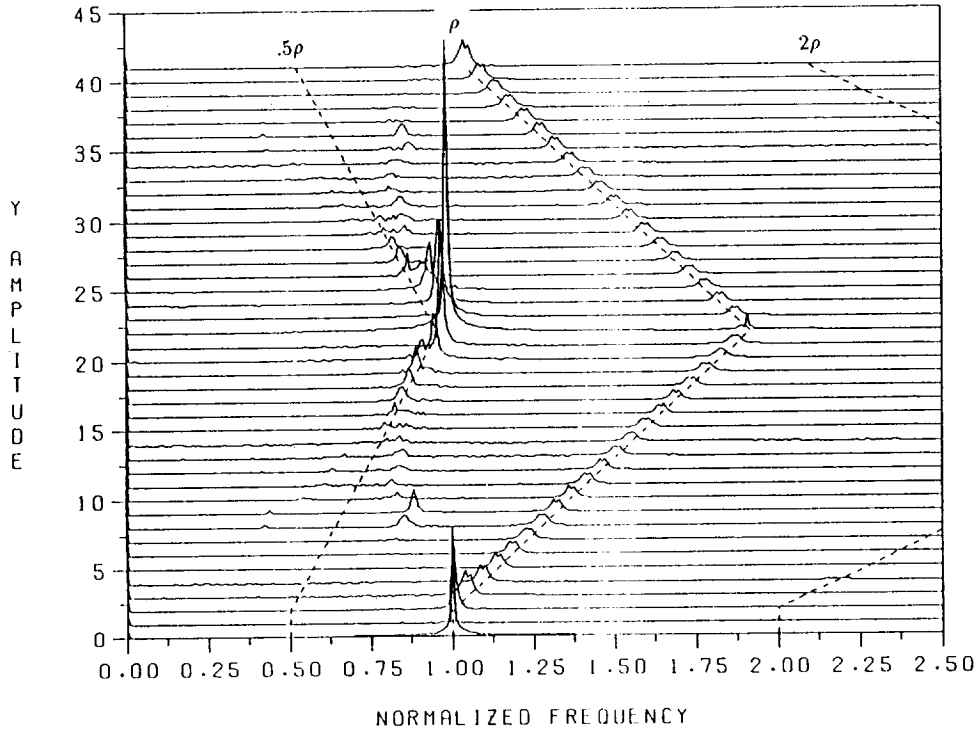

Figure 67. Cascade spectral plot of figure 66. Spectra taken in dimensionless time increments of 400. $\sigma = 0.52$, $g_y = 1.0$, $a = 1.0$, and $\overline{\eta} = 0.5$.

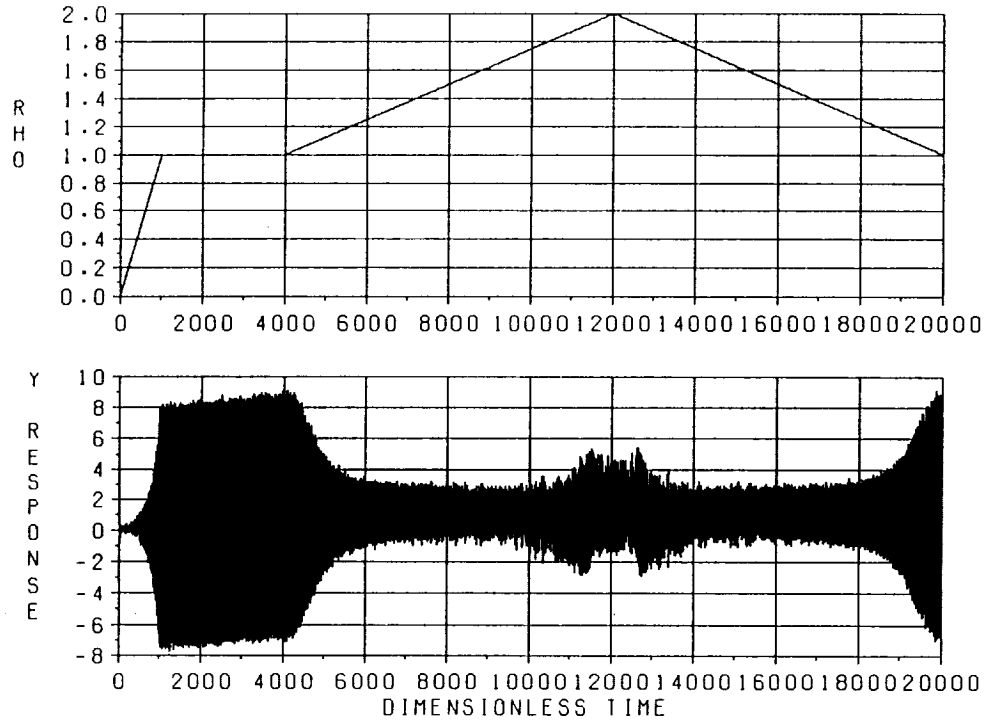

Figure 68. Effects of other system parameters on interacting responses. $\gamma = 0.5$, $g_y = 1.0$, $a = 1.0$, and $\overline{\eta} = 0.5$.

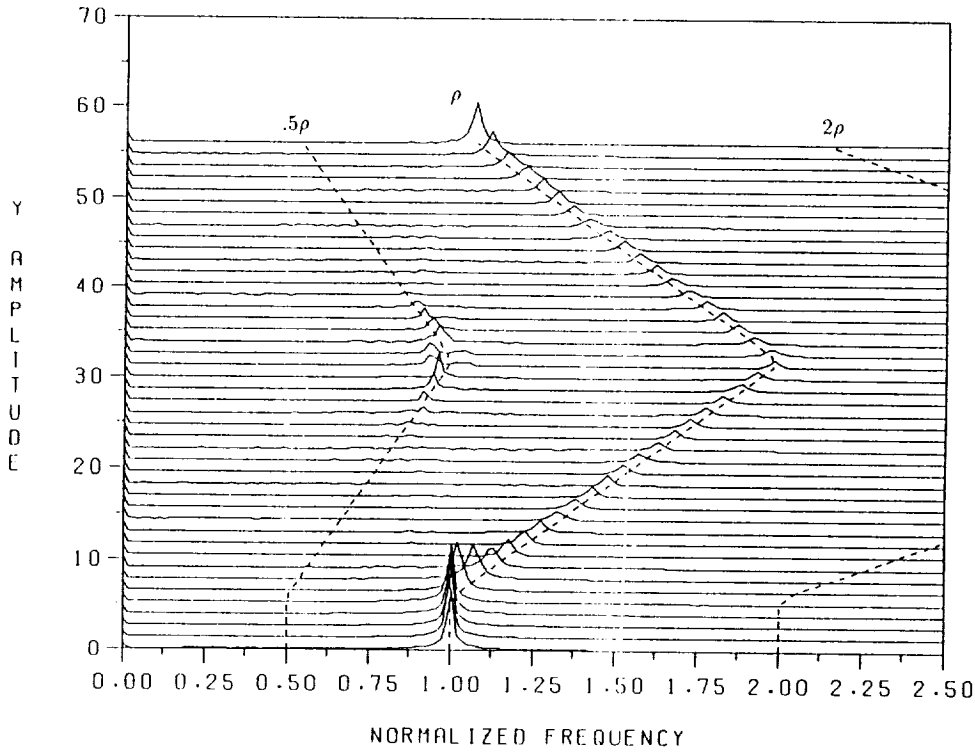

Figure 69. Cascade spectral plot of figure 68. Spectra taken in dimensionless time increments of 400. $\gamma = 0.5$, $g_y = 1.0$, $a = 1.0$, and $\overline{\eta} = 0.5$.

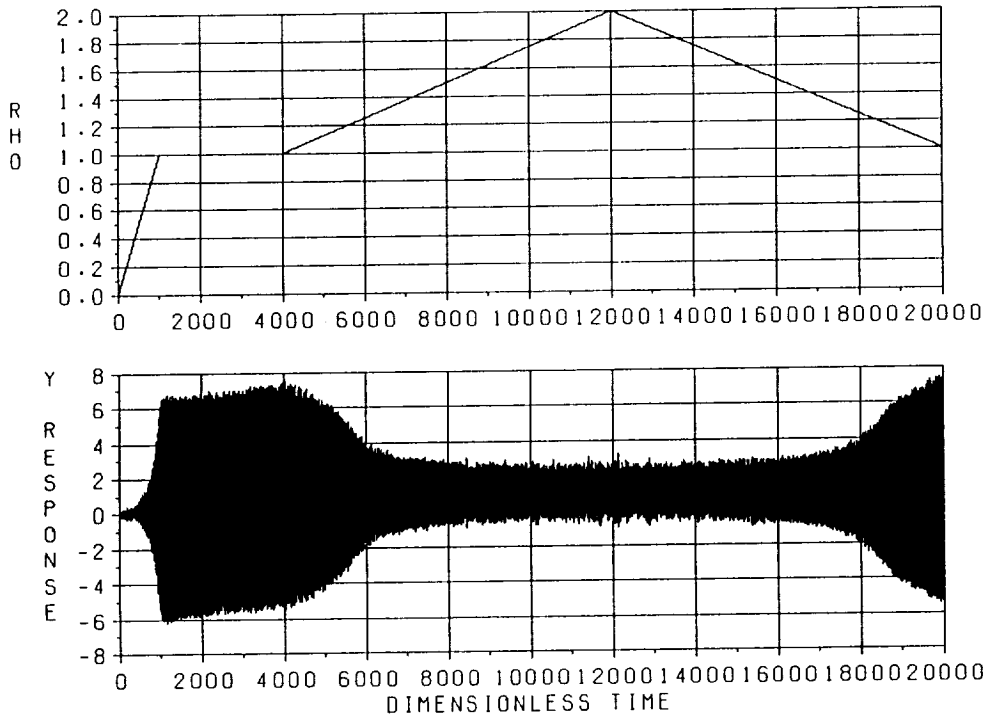

Figure 70. Effects of other system parameters on interacting responses. $\gamma = 0.25$, $g_y = 1.0$, $a = 1.0$, and $\overline{\eta} = 0.5$.

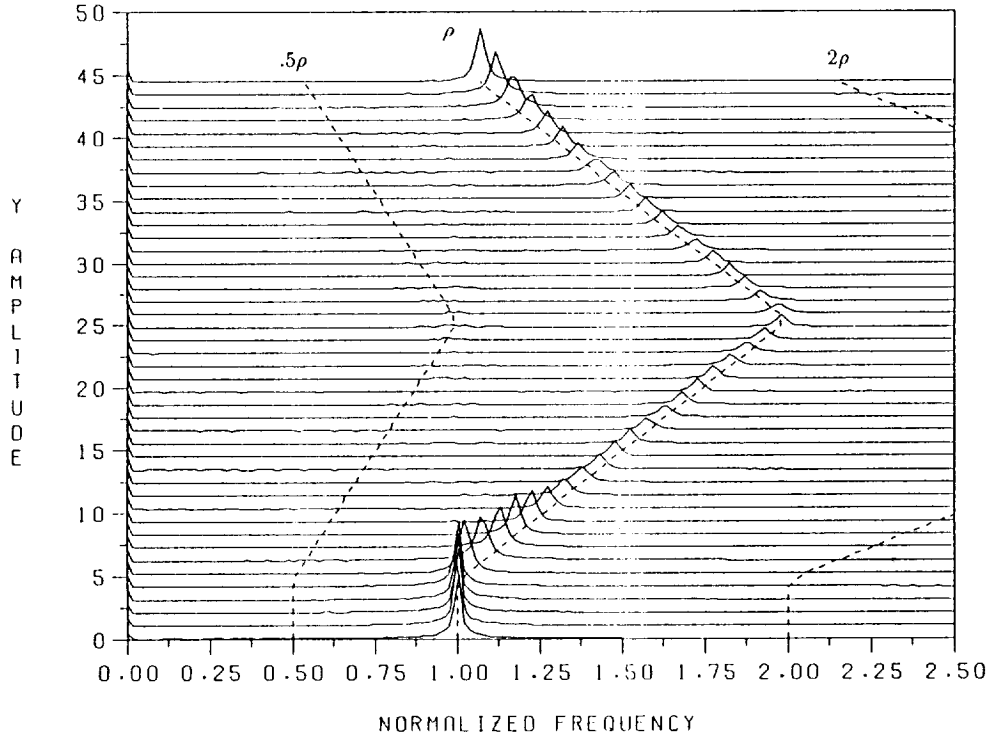

Figure 71. Cascade spectral plot of figure 70. Spectra taken in dimensionless time increments of 400. $\gamma = 0.25$, $g_y = 1.0$, $a = 1.0$, and $\overline{\eta} = 0.5$.

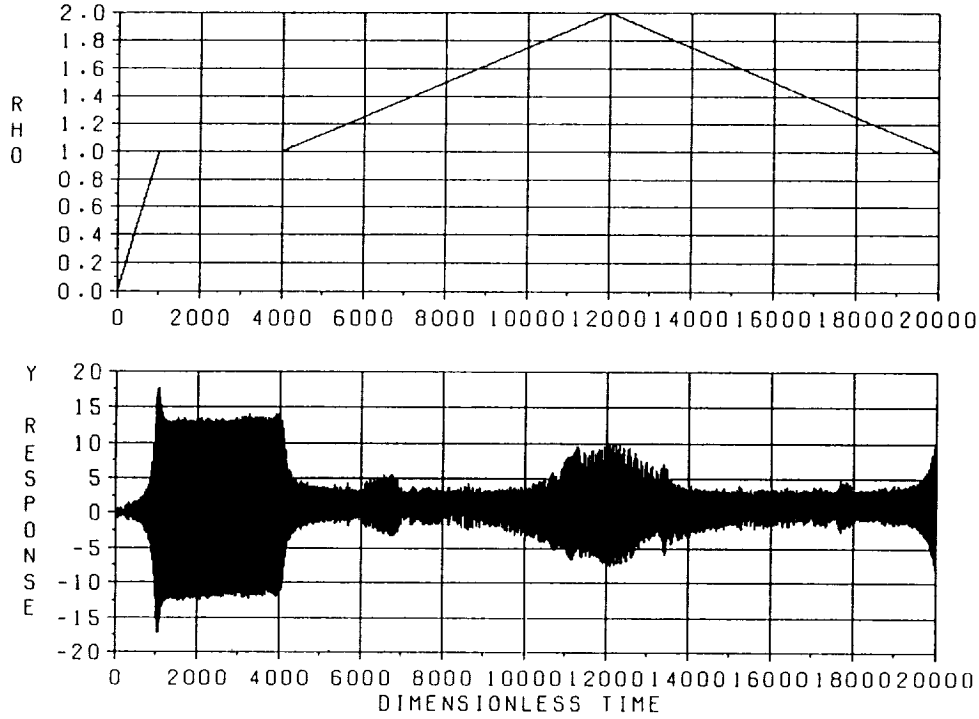

Figure 72. Effects of other system parameters on interacting responses. $\zeta = 0.05$, $g_y = 1.0$, $a = 1.0$, and $\overline{\eta} = 0.5$.

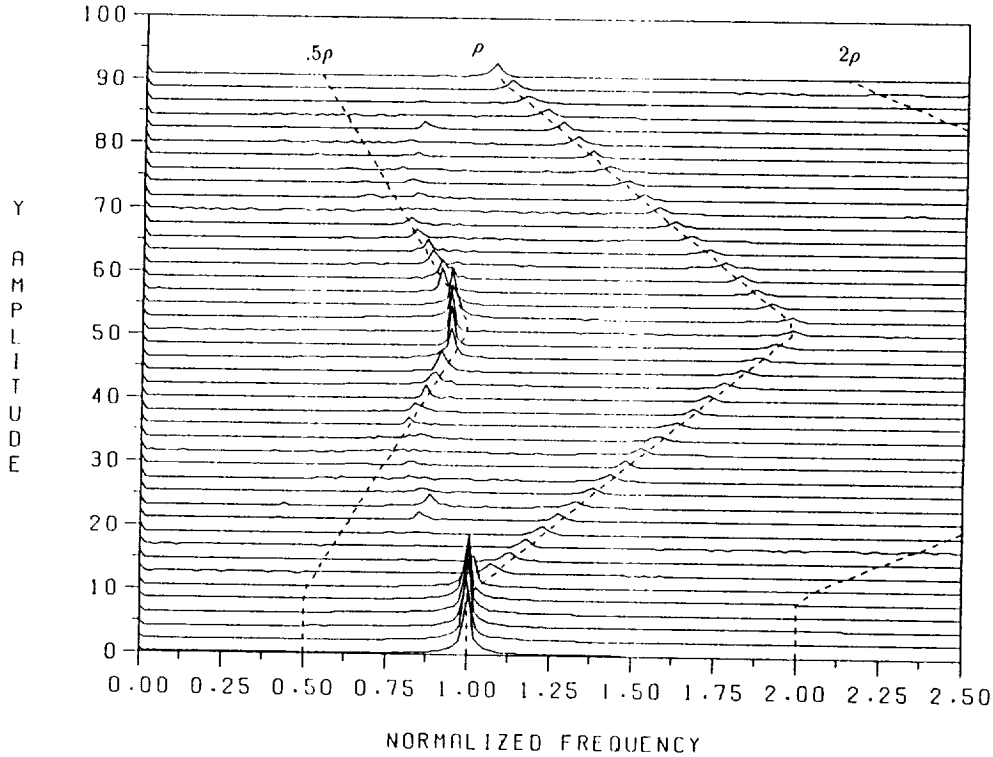

Figure 73. Cascade spectral plot of figure 72. Spectra taken in dimensionless time increments of 400. $\zeta = 0.05$, $g_y = 1.0$, $a = 1.0$, and $\overline{\eta} = 0.5$.

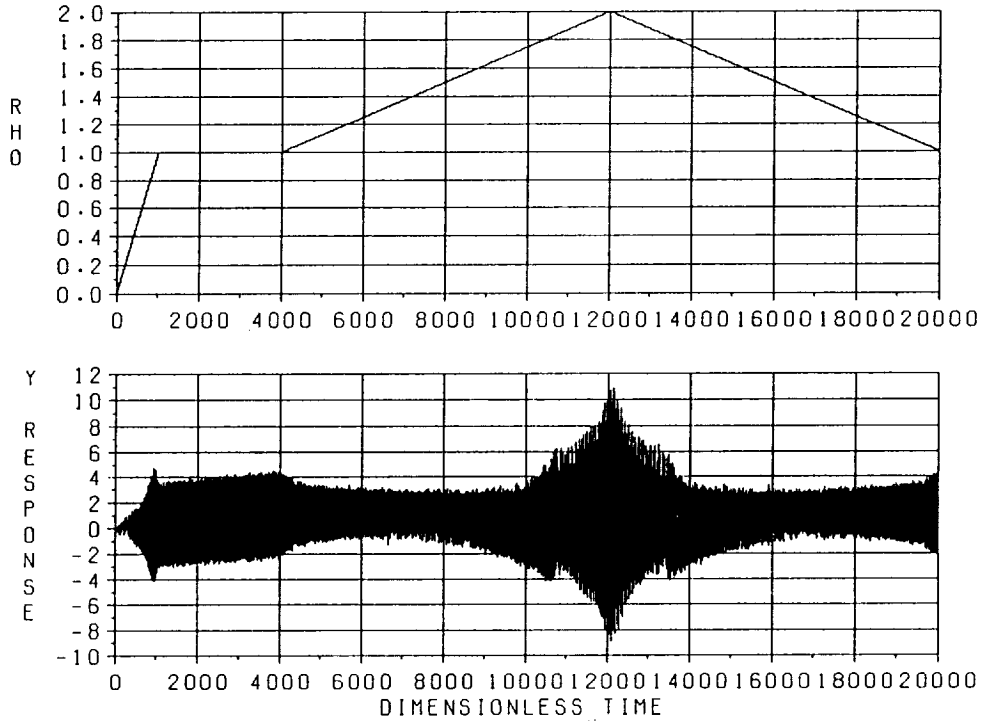

Figure 74. Effects of other system parameters on interacting responses. $\zeta = 0.20$, $g_y = 1.0$, $a = 1.0$, and $\overline{\eta} = 0.5$.

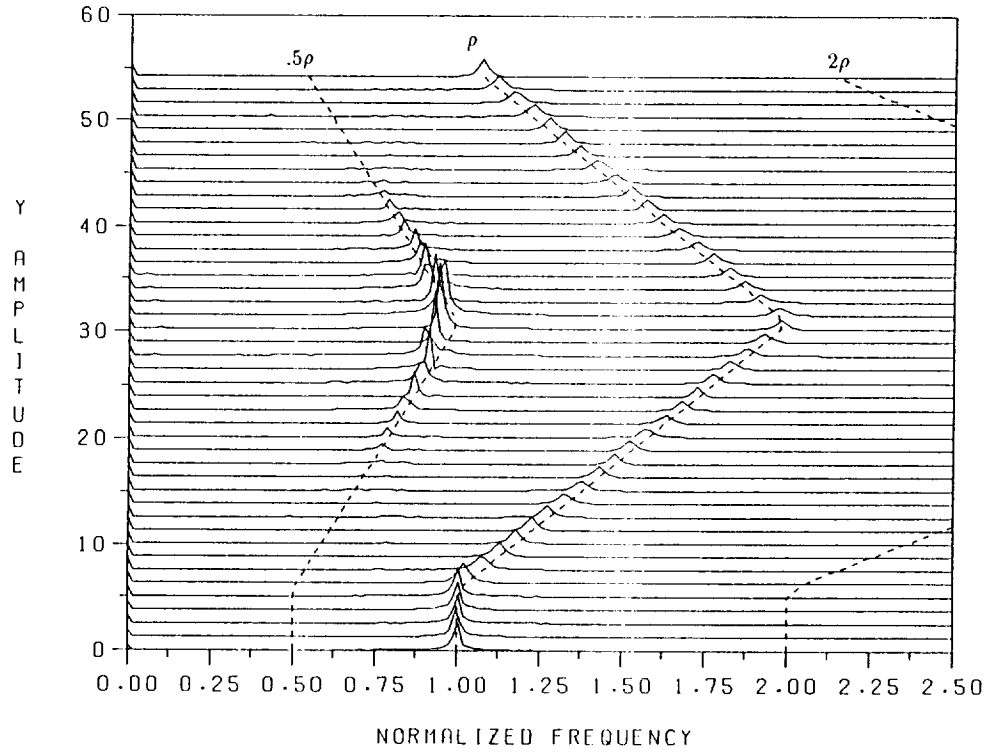

Figure 75. Cascade spectral plot of figure 74. Spectra taken in dimensionless time increments of 400. $\zeta = 0.20$, $g_y = 1.0$, $a = 1.0$, and $\overline{\eta} = 0.5$.

G. Nonuniqueness of Solutions

The nonuniqueness of either the subharmonic response solution or the limit cycle solution when mass unbalance and side force excitations are applied simultaneously has already been indicated by the hysteretic behavior of some of the simulations. This occurred for both side-force ramps and speed ramps. Results for another simulation which clearly illustrates this are shown in figures 76 and 77. This case is the same as that shown in figures 58 and 59 (a = 1.0, g_y = 1.0, ζ, σ, and γ nominal) with two exceptions. First, random noise ($\overline{\eta}$ = 0.5) has been added. Second, the speed profile has been altered to dwell on the up ramp at ρ = 1.845 and remain at

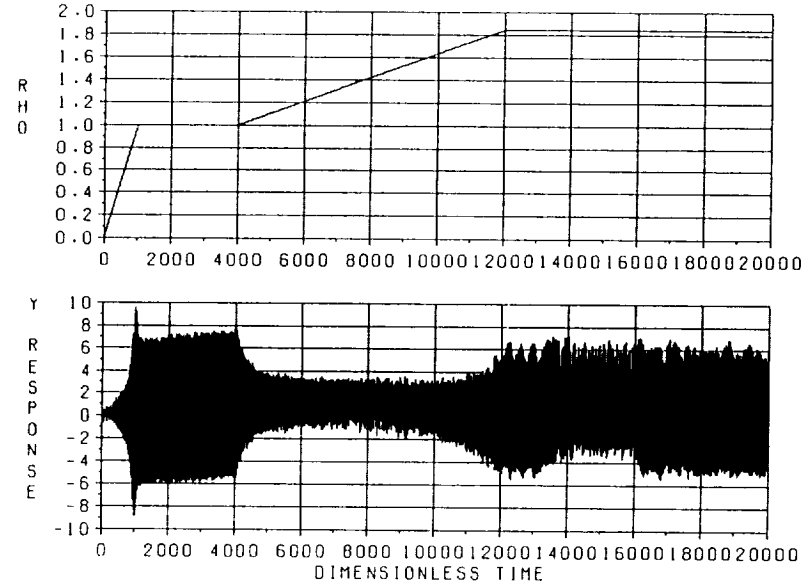

Figure 76. Nonuniqueness of interacting response solution. Dwell in operating profile at ρ = 1.845 (dimensionless time equal 12,000). g_y = 1.0, a = 1.0, and $\overline{\eta}$ = 0.5.

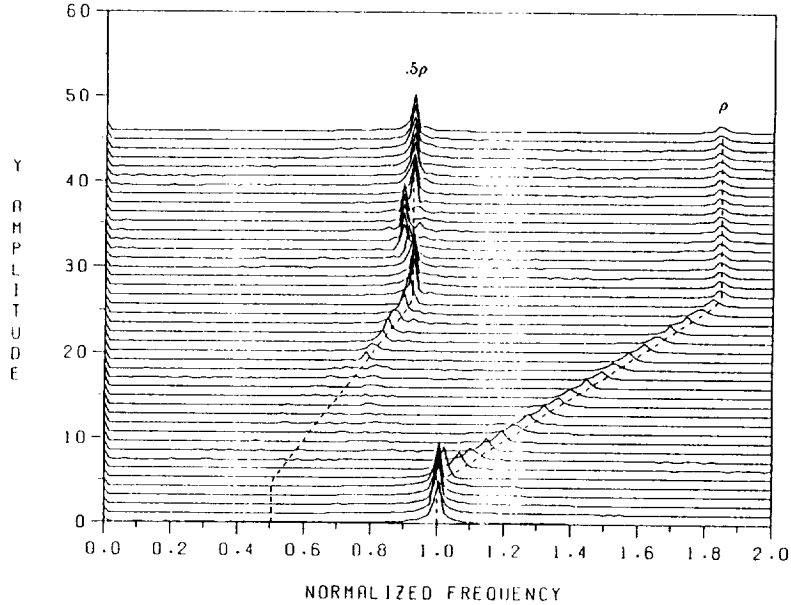

Figure 77. Cascade spectral plot of figure 76. Spectra taken in dimensionless time increments of 400. g_y = 1.0, a = 1.0, and $\overline{\eta}$ = 0.5.

that value for the remainder of the simulation. From the figures it can be seen that the response is initially a subharmonic. After some time it changes to limit cycle. Some time after this it changes back to a subharmonic. All model parameters are fixed during this time period. The random noise has the effect of superimposing a variation on the side force. This behavior of changing back and forth between solutions when no apparent change has occurred in the system is very significant when reviewing test data. This will become more apparent when test data from the SSME HPFTP is presented in section VI.

H. Effects of Mass Unbalance on the Stability of Side-Force Equilibria

The stability of the side-force equilibrium was analyzed in section III and demonstrated with simulations earlier in this section. The possible effects of mass unbalance perturbing the stability of this equilibrium were discussed. The effects have been explored using simulations of the nominal model with $g_y = 1.5$ and two values of unbalance ($a = 0.5$ and $a = 1.0$). The stability threshold for the side-force equilibrium in this case is $\rho \approx 2.7$. Speed was ramped from $\rho = 1.0$ to $\rho = 3.0$ after initiating the simulations as discussed previously. Results for both cases are presented in figure 78. Results for $a = 0.5$ show that this value of unbalance does not perturb the equilibrium beyond its range of stability. It remains stable for values of ρ up to 2.7. For $a = 1.0$, the unbalance is sufficient to initiate a subharmonic response at $\rho \approx 1.6$. As speed increases, this transitions to limit cycle instability at $\rho \approx 1.9$. Now the system is in a limit cycle instability when the speed increases beyond the global instability threshold ($\rho_{gi} = 2.08$) and the response diverges. The effect of the unbalance is to alter the state of the system when the global instability threshold is crossed. In another sense, the subharmonic response causes the initiation of the limit cycle which diverges when the threshold is crossed. If the unbalance and side-force parameters are such that the subharmonic does not occur, the side force can stabilize the system beyond the global threshold even in the presence of unbalance and noise perturbation.

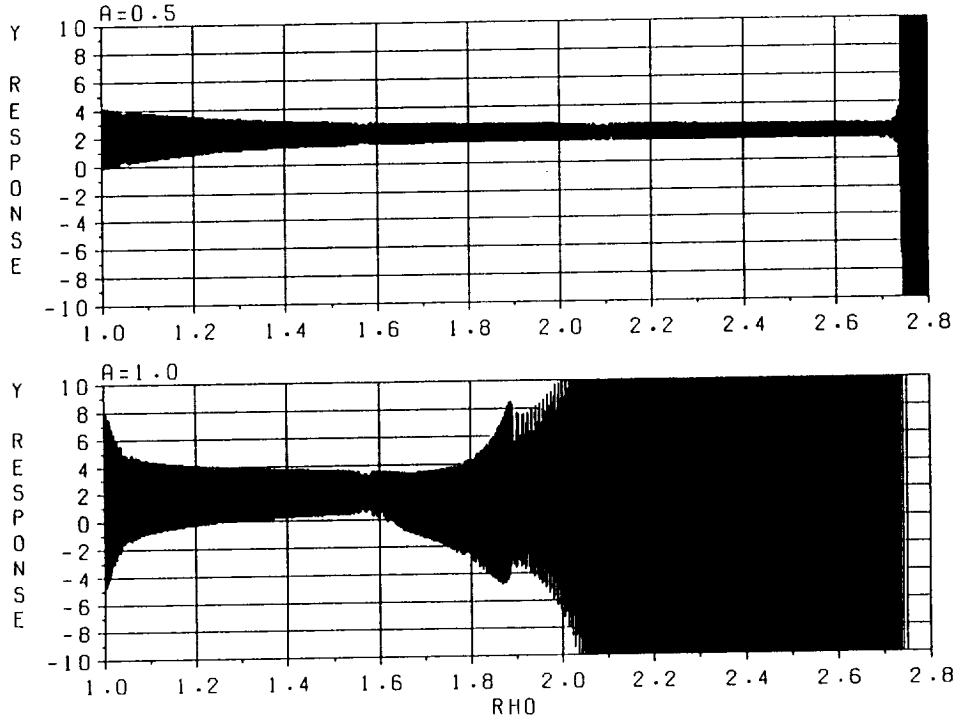

Figure 78. Effects of mass unbalance on the stability of side-force equilibria. Stability threshold is $\rho \approx 2.7$. $g_y = 1.5$, $\overline{\eta} = 0.0001$, $a = 0.5$, and $a = 1.0$.

The behavior of the model under general loading conditions has been characterized in terms of its behavior under certain restricted conditions. These restricted conditions are the homogeneous response (which describes the limit cycle behavior), the mass unbalance equilibrium, the side-force equilibrium, and the general loading case with the assumption of harmonic and subharmonic response. These results will be extended to the SSME HPFTP in section VI.

VI. EXTENSION OF RESULTS TO COMPLEX MODEL

The previous sections have dealt with a simplified model of a turbopump in order to enhance the understanding of the basic phenomena being studied. The objective of this section is to demonstrate that these results extend to a more complex, realistic model of an actual turbopump. This will be achieved by examining the HPFTP of the SSME. Test data will be presented for cases where the phenomena appear to have occurred. Analyses and simulations of a model of the HPFTP will also be discussed.

A. Description of SSME HPFTP

The SSME is manufactured by Rockwell International, Rocketdyne Division for NASA. It is a liquid hydrogen/liquid oxygen staged combustion rocket engine. The primary components of such an engine are the main combustion chamber and nozzle, the high pressure turbopumps which feed the fuel and oxidizer to the main combustion chamber, and the combustion system which drives the turbopumps. In the case of the SSME, each pump has its own combustion device known as a preburner. The fuel is partially burned in these preburners (oxygen/hydrogen mixture ratio approximately one to one) and the resulting combustion gases drive the turbines. These gases then proceed to the main chamber where they are completely burned according to stoichiometric balance (mixture ratio approximately six to one). A schematic diagram of the propellant flow is shown in figure 79a. The HPFTP is shown in figure 79b. For engine operation at 109 percent of rated power level, the HPFTP runs at approximately 36,600 r/min, depending on actual engine performance. It consists of a three-stage centrifugal pump section which is driven by a two-stage turbine. The rotor is supported primarily by two pairs of angular contact ball bearings, one pair on each end. The two-pump interstage seals also provide significant restoring forces for relative lateral rotor motion. These seals provide the majority of the damping and cross-coupled stiffness forces. The turbine section provides significant additional cross-coupled stiffness due primarily to the Alford effect. The Alford effect is a variation in the aerodynamic efficiency of individual turbine blades as the turbine disk moves eccentric with respect to the stator. The blades on one side will be more efficient than those on the other due to their smaller tip clearance. The net effect is a tangential force proportional to the radial displacement which is modeled as a cross-coupled stiffness. Additional stiffness, damping, and cross-coupled stiffness forces arise at the turbine interstage seal. The impellers and their associated seals produce forces as well; however, their magnitudes are much smaller than the pump interstage seal forces. These forces will be neglected here in order to simplify the model. The error introduced by doing so is no greater than the error due to the uncertainty in the dominant pump interstage seal and ball bearing forces.

The nominal data used to define the HPFTP model used in this study are contained in appendix B. These data were adjusted within their uncertainties in order to achieve the desired

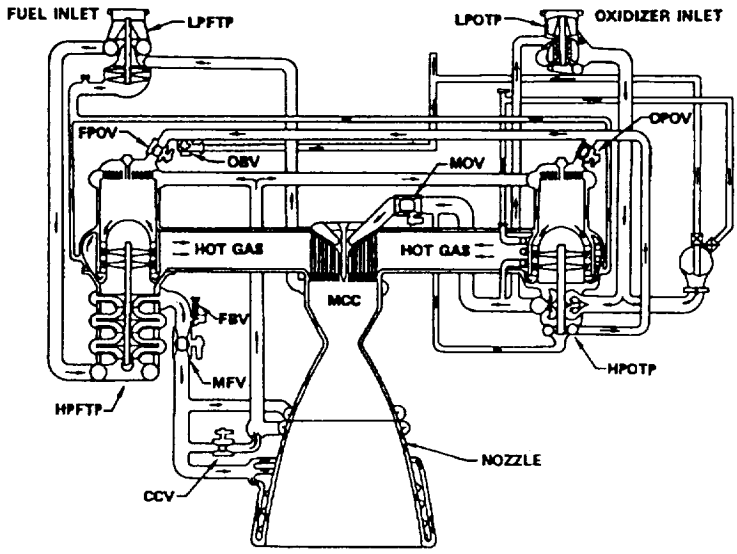

(a)

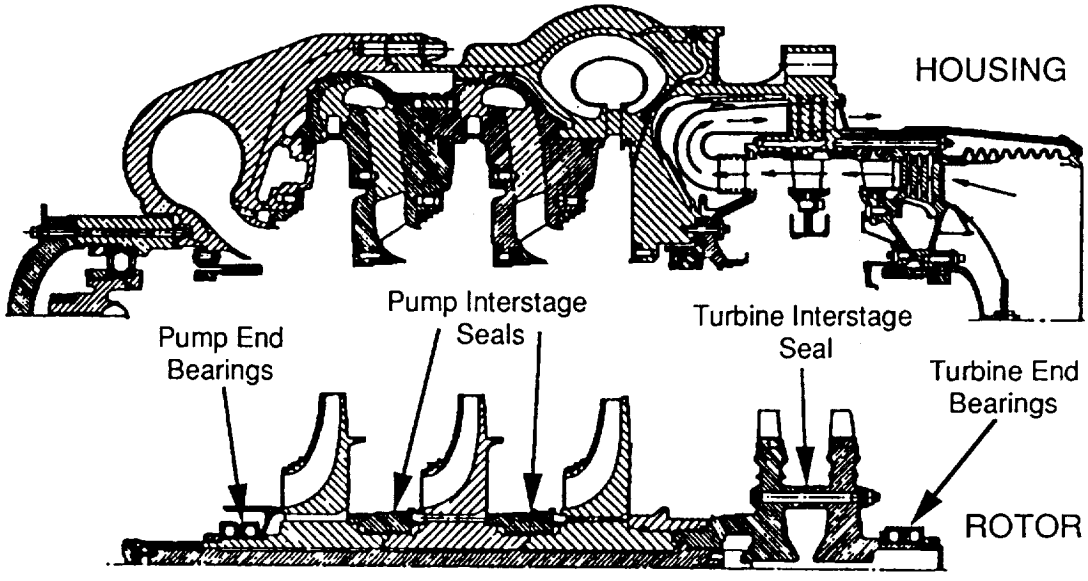

(b)

Figure 79. SSME description. (a) Propellant flow schematic. (b) HPFTP cross-sectional view.

C-2

behaviors as observed in tests. The adjustments are discussed in the section dealing with model results. These data were provided by the turbopump manufacturer (Rocketdyne) with the exception of the pump interstage seal cross-coupled stiffness. This data has been replaced by a function of the form of equation (125). The damping value supplied by the manufacturer is multiplied by the shaft angular velocity and then by the destabilizing force parameter σ. This simplifies the process of relating the HPFTP model results to the simplified model results.

The model for the HPFTP is more complex than the single mass model in several respects. One of the most obvious differences is the addition of the housing dynamics to the model. Another distinction is that all parameters are distributed along the axis of the rotor. The support characteristics (both linear and nonlinear), rotor and housing mass and stiffness properties, and the excitation forces all have independent (discrete) distributions along the rotor, in general. These differences are complicating enough, however, the most significant complexity is not as obvious. Virtually every parameter in the model varies with turbopump operating speed either directly or indirectly. The rotor and housing free-free dynamic characteristics and the mass unbalance distribution are exceptions. The stiffness and damping coefficients and the side-force excitation vary either with speed directly or with engine power level (which can be related to speed). The clearances, geometric eccentricities from centerline, and random noise excitations would be expected to vary in the actual machine. These variations are unknown, however, and are not prescribed in the model. The fact that they probably occur must be recalled when interpreting test data and simulation results. Finally, simply the number of parameters in the model make interpretation of results difficult. The same result or trend could probably be obtained with more than one set of parameters (or "recipe").

B. HPFTP Test Data

Development of the SSME began in 1971. High power level testing began in 1978. Since that time hundreds of engine tests have been performed yielding massive amounts of data. During the course of the engine's development, the design of the HPFTP has evolved and there are many different configurations that have been tested. The subsynchronous vibration problems that motivated this work have changed with the design changes. An in-depth review of the history of the problems and the design changes would take volumes, however, Hawkins[17] provides a good summary. There are three primary conclusions with relevance to this work which can be drawn from the historical data. First, the occurrence of the subsynchronous vibration, its amplitude, and its frequency are erratic. Only a certain percentage of all tests exhibit the phenomena and the frequencies and amplitudes vary. The frequencies fall within the range of 47 to 56 percent of rotor speed for all configurations and 47 to 52 percent for the current configuration. Second, configurations with higher side forces do not exhibit the phenomena as often and the amplitudes tend to be lower. The side-force differences are due to changes in the turbine discharge section which altered the pressure distribution in the turbine section. Third, the increased stiffness of the currently used pump interstage seals reduces the amplitudes of the phenomena. The initial seals used in high power level testing were three step, smooth seals and the current seals are straight, smooth seals. One might expect that these configurations would also have a lower frequency of occurrence; however, they were generally tested to higher power levels at which they are less stable.

In most tests, the rotordynamic instrumentation on the HPFTP has been limited to accelerometers mounted externally on the housing. This makes it somewhat difficult to determine what dynamic behavior of the rotor might be creating a particular vibration response on the

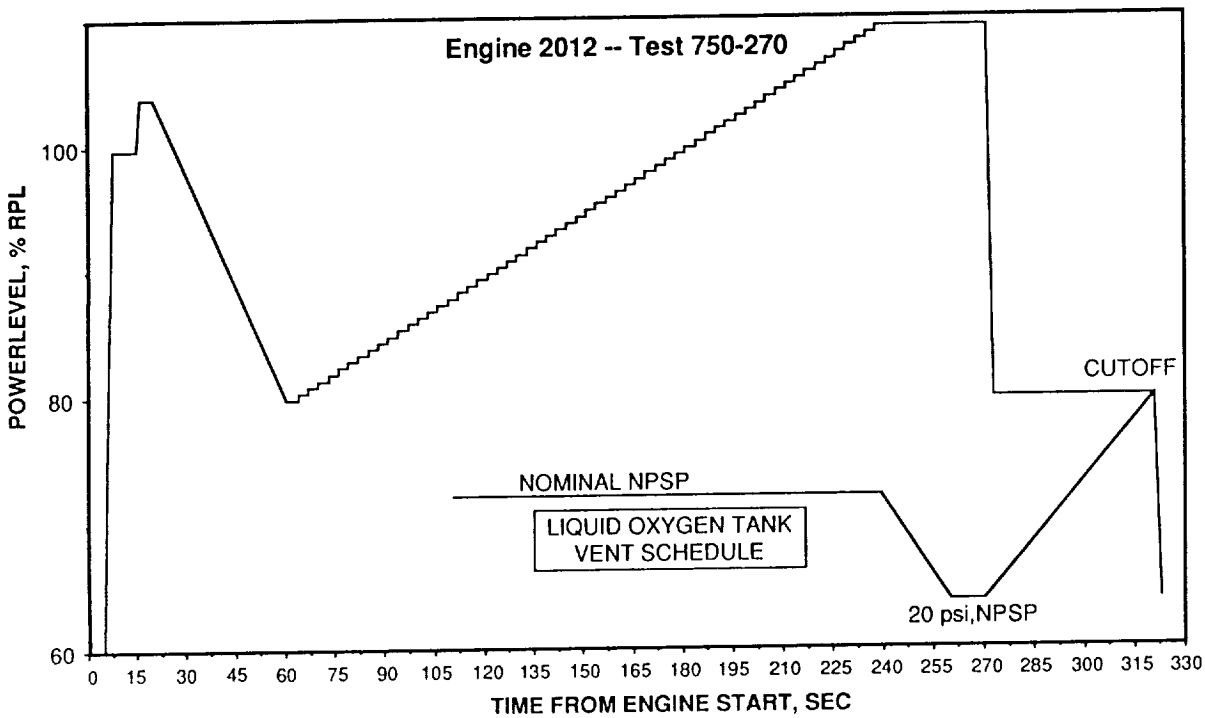

Figure 80. Engine power level profile for SSME test 750-270.

housing. Specially instrumented units have been built on occasion which have internal rotor displacement measurements. One test of one of these units has been selected for discussion here. The HPFTP in this test displayed significant levels of subsynchronous vibration with very interesting characteristics. The test was designated as 750-270 and the HPFTP was unit number 2708R1. The turbopump was instrumented with radial displacement measurements in two axes at the seal between the first and second pump stages. It also contained the normal set of external accelerometers.

The power level profile for test 750-270 is shown in figure 80. After throttling down to 80-percent power level, the level was slowly increased to 109-percent power level. The actual profile was a series of steps of one-half percent power level with 3-s dwells at each step. Upon reaching 109-percent power level at 238 s, the level was held constant until 271 s. During this period, the liquid oxygen tank pressure was reduced (vented) to simulate flight conditions. This lowers the liquid oxygen inlet pressure to the low pressure oxidizer turbopump and, hence, lowers the liquid oxygen outlet pressures throughout the system. The engine controller compensates for this perturbation by adjusting valves in the system and maintains system thrust (power level) and mixture ratio. The liquid oxygen vent schedule is superimposed on the power profile in figure 80.

The response of the HPFTP to the power profile described above is shown in figures 81a through 81g. The figures contain frequency spectra of one of the radial displacement measurements. These data were provided by the engine manufacturer (Rocketdyne). Many measurements and many methods of processing the data are available. This measurement is representative of the response of the HPFTP, and this method of processing yields a concise representation of the important features of the response. This series of plots presents a sequence of frequency spectra beginning at 170.8 s and continuing until 272.7 s. Each spectrum represents nine spectral averages (to reduce noise). The frequency resolution of the spectra is 5.0 Hz, therefore, each individual spectrum requires 0.20 s of data for analysis. Each plot of the average of nine spectra, then, represents 1.80 s of data. The samples are taken at 3-s intervals

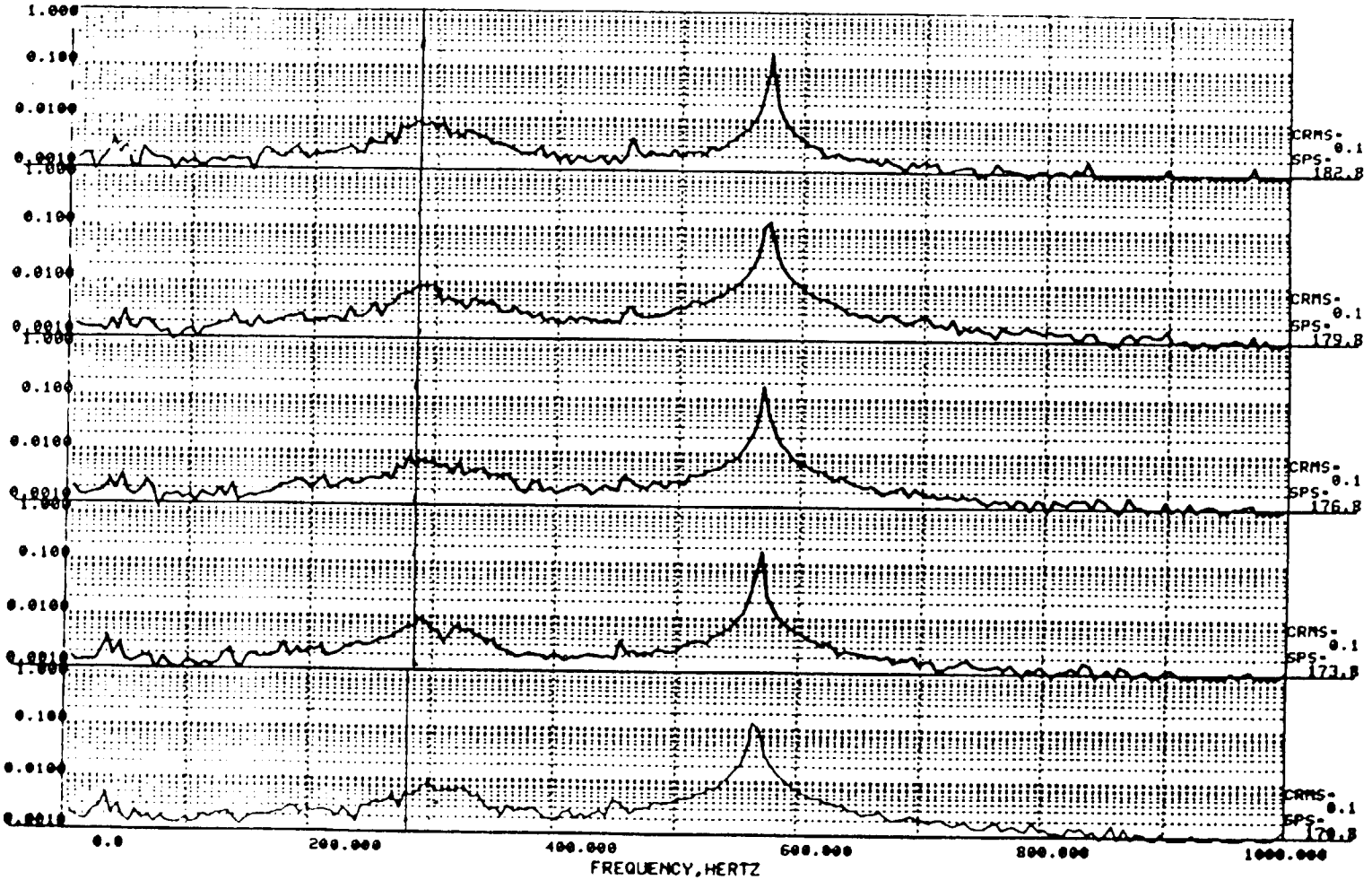

Figure 81a. Test 750-270 displacement measurement spectral data. Beginning 170.8 s after engine start.

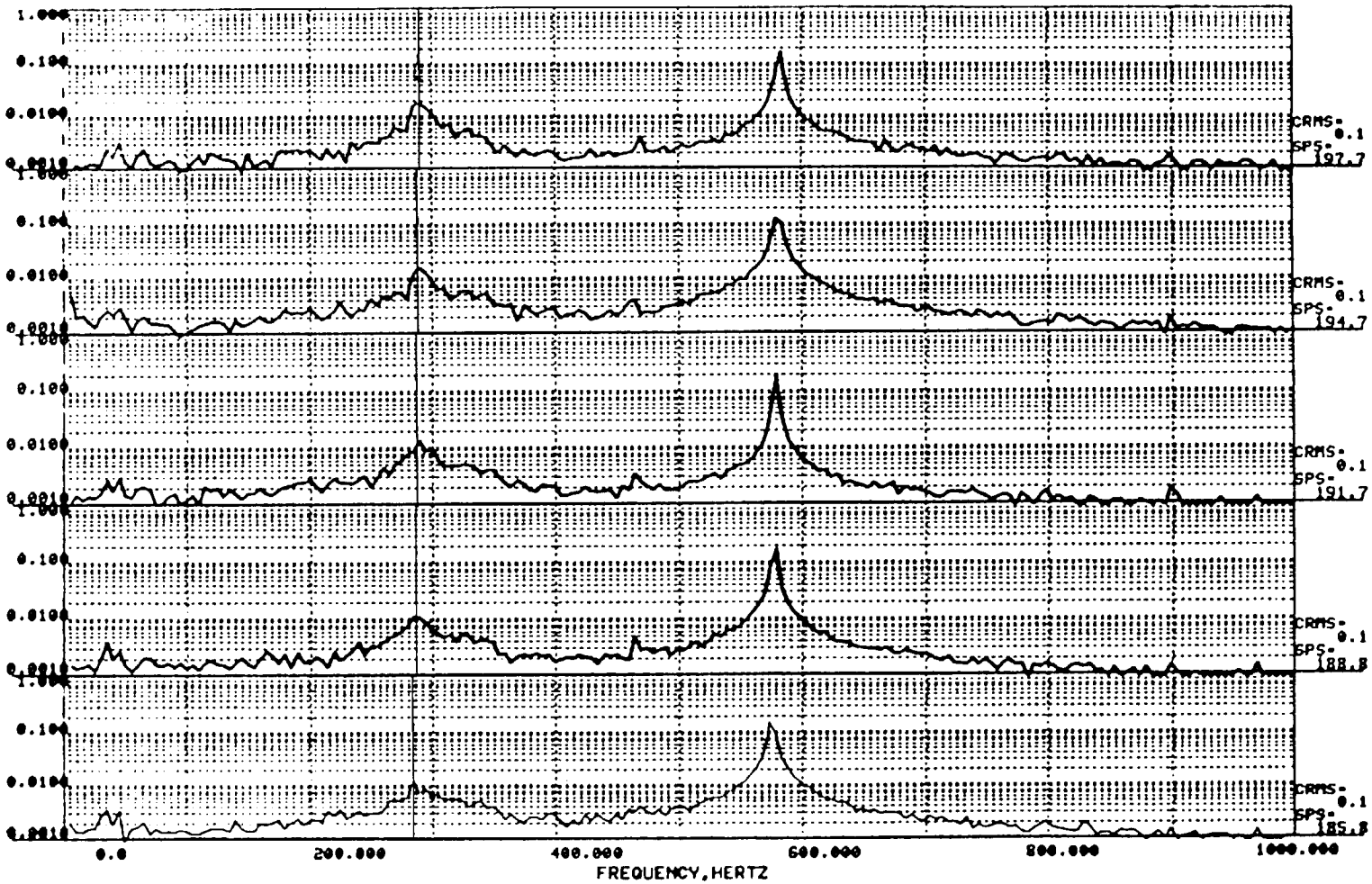

Figure 81b. Test 750-270 displacement measurement spectral data. Beginning 185.8 s after engine start.

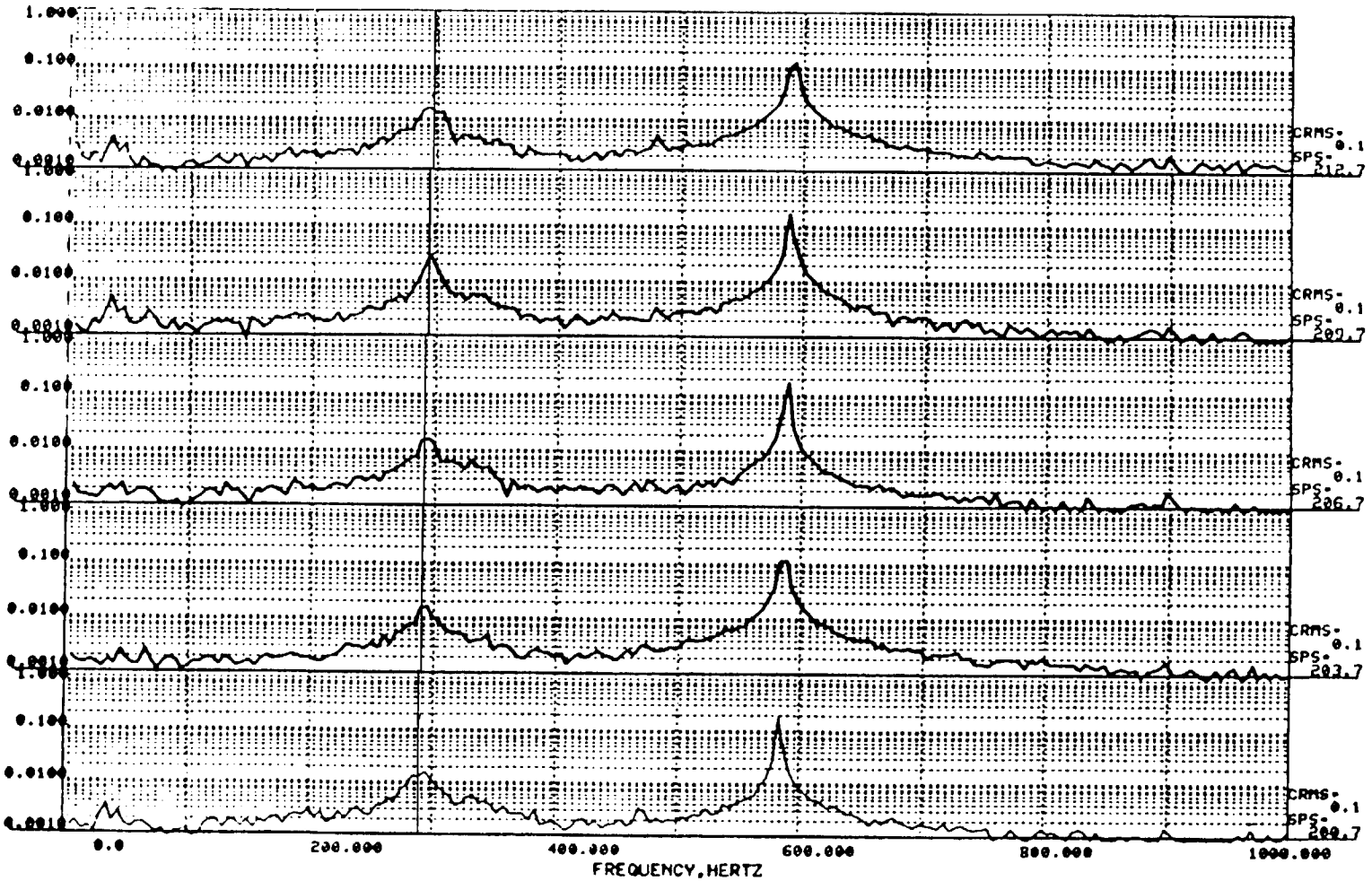

Figure 81c. Test 750-270 displacement measurement spectral data. Beginning 200.7 s after engine start.

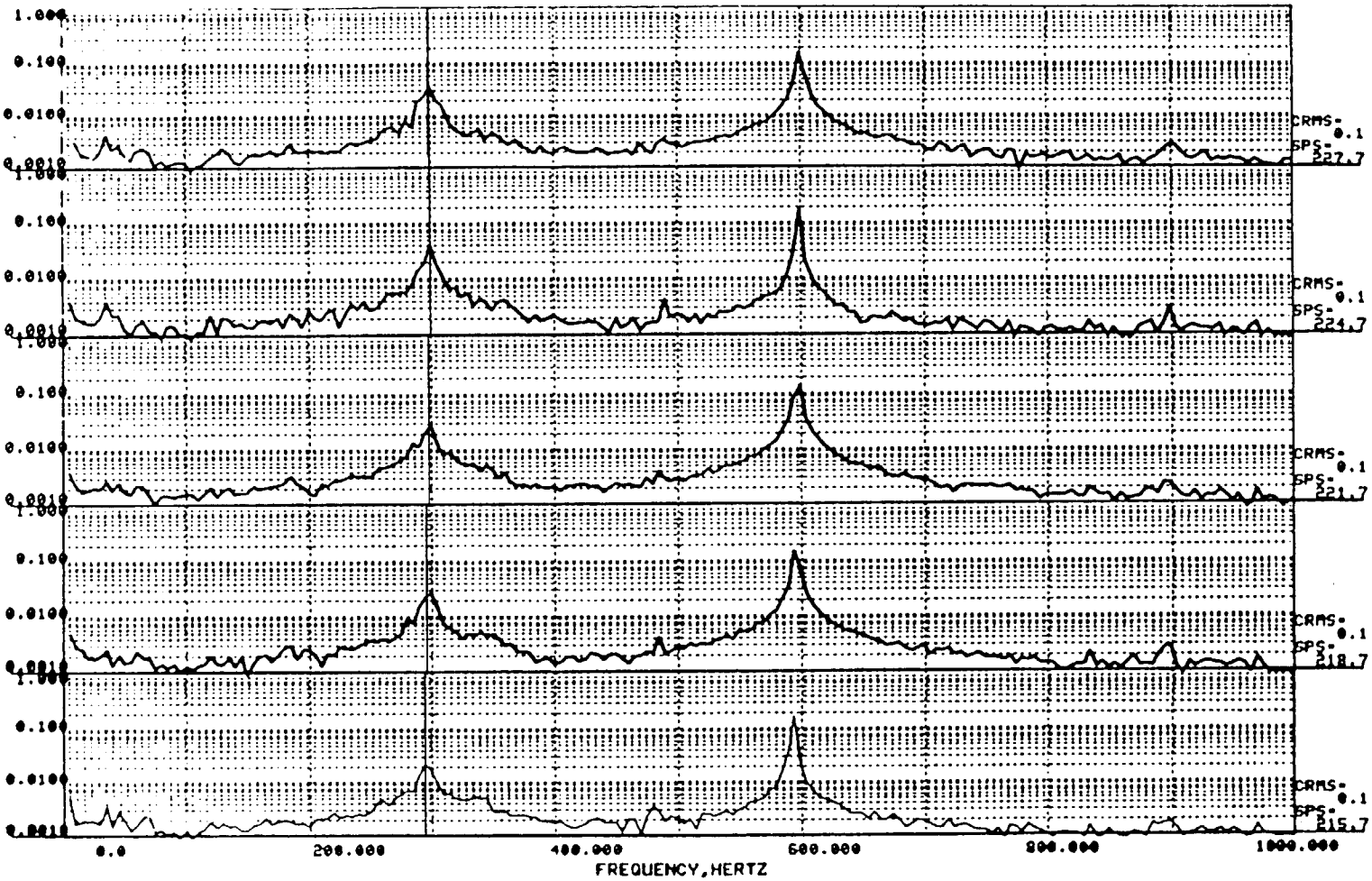

Figure 81d. Test 750-270 displacement measurement spectral data. Beginning 215.8 s after engine start.

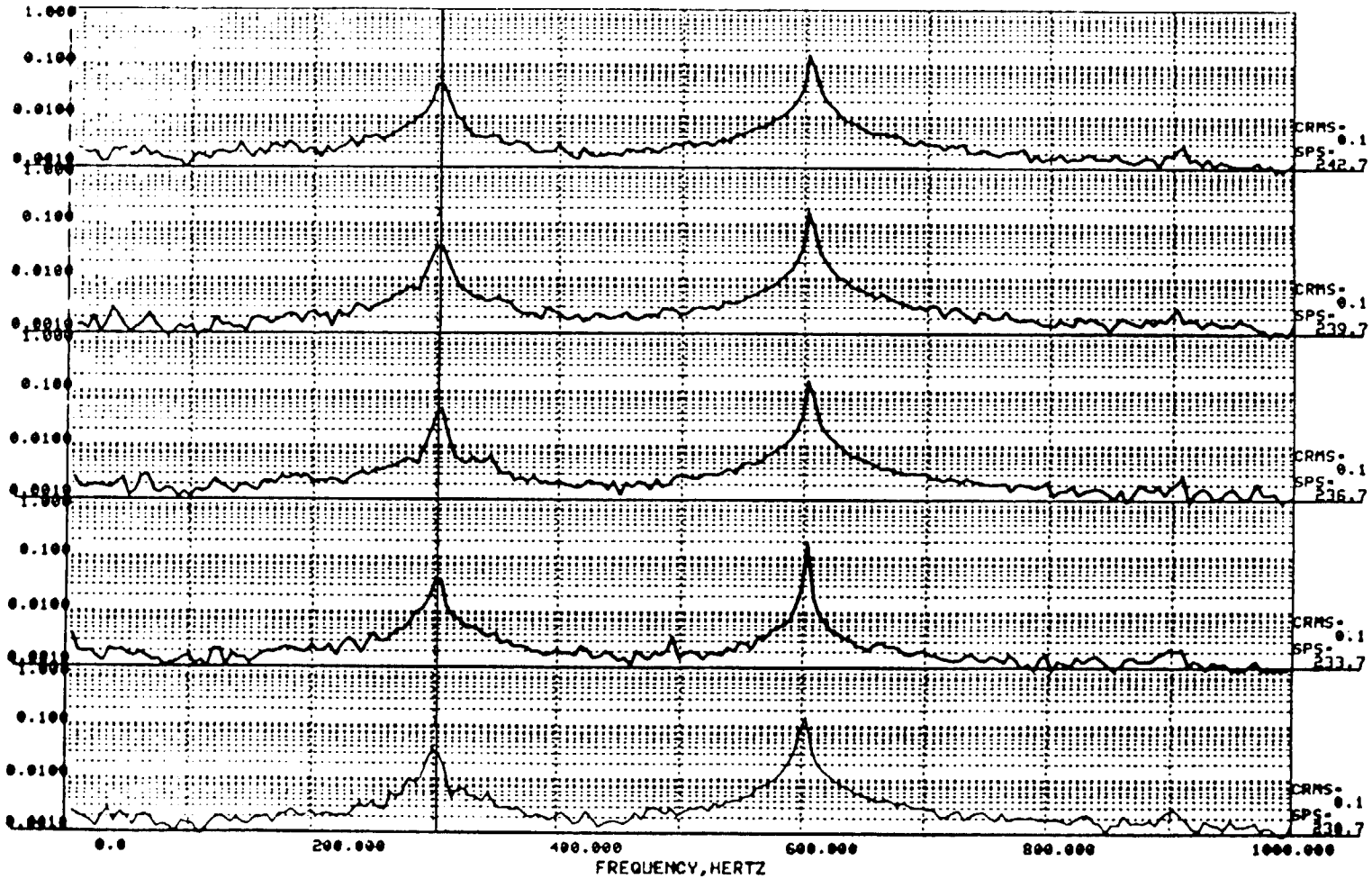

Figure 81e. Test 750-270 displacement measurement spectral data. Beginning 230.7 s after engine start.

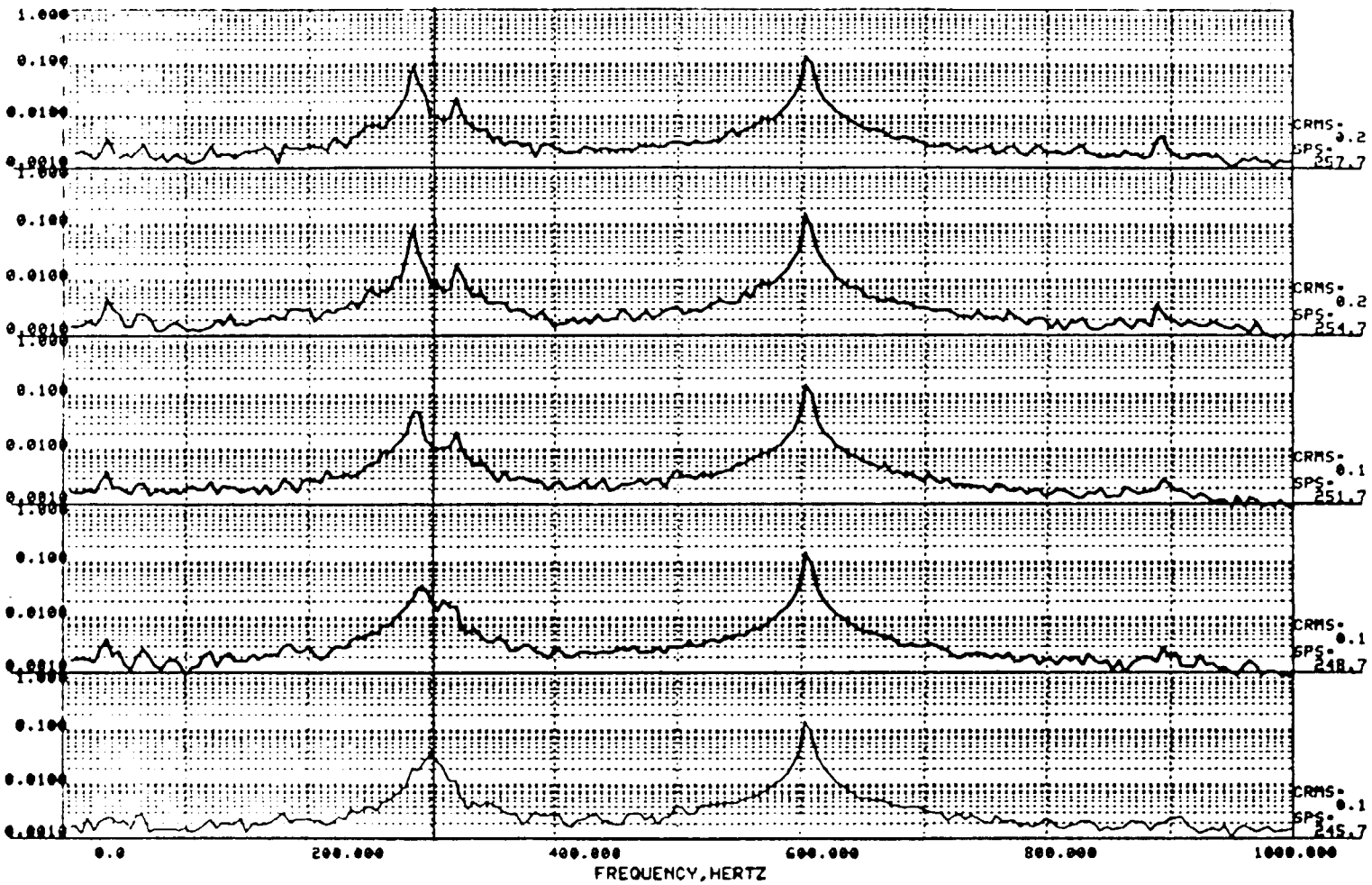

Figure 81f. Test 750-270 displacement measurement spectral data. Beginning 245.7 s after engine start.

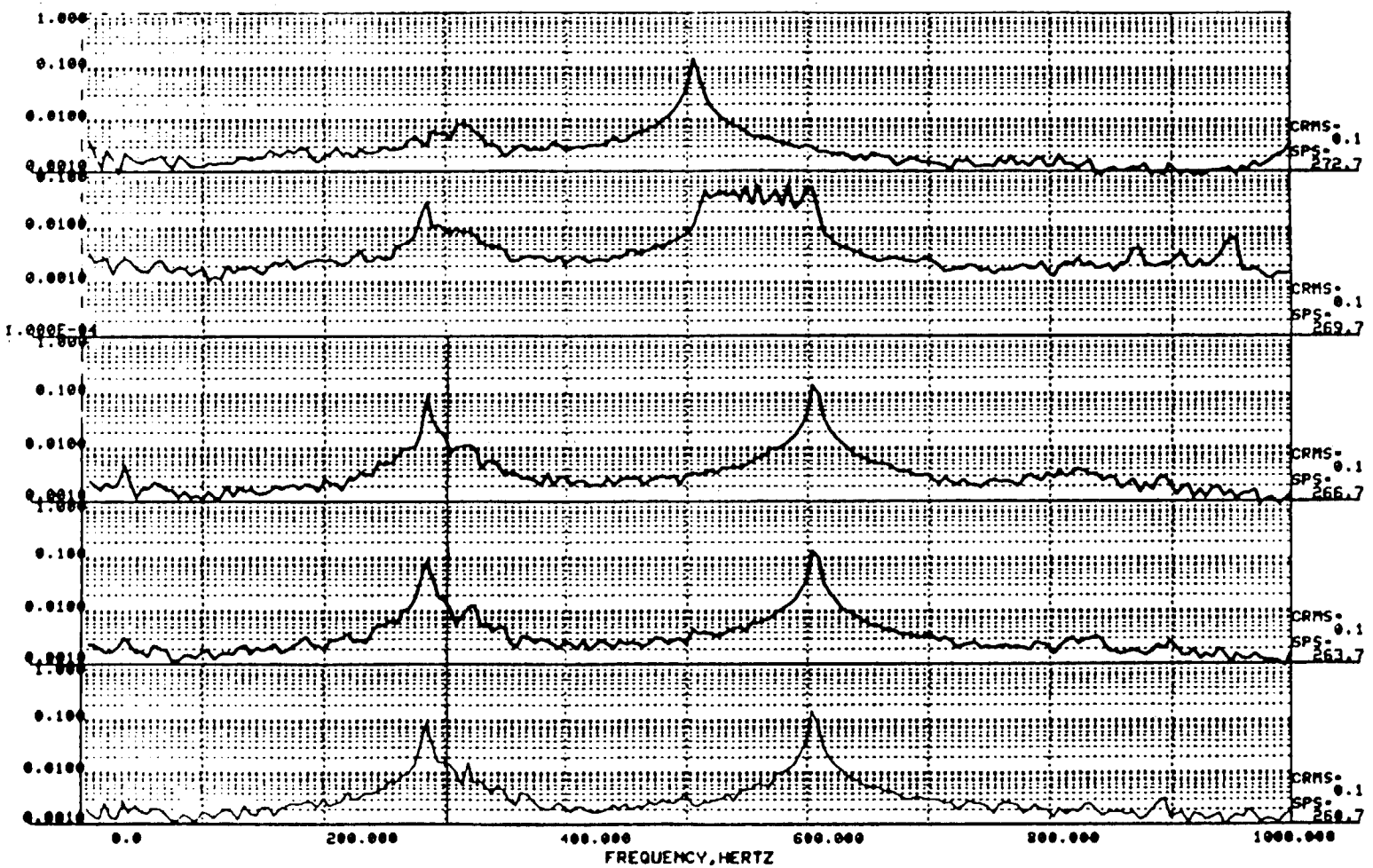

Figure 81g. Test 750-270 displacement measurement spectral data. Beginning 260.7 s after engine start.

in order to correspond to the dwells in the profile. The spectra are arranged in the figures from bottom to top for increasing time. The distinct spike near 600 Hz is the synchronous component due to mass unbalance excitation. A line has been superimposed on the plots at the frequency corresponding to one-half this synchronous frequency. This is to highlight any occurrence of subharmonic response.

The spectra in figure 81a are typical of responses earlier in the profile. The noise in the system is exciting the first resonance; however, neither subharmonic response nor limit-cycle instability appear to be present. It should be noted that the vertical axis scale is logarithmic for these plots. As the power level increases, figures 81b through 81e show the inception of one-half order subharmonic response. The subharmonic increases in amplitude throughout this interval. The last two plots in figure 81e occur after the power level is held constant at 109 percent. All plots in figure 81f are also at this constant power level. The first plot in this figure shows that the system is still exhibiting subharmonic response. The remaining plots indicate a transition between subharmonic response and limit-cycle instability. This is very similar to the behavior described in section V (figs. 76 and 77) for the simplified model. The amplitude increases significantly as the transition occurs. The modulation frequency of the excitation frequency and the limit cycle frequency which was discussed in section V (fig. 32) is evident during the transition. Figure 81g shows the fully developed limit-cycle behavior. The frequency of the limit cycle is approximately 47 percent of the rotation frequency. The last two plots in this figure occur after power is reduced from 109 percent and are not of interest here. It should be noted that the liquid oxygen venting was initiated during the period of fixed power level when the transition from subharmonic response to limit cycle occurred. Although an exact mechanism is not known, the venting may have created a small perturbation to the HPFTP which initiated the transition. Also, as demonstrated in section V, the system noise itself may have been sufficient to initiate the transition and the timing with the vent profile may have been just coincidence.

The test data described above can be interpreted in the context of the analytical and numerical results of the previous sections. The machine appears to be operating at the upper limit of the range of possible subharmonic response. For the simplified model, this upper limit ranged from about 1.7 to about 1.9 times the zero deadband linear system resonance, depending on the system parameters. In addition, the transition to limit cycle instability with higher vibration amplitudes indicates that the machine is approaching the global onset speed of instability as defined in section III. For the simplified model, the 47-percent limit cycle frequency ratio would imply that the global onset speed would be 2.13 times the linear system resonance. For the 109-percent power level speed of approximately 36,300 r/min, using the upper limit of possible subharmonic given above yields a linear system resonance between 19,105 r/min (318 Hz) and 21,353 r/min (356 Hz). The corresponding range of onset speeds of instability is 40,694 r/min to 45,482 r/min. These values will be used as a guide in assessing the results from the mathematical model.

C. Linear Analysis Results

The mathematical model results can be separated into linear analysis results and nonlinear simulation results. The primary linear analysis results of interest here are the eigenvalues and eigenvectors of the linear system obtained from the zero deadband assumption. Since the parameters of the system model are functions of operating speed, the eigenvalue problem must be solved for many speed values in the range of interest. For each different value of speed, the entire set of eigenvalues and eigenvectors (in this case, 39 complex conjugate pairs)

are recalculated. In general, since the system matrix is different at each speed, the eigenvalues and vectors for one speed may not be related to those at another. However, there is a known relationship between the elements of the system matrix at different speeds. Because of this, one would expect to be able to relate the system characteristics for one speed to those at another speed which is relatively close to the first. This is in fact the case, however, it is not entirely straightforward. As speed is varied, the eigenvalues tend to move along loci whose patterns become apparent by visual observation. The associated eigenvector of an eigenvalue at one speed for a particular locus is usually very similar to that at another speed on the same locus. This is not always the case, however. For large speed changes, the dynamics of the system can change dramatically, and there may be no recognizable relationship between eigenvectors at one speed and those at another. This may be true even though the eigenvalues traced out clearly identifiable loci when migrating as speed varied. Another difficulty is when two loci intersect or nearly intersect. In these instances, the characteristics of the eigenvectors associated with the loci may switch. This type of behavior is observed in the results from the HPFTP model. When this occurs, the only meaningful association between eigenvalues at one speed and those at another must be based on similarity of their associated eigenvectors, not on the patterns of their loci.

The eigenanalysis results can be presented in several ways. One way is to plot the eigenvalues in the complex plane where the locus patterns are evident (root locus). This presentation has the disadvantage that the corresponding speeds are not readily visible. Another way is to plot the real and imaginary parts of the eigenvalues versus speed. This presentation does not provide as much visibility to the loci patterns but clearly indicates the speed correspondence. Yet another method is to plot the critical damping ratio associated with each pair of complex roots versus speed. This provides some "calibration" for the real part of the eigenvalue indicating its relative stability. The complex eigenvectors are presented in the manner described in appendix A. Due to the large number of eigenvalues for this system, eigenvalue and eigenvector information will only be provided for those eigenvalues related to the limit cycle instability and subharmonic response.

The linear analysis (zero deadband assumption) results for the HPFTP using the nominal data discussed in appendix B are presented in figures 82 through 84. These figures present the root loci, imaginary components, and critical damping ratio, respectively, for two eigenvalues designated No. 3 and No. 4. On the root loci (fig. 82), the "X" symbol indicates the starting speed (10,000 r/min) and each circle corresponds to a 1,000-r/min increment. These eigenvalue loci exhibit the switching behavior discussed previously. At the higher speeds, the eigenvector associated with eigenvalue No. 3 possesses the characteristics of the unstable behavior. This eigenvector is shown in figure 85. This figure displays the relative component (rotor minus housing) of the eigenvector. The rotor precesses in a forward direction (except at the pump end bearings) with only a small amount of housing motion. The motion can be described as a rigid body translation with superimposed rotor flexing. From figures 82 and 84, it can be seen that the locus for this eigenvector is moving toward instability. From figure 83, the frequency is observed to vary between 250 and 360 Hz with a value of about 335 Hz at the 109-percent power level speed (36,300 r/min). At the lower speeds, the eigenvector associated with eigenvalue No. 4 possesses the characteristics of the unstable behavior. The locus for this eigenvalue heads toward the right half plane initially. The critical damping ratio reaches a minimum at 25,000 r/min and the locus then reverses direction. This is due to the switching which takes place between this locus and the one for eigenvalue No. 3.

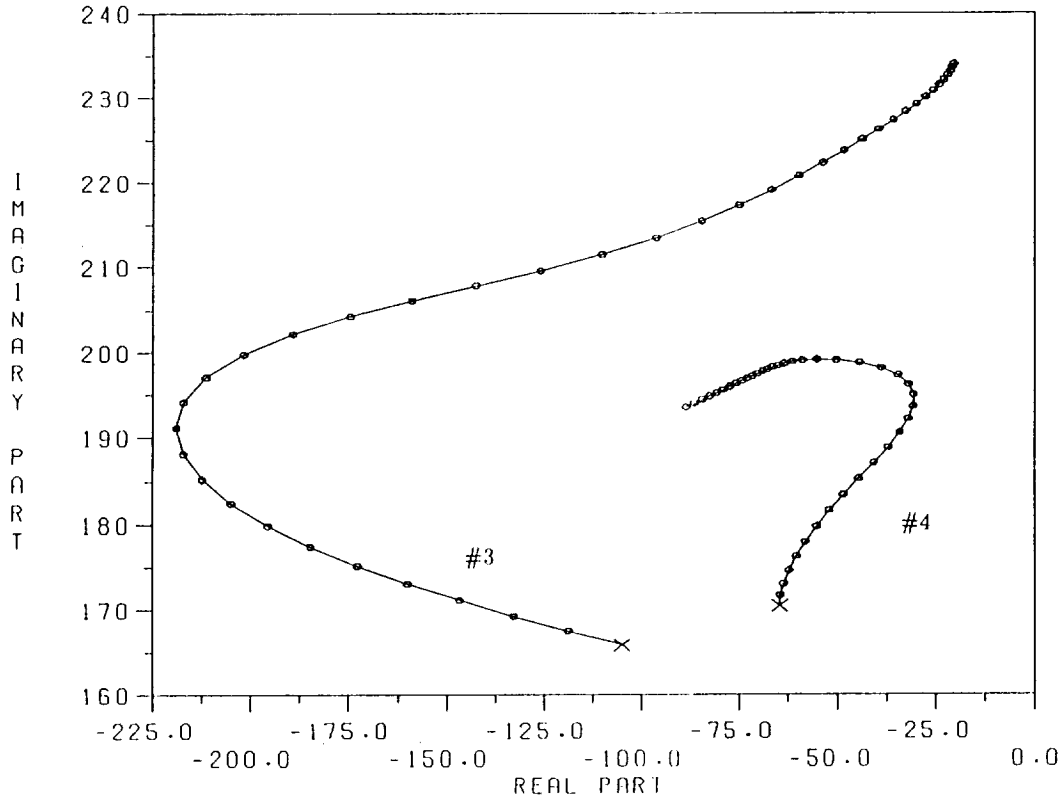

Figure 82. Root loci for eigenvalues No. 3 and No. 4 of the nominal HPFTP linear model.

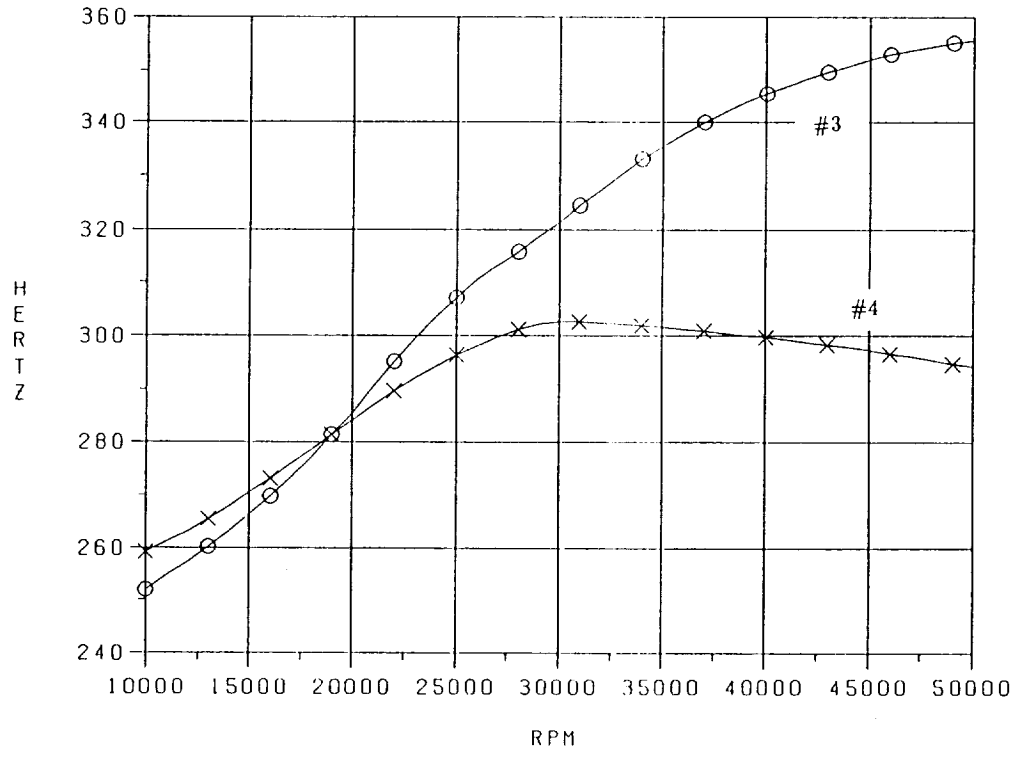

Figure 83. Imaginary part versus speed for eigenvalues No. 3 and No. 4 of the nominal HPFTP linear model.

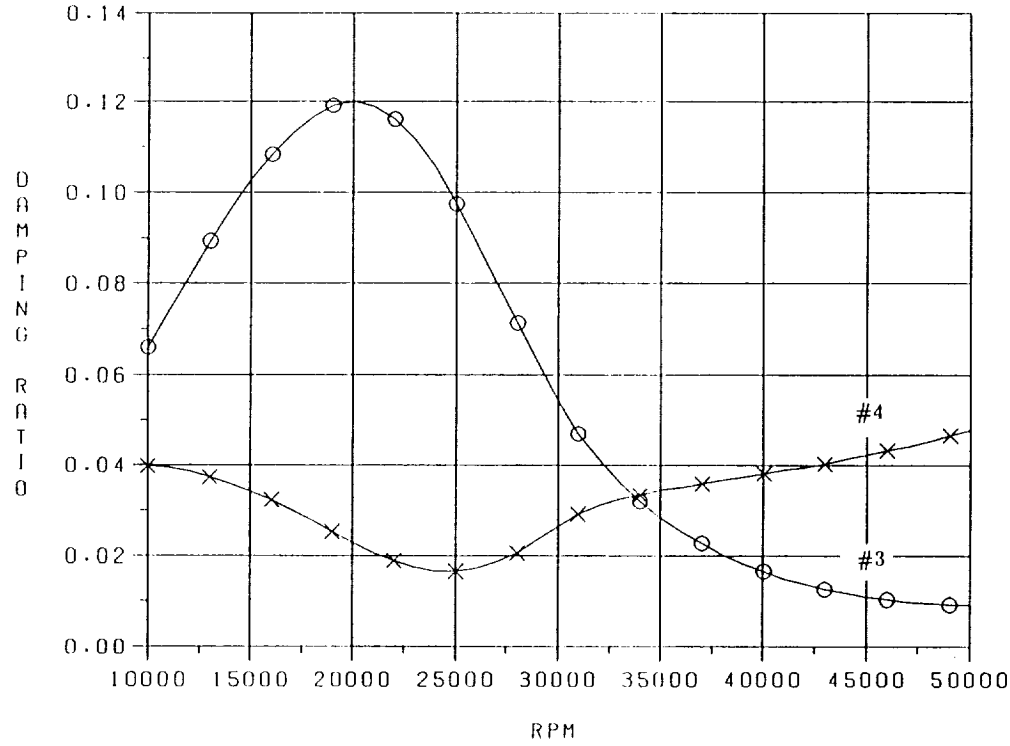

Figure 84. Critical damping ratio versus speed for eigenvalues No. 3 and No. 4 of the nominal HPFTP linear model.

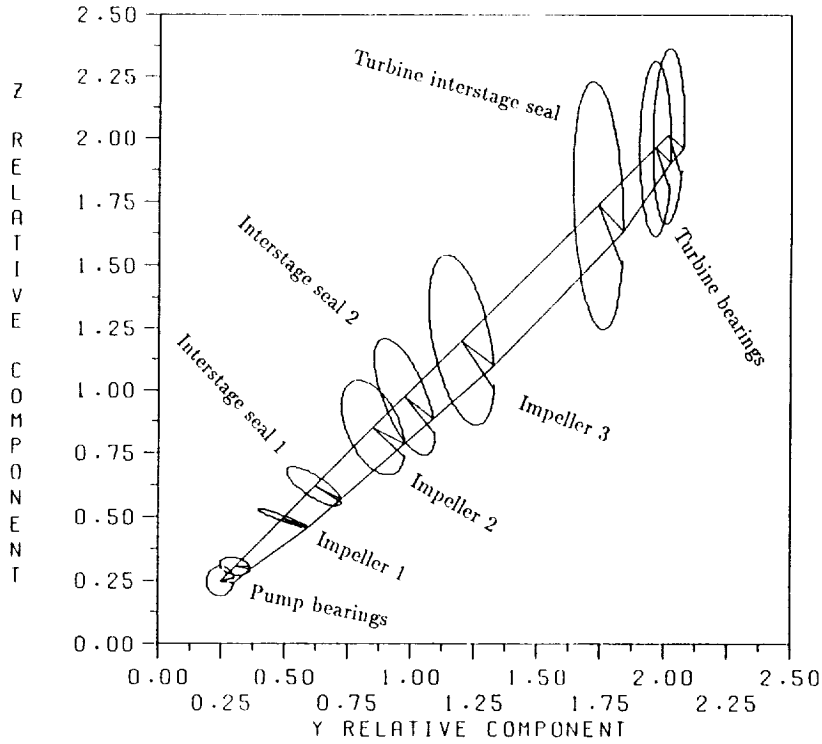

Figure 85. Eigenvector display for eigenvalue No. 3 at 40,000 r/min for the nominal HPFTP linear model.

While systems of this sort are generally less stable at higher speeds, the interaction between eigenvalue loci creates a range of speed where stability is actually enhanced. This particular occurrence appears to be related to the asymmetry in the housing; in particular, asymmetry in the frequency-dependent dynamic impedance of the housing which is an integral part of the rotor support. The stabilizing capacity of asymmetry is well known and documented (see references 12 and 18, for example). The housing impedance asymmetry effect can be shown by modifying the housing model so that the rotor dynamics do not "tune" with the housing dynamics and create this behavior. Figure 86 shows the root loci for the case where the frequencies of the third and fourth housing input modes are increased 20 percent. For this case, the switching does not occur, and the locus for eigenvalue No. 4 progresses fairly quickly into the right half plane. The stabilizing capacity of the switching behavior will complicate comparisons of the HPFTP model's behavior with the simplified model results. However, the model will not be adjusted to remove this characteristic since it may truly be representative of the behavior of the HPFTP.

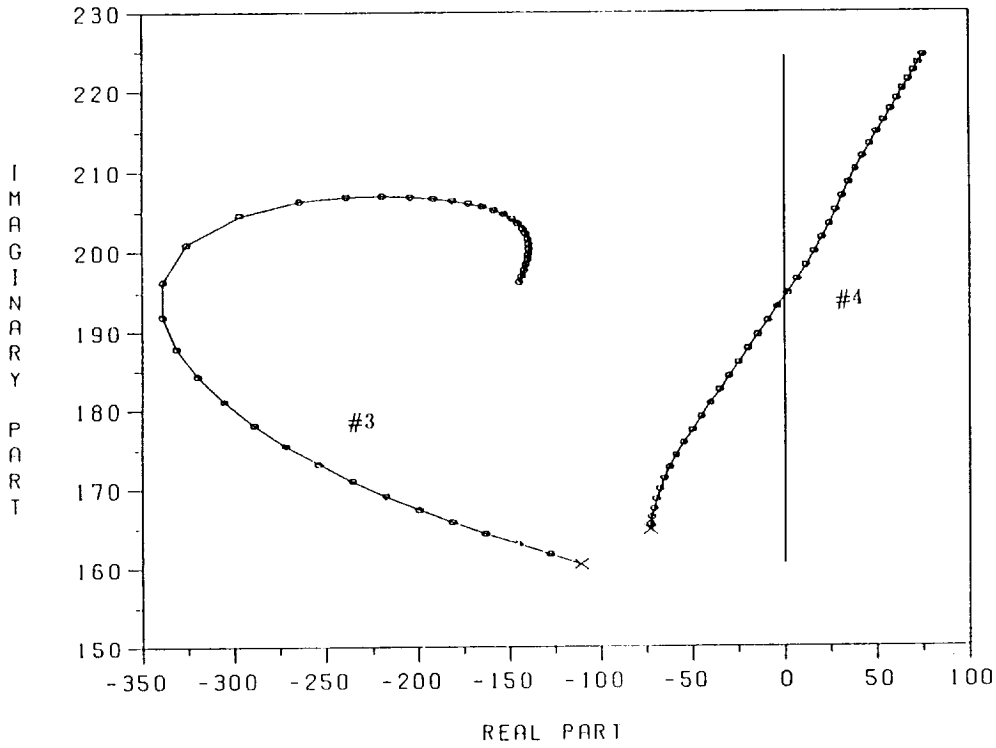

Figure 86. Root loci for eigenvalues No. 3 and No. 4 of the nominal HPFTP linear model with modified housing modal data.

The linear analysis results for the nominal HPFTP model indicate that the model is too stable to exhibit limit cycle instability. Based on the analytical results from the simplified model there are two ways to reduce the stability of the system: increase the cross-coupled stiffness parameter σ and reduce the pertinent natural frequency (most likely by reducing the rotor support stiffness). The first method will increase the frequency ratio of a limit cycle while the second will not. The specific test data being examined here indicates a limit cycle frequency ratio of 47 percent; therefore, it is undesirable to adjust the model by increasing the parameter σ. The stiffness of the bearings and seals was decreased by trial and error until suitable results were achieved. Greater reduction was made in the seal stiffness than in the bearing stiffness in order to maintain a strong effect from the nonlinearity (γ parameter). The final values chosen were

92 percent of the nominal bearing stiffness and 60 percent of the nominal seal stiffness. The cross-coupled stiffness parameter for the pump interstage seals (σ) was reduced from 0.6 to 0.55 and the turbine interstage seal and Alford effect cross-coupling was reduced to 75 percent of the nominal value. These changes were based on results of simulation trials.

The linear analysis results for the modified model are presented in figures 87 through 89. Figures 87 (root loci) and 89 (critical damping ratio) show the same switching behavior as the nominal model. The transition occurs at a higher speed for the modified model. The frequency of eigenvalue No. 3 is about 310 Hz at the 109-percent power level speed. The onset speed of instability is 44,000 r/min. At the imaginary axis crossing, the frequency of the eigenvalue is approximately 328 Hz. This translates into a ratio of 45 percent. These values compare favorably with the guideline values inferred from the test data.

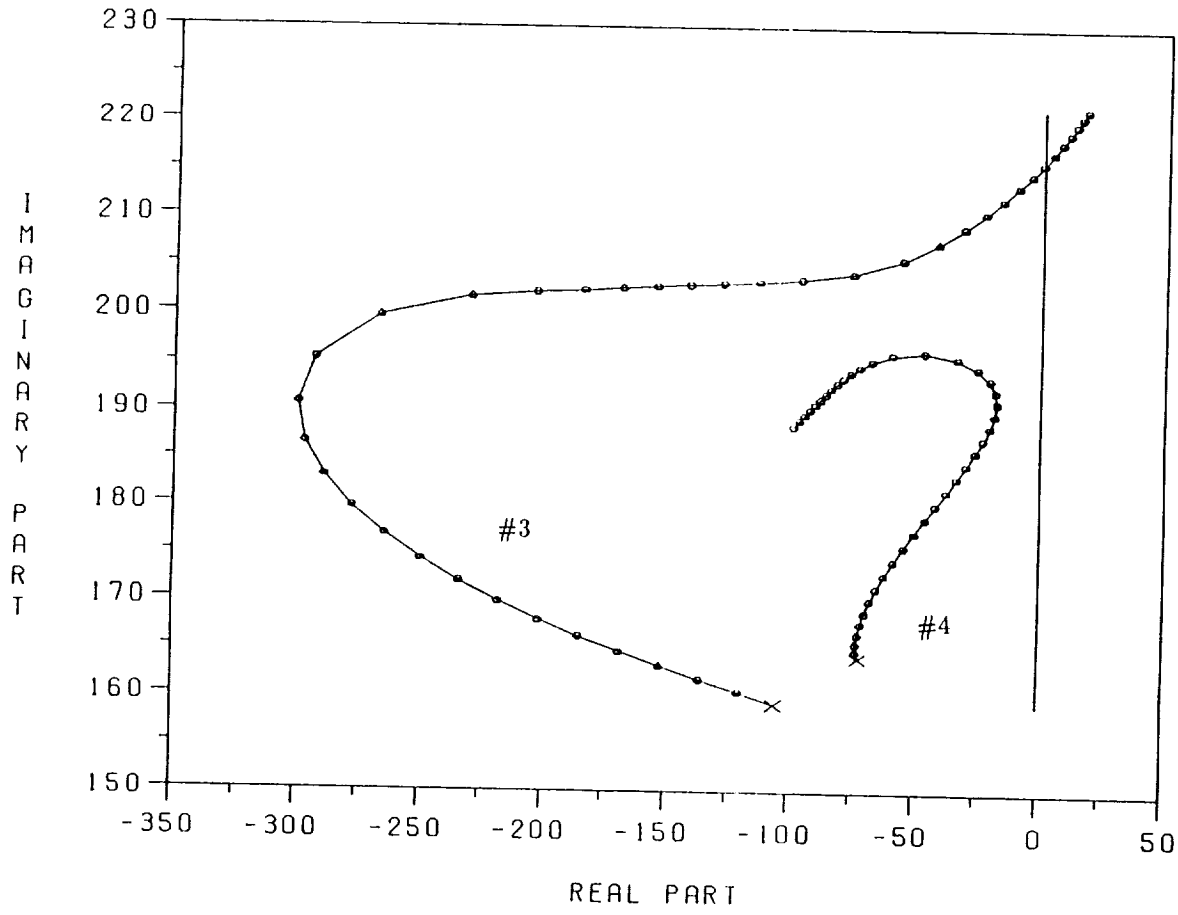

Figure 87. Root loci for eigenvalues No. 3 and No. 4 of the modified HPFTP linear model.

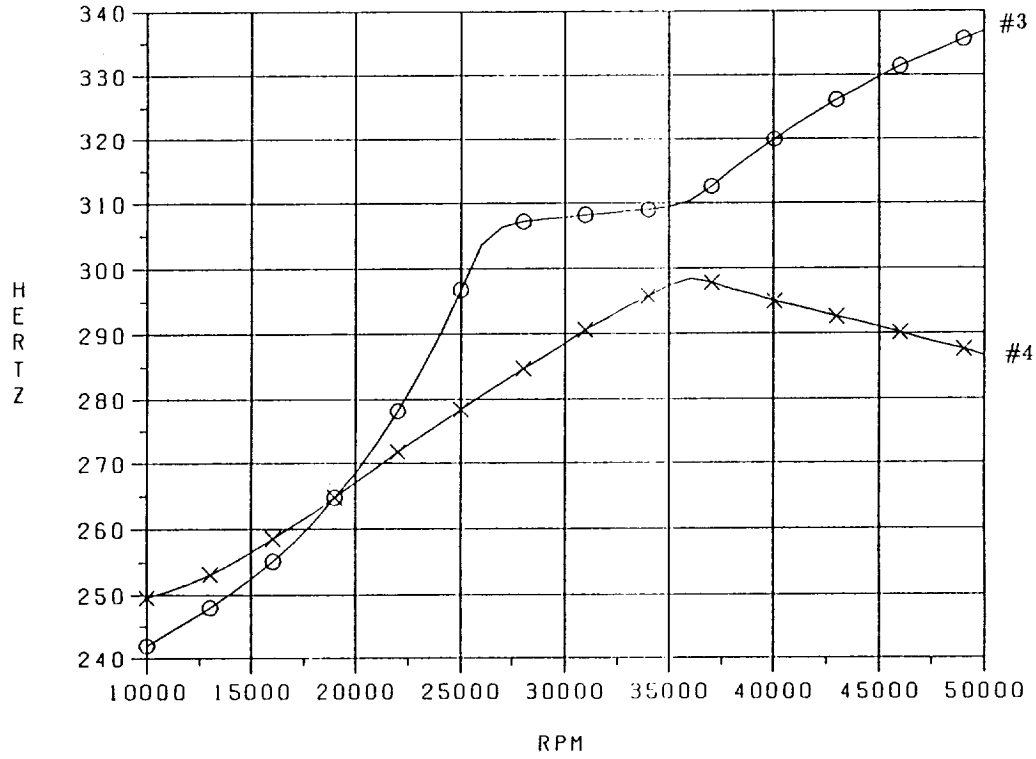

Figure 88. Imaginary part versus speed for eigenvalues No. 3 and No. 4 of the modified HPFTP linear model.

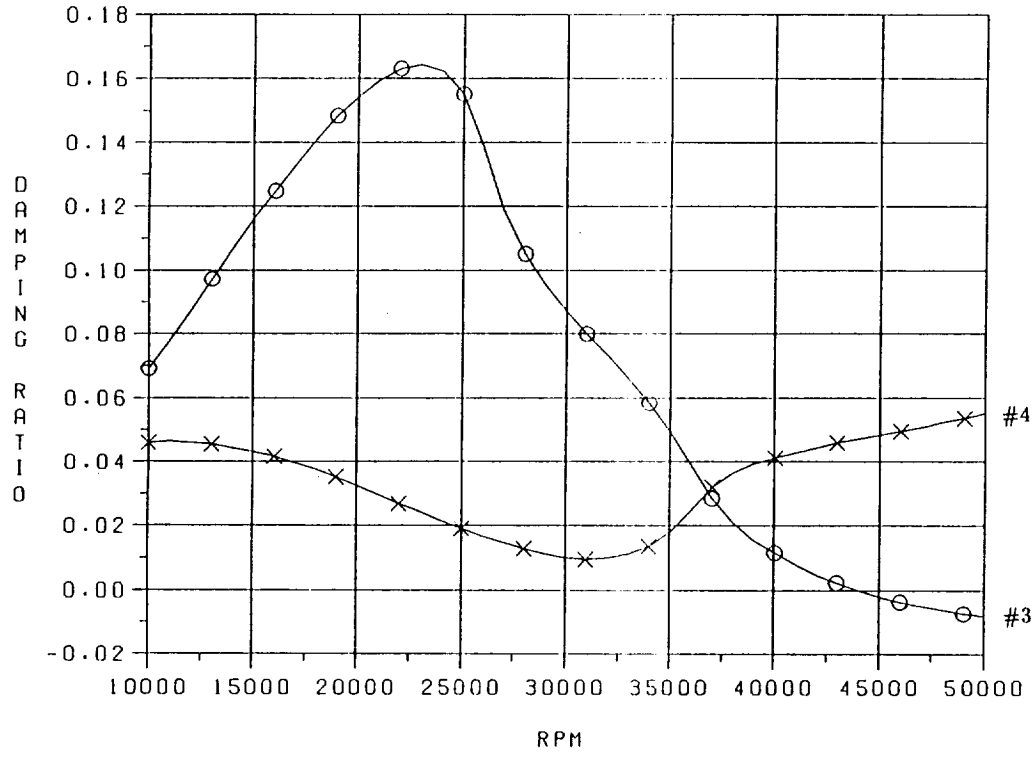

Figure 89. Critical damping ratio versus speed for eigenvalues No. 3 and No. 4 of the modified HPFTP linear model.

D. Nonlinear Simulation Results

The general behavior of the simplified model was characterized in terms of its behavior under certain restricted conditions in section V. The restricted conditions were analyzed in sections III and IV. The homogeneous equilibrium, unbalance mass equilibrium, and side-force equilibrium and their respective linearizations provided bounds for parameter ranges where limit cycle behavior is possible. The subharmonic response harmonic balance solution provided bounds for parameter ranges where subharmonic response is possible. These results were based on analytical and combined analytical/numerical solutions to the nonlinear system equations. These approaches were rather straightforward for the simplified model. Analogous methods for the more general and complex turbopump model have not been developed; however, the approach of using the restricted case results to characterize the general case results is still valid. Simulation must be used rather than analytical means to obtain the restricted case results. The HPFTP model will, therefore, be simulated for the three restricted excitation cases analyzed for the simplified model. The first is the homogeneous case. This case is not truly homogeneous since noise excitation is imposed, but it will serve to characterize the lower limit, amplitude, frequency, and global stability limit of the limit cycle behavior. The second is the unbalance mass equilibrium case (again with noise excitation). This case will show the limits where stable unbalance equilibrium is possible and where limit cycle will exist along with the unbalance response. The third is the side-force equilibrium case (also with noise). This case will show the limits where limit cycle is possible under the stabilizing influence of side force. These cases will be examined by executing a speed ramp up to just beyond the global onset speed of instability and then back down. A general loading case will then be examined with the same ramp profile. The response to this loading can then be characterized in terms of the limits and characteristics of the three restricted cases. The subharmonic response analysis of the simplified model was not based on a restricted excitation but, rather, on a specific assumed form of solution. No special simulation case is required to investigate this behavior. The general excitation case will be examined to determine whether subharmonic response occurs.

Simulation results for the homogeneous case are presented in figures 90 and 91. Figure 90 displays the "z" axis relative displacement at the inboard turbine end bearing location. The top graph shows the response to the ramp up, and the bottom graph shows the response to the ramp down. The speed profile consisted of a 4.5-s ramp from zero to 45,000 r/min and a 2.5-s ramp back down to 20,000 r/min. Figure 91 displays the cascade spectral plots corresponding to figure 90. Limit cycle instability initiates at approximately 25,000 r/min with a low amplitude. The frequency ratio is about 55 percent. The amplitude increases steadily until a speed of about 32,000 r/min is reached. Between this speed and about 35,000 r/min, the amplitude decreases slightly and the frequency ratio drops to about 47 percent. This transition corresponds to the eigenvalue switching observed in the linear analysis. As speed is increased beyond this transition, the amplitude increases in the same manner as the limit cycle in the simplified model. The reverse behavior occurs on the down ramp with no apparent hysteresis. The mass unbalance excitation case produced similar results (figs. 92 and 93). The limit cycle initiation was suppressed until about 32,000 r/min by the unbalance equilibrium. On the down ramp, the limit cycle was maintained until about 29,000 r/min. This is similar to the hysteretic behavior observed for the simplified model.

The side-force excitation exhibited the greatest amount of hysteresis (fig. 94). On the up ramp, the limit cycle did not initiate until the global onset speed of instability was reached (44,000 r/min). On the down ramp, the limit cycle was sustained until about 35,500 r/min.

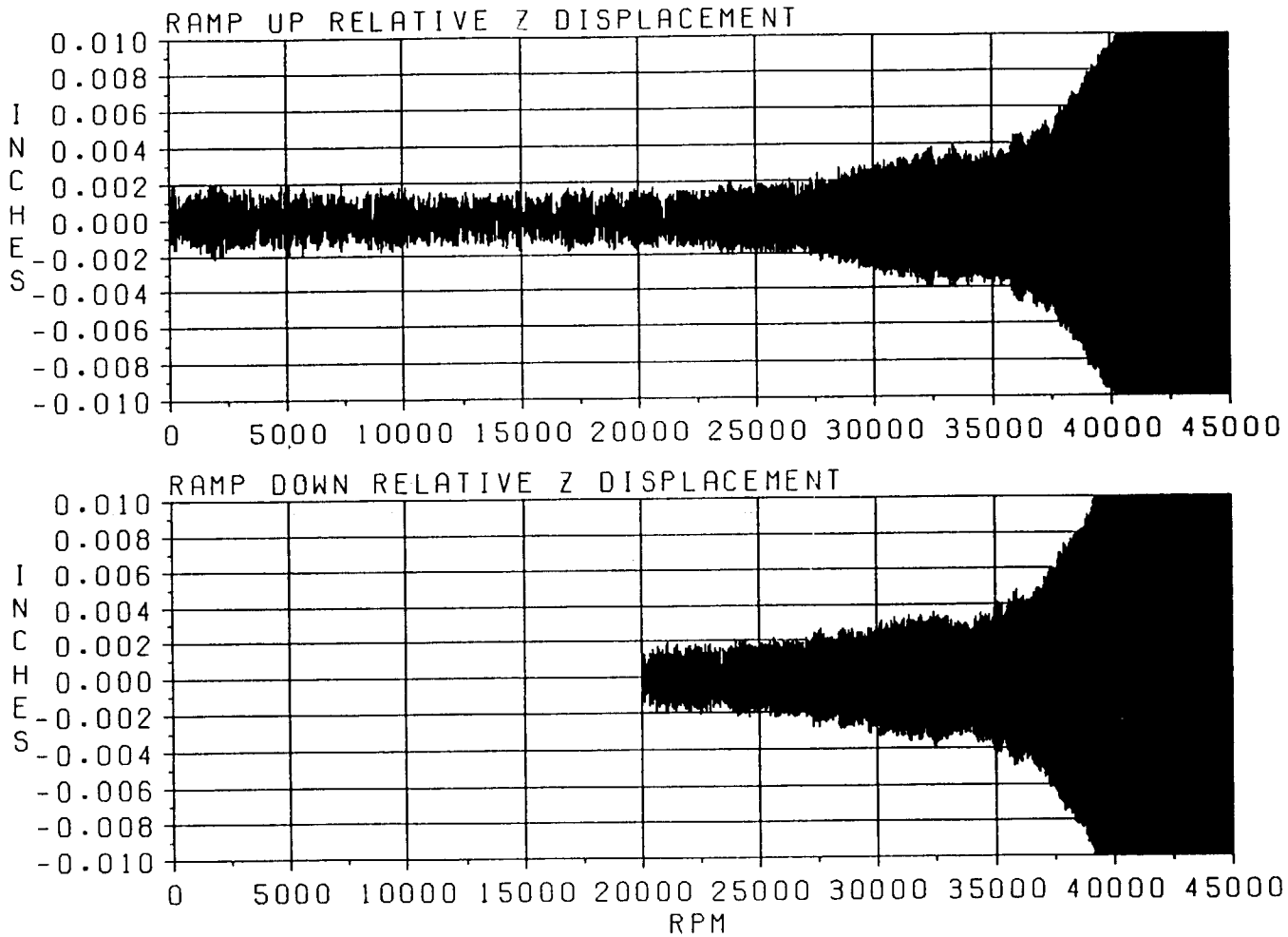

Figure 90. Homogeneous simulation results for modified HPFTP nonlinear model. Inboard turbine bearing response.

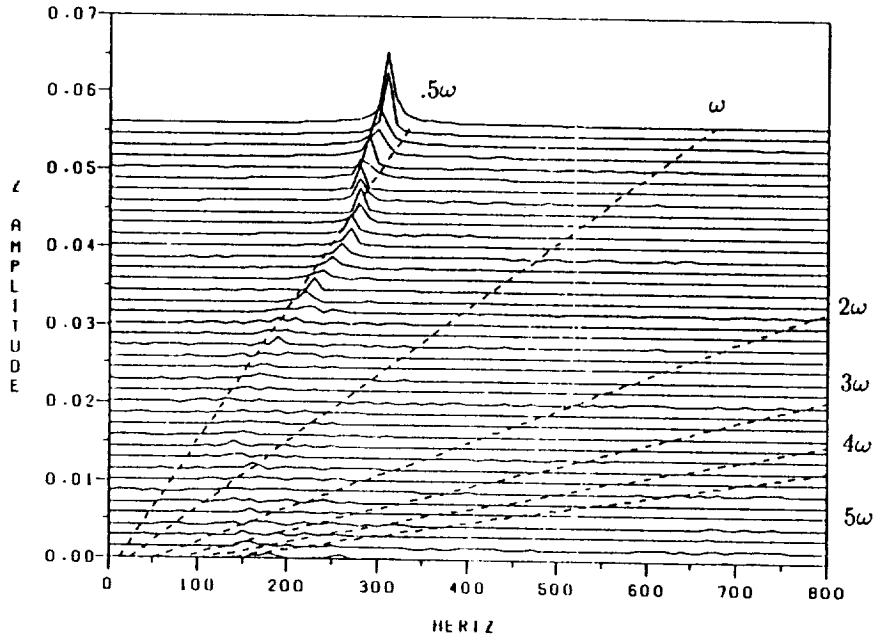

(a) Up ramp response.

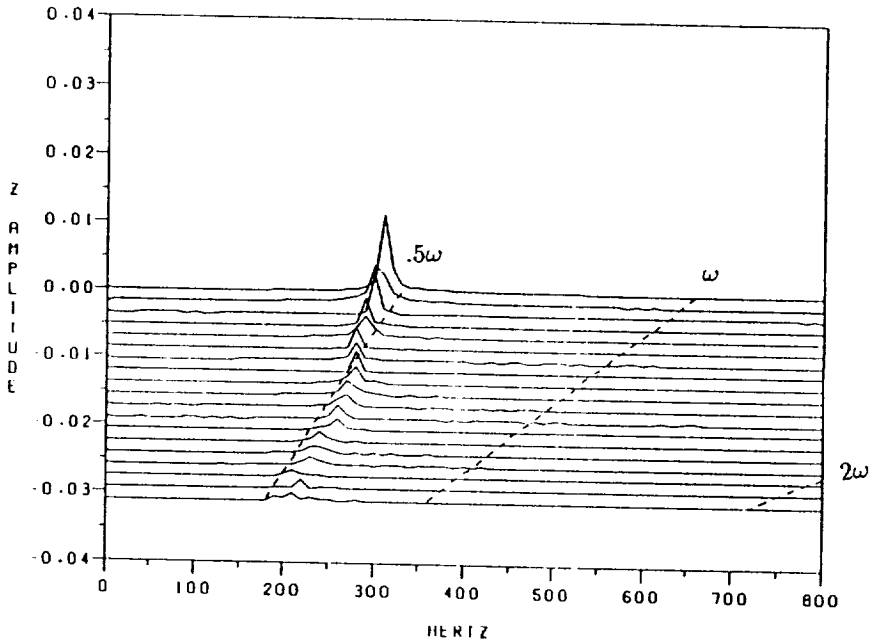

(b) Down ramp response.

Figure 91. Cascade spectral plots corresponding to figure 90.

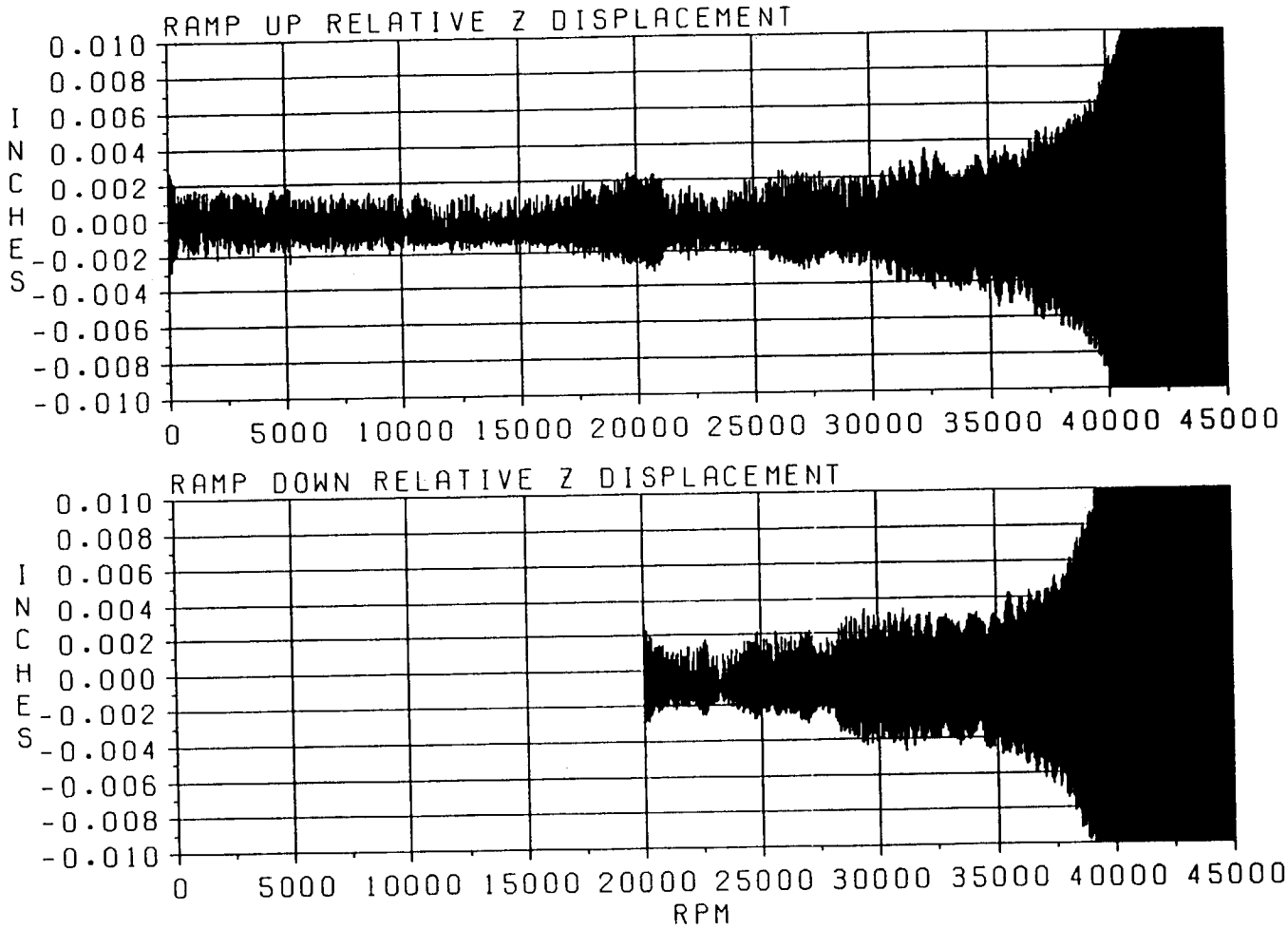

Figure 92. Mass unbalance excitation simulation results for modified HPFTP nonlinear model. Inboard turbine bearing response.

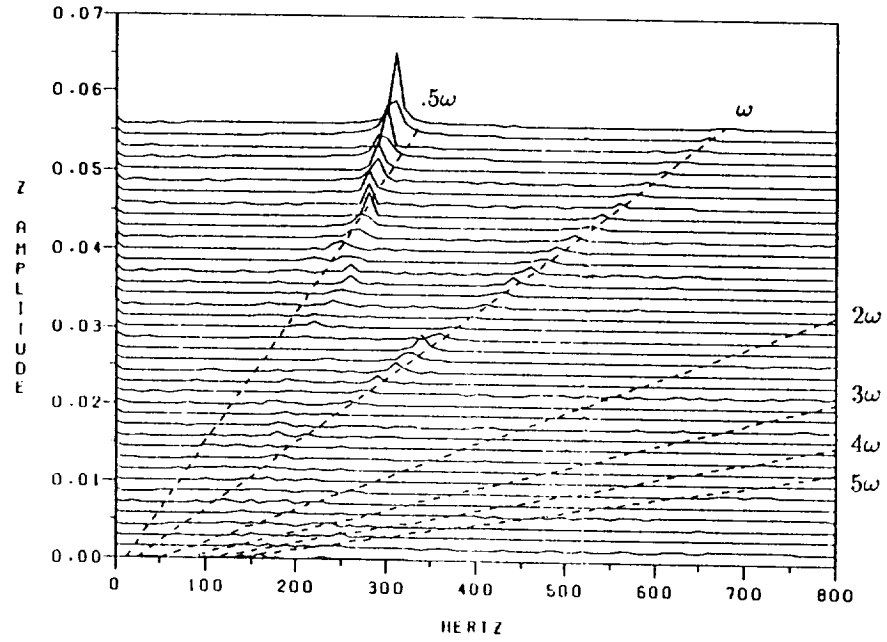

(a) Up ramp response.

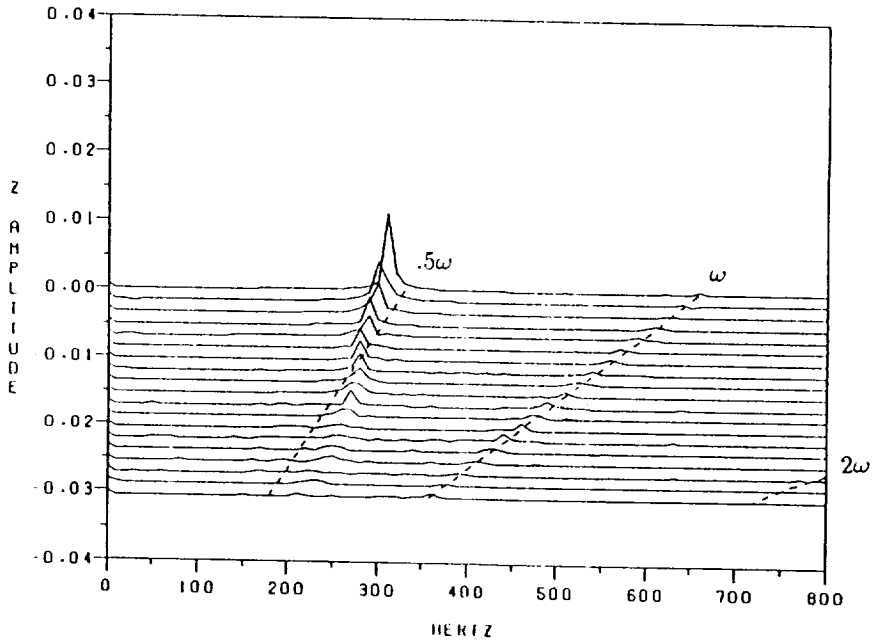

(b) Down ramp response.

Figure 93. Cascade spectral plots corresponding to 92.

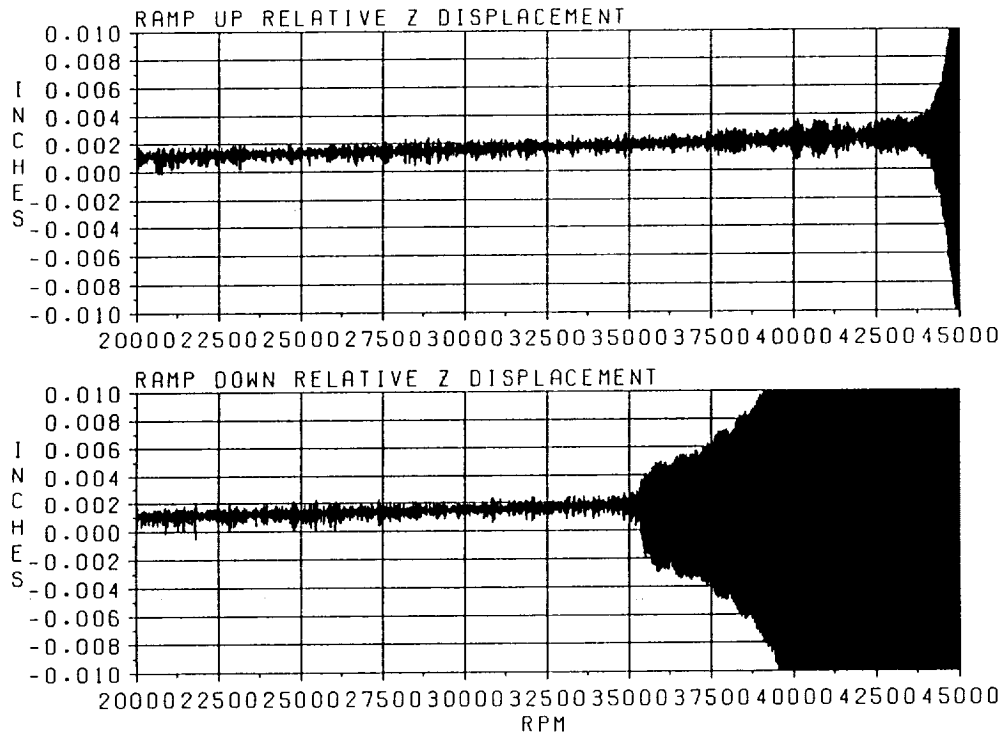

Figure 94. Nominal side-force excitation simulation results for modified HPFTP nonlinear model. Inboard turbine bearing response.

This value represents the lowest speed for which a limit cycle is possible with the given side-force excitation. This limit must be lowered in order to obtain general loading results which exhibit limit cycle at the 109-percent power level speed (36,300). This was accomplished by reducing the side force to 75 percent of its nominal value. This produced the results shown in figures 95 and 96. The limit cycle was sustained in this case until about 31,000 r/min.

Results have been presented for the three restricted cases with bounds identified for the occurrence of limit cycle instability. The general combined loading case will now be presented. The initial case simulated consisted of a direct combination of the previous cases; i.e., nominal mass unbalance, 75 percent of the nominal side force, and the same noise excitation. This case exhibited limit-cycle behavior but did not exhibit any subharmonic response. One of the objectives of this examination is to determine if the behavior of the simplified model (subharmonic entrainment and transition to limit cycle) extends to the more complex HPFTP model. In order to determine this, the mass unbalance was varied by trial and error in an attempt to find a combination of parameters which resulted in subharmonic. Increasing the unbalance uniformly by 50 percent produced the desired results.

Figures 97 and 98 present the time and spectral data for the response to the same profile as the three restricted cases. As speed reaches about 30,000 r/min, limit cycle initiates at a low amplitude with a frequency ratio just above 50 percent. At about 33,000 r/min, this limit cycle becomes entrained by subharmonic response at the 50-percent ratio. This entrained response transitions to a limit cycle of about 47-percent frequency above 35,000 r/min. The down ramp did not exhibit subharmonic entrainment but behaved very similarly to the unbalance excitation case (figs. 92 and 93). The up ramp behavior can be more clearly seen in figures 99 and 100. This case

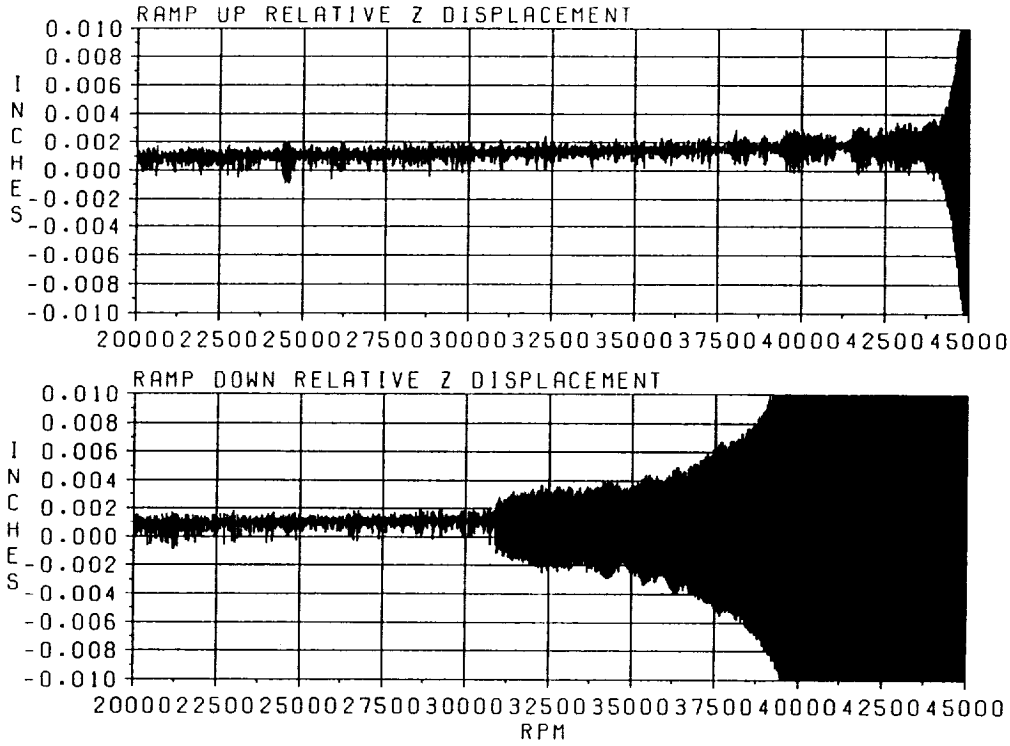

Figure 95. Reduced side-force excitation simulation results for modified HPFTP nonlinear model. Inboard turbine bearing response.

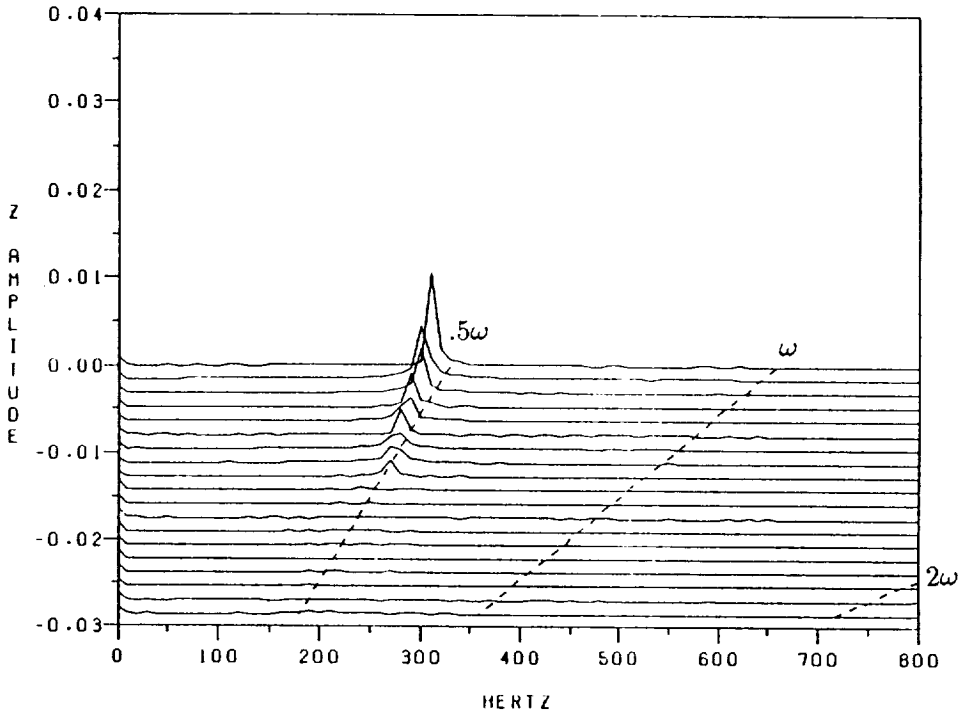

Figure 96. Cascade spectral plot corresponding to figure 95 down ramp.

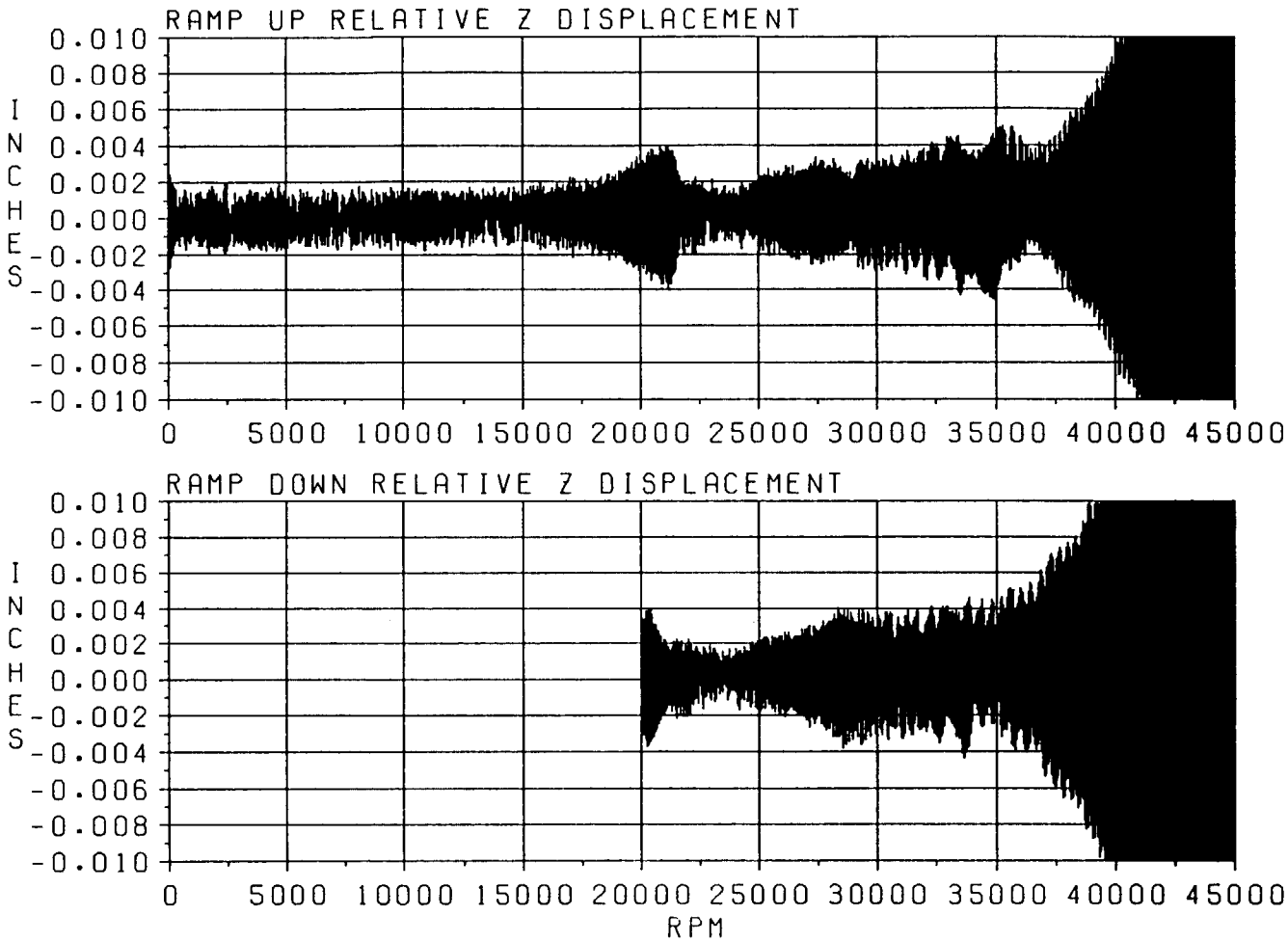

Figure 97. Combined excitation simulation results for modified HPFTP nonlinear model. Inboard turbine bearing response.

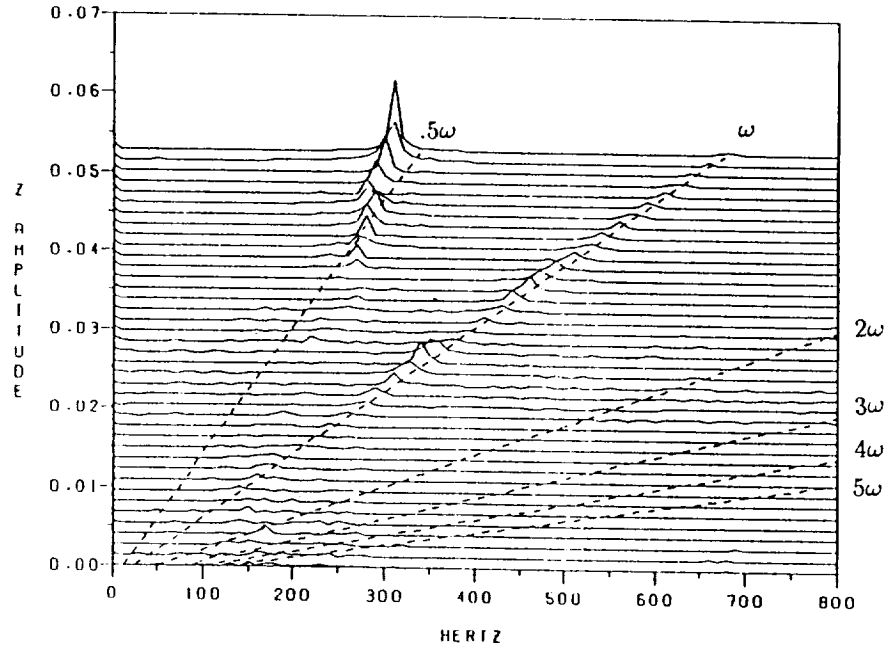

(a) Up ramp response.

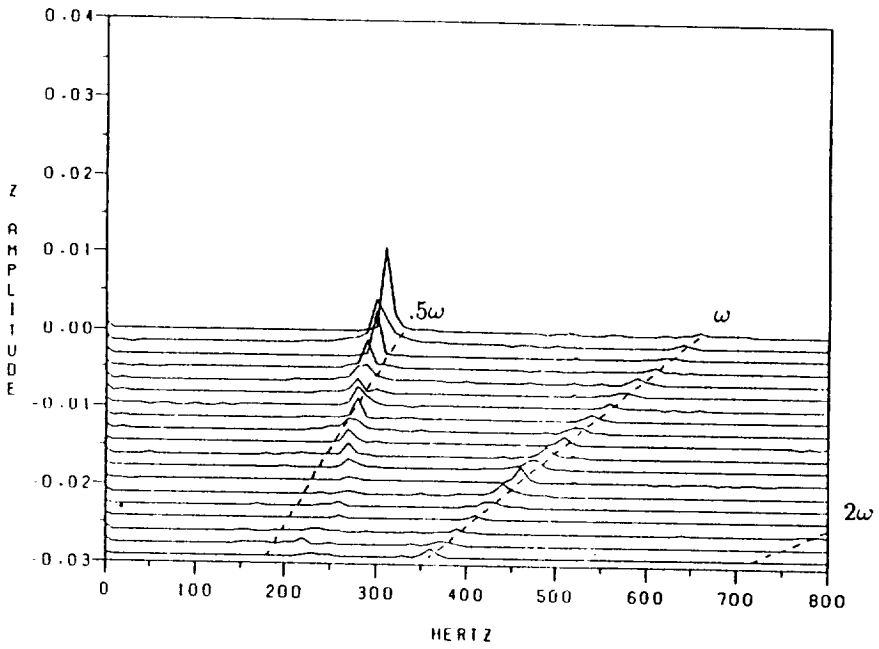

(b) Down ramp response.

Figure 98. Cascade spectral plots corresponding to figure 97.

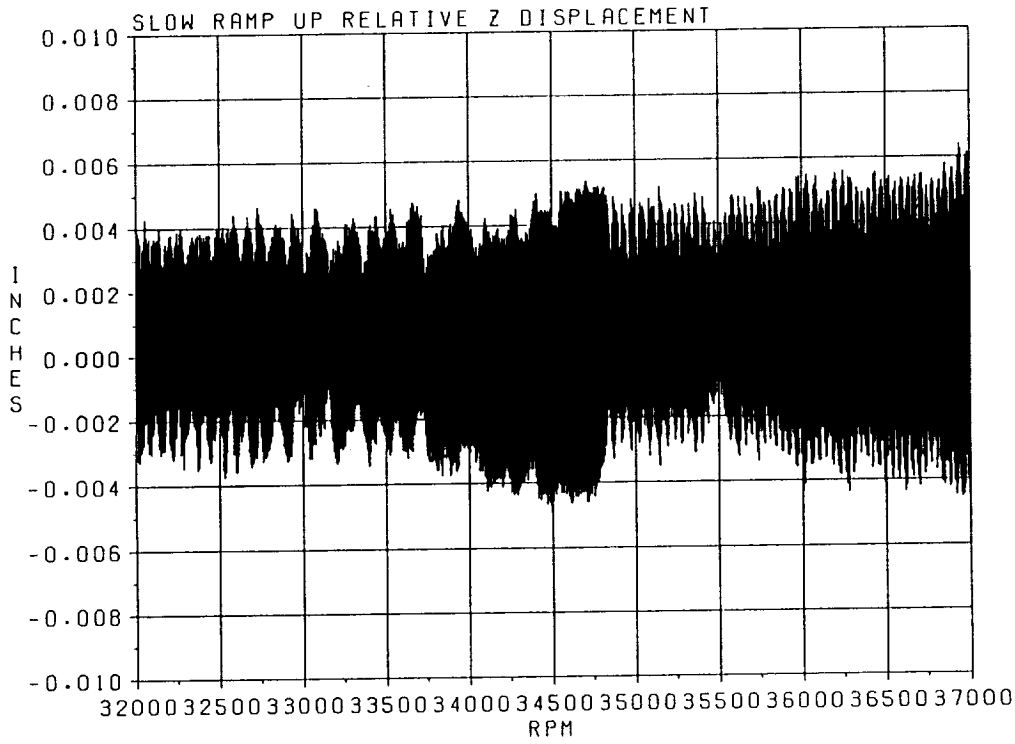

Figure 99. Combined excitation simulation results for modified HPFTP nonlinear model. Slow ramp from 32,000 r/min to 37,000 r/min. Inboard turbine bearing response.

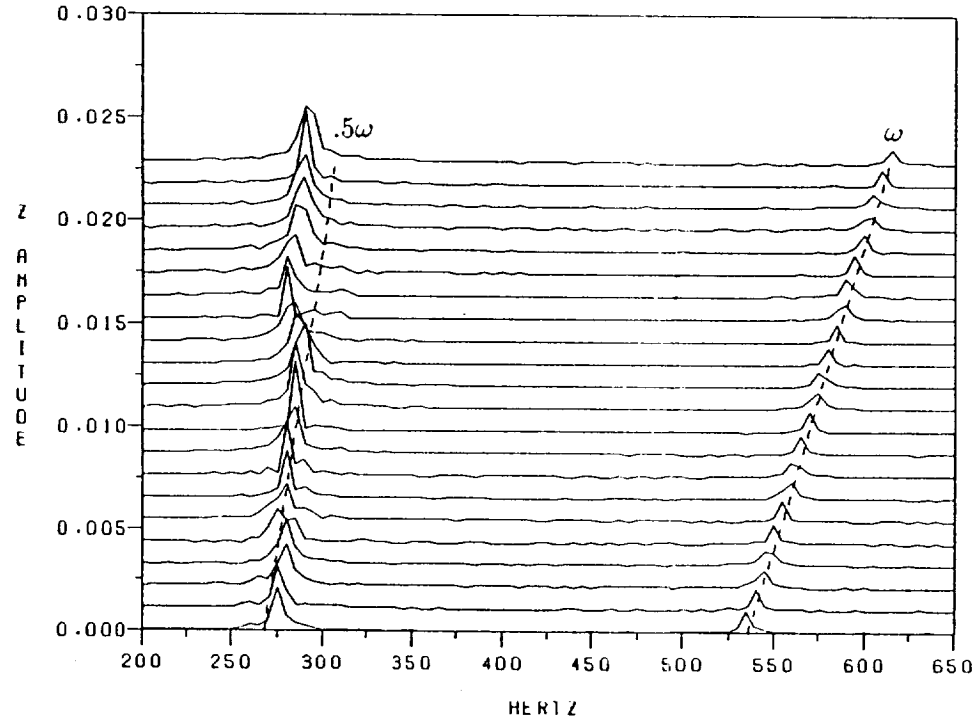

Figure 100. Cascade spectral plot corresponding to figure 99.

is identical to the other except that the speed profile was altered about 32,000 r/min. For this case, speed was increased from 32,000 r/min to 37,000 r/min in 4.5 s, the same length of time as the original ramp from zero to 45,000 r/min. The three zones of behavior are observable in both the time data and in the spectral data. The movement from the higher frequency ratio to the lower frequency ratio was observed for the homogeneous case and the mass unbalance case and was attributed to the eigenvalue loci switching behavior. However, the entrainment at the subharmonic frequency is unique to the general combined loading case.

Another important result which was presented for the simplified model in section V (figs. 76 and 77) is the nonuniqueness of the solution. This behavior is demonstrated for the HPFTP model by holding the speed profile for this case at 35,000 r/min. The time response for this simulation is shown in figure 101 with an expanded portion shown in figure 102. The spectral results are shown in figure 103. The system is clearly jumping between limit cycle entrained by subharmonic response and pure limit cycle. The frequency of the limit cycle at this speed is close to 0.5 due to the shift from the higher to lower ratio noted earlier. This proximity and the rapid manner in which the transitions occur make it difficult to obtain FFT results as clear as for the simplified model. The only change occurring in the parameters of the model is the random noise excitation. The response remains in one form for as long as 0.3 s.

The results of the combined excitation case have clear implications related to interpretation of test results. For one set of parameter values, the model exhibits subharmonic response, limit cycle with a frequency greater than subharmonic, and limit cycle with frequency less than subharmonic, all within a narrow speed range. The model also exhibited transitions

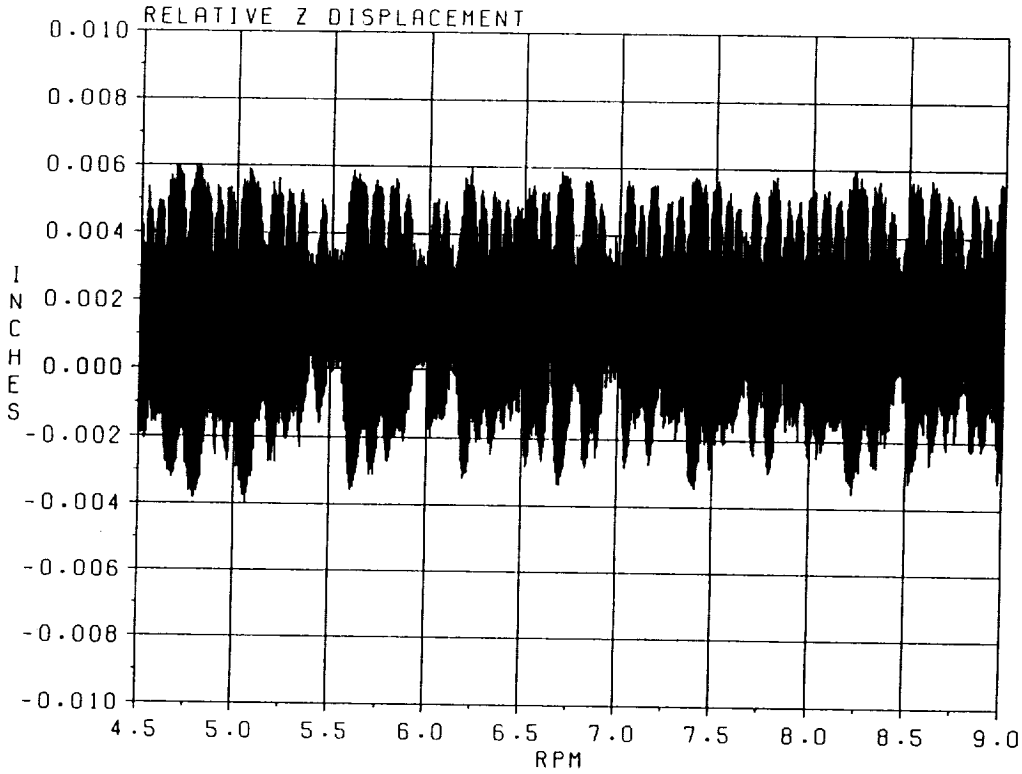

Figure 101. Combined excitation simulation results for modified HPFTP nonlinear model. Dwell at 35,000 r/min. Inboard turbine bearing response.

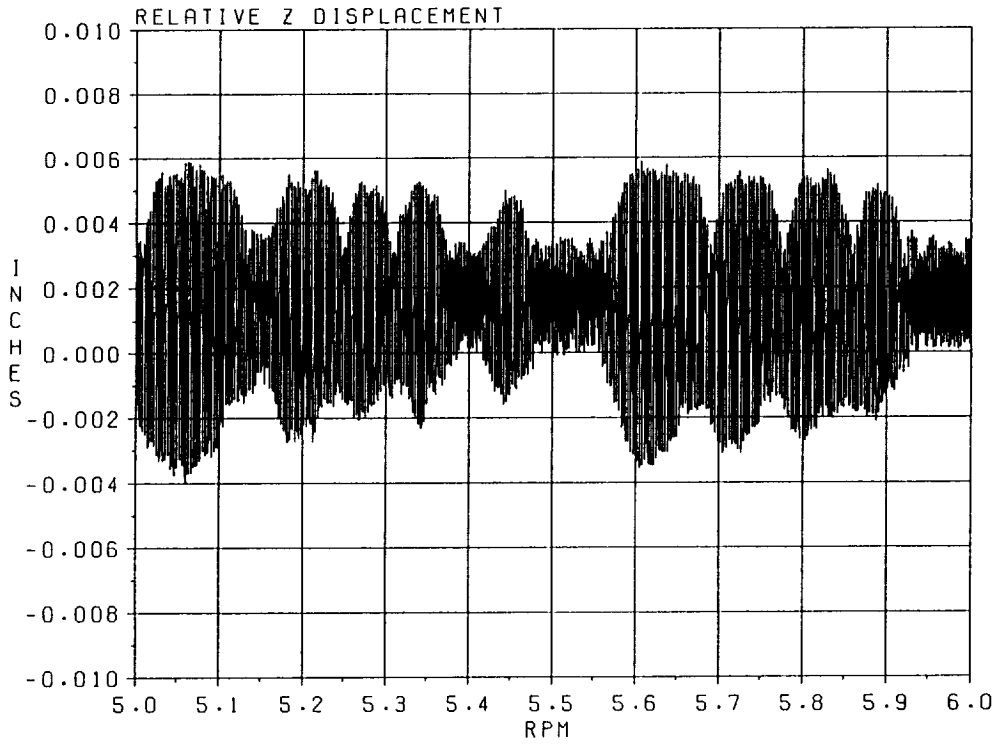

Figure 102. Combined excitation simulation results for modified HPFTP nonlinear model. Dwell at 35,000 r/min. Expanded between 5 and 6 s. Inboard turbine bearing response.

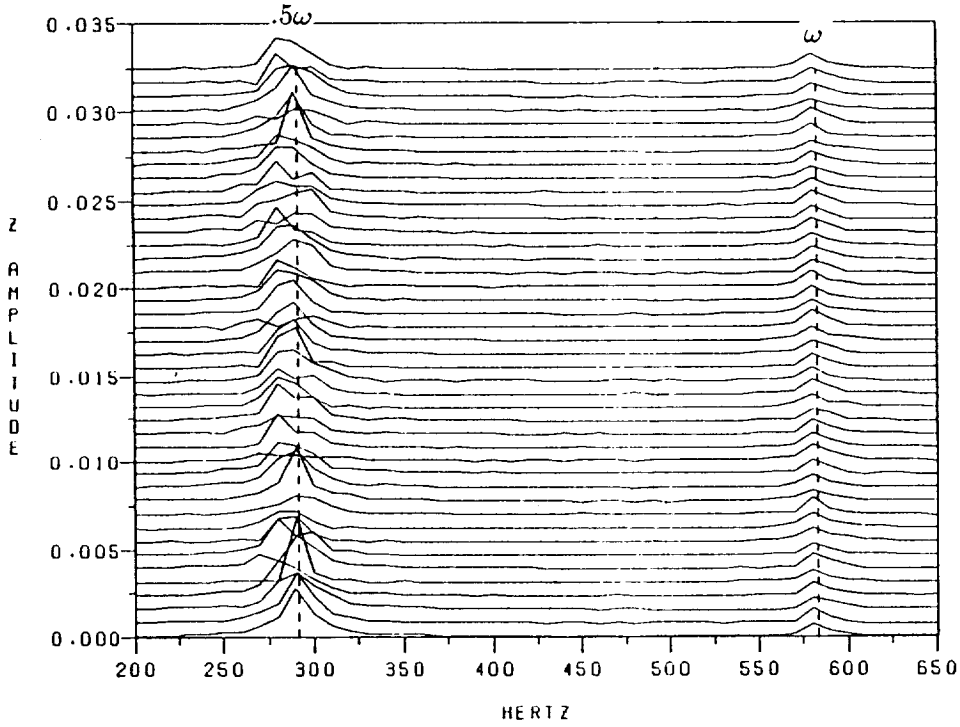

Figure 103. Cascade spectral plot corresponding to figure 101.

between subharmonic and limit cycle at a fixed speed. All of these behaviors have been observed in test data. The model results indicate that the specific ranges of occurrence, frequency ratios, amplitudes, and transition speeds are quite sensitive to many model parameters which are not known with much certainty. The nonuniqueness and sensitivity of the solutions can easily account for the behaviors observed in test data.

The results of the previous sections for the simplified model have been shown to extend to a more complex and realistic model of the HPFTP of the SSME. This was accomplished by examining engine test data, performing linear analysis of the model, and simulating the model for various conditions. The conclusions of this and the previous sections will be summarized in the next and final section.

VII. CONCLUSIONS

An extensive investigation has been conducted of the interaction between limit-cycle instability and subharmonic response in a rotordynamic system. The primary tool used in the study was a dimensionless, normalized model of a single mass rotor. Equilibria were determined for various excitations; linearizations and stability analyses were performed. A harmonic balance procedure was implemented to analyze subharmonic response potential. The model was simulated for the conditions which were analyzed and then for conditions which could not be treated analytical. Generalization of the results to a complex, realistic model were confirmed by examining the HPFTP of the SSME. This was accomplished using linear analysis and nonlinear simulation and by examining engine test data. The analyses and simulations were conducted using a general turbopump rotordynamic analysis package developed for this research. The conclusions which are drawn from this work can be separated into two groups: conclusions regarding the characteristics of the behavior, and conclusions regarding analysis and simulation methods. The conclusions are summarized below.

A. Characteristics of the Behavior

The most significant conclusion from this work is the determination that subharmonic response can entrain self-excited limit-cycle oscillations in rotordynamic systems. There is an important implication from this conclusion. The occurrence of a subsynchronous vibration at a frequency exactly equal to one half the shaft rotational speed is sometimes interpreted as evidence that the vibration is only subharmonic response and is benign in the sense of instability (subharmonic response may have adverse results due to overloading and fatigue which are unrelated to stability). These results indicate that this interpretation should not be made in any system in which self-excited vibration is possible. This covers virtually all turbomachinery which operates above a system critical speed characterized primarily by rotor motion.

Another conclusion drawn from this investigation is that the behavior under given conditions is nonunique. This is known for nonlinear systems in general; however, the specific possible solutions were determined and demonstrated. The most striking demonstration was the repeated transitions between limit-cycle instability and subharmonic entrainment in the presence of random noise excitation.

Finally, the ability of side-force and mass-unbalance excitations to suppress the limit-cycle behavior was demonstrated. The side-force excitation may, in addition, stabilize the system in the small for speeds beyond the global onset speed of instability.

B. Analysis and Simulation Methods

Nonlinear simulation studies typically consist of extensive studies involving numerous variations in model parameters and excitation forces. These studies begin with the best available estimates of these parameters and forces. One beneficial approach identified in this study is to simulate the model with no excitation (homogeneous case) except random noise. The results of this simulation provide a bound on the speed range in which limit cycle is possible with the excitations applied. In addition, the amplitude for this case bounds the limit-cycle amplitudes, and the frequency is near the frequency obtained under general excitation. These bounds provide a basis for determining whether extensive investigation of limit cycle is needed.

The important benefit of applying representative random noise excitation was clearly evident in this study. Without perturbation, many significant occurrences of limit cycle will be missed. It is also important for the perturbation to be realistic so that conclusions regarding comparisons with test data will not be erroneous.

It became evident during the conduct of this study that simulations must be conducted for representative time durations. The transient growth of a limit cycle or the transition between subharmonic entrainment and limit cycle might easily be missed with short durations.

C. Suggested Future Research

While many important conclusions were reached in this investigation, there remain many unanswered questions and opportunities for further work. As with any analytical and numerical investigation, it is important to obtain experimental verification. The engine test data provide some verification for this work; however, a laboratory experimental program with well-defined conditions and adequate instrumentation would provide much better verification of the fundamental assumptions and conclusions. With regard to the HPFTP model, improvements in the certainty of the model parameters would simplify investigations and correlation with test data. Even with better parameter data, however, absolute certainty in parameter values is impossible. Therefore, an extensive parametric study of the HPFTP conducted in light of the results of this research would provide important new insight into the characteristics of the actual machine. This should include a penetrating review of the extensive data base of engine tests.

With regard to test data interpretation, although the threat of divergent instability cannot be ruled out when subharmonic entrainment occurs, it may be possible to deduce a qualitative margin of stability from its occurrence. The subharmonic response analyses conducted for the simplified model indicated that the subharmonic ceased to exist above a threshold speed that was near, but below, twice the linear (zero deadband assumption) system resonance. The specific value depended on the system parameters. If subharmonic occurs in the response, the system must be operating below twice this resonance. If the destabilizing forces are known to be characterized by frequency ratios less than one half, then the global onset speed is known to be greater than twice this resonance. An investigation should be made into the potential for developing such an indicator of stability. Development of analytical tools for the complex model

which are analogous to the homogeneous equilibrium and subharmonic response harmonic balance methods applied to the simplified model would facilitate an investigation of this. These tools would provide characteristics and ranges of occurrence of the limit cycle and the subharmonic response without requiring costly simulations.

Finally, a word about the basic modeling assumptions made in this work. The assumption was made here that the rotor was supported by a combination of linear and nonlinear support elements. The nonlinear support elements were treated as piecewise linear elements in radial deflection with only two linear regions (i.e., one break point in the load deflection curve). One significant situation that cannot be treated using this assumption is that of rotor-stator rubbing. A model of rubbing interaction by itself is very similar to a bearing with deadband. The stiffness and the clearance are usually larger than for a bearing and an addition force is included; the tangential friction force. This interaction could be handled with the bilinear assumption with the appropriate additions for the friction. However, the difficulty arises when there are bearings with deadband and rub with a much larger clearance (or deadband). This combination requires multilinear approximations. In a realistic model such as the HPFTP, these effects would be distributed as well. The implications of this for the results and conclusions presented here would be to introduce an additional level of potential equilibria and limit cycle instability. For example, for speeds beyond the global onset speed of instability in the current model, the amplitude of the vibration would grow until the rotor began to rub on the housing. This would, then, create a new limit cycle at a higher amplitude with its own global stability limit. While general results can be inferred by scaling the results already obtained, the application of these results to a realistic model such as the HPFTP require careful scrutiny. The HPFTP model examined here did not include the rub model and it produced results similar to test data. However, this might also be accomplished using a very different "recipe" of parameters (representing a less stable condition) which includes the rub model and its amplitude limiting effects. In order to assure that erroneous conclusions are not drawn regarding the HPFTP, or any machinery that is known to rub, the parametric study discussed above should include models of rubbing interaction. This should be anchored to reality by closely examining the wear which occurs in the test hardware due to rubbing. The mechanical work done by the rub which occurs in the model should be compared with the observed wear. This requires the development of material wear models which relate the work to estimated wear. In addition, the power loss due to the rub should be compared to total turbopump power and its impact assessed using an overall engine system model. This would determine whether the power loss would be observed in the engine performance and, if so, the test data related to engine performance should be examined. These reality checks (wear and power loss) would provide the guidance needed to determine which assumptions and parameter "recipe" most accurately represent the actual machinery.

REFERENCES

1. Hayashi, C.: "Nonlinear Oscillations In Physical Systems." McGraw-Hill, New York, 1964.

2. Den Hartog, J.P.: "Mechanical Vibrations." McGraw-Hill, New York, 1956.

3. Timoshenko, S.: "Vibration Problems in Engineering." Van Nostrand, Princeton, 1955.

4. Tondl, A.: "Some Problems of Rotordynamics." Chapman & Hall, London, 1965.

5. Ehrich, F.F.: "Subharmonic Vibration of Rotors in Bearing Clearance." ASME Paper 66-MD-1, Design Engineering Conference and Show, Chicago, Illinois, May 9–12, 1966.

6. Childs, D.W.: "Fractional-Frequency Rotor Motion Due to Nonsymmetric Clearance Effects." ASME Paper 81-GT-145, International Gas Turbine Conference and Products Show, Houston, Texas, March 9–12, 1981.

7. Bently, D.E.: "Forced Subrotative Speed Dynamic Action of Rotating Machinery." ASME Paper 74-PET-16, Petroleum Mechanical Engineering Conference, Dallas, Texas, September 15–18, 1974.

8. Vance, J.M.: "Rotordynamics of Turbomachinery." John Wiley & Sons, New York, 1988.

9. Ehrich, F.F." "Identification and Avoidance of Instabilities and Self-Excited Vibrations in Rotating Machinery." ASME Paper 72-DE-21, Design Engineering Conference and Show, Chicago, Illinois, May 8–11, 1972.

10. Black, H.F.: "Effects of Hydraulic Forces in Annular Pressure Seals on the Vibrations of Centrifugal Pump Rotors." Journal of Mechanical Engineering Science, vol. II, No. 2, 1969.

11. Muszynska, A.: "Improvements in Lightly Loaded Rotor/Bearing and Rotor/Seal Models." Presented at 11th Biennial ASME Design Engineering Division Conference on Vibration and Noise, Boston, Massachusetts, September 27–30, 1987.

12. Gunter, E.J.: "Dynamic Stability of Rotor-Bearing Systems." NASA Report No. NAS3-6473, Washington, 1966.

13. Control Dynamics Company: "Effects of Bearing Deadbands on Bearing Loads and Rotor Stability." NASA MSFC Contract Final Report NAS8-35050, January 20, 1984.

14. Day, W.B.: "Nonlinear Rotordynamics Analysis." NASA MSFC Contract Final Report NAS8-35992, March 15, 1985.

15. Muszynska, A.: "Multi-Mode Whirl and Whip in Rotor/Bearing Systems." Presented at the Second International Symposium on Transport Phenomena, Dynamics, and Design of Rotating Machinery, Honolulu, Hawaii, April 46, 1988.

16. Noah, S.T.: "Hybrid Methods for Rotordynamic Analysis." NASA MSFC Contract Final Report NAS8-36182, December 1986.

17. Hawkins, L.A.: "A Parametric Study of HPFTP Subsynchronous Vibration and Stability." Rockwell International Internal Letter, IL 8128-0218, SSME 88-001272, November 15, 1988.

18. Murphy, B.T.: "Eigenvalues of Rotating Machinery." Texas A&M University, Ph.D. dissertation, May 1984.

19. von Pragenau, G.L.: Unpublished notes describing rotor rub model formulation, NASA MSFC, May 1981.

20. Ryan, S.G.: "Improved Rotordynamic Stability Analysis Through Matrix Condensation." University of Alabama in Huntsville, Master's thesis, May 1985.

APPENDIX A
TURBOPUMP MODEL DEVELOPMENT

Introduction

A general turbopump model has been developed in order to carry out the numerical studies in this investigation. This model has been implemented in a package of FORTRAN computer programs that is referred to as the Turbomachinery Rotordynamics Analysis Package. There are three basic components to the package: a linear eigenvalue analysis provides stability and critical speed information; a linear forced response analysis provides steady-state response to static and dynamic loads; and a nonlinear time domain simulation provides the total solution (transient and steady-state) and incorporates important non-linear effects such as bearing clearance (deadband) and seal rubbing. The simplified model developed in chapter II can be implemented using this package by specifying the input data appropriately. This appendix covers the development of the equations of motion for the model and the solution procedures employed.

Conceptual Model

The turbomachinery rotordynamics analysis package is based on a conceptual model of a symmetric flexible rotor supported in a nonsymmetric flexible housing by flexible connection elements. This is illustrated schematically in figure 104. The rotor is characterized by its free-free normal modes of vibration. Likewise, the housing is characterized by its free interface (no rotor) normal modes. One axial rigid body degree of freedom is included for the rotor. This is included to couple with the axial component that may be present for each housing mode. This coupling usually takes place across a hydrodynamic thrust balance piston. Damping is added to the rotor and housing by specifying a damping ratio for each mode. Gyroscopic effects are included as generalized forces on the rotor and they create coupling between the rotor modes. The normal modes of the rotor and housing must be predetermined using structural models or other available means.

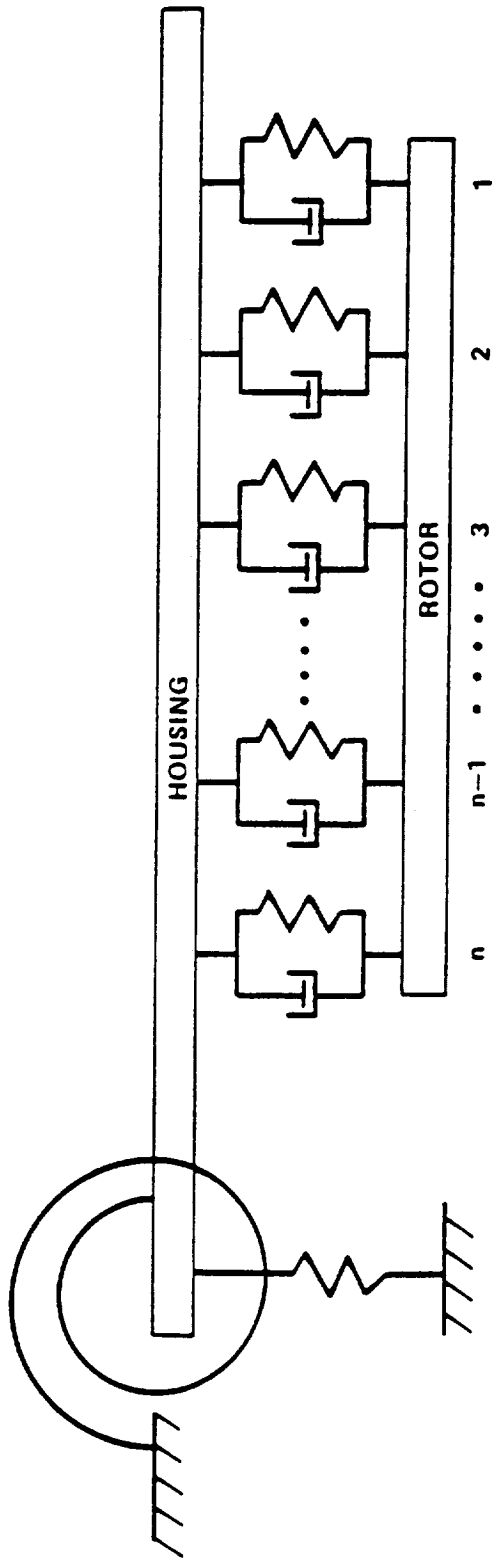

Figure 104. Turbopump conceptual model schematic.

The connection elements are typically rolling element bearings and fluidic seals and are characterized by stiffness, damping, and inertia matrices that can contain coupling terms between orthogonal lateral axes (cross-coupling). In general, the elements of these matrices are functions of engine power level. This is caused by such factors as centrifugal loading on ball bearings and different pressure drops across fluidic seals. Since turbopump rotational speed is also a function of power level the stiffness, damping and inertia coefficients can be expressed as functions of speed. These functions can be represented in a number of ways. In its present form the package can use two methods to define each function: a polynominal in speed, or a table lookup. The polynomial coefficients must be pre-determined by curve fitting tables of data for each function. The table lookup can use linear or Hermite cubic interpolation.

The equations of motion for the turbopump system are developed by deriving the equations of motion for the rotor and housing separately. The forces due to the relative motion across the connection elements are then added as generalized forces acting on the rotor and housing. The coordinate system used to define the model is an inertial, right handed system with the x axis along the undeflected rotor centerline. The y and z axes are in orthogonal, lateral directions. The orientation of the y and z axes is usually determined by the structural model of the housing since the rotor is symmetric. Care must be taken to ensure that the proper algebraic sign is used for the rotation speed based on the right hand rule for the coordinate system.

Rotor Equations of Motion

The rotor is treated as a collection of rigid bodies. The equations of motion for the rotor are derived using Lagrange's equations. The kinetic energy, potential function, dissipation function, and virtual work expression are first defined in terms of the physical coordinates of the individual rigid bodies. These functions are then expressed in terms of the rotor free-free normal modal coordinates. The equations of motion are obtained by substituting these functions into Lagrange's equations.

The coordinate system used to define the motion of an individual rigid body segment of the rotor is shown in figure 105. The x, y, z axes define the inertial reference frame. The $\bar{x}$, $\bar{y}$, $\bar{z}$ axes define the body fixed reference frame. The Euler angles θ_y, θ_z, and θ_x are defined in the figure.

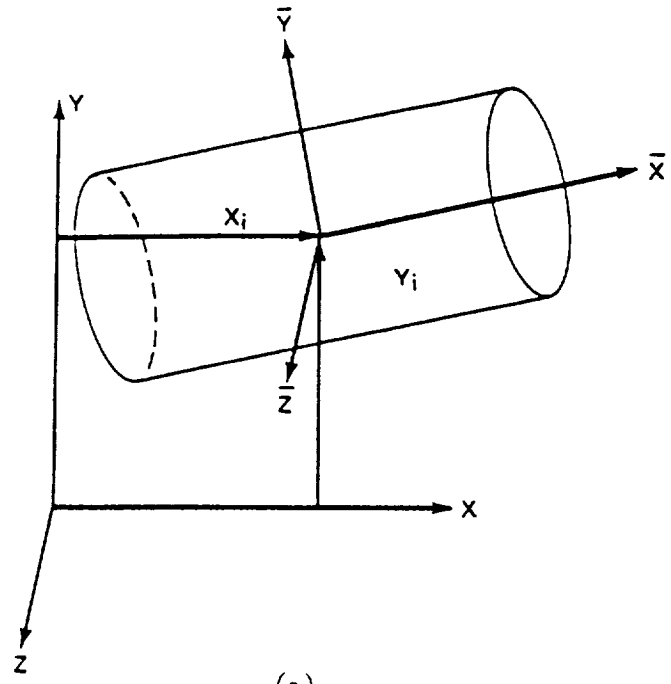

(a)

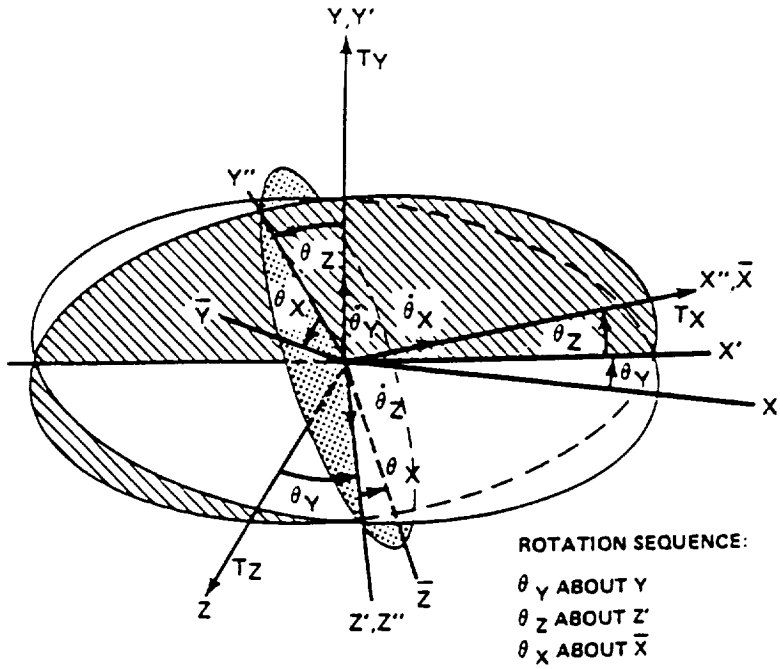

(b)

Figure 105. Coordinate system for *ith* rotor segment. (a) Translation coordinates. (b) Rotation coordinates (Euler angles.

The kinetic energy for the i^{th} rigid body can be written as the sum of the translational and rotational kinetic energies

$$T_i = \frac{1}{2}m_i(\dot{x}_i^2 + \dot{y}_i^2 + \dot{z}_i^2) + \frac{1}{2}\begin{Bmatrix} \omega_{\bar{x}_i} \\ \omega_{\bar{y}_i} \\ \omega_{\bar{z}_i} \end{Bmatrix}^T \begin{bmatrix} I_{xx_i} & I_{xy_i} & I_{xz_i} \\ I_{yx_i} & I_{yy_i} & I_{yz_i} \\ I_{zx_i} & I_{zy_i} & I_{zz_i} \end{bmatrix} \begin{Bmatrix} \omega_{\bar{x}_i} \\ \omega_{\bar{y}_i} \\ \omega_{\bar{z}_i} \end{Bmatrix} \tag{A1}$$

where $\omega_{\bar{x}}$, $\omega_{\bar{y}}$, and $\omega_{\bar{z}}$ are the body axis components of the angular velocity. Since the $\bar{x}$ axis is taken to be the axis of symmetry and each body is considered to be a body of revolution, the product of inertia terms will be zero and equation (A1) can be written as

$$T_i = \frac{1}{2}m_i(\dot{x}_i^2 + \dot{y}_i^2 + \dot{z}_i^2) + \frac{1}{2}I_{a_i}\omega_{\bar{x}_i}^2 + \frac{1}{2}I_{t_i}(\omega_{\bar{y}_i}^2 + \omega_{\bar{z}_i}^2) \tag{A2}$$

The angular velocity components $\omega_{\bar{x}_i}$, $\omega_{\bar{y}_i}$, and $\omega_{\bar{z}_i}$ can be written in terms of the Euler angle rates as follows

$$\begin{aligned} \omega_{\bar{x}_i} &= \dot{\theta}_{x_i} + \dot{\theta}_{y_i}\sin(\theta_{z_i}) \\ \omega_{\bar{y}_i} &= \dot{\theta}_{y_i}\cos(\theta_{z_i})\cos(\theta_{x_i}) + \dot{\theta}_{z_i}\sin(\theta_{x_i}) \\ \omega_{\bar{z}_i} &= -\dot{\theta}_{y_i}\cos(\theta_{z_i})\sin(\theta_{x_i}) + \dot{\theta}_{z_i}\cos(\theta_{x_i}) \end{aligned} \tag{A3}$$

Substituting equation (A3) into equation (A2) yields

$$T_i = \frac{1}{2}m_i(\dot{x}_i^2 + \dot{y}_i^2 + \dot{z}_i^2) + \frac{1}{2}I_{a_i}\left(\dot{\theta}_{x_i} + \dot{\theta}_{y_i}\sin(\theta_{z_i})\right)^2 + \frac{1}{2}I_{t_i}\left(\dot{\theta}_{y_i}^2\cos^2(\theta_{z_i}) + \dot{\theta}_{z_i}^2\right) \tag{A4}$$

The rotor will be constrained by the bearings to have small motion, therefore, the angles θ_{y_i} and θ_{z_i} can be considered to be small quantities. Substituting Taylor series expansions for $\sin(\theta_{z_i})$ and $\cos(\theta_{z_i})$ into equation (A4) yields

$$\begin{aligned} T_i = &\frac{1}{2}m_i(\dot{x}_i^2 + \dot{y}_i^2 + \dot{z}_i^2) + \frac{1}{2}I_{a_i}\dot{\theta}_{x_i}^2 + I_{a_i}\dot{\theta}_{x_i}\dot{\theta}_{y_i}\left(\theta_{z_i} - \frac{\theta_{z_i}^3}{3} + \cdots\right) \\ &+ \frac{1}{2}I_{a_I}\dot{\theta}_{y_i}^2\left(\theta_{z_i} - \frac{\theta_{z_i}^3}{3} + \cdots\right)^2 + \frac{1}{2}I_{t_i}\dot{\theta}_{z_i}^2 + \frac{1}{2}I_{t_i}\dot{\theta}_{y_i}^2\left(1 - \frac{\theta_{z_i}^2}{2} + \cdots\right)^2 \end{aligned} \tag{A5}$$

Since the kinetic energy expression will be differentiated once in Lagrange's equations, terms of second order in small quantities must be retained here. Neglecting terms of higher order yields

$$T_i = \frac{1}{2}m_i(\dot{x}_i^2 + \dot{y}_i^2 + \dot{z}_i^2) + \frac{1}{2}I_{a_i}\dot{\theta}_{x_i}^2 + I_{a_i}\dot{\theta}_{x_i}\dot{\theta}_{y_i}\theta_{z_i} + \frac{1}{2}I_{t_i}(\dot{\theta}_{y_i}^2 + \dot{\theta}_{z_i}^2) \tag{A6}$$

The total kinetic energy of the rotor is the sum of the individual kinetic energies,

$$T = \sum_i T_i \tag{A7}$$

It is assumed here that the rotor is axially and torsionally rigid so that equation (A7) becomes

$$\begin{aligned} T = \frac{1}{2}\left(\sum_i m_i\right)\dot{x}^2 + \frac{1}{2}\sum_i m_i(\dot{y}_i^2 + \dot{z}_i^2) + \frac{1}{2}\left(\sum_i I_{a_i}\right)\Omega^2 \\ + \frac{1}{2}\sum_i I_{t_i}(\dot{\theta}_{y_i}^2 + \dot{\theta}_{z_i}^2) + \Omega\left(\sum_i I_{a_i}\dot{\theta}_{y_i}\theta_{z_i}\right) \end{aligned} \tag{A8}$$

where Ω replaces $\dot{\theta}_{x_i}$. Equation (A8) can be written in matrix notation as

$$\begin{aligned} T = \frac{1}{2}M\dot{x}^2 + \frac{1}{2}\Omega^{\mathrm{T}}\mathbf{I}_{\mathbf{a}}\Omega + \frac{1}{2}\dot{\mathbf{y}}^{\mathrm{T}}\mathbf{m}\dot{\mathbf{y}} + \frac{1}{2}\dot{\mathbf{z}}^{\mathrm{T}}\mathbf{m}\dot{\mathbf{z}} \\ + \frac{1}{2}\dot{\Theta}_{\mathbf{y}}^{\mathrm{T}}\mathbf{I}_{\mathbf{t}}\dot{\Theta}_{\mathbf{y}} + \frac{1}{2}\dot{\Theta}_{\mathbf{z}}^{\mathrm{T}}\mathbf{I}_{\mathbf{t}}\dot{\Theta}_{\mathbf{z}} + \Omega\dot{\Theta}_{\mathbf{y}}^{\mathrm{T}}\mathbf{I}_{\mathbf{a}}\Theta_{\mathbf{z}} \end{aligned} \tag{A9}$$

where

$$M = \sum_i m_i \tag{A10}$$

$$\mathbf{y} = \begin{Bmatrix} y_1 \\ y_2 \\ \vdots \\ y_n \end{Bmatrix} \tag{A11}$$

and similarly for $\mathbf{z}$, $\Theta_\mathbf{y}$, and $\Theta_\mathbf{z}$,

$$\Omega = \begin{Bmatrix} \Omega \\ \Omega \\ \vdots \\ \Omega \end{Bmatrix} \tag{A12}$$

$$\mathbf{m} = \begin{bmatrix} m_1 & 0 & \dots & 0 \\ 0 & m_2 & \dots & 0 \\ \vdots & \vdots & \ddots & \vdots \\ 0 & 0 & \dots & m_n \end{bmatrix} \tag{A13}$$

and similarly for $\mathbf{I_t}$ and $\mathbf{I_a}$.

The potential and dissipation functions will be defined in terms of the rotor physical coordinates. Since the rotor is axially and torsionally rigid, only the $\mathbf{y}$, $\mathbf{z}$, $\Theta_\mathbf{y}$, and $\Theta_\mathbf{z}$ coordinates will contribute to these functions. The potential function is written

$$V = \frac{1}{2}\mathbf{w}^\mathbf{T}\kappa\,\mathbf{w} = \frac{1}{2}\begin{Bmatrix} \mathbf{y} \\ \Theta_\mathbf{z} \\ \mathbf{z} \\ \Theta_\mathbf{y} \end{Bmatrix}^T \begin{bmatrix} \kappa_{yy} & \kappa_{y\theta_z} & 0 & 0 \\ \kappa_{\theta_z y} & \kappa_{\theta_z\theta_z} & 0 & 0 \\ 0 & 0 & \kappa_{zz} & \kappa_{z\theta_y} \\ 0 & 0 & \kappa_{\theta_y z} & \kappa_{\theta_y\theta_y} \end{bmatrix} \begin{Bmatrix} \mathbf{y} \\ \Theta_\mathbf{z} \\ \mathbf{z} \\ \Theta_\mathbf{y} \end{Bmatrix} \tag{A14}$$

where κ represents the rotor stiffness matrix; the upper left and lower right quadrants are identical (symmetric rotor).

The dissipation function can be more easily treated using coordinates that rotate with the rotor at speed Ω. The following transformation defines the new coordinates

$$\begin{Bmatrix} \mathbf{r}_\eta \\ \mathbf{r}_\zeta \end{Bmatrix} = \begin{bmatrix} \cos(\Omega t) & \sin(\Omega t) \\ -\sin(\Omega t) & \cos(\Omega t) \end{bmatrix} \begin{Bmatrix} \mathbf{w_y} \\ \mathbf{w_z} \end{Bmatrix} \tag{A15}$$

where

$$\mathbf{w_y} = \begin{Bmatrix} \mathbf{y} \\ \Theta_\mathbf{z} \end{Bmatrix} \tag{A16}$$

$$\mathbf{w_z} = \begin{Bmatrix} \mathbf{z} \\ \Theta_\mathbf{y} \end{Bmatrix} \tag{A17}$$

$$\mathbf{r}_\eta = \begin{Bmatrix} \eta \\ \Theta_\zeta \end{Bmatrix} \tag{A18}$$

$$\mathbf{r}_\zeta = \begin{Bmatrix} \zeta \\ \Theta_\eta \end{Bmatrix} \tag{A19}$$

In terms of the rotating coordinates $\mathbf{r}$, the dissipation function is written as

$$G = \frac{1}{2}\dot{\mathbf{r}}^{\mathbf{T}}\mathbf{B}\,\dot{\mathbf{r}} \tag{A20}$$

Differentiating equation (A15) with respect to time gives

$$\dot{\mathbf{r}} = \begin{bmatrix} \cos(\Omega t) & \sin(\Omega t) \\ -\sin(\Omega t) & \cos(\Omega t) \end{bmatrix} \begin{Bmatrix} \dot{\mathbf{w}}_\mathbf{y} + \Omega \mathbf{w}_\mathbf{z} \\ \dot{\mathbf{w}}_\mathbf{z} - \Omega \mathbf{w}_\mathbf{y} \end{Bmatrix} \tag{A21}$$

Substituting equation (A21) into equation (A20) yields

$$G = \frac{1}{2} \begin{Bmatrix} \dot{\mathbf{w}}_\mathbf{y} + \Omega \mathbf{w}_\mathbf{z} \\ \dot{\mathbf{w}}_\mathbf{z} - \Omega \mathbf{w}_\mathbf{y} \end{Bmatrix}^T \begin{bmatrix} \cos(\Omega t) & -\sin(\Omega t) \\ \sin(\Omega t) & \cos(\Omega t) \end{bmatrix} \begin{bmatrix} \mathbf{B}_\eta & 0 \\ 0 & \mathbf{B}_\zeta \end{bmatrix}$$
$$\begin{bmatrix} \cos(\Omega t) & \sin(\Omega t) \\ -\sin(\Omega t) & \cos(\Omega t) \end{bmatrix} \begin{Bmatrix} \dot{\mathbf{w}}_\mathbf{y} + \Omega \mathbf{w}_\mathbf{z} \\ \dot{\mathbf{w}}_\mathbf{z} - \Omega \mathbf{w}_\mathbf{y} \end{Bmatrix} \tag{A22}$$

where $\mathbf{B}_\eta$ and $\mathbf{B}_\zeta$ are identical and represent the damping matrix for the nonspinning rotor. Equation (A22) can be rewritten as

$$G = \frac{1}{2} \begin{Bmatrix} \dot{\mathbf{y}} + \Omega \mathbf{z} \\ \dot{\Theta}_\mathbf{z} + \Omega \Theta_\mathbf{y} \\ \dot{\mathbf{z}} - \Omega \mathbf{y} \\ \dot{\Theta}_\mathbf{y} - \Omega \Theta_\mathbf{z} \end{Bmatrix}^T \begin{bmatrix} \mathbf{B}_{\eta\eta} & \mathbf{B}_{\eta\theta_\zeta} & 0 & 0 \\ \mathbf{B}_{\theta_\zeta\eta} & \mathbf{B}_{\theta_\zeta\theta_\zeta} & 0 & 0 \\ 0 & 0 & \mathbf{B}_{\zeta\zeta} & \mathbf{B}_{\zeta\theta_\eta} \\ 0 & 0 & \mathbf{B}_{\theta_\eta\zeta} & \mathbf{B}_{\theta_\eta\theta_\eta} \end{bmatrix} \begin{Bmatrix} \dot{\mathbf{y}} + \Omega \mathbf{z} \\ \dot{\Theta}_\mathbf{z} + \Omega \Theta_\mathbf{y} \\ \dot{\mathbf{z}} - \Omega \mathbf{y} \\ \dot{\Theta}_\mathbf{y} - \Omega \Theta_\mathbf{z} \end{Bmatrix} \tag{A23}$$

The generalized forces acting on the rotor are treated through the virtual work expression. The virtual work is the product of a virtual displacement of a coordinate and the component of a generalized force acting on the coordinate. The virtual work can be written as

$$\delta W = \sum_i \left[(F_{x_i}\hat{e}_{x_i} + F_{y_i}\hat{e}_{y_i} + F_{z_i}\hat{e}_{z_i}) \cdot (\delta x_i \hat{e}_{x_i} + \delta y_i \hat{e}_{y_i} + \delta z_i \hat{e}_{z_i}) \right.$$
$$\left. + (T_{x_i}\hat{e}_{\bar{x}_i} + T_{y_i}\hat{e}_{y_i} + T_{z_i}\hat{e}_{z_i}) \cdot (\delta\theta_{x_i}\hat{e}_{\bar{x}_i} + \delta\theta_{y_i}\hat{e}_{y_i} + \delta\theta_{z_i}\hat{e}_{z_i'}) \right] \tag{A24}$$

where $\hat{e}_q$ is a unit vector along the q axis. Equation (A24) can be simplified to

$$\delta W = \sum_i \left[F_{x_i}\delta x_i + F_{y_i}\delta y_i + F_{z_i}\delta z_i + T_{x_i}\delta\theta_{x_i} + T_{y_i}\delta\theta_{y_i} + T_{x_i}\delta\theta_{y_i}(\hat{e}_{\bar{x}_i}\cdot\hat{e}_{y_i}) \right.$$
$$\left. + T_{y_i}\delta\theta_{x_i}(\hat{e}_{y_i}\cdot\hat{e}_{\bar{x}_i}) + T_{z_i}\delta\theta_{x_i}(\hat{e}_{z_i}\cdot\hat{e}_{\bar{x}_i}) + T_{z_i}\delta\theta_{z_i}(\hat{e}_{z_i}\cdot\hat{e}_{z_i'}) \right] \quad \text{(A25)}$$

From figure 105, the unit vector dot products are determined to be

$$\hat{e}_{\bar{x}_i}\cdot\hat{e}_{y_i} = \hat{e}_{y_i}\cdot\hat{e}_{\bar{x}_i} = \sin(\theta_{z_i}) \approx \theta_{z_i} \quad \text{(A26)}$$

$$\hat{e}_{z_i}\cdot\hat{e}_{\bar{x}_i} = -\sin(\theta_{y_i}) \approx -\theta_{y_i} \quad \text{(A27)}$$

$$\hat{e}_{z_i}\cdot\hat{e}_{z_i'} = \cos(\theta_{y_i}) \approx 1 \quad \text{(A28)}$$

for small angles. Substituting equations (A26) - (A28) into (A25) and simplifying yields

$$\delta W = \sum_i \left[F_{x_i}\delta x_i + F_{y_i}\delta y_i + F_{z_i}\delta z_i + (T_{x_i} - T_{z_i}\theta_{y_i} + T_{y_i}\theta_{z_i})\delta\theta_{x_i} \right.$$
$$\left. + (T_{x_i}\theta_{z_i} + T_{y_i})\delta\theta_{y_i} + T_{z_i}\delta\theta_{z_i} \right] \quad \text{(A29)}$$

The torques T_{y_i} and T_{z_i} will be linear functions of the displacements θ_{y_i} and θ_{z_i}. Since these angles are considered to be small quantities, the products of the torques T_{y_i} and T_{z_i} and these angles become proportional to terms of second order in small quantities. Neglecting terms of second order and higher in small quantities simplifies equation (A29) to

$$\delta W = \sum_i \left[F_{x_i}\delta x_i + F_{y_i}\delta y_i + F_{z_i}\delta z_i + T_{x_i}\delta\theta_{x_i} + T_{z_i}\delta\theta_{z_i} + (T_{y_i} + T_{x_i}\theta_{z_i})\delta\theta_{y_i} \right] \quad \text{(A30)}$$

The kinetic energy, potential function, dissipation function, and virtual work have all been defined in terms of the rotor physical coordinates $\mathbf{y}$, $\mathbf{z}$, $\mathbf{\Theta_y}$, and $\mathbf{\Theta_z}$. These functions can be expressed in terms of the rotor free-free modal coordinates using the following transformations

$$\mathbf{y} = \Phi \mathbf{q_y} \tag{A31}$$

$$\Theta_\mathbf{z} = \Psi \mathbf{q_y} \tag{A32}$$

$$\mathbf{z} = \Phi \mathbf{q_z} \tag{A33}$$

$$\Theta_\mathbf{y} = -\Psi \mathbf{q_z} \tag{A34}$$

where Φ is the rotor free-free modal displacement matrix, Ψ is the rotor free-free modal rotation matrix, $\mathbf{q_y}$ is the rotor free-free modal coordinate vector in the $y-x$ plane, and $\mathbf{q_z}$ is the rotor free-free modal coordinate vector in the $z-x$ plane. It can be noted that the rigid body modes must be included in Φ and Ψ. Substituting equations (A31)-(A34) into equation (A9) yields the kinetic energy in terms of rotor modal coordinates:

$$\begin{aligned} T = \frac{1}{2}M\dot{x}^2 + \frac{1}{2}\Omega^\mathbf{T}\mathbf{I_a}\Omega + \frac{1}{2}\dot{\mathbf{q}}_\mathbf{y}^\mathbf{T}\Phi^\mathbf{T}\mathbf{m}\Phi\dot{\mathbf{q}}_\mathbf{y} + \frac{1}{2}\dot{\mathbf{q}}_\mathbf{z}^\mathbf{T}\Phi^\mathbf{T}\mathbf{m}\Phi\dot{\mathbf{q}}_\mathbf{z} \\ + \frac{1}{2}\dot{\mathbf{q}}_\mathbf{y}^\mathbf{T}\Psi^\mathbf{T}\mathbf{I_t}\Psi\dot{\mathbf{q}}_\mathbf{y} + \frac{1}{2}\dot{\mathbf{q}}_\mathbf{z}^\mathbf{T}\Psi^\mathbf{T}\mathbf{I_t}\Psi\dot{\mathbf{q}}_\mathbf{z} - \Omega\dot{\mathbf{q}}_\mathbf{z}^\mathbf{T}\Psi^\mathbf{T}\mathbf{I_a}\Psi\mathbf{q_y} \end{aligned} \tag{A35}$$

The rotor free-free normal modal vectors are orthogonal and properly scaled so that

$$\Phi^\mathbf{T}\mathbf{m}\Phi + \Psi^\mathbf{T}\mathbf{I_t}\Psi = \mathbf{I} \tag{A36}$$

Therefore, equation (A35) reduces to

$$T = \frac{1}{2}M\dot{x}^2 + \frac{1}{2}\Omega^\mathbf{T}\mathbf{I_a}\Omega + \frac{1}{2}\dot{\mathbf{q}}_\mathbf{y}^\mathbf{T}\dot{\mathbf{q}}_\mathbf{y} + \frac{1}{2}\dot{\mathbf{q}}_\mathbf{z}^\mathbf{T}\dot{\mathbf{q}}_\mathbf{z} - \Omega\dot{\mathbf{q}}_\mathbf{z}^\mathbf{T}\Gamma\mathbf{q_y} \tag{A37}$$

where

$$\Gamma = \Psi^\mathbf{T}\mathbf{I_a}\Psi \tag{A38}$$

Substituting equations (A31)-(A34) into equation (A14) yields the potential function in terms of rotor modal coordinates:

$$V = \frac{1}{2}\begin{Bmatrix} \Phi \mathbf{q_y} \\ \Psi \mathbf{q_y} \\ \Phi \mathbf{q_z} \\ -\Psi \mathbf{q_z} \end{Bmatrix}^T \begin{bmatrix} \kappa_{yy} & \kappa_{y\theta_z} & 0 & 0 \\ \kappa_{\theta_z y} & \kappa_{\theta_z \theta_z} & 0 & 0 \\ 0 & 0 & \kappa_{zz} & \kappa_{z\theta_y} \\ 0 & 0 & \kappa_{\theta_y z} & \kappa_{\theta_y \theta_y} \end{bmatrix} \begin{Bmatrix} \Phi \mathbf{q_y} \\ \Psi \mathbf{q_y} \\ \Phi \mathbf{q_z} \\ -\Psi \mathbf{q_z} \end{Bmatrix} \tag{A39}$$

Due to the orthogonality and proper scaling

$$[\,\Phi^{\mathbf{T}} \quad \Psi^{\mathbf{T}}\,] \begin{bmatrix} \kappa_{yy} & \kappa_{y\theta_z} \\ \kappa_{\theta_z y} & \kappa_{\theta_z \theta_z} \end{bmatrix} \begin{bmatrix} \Phi \\ \Psi \end{bmatrix} = \omega_{\mathrm{n}}^2 \tag{A40}$$

and

$$[\,\Phi^{\mathbf{T}} \quad -\Psi^{\mathbf{T}}\,] \begin{bmatrix} \kappa_{zz} & \kappa_{z\theta_y} \\ \kappa_{\theta_y z} & \kappa_{\theta_y \theta_y} \end{bmatrix} \begin{bmatrix} \Phi \\ -\Psi \end{bmatrix} = \omega_{\mathrm{n}}^2 \tag{A41}$$

which gives

$$V = \frac{1}{2}\begin{Bmatrix} \mathbf{q_y} \\ \mathbf{q_z} \end{Bmatrix}^T \begin{bmatrix} \omega_{\mathrm{n}}^2 & 0 \\ 0 & \omega_{\mathrm{n}}^2 \end{bmatrix} \begin{Bmatrix} \mathbf{q_y} \\ \mathbf{q_z} \end{Bmatrix} \tag{A42}$$

where

$$\omega_{\mathrm{n}}^2 = \begin{bmatrix} \omega_{n_1}^2 & 0 & \cdots & 0 \\ 0 & \omega_{n_2}^2 & \cdots & 0 \\ \vdots & \vdots & \ddots & \vdots \\ 0 & 0 & \cdots & \omega_{n_k}^2 \end{bmatrix} \tag{A43}$$

Substituting equations (A31)-(A34) into equation (A23) yields the dissipation function in terms of rotor modal coordinates:

$$G = \frac{1}{2}\begin{Bmatrix} \Phi(\dot{\mathbf{q}}_\mathbf{y} + \Omega \mathbf{q_z}) \\ \Psi(\dot{\mathbf{q}}_\mathbf{y} - \Omega \mathbf{q_z}) \\ \Phi(\dot{\mathbf{q}}_\mathbf{z} - \Omega \mathbf{q_y}) \\ -\Psi(\dot{\mathbf{q}}_\mathbf{z} + \Omega \mathbf{q_y}) \end{Bmatrix}^T \begin{bmatrix} \mathbf{B}_{\eta\eta} & \mathbf{B}_{\eta\theta_\zeta} & 0 & 0 \\ \mathbf{B}_{\theta_\zeta \eta} & \mathbf{B}_{\theta_\zeta \theta_\zeta} & 0 & 0 \\ 0 & 0 & \mathbf{B}_{\zeta\zeta} & \mathbf{B}_{\zeta\theta_\eta} \\ 0 & 0 & \mathbf{B}_{\theta_\eta \zeta} & \mathbf{B}_{\theta_\eta \theta_\eta} \end{bmatrix} \begin{Bmatrix} \Phi(\dot{\mathbf{q}}_\mathbf{y} + \Omega \mathbf{q_z}) \\ \Psi(\dot{\mathbf{q}}_\mathbf{y} - \Omega \mathbf{q_z}) \\ \Phi(\dot{\mathbf{q}}_\mathbf{z} - \Omega \mathbf{q_y}) \\ -\Psi(\dot{\mathbf{q}}_\mathbf{z} + \Omega \mathbf{q_y}) \end{Bmatrix} \tag{A44}$$

If the rotor damping is assumed to be proportional damping, the damping matrix can be diagonalized by the modal matrices just as the stiffness matrix was diagonalized. This allows equation (A44) to be written as

$$G = \frac{1}{2} \left\{ \begin{matrix} \dot{\mathbf{q}}_\mathbf{y} + \Omega \mathbf{q}_\mathbf{z} \\ \dot{\mathbf{q}}_\mathbf{z} - \Omega \mathbf{q}_\mathbf{y} \end{matrix} \right\}^T \begin{bmatrix} 2\zeta\omega_\mathbf{n} & 0 \\ 0 & 2\zeta\omega_\mathbf{n} \end{bmatrix} \left\{ \begin{matrix} \dot{\mathbf{q}}_\mathbf{y} + \Omega \mathbf{q}_\mathbf{z} \\ \dot{\mathbf{q}}_\mathbf{z} - \Omega \mathbf{q}_\mathbf{y} \end{matrix} \right\} \tag{A45}$$

where

$$2\zeta\omega_\mathbf{n} = \begin{bmatrix} 2\zeta_1\omega_{n_1} & 0 & \dots & 0 \\ 0 & 2\zeta_2\omega_{n_2} & \dots & 0 \\ \vdots & \vdots & \ddots & \vdots \\ 0 & 0 & \dots & 2\zeta_k\omega_{n_k} \end{bmatrix} \tag{A46}$$

Substituting equations (A31)-(A34) into equation (A30) yields the virtual work expression in terms of rotor modal coordinates:

$$\delta W = F_x \delta x + \delta\Theta_\mathbf{x}^\mathbf{T}\mathbf{T}_\mathbf{x} + \delta\mathbf{q}_\mathbf{y}^\mathbf{T}(\Phi^\mathbf{T}\mathbf{F}_\mathbf{y} + \Psi^\mathbf{T}\mathbf{T}_\mathbf{z}) + \delta\mathbf{q}_\mathbf{z}^\mathbf{T}\left[\Phi^\mathbf{T}\mathbf{F}_\mathbf{z} - \Psi^\mathbf{T}(\mathbf{T}_\mathbf{y} + \mathbf{T}_\mathbf{x}^*\Psi\mathbf{q}_\mathbf{y})\right] \tag{A47}$$

where

$$\mathbf{T}_\mathbf{x}^* = \begin{bmatrix} T_{x_1} & 0 & \dots & 0 \\ 0 & T_{x_2} & \dots & 0 \\ \vdots & \vdots & \ddots & \vdots \\ 0 & 0 & \dots & T_{x_k} \end{bmatrix} \tag{A48}$$

is the diagonal matrix formed from the vector $\mathbf{T}_\mathbf{x}$.

The kinetic energy, potential function, dissipation function, and virtual work expression are now in the form desired for use with Lagrange's equations. Lagrange's equations can be written in the following form

$$\frac{d}{dt}\left(\frac{\partial T}{\partial \dot{q}_i}\right) - \frac{\partial T}{\partial q_i} + \frac{\partial V}{\partial q_i} + \frac{\partial G}{\partial \dot{q}_i} = Q_i \tag{A49}$$

where Q_i is the generalized force acting at coordinate q_i and is implicitly defined by

$$\delta W = \sum_i Q_i \delta q_i \tag{A50}$$

Substituting equations (A37), (A42), and (A45) into equation (A49) and comparing equation (A47) with equation (A50) yields the following set of equations of motion for the rotor:

$$M\ddot{x} = F_x \tag{A51}$$

$$\mathbf{I_a\dot{\Omega} - \ddot{q}_z^T\Gamma q_y - \dot{q}_z^T\Gamma\dot{q}_y = T_x} \tag{A52}$$

$$\mathbf{\ddot{q}_y + \Omega\Gamma\dot{q}_z + \omega_n^2 q_y + 2\zeta\omega_n\dot{q}_y + \Omega 2\zeta\omega_n q_z = \Phi^T F_y + \Psi^T T_z} \tag{A53}$$

$$\mathbf{\ddot{q}_z - \Omega\Gamma\dot{q}_y + \omega_n^2 q_z + 2\zeta\omega_n\dot{q}_z - \Omega 2\zeta\omega_n q_y - \dot{\Omega}\Gamma q_y = \Phi^T F_z - \Psi^T T_y - \Psi^T T_x^* \Psi q_y} \tag{A54}$$

Neglecting second order terms for small angles, it can be seen from equation (A52) that

$$\mathbf{T_x = I_a\dot{\Omega}} \tag{A55}$$

However, since the rotor is torsionally rigid, all elements of the vector $\mathbf{\Omega}$ are equal, and therefore

$$\mathbf{T_x^* = \dot{\Omega} I_a} \tag{A56}$$

Substituting equation (A56) into equation (A54) yields

$$\mathbf{\ddot{q}_z - \Omega\Gamma\dot{q}_y + \omega_n^2 q_z + 2\zeta\omega_n\dot{q}_z - \Omega 2\zeta\omega_n q_y = \Phi^T F_z - \Psi^T T_y} \tag{A57}$$

Rewriting the complete set

$$\mathbf{I_a\dot{\Omega} = T_x} \tag{A58}$$

$$\ddot{x} = \frac{F_x}{M} \tag{A59}$$

$$\mathbf{\ddot{q}_y + 2\zeta\omega_n\dot{q}_y + \Omega\Gamma\dot{q}_z + \omega_n^2 q_y + \Omega 2\zeta\omega_n q_z = \Phi^T F_y + \Psi^T T_z} \tag{A60}$$

$$\ddot{\mathbf{q}}_z + 2\zeta\omega_n\dot{\mathbf{q}}_z - \Omega\Gamma\dot{\mathbf{q}}_y + \omega_n^2\mathbf{q}_z - \Omega 2\zeta\omega_n\mathbf{q}_y = \Phi^T\mathbf{F}_z - \Psi^T\mathbf{T}_y \qquad \text{(A61)}$$

Equations (A58)-(A61) are the rotor equations of motion. Equation (A58) defines the torsional motion. The rotor speed Ω will be a specified function of time, therefore, equation (A58) will not be needed. The forces and torques F_x, $\mathbf{F}_y$, $\mathbf{F}_z$, $\mathbf{T}_y$, and $\mathbf{T}_z$ contain the linear and nonlinear forces due to the elements connecting the rotor to the housing as well as externally applied forces.

Housing Equations of Motion

The equations of motion for the housing are derived in the same manner as for the rotor with the following exceptions. The housing doesn't rotate so that all terms involving Ω are absent from the housing equations. Also, the modal matrix used to diagonalize the housing equations is derived from fixed-free boundary conditions. However, the housing-rotor interface coordinates are free. The housing is not symmetric and its modes are not entirely planar so the modal coordinates can not be separated into y and z coordinates as in the case with the rotor. With these exceptions noted, the housing equations of motion can be written directly

$$\ddot{\mathbf{p}} + 2\zeta_h\omega_{n_h}\dot{\mathbf{p}} + \omega_{n_h}^2\mathbf{p} = \Phi_{h_x}^T F_{h_x} + \Phi_{h_y}^T\mathbf{F}_{h_y} + \Phi_{h_z}^T\mathbf{F}_{h_z} + \Psi_{h_y}^T\mathbf{T}_{h_y} + \Psi_{h_z}^T\mathbf{T}_{h_z} \qquad \text{(A62)}$$

Combined System Equations of Motion

With the rotor and housing equations determined, the system equations of motion can be written,

$$\begin{Bmatrix} \ddot{x} \\ \ddot{\mathbf{q}}_y \\ \ddot{\mathbf{q}}_z \\ \ddot{\mathbf{p}} \end{Bmatrix} + \begin{bmatrix} 0 & 0 & 0 & 0 \\ 0 & 2\zeta_r\omega_{n_r} & \Omega\Gamma & 0 \\ 0 & -\Omega\Gamma & 2\zeta_r\omega_{n_r} & 0 \\ 0 & 0 & 0 & 2\zeta_h\omega_{n_h} \end{bmatrix} \begin{Bmatrix} \dot{x} \\ \dot{\mathbf{q}}_y \\ \dot{\mathbf{q}}_z \\ \dot{\mathbf{p}} \end{Bmatrix} + \begin{bmatrix} 0 & 0 & 0 & 0 \\ 0 & \omega_{n_r}^2 & \Omega 2\zeta_r\omega_{n_r} & 0 \\ 0 & -\Omega 2\zeta_r\omega_{n_r} & \omega_{n_r}^2 & 0 \\ 0 & 0 & 0 & \omega_{n_h}^2 \end{bmatrix} \begin{Bmatrix} x \\ \mathbf{q}_y \\ \mathbf{q}_z \\ \mathbf{p} \end{Bmatrix}$$

$$= \begin{Bmatrix} \frac{F_x}{M} \\ \Phi^T\mathbf{F}_y + \Psi^T\mathbf{T}_z \\ \Phi^T\mathbf{F}_z - \Psi^T\mathbf{T}_y \\ \Phi_{h_x}^T F_{h_x} + \Phi_{h_y}^T\mathbf{F}_{h_y} + \Phi_{h_z}^T\mathbf{F}_{h_z} + \Psi_{h_y}^T\mathbf{T}_{h_y} + \Psi_{h_z}^T\mathbf{T}_{h_z} \end{Bmatrix} \qquad \text{(A63)}$$

At this point the rotor and housing appear to be uncoupled. However, the force vectors on the right hand side of equation (A63) are partially due to rotor-housing interaction and can be expressed as functions of the modal coordinates. First, the forces are written in terms of physical coordinates:

$$F_x = -k_x(x - x_h) - c_x(\dot{x} - \dot{x}_h) \tag{A64}$$

$$F_{h_x} = -F_x \tag{A65}$$

where k_x and c_x are the axial stiffness and damping coefficients connecting the rotor to the housing;

$$\begin{aligned} \mathrm{F_y} = &-\mathrm{k_y y} - \mathrm{Q_y z} + \mathrm{k_y y_h} + \mathrm{Q_y z_h} - \mathrm{c_y \dot{y}} - \mathrm{C_{Q_y} \dot{z}} + \mathrm{c_y \dot{y}_h} + \mathrm{C_{Q_y} \dot{z}_h} \\ &- \mathrm{m_y \ddot{y}} - \mathrm{M_{Q_y} \ddot{z}} + \mathrm{m_y \ddot{y}_h} + \mathrm{M_{Q_y} \ddot{z}_h} + \mathrm{F_{Er_y}} + \mathrm{F_{n_y}} \end{aligned} \tag{A66}$$

$$\begin{aligned} \mathrm{F_z} = &\ \mathrm{Q_z y} - \mathrm{k_z z} - \mathrm{Q_z y_h} + \mathrm{k_z z_h} + \mathrm{C_{Q_z} \dot{y}} - \mathrm{c_z \dot{z}} - \mathrm{C_{Q_z} \dot{y}_h} + \mathrm{c_z \dot{z}_h} \\ &+ \mathrm{M_{Q_z} \ddot{y}} - \mathrm{m_z \ddot{z}} - \mathrm{M_{Q_z} \ddot{y}_h} + \mathrm{m_z \ddot{z}_h} + \mathrm{F_{Er_z}} + \mathrm{F_{n_z}} \end{aligned} \tag{A67}$$

$$\mathrm{F_{h_y}} = -(\mathrm{F_y} - \mathrm{F_{Er_y}}) - \mathrm{F_{Eh_y}} \tag{A68}$$

$$\mathrm{F_{h_z}} = -(\mathrm{F_z} - \mathrm{F_{Er_z}}) - \mathrm{F_{Eh_z}} \tag{A69}$$

where the coefficient matrices k, Q, c, $\mathrm{C_Q}$, m, and $\mathrm{M_Q}$, are diagonal;

$$\mathrm{T_z} = -\mathrm{k_t} \Theta_\mathrm{z} + \mathrm{k_t} \Theta_{\mathrm{z_h}} \tag{A70}$$

$$\mathrm{T_y} = -\mathrm{k_t} \Theta_\mathrm{y} + \mathrm{k_t} \Theta_{\mathrm{y_h}} \tag{A71}$$

$$\mathrm{T_{h_z}} = -\mathrm{T_z} \tag{A72}$$

$$\mathrm{T_{h_y}} = -\mathrm{T_y} \tag{A73}$$

where the coefficient matrix $\mathbf{k_t}$ is diagonal. The external excitation forces ($\mathbf{F_{Er}}$ and $\mathbf{F_{Eh}}$) and nonlinear interaction forces ($\mathbf{F_n}$) will be defined in later sections.

The physical coordinates (x, y, z, etc.) can be replaced by the modal transformation given by equations (A31)-(A34) for the rotor and the following for the housing:

$$x_h = \Phi_{h_x} p \tag{A74}$$

$$y_h = \Phi_{h_y} p \tag{A75}$$

$$\Theta_{z_h} = \Psi_{h_z} p \tag{A76}$$

$$z_h = \Phi_{h_z} p \tag{A77}$$

$$\Theta_{y_h} = \Psi_{h_y} p \tag{A78}$$

Performing these transformations and substituting the resulting force expressions into equation (A63) yields:

$$\ddot{x} = -\frac{k_x}{M}(x - \Phi_{h_x} p) - \frac{c_x}{M}(\dot{x} - \Phi_{h_x} \dot{p}) \tag{A79}$$

$$\begin{aligned}
&\ddot{q}_y + 2\zeta_r \omega_{n_r} \dot{q}_y + \Omega\Gamma \dot{q}_z + \omega_{n_r}^2 q_y + \Omega 2\zeta_r \omega_{n_r} q_z \\
&\qquad = -\Phi^T k_y \Phi q_y - \Phi^T Q_y \Phi q_z + \Phi^T k_y \Phi_{h_y} p + \Phi^T Q_y \Phi_{h_z} p \\
&\qquad - \Phi^T c_y \Phi \dot{q}_y - \Phi^T C_{Q_y} \Phi \dot{q}_z + \Phi^T c_y \Phi_{h_y} \dot{p} + \Phi^T C_{Q_y} \Phi_{h_z} \dot{p} \\
&\qquad - \Phi^T m_y \Phi \ddot{q}_y - \Phi^T M_{Q_y} \Phi \ddot{q}_z + \Phi^T m_y \Phi_{h_y} \ddot{p} + \Phi^T M_{Q_y} \Phi_{h_z} \ddot{p} \\
&\qquad - \Psi^T k_t \Psi q_y + \Psi^T k_t \Psi_{h_z} p + \Phi^T (F_{Er_y} + F_{n_y})
\end{aligned} \tag{A80}$$

$$\begin{aligned}
&\ddot{q}_z + 2\zeta_r \omega_{n_r} \dot{q}_z - \Omega\Gamma \dot{q}_y + \omega_{n_r}^2 q_z - \Omega 2\zeta_r \omega_{n_r} q_y \\
&\qquad = \Phi^T Q_z \Phi q_y - \Phi^T k_z \Phi q_z - \Phi^T Q_z \Phi_{h_y} p + \Phi^T k_z \Phi_{h_z} p \\
&\qquad + \Phi^T C_{Q_z} \Phi \dot{q}_y - \Phi^T c_z \Phi \dot{q}_z - \Phi^T C_{Q_z} \Phi_{h_y} \dot{p} + \Phi^T c_z \Phi_{h_z} \dot{p} \\
&\qquad + \Phi^T M_{Q_z} \Phi \ddot{q}_y - \Phi^T m_z \Phi \ddot{q}_z - \Phi^T M_{Q_z} \Phi_{h_y} \ddot{p} + \Phi^T m_z \Phi_{h_z} \ddot{p} \\
&\qquad - \Psi^T k_t \Psi q_z - \Psi^T k_t \Psi_{h_y} p + \Phi^T (F_{Er_z} + F_{n_z})
\end{aligned} \tag{A81}$$

$$
\begin{aligned}
\ddot{\mathrm{p}} + 2\zeta_{\mathrm{h}}\omega_{\mathrm{n_h}}\dot{\mathrm{p}} + \omega_{\mathrm{n_h}}^2\mathrm{p} = {} & \Phi_{\mathrm{h_x}}^{\mathrm{T}} k_x x - \Phi_{\mathrm{h_x}}^{\mathrm{T}} k_x \Phi_{\mathrm{h_x}} \mathrm{p} + \Phi_{\mathrm{h_x}}^{\mathrm{T}} c_x \dot{x} - \Phi_{\mathrm{h_x}}^{\mathrm{T}} c_x \Phi_{\mathrm{h_x}} \dot{\mathrm{p}} \\
& + \Phi_{\mathrm{h_y}}^{\mathrm{T}} \mathrm{k_y} \Phi \mathrm{q_y} + \Phi_{\mathrm{h_y}}^{\mathrm{T}} \mathrm{Q_y} \Phi \mathrm{q_z} - \Phi_{\mathrm{h_y}}^{\mathrm{T}} \mathrm{k_y} \Phi_{\mathrm{h_y}} \mathrm{p} - \Phi_{\mathrm{h_y}}^{\mathrm{T}} \mathrm{Q_y} \Phi_{\mathrm{h_z}} \mathrm{p} \\
& - \Phi_{\mathrm{h_z}}^{\mathrm{T}} \mathrm{Q_z} \Phi \mathrm{q_y} + \Phi_{\mathrm{h_z}}^{\mathrm{T}} \mathrm{k_z} \Phi \mathrm{q_z} + \Phi_{\mathrm{h_z}}^{\mathrm{T}} \mathrm{Q_z} \Phi_{\mathrm{h_y}} \mathrm{p} - \Phi_{\mathrm{h_z}}^{\mathrm{T}} \mathrm{k_z} \Phi_{\mathrm{h_z}} \mathrm{p} \\
& + \Phi_{\mathrm{h_y}}^{\mathrm{T}} \mathrm{c_y} \Phi \dot{\mathrm{q}}_{\mathrm{y}} + \Phi_{\mathrm{h_y}}^{\mathrm{T}} \mathrm{C_{Q_y}} \Phi \dot{\mathrm{q}}_{\mathrm{z}} - \Phi_{\mathrm{h_y}}^{\mathrm{T}} \mathrm{c_y} \Phi_{\mathrm{h_y}} \dot{\mathrm{p}} - \Phi_{\mathrm{h_y}}^{\mathrm{T}} \mathrm{C_{Q_y}} \Phi_{\mathrm{h_z}} \dot{\mathrm{p}} \\
& - \Phi_{\mathrm{h_z}}^{\mathrm{T}} \mathrm{C_{Q_z}} \Phi \dot{\mathrm{q}}_{\mathrm{y}} + \Phi_{\mathrm{h_z}}^{\mathrm{T}} \mathrm{c_z} \Phi \dot{\mathrm{q}}_{\mathrm{z}} + \Phi_{\mathrm{h_z}}^{\mathrm{T}} \mathrm{C_{Q_z}} \Phi_{\mathrm{h_y}} \dot{\mathrm{p}} - \Phi_{\mathrm{h_z}}^{\mathrm{T}} \mathrm{c_z} \Phi_{\mathrm{h_z}} \dot{\mathrm{p}} \\
& + \Phi_{\mathrm{h_y}}^{\mathrm{T}} \mathrm{m_y} \Phi \ddot{\mathrm{q}}_{\mathrm{y}} + \Phi_{\mathrm{h_y}}^{\mathrm{T}} \mathrm{M_{Q_y}} \Phi \ddot{\mathrm{q}}_{\mathrm{z}} - \Phi_{\mathrm{h_y}}^{\mathrm{T}} \mathrm{m_y} \Phi_{\mathrm{h_y}} \ddot{\mathrm{p}} - \Phi_{\mathrm{h_y}}^{\mathrm{T}} \mathrm{M_{Q_y}} \Phi_{\mathrm{h_z}} \ddot{\mathrm{p}} \\
& - \Phi_{\mathrm{h_z}}^{\mathrm{T}} \mathrm{M_{Q_z}} \Phi \ddot{\mathrm{q}}_{\mathrm{y}} + \Phi_{\mathrm{h_z}}^{\mathrm{T}} \mathrm{m_z} \Phi \ddot{\mathrm{q}}_{\mathrm{z}} + \Phi_{\mathrm{h_z}}^{\mathrm{T}} \mathrm{M_{Q_z}} \Phi_{\mathrm{h_y}} \ddot{\mathrm{p}} - \Phi_{\mathrm{h_z}}^{\mathrm{T}} \mathrm{m_z} \Phi_{\mathrm{h_z}} \ddot{\mathrm{p}} \\
& + \Psi_{\mathrm{h_z}}^{\mathrm{T}} \mathrm{k_t} \Psi \mathrm{q_y} - \Psi_{\mathrm{h_z}}^{\mathrm{T}} \mathrm{k_t} \Psi_{\mathrm{h_z}} \mathrm{p} - \Psi_{\mathrm{h_y}}^{\mathrm{T}} \mathrm{k_t} \Psi \mathrm{q_z} - \Psi_{\mathrm{h_y}}^{\mathrm{T}} \mathrm{k_t} \Psi_{\mathrm{h_y}} \mathrm{p} \\
& - \Phi_{\mathrm{h_y}}^{\mathrm{T}} (\mathrm{F_{Eh_y}} + \mathrm{F_{n_y}}) - \Phi_{\mathrm{h_z}}^{\mathrm{T}} (\mathrm{F_{Eh_z}} + \mathrm{F_{n_z}})
\end{aligned}
\tag{A82}
$$

Each force expression on the right-hand side of equations (A80)-(A82) should be recognized as the sum of the generalized forces due to the physical forces, i.e.,

$$
\Phi^{\mathrm{T}} \mathrm{F_y} = \sum_{\mathrm{i}=1}^{\mathrm{N}} \phi_{\mathrm{i}}^{\mathrm{T}} \mathrm{F_{y_i}} \tag{A83}
$$

where ϕ_i^T represents the i^{th} row of Φ. These equations can be written more compactly by combining the coefficients of the generalized coordinates on the left-hand side of the equations as follows:

$$
\mathrm{M} \begin{Bmatrix} \ddot{x} \\ \ddot{\mathrm{q}}_{\mathrm{y}} \\ \ddot{\mathrm{q}}_{\mathrm{z}} \\ \ddot{\mathrm{p}} \end{Bmatrix} + \mathrm{C} \begin{Bmatrix} \dot{x} \\ \dot{\mathrm{q}}_{\mathrm{y}} \\ \dot{\mathrm{q}}_{\mathrm{z}} \\ \dot{\mathrm{p}} \end{Bmatrix} + \mathrm{K} \begin{Bmatrix} x \\ \mathrm{q_y} \\ \mathrm{q_z} \\ \mathrm{p} \end{Bmatrix} = \begin{Bmatrix} 0 \\ \Phi^{\mathrm{T}} (\mathrm{F_{Er_y}} + \mathrm{F_{n_y}}) \\ \Phi^{\mathrm{T}} (\mathrm{F_{Er_z}} + \mathrm{F_{n_z}}) \\ -\Phi_{\mathrm{h_y}}^{\mathrm{T}} (\mathrm{F_{Eh_y}} + \mathrm{F_{n_y}}) - \Phi_{\mathrm{h_z}}^{\mathrm{T}} (\mathrm{F_{Eh_z}} + \mathrm{F_{n_z}}) \end{Bmatrix} \tag{A84}
$$

where

$$
M = \begin{bmatrix}
1 & 0 & 0 & 0 \\
0 & I + \Phi^T m_y \Phi & \Phi^T M_{Q_y} \Phi & \begin{pmatrix} -\Phi^T m_y \Phi_{h_y} \\ -\Phi^T M_{Q_y} \Phi_{h_z} \end{pmatrix} \\
0 & -\Phi^T M_{Q_z} \Phi & I + \Phi^T m_z \Phi & \begin{pmatrix} \Phi^T M_{Q_z} \Phi_{h_y} \\ -\Phi^T m_z \Phi_{h_z} \end{pmatrix} \\
0 & \begin{pmatrix} -\Phi_{h_y}^T m_y \Phi \\ +\Phi_{h_z}^T M_{Q_z} \Phi \end{pmatrix} & \begin{pmatrix} -\Phi_{h_y}^T M_{Q_y} \Phi \\ -\Phi_{h_z}^T m_z \Phi \end{pmatrix} & \begin{pmatrix} I + \Phi_{h_y}^T m_y \Phi_{h_y} \\ +\Phi_{h_y}^T M_{Q_y} \Phi_{h_z} - \Phi_{h_z}^T M_{Q_z} \Phi_{h_y} \\ +\Phi_{h_z}^T m_z \Phi_{h_z} \end{pmatrix}
\end{bmatrix} \tag{A85}
$$

$$
C = \begin{bmatrix}
\frac{c_x}{M} & 0 & 0 & -\Phi_{h_x} \frac{c_x}{M} \\
0 & \begin{pmatrix} 2\zeta_r \omega_{n_r} \\ +\Phi^T c_y \Phi \end{pmatrix} & \begin{pmatrix} \Omega\Gamma \\ +\Phi^T C_{Q_y} \Phi \end{pmatrix} & \begin{pmatrix} -\Phi^T c_y \Phi_{h_y} \\ -\Phi^T C_{Q_y} \Phi_{h_z} \end{pmatrix} \\
0 & \begin{pmatrix} -\Omega\Gamma \\ -\Phi^T C_{Q_z} \Phi \end{pmatrix} & \begin{pmatrix} 2\zeta_r \omega_{n_r} \\ +\Phi^T c_z \Phi \end{pmatrix} & \begin{pmatrix} \Phi^T C_{Q_z} \Phi_{h_y} \\ -\Phi^T c_z \Phi_{h_z} \end{pmatrix} \\
-c_x \Phi_{h_x}^T & \begin{pmatrix} -\Phi_{h_y}^T c_y \Phi \\ +\Phi_{h_z}^T C_{Q_z} \Phi \end{pmatrix} & \begin{pmatrix} -\Phi_{h_y}^T C_{Q_y} \Phi \\ -\Phi_{h_z}^T c_z \Phi \end{pmatrix} & \begin{pmatrix} 2\zeta_h \omega_{n_h} + \Phi_{h_y}^T c_y \Phi_{h_y} \\ +\Phi_{h_y}^T C_{Q_y} \Phi_{h_z} - \Phi_{h_z}^T C_{Q_z} \Phi_{h_y} \\ +\Phi_{h_z}^T c_z \Phi_{h_z} + \Phi_{h_x}^T c_x \Phi_{h_x} \end{pmatrix}
\end{bmatrix} \tag{A86}
$$

and

$$
K = \begin{bmatrix}
\frac{k_x}{M} & 0 & 0 & -\Phi_{h_x}\frac{k_x}{M} \\
0 & \begin{pmatrix} \omega_{n_r}^2 \\ +\Phi^T k_y \Phi \\ +\Psi^T k_t \Psi \end{pmatrix} & \begin{pmatrix} \Omega 2\zeta_r \omega_{n_r} \\ +\Phi^T Q_y \Phi \end{pmatrix} & \begin{pmatrix} -\Phi^T k_y \Phi_{h_y} \\ -\Phi^T Q_y \Phi_{h_z} \\ -\Psi^T k_t \Psi_{h_z} \end{pmatrix} \\
0 & \begin{pmatrix} -\Omega 2\zeta_r \omega_{n_r} \\ -\Phi^T Q_z \Phi \end{pmatrix} & \begin{pmatrix} \omega_{n_r}^2 \\ +\Phi^T k_z \Phi \\ +\Psi^T k_t \Psi \end{pmatrix} & \begin{pmatrix} \Phi^T Q_z \Phi_{h_y} \\ -\Phi^T k_z \Phi_{h_z} \\ +\Psi^T k_t \Psi_{h_y} \end{pmatrix} \\
-k_x \Phi_{h_x}^T & \begin{pmatrix} -\Phi_{h_y}^T k_y \Phi \\ +\Phi_{h_z}^T Q_z \Phi \\ -\Psi_{h_z}^T k_t \Psi \end{pmatrix} & \begin{pmatrix} -\Phi_{h_y}^T Q_y \Phi \\ -\Phi_{h_z}^T k_z \Phi \\ -\Psi_{h_y}^T k_t \Psi \end{pmatrix} & \begin{pmatrix} \omega_{n_h}^2 + \Phi_{h_y}^T k_y \Phi_{h_y} \\ +\Phi_{h_y}^T Q_y \Phi_{h_z} - \Phi_{h_z}^T Q_z \Phi_{h_y} \\ +\Phi_{h_z}^T k_z \Phi_{h_z} + \Phi_{h_x}^T k_x \Phi_{h_x} \\ +\Psi_{h_z}^T k_t \Psi_{h_z} + \Psi_{h_y}^T k_t \Psi_{h_y} \end{pmatrix}
\end{bmatrix} \tag{A87}
$$

Each of these system matrices is, in general, a function of speed since the coefficient matrices are functions of speed. The right-hand side of equation (A84) contains only externally applied forces and nonlinear interaction forces. These will be discussed next.

External Forces

There are four external excitations that can be considered using the rotordynamic analyses package: rotor mass unbalance forces, static side forces, white noise forces, and pulse perturbation forces. The first three represent actual forces in the turbopump. The pulse perturbation is a tool used to study the characteristics of the nonlinear system.

The unbalance forces are the inertia forces due to the acceleration of the eccentric mass of the rotor. Since they are inertial, they are applied only to the rotor. The y and z axis components are ± 90 degrees out of phase, depending on the direction of rotation. The side forces are due to non-uniform circumferential pressure distributions that occur in the turbines and the pump discharge volutes. These forces are applied to the rotor and the housing with equal magnitude, but opposite direction. The white noise forces represent the various random excitations that occur in the turbopump. Random pressure fluctuations in the turbines and pumps and external acoustic noise are examples. Noise can be applied to the rotor and housing with equal but opposite forces, as with the side forces, or to the rotor and/or housing independently. The pulse perturbation is applied

at only one axial position and is applied to the rotor only. It can be defined as a square pulse or a short duration oscillating force with a prescribed frequency.

The unbalance force is defined by specifying the product of mass and eccentricity along with the phase for each axial location. For one location, the force is written as

$$F_{Uy_i} = (ma)_i\dot{\theta}^2 \cos(\theta + \phi_i) + (ma)_i\alpha \sin(\theta + \phi_i) \tag{A88}$$

$$F_{Uz_i} = (ma)_i\dot{\theta}^2 \sin(\theta + \phi_i) - (ma)_i\alpha \cos(\theta + \phi_i) \tag{A89}$$

where

$$\theta = \int_0^t \int_0^\tau \alpha(\rho) d\rho d\tau \tag{A90}$$

The side force is defined by specifying the y and z axis components for each axial location as quadratic polynominals in pump speed

$$F_{Sy_i} = C_{y0_i} + \Omega C_{y1_i} + \Omega^2 C_{y2_i} \tag{A91}$$

$$F_{Sz_i} = C_{z0_i} + \Omega C_{z1_i} + \Omega^2 C_{z2_i} \tag{A92}$$

The white noise forces ($F_{N\tau_{y_i}}$, $F_{N\tau_{z_i}}$, $F_{Nh_{y_i}}$, and $F_{Nh_{z_i}}$) are defined by scaling a uniform random number sequence with range $(-1,1)$ to a desired range. The pulse perturbation is either of the form

$$F_{Py} = \frac{A_{Py}}{\tau}\Big[\delta(t-\tau) - \delta\big(t-(T+\tau)\big)\Big] \tag{A93}$$

$$F_{Pz} = \frac{A_{Pz}}{\tau}\Big[\delta(t-\tau) - \delta\big(t-(T+\tau)\big)\Big] \tag{A94}$$

or

$$F_{Py} = A_{Py}\cos(\omega_p t)\Big[\delta(t-\tau) - \delta\big(t-(T+\tau)\big)\Big] \tag{A95}$$

$$F_{Pz} = A_{Pz}\sin(\omega_p t)\Big[\delta(t-\tau) - \delta\big(t-(T+\tau)\big)\Big] \tag{A96}$$

where

$$\delta(t) = \begin{cases} 1 & \text{if } t \geq 0 \\ 0 & \text{if } t < 0 \end{cases} \tag{A97}$$

The total of all external excitation forces can now be written as

$$F_{Er_{y_i}} = F_{Sy_i} + F_{Nr_{y_i}} + F_{Uy_i} + \delta_{ik}F_{Py_k} \tag{A98}$$

$$F_{Er_{z_i}} = F_{Sz_i} + F_{Nr_{z_i}} + F_{Uz_i} + \delta_{ik}F_{Pz_k} \tag{A99}$$

$$F_{Eh_{y_i}} = F_{Sy_i} + F_{Nh_{y_i}} \tag{A100}$$

$$F_{Eh_{z_i}} = F_{Sz_i} + F_{Nh_{z_i}} \tag{A101}$$

Nonlinear Interaction Forces

Rotor-housing interaction forces are functions of the physical coordinates at particular locations. The linear interaction forces can be expressed as functions of the generalized coordinates using coordinate transformations. This was done to arrive at equations (A79)-(A82) and (A84). The nonlinear interaction forces, however, cannot be treated in this way. At each instant in time, the generalized coordinates must be transformed into physical coordinates. The nonlinear forces are then calculated as functions of the physical coordinates. The physical forces are then transformed into generalized forces and applied to the generalized coordinates.

There are three generic types of nonlinear force elements that can be represented using the rotordynamics analysis package. The first is bearing clearance or deadband. For this type of element, no force is produced until the relative displacement between the rotor and housing exceeds some specified clearance. After this clearance has been exceeded, the force is represented as a piecewise linear spring and damper. Figure 106 illustrates the piecewise linear spring force versus radial deflection. Figure 107 shows the relative displacement and velocity vector diagram which is used to aid in writing the y

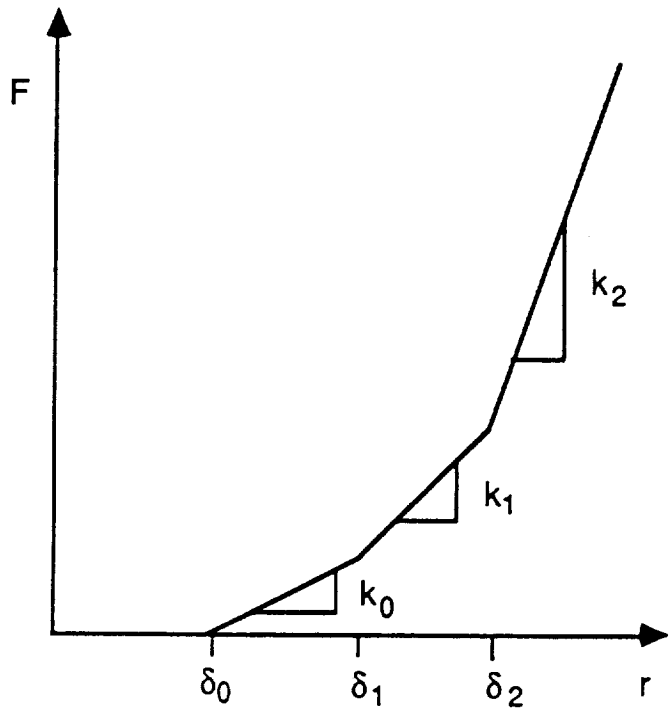

Figure 106. Deadband nonlinear element piecewise linear restoring force versus radial deflection.

and z axis components of the nonlinear force. The element can be conceptualized as shown in figure 108. This figure shows a separate spring damper subelement for each clearance. The coefficients for the second and third of these are defined to be the changes in the coefficients defined in figure 106. This makes it possible to write the force equation as if the three parts were independent when they are actually not (figure 109). Referring to figure 107, the actual displacement and velocity components across a given subelement are

$$y_{e_i} = y - \delta_i \cos\theta \tag{A102}$$

$$z_{e_i} = z - \delta_i \sin\theta \tag{A103}$$

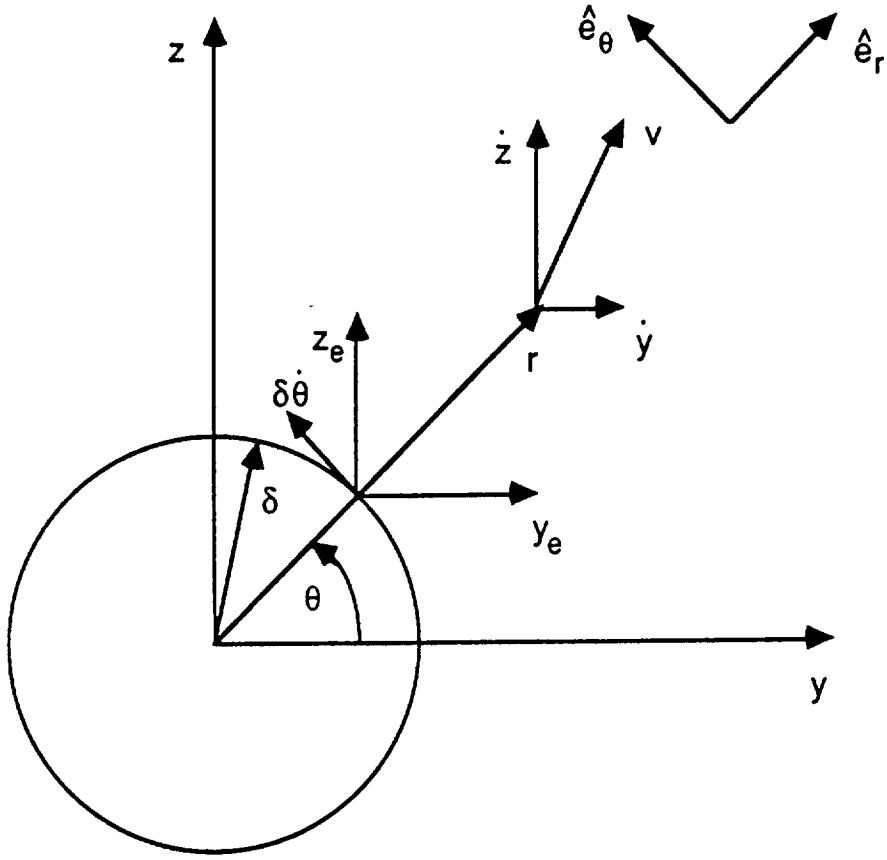

Figure 107. Relative displacement and velocity vector diagram for deadband nonlinear element.

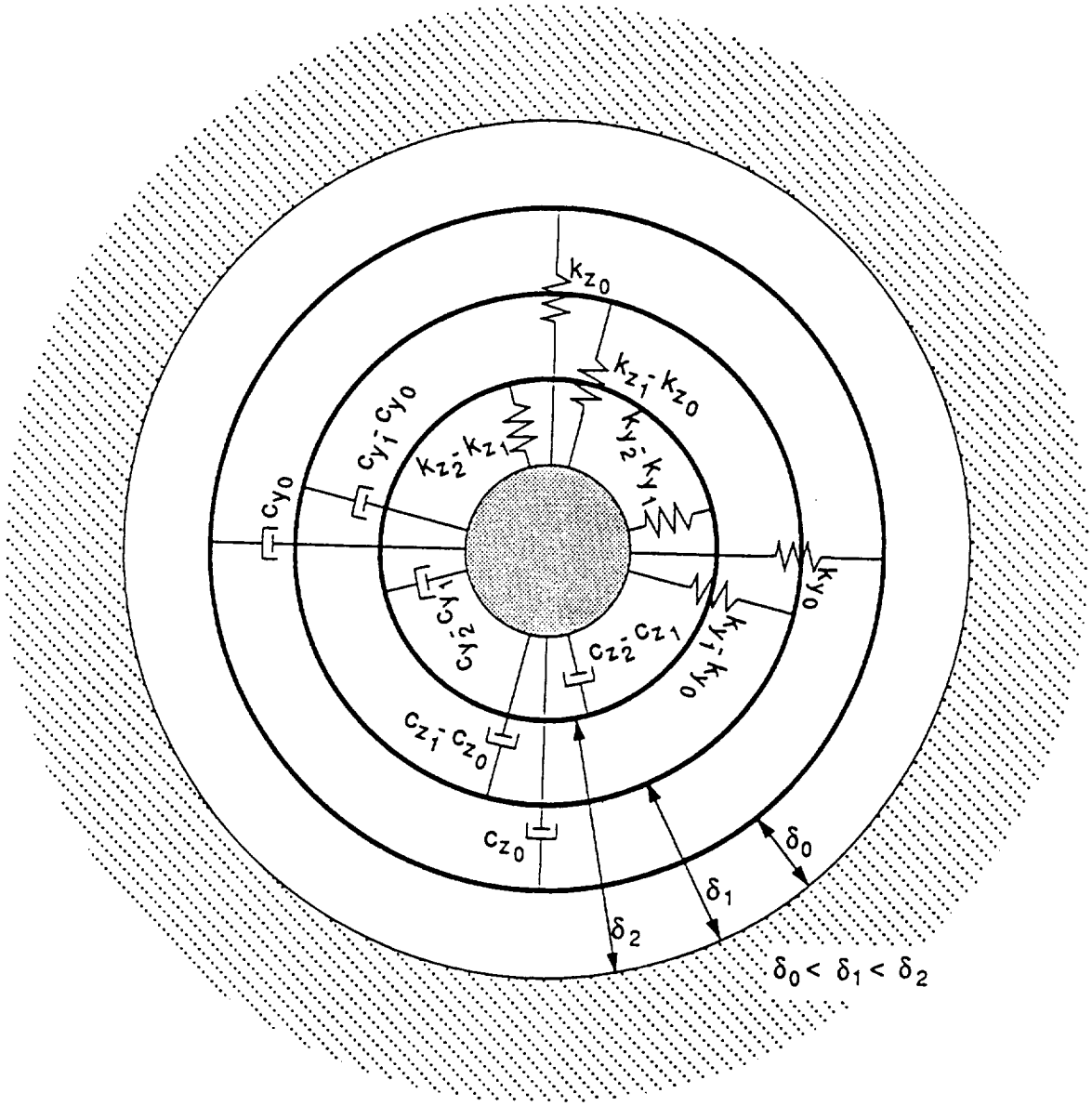

Figure 108. Conceptual representation of deadband nonlinear element. Heavy-lined circles represent massless rings.

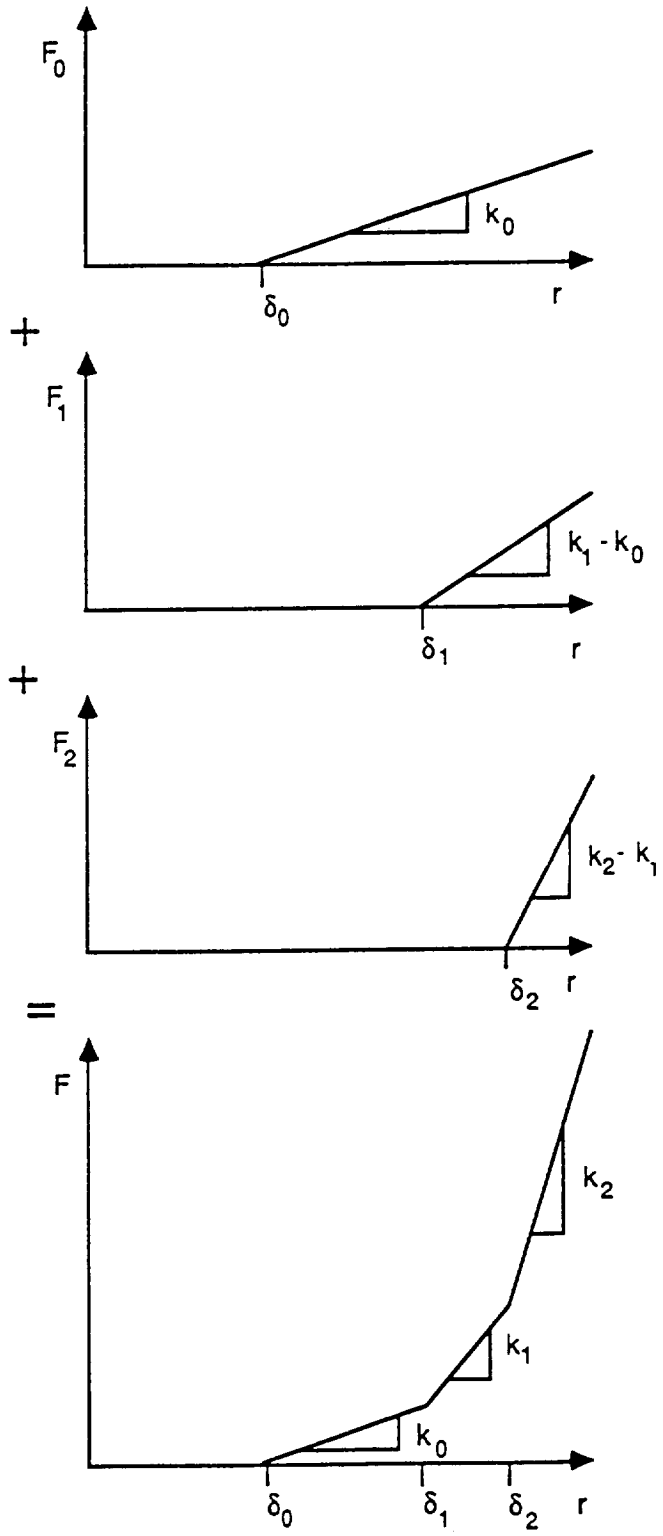

Figure 109. Superposition of subelement piecewise linear force functions to yield overall function for deadband nonlinear element.

$$\dot{y}_{e_i} = \dot{y} + \delta_i \dot{\theta} \sin\theta \tag{A104}$$

$$\dot{z}_{e_i} = \dot{z} - \delta_i \dot{\theta} \cos\theta \tag{A105}$$

where

$$\dot{\theta} = \frac{y\dot{z} - z\dot{y}}{r^2} \tag{A106}$$

and

$$r = \sqrt{y^2 + z^2} \tag{A107}$$

Recognizing that

$$\cos\theta = \frac{y}{r} \tag{A108}$$

and

$$\sin\theta = \frac{z}{r} \tag{A109}$$

equations (A102)-(A105) can be rewritten as

$$y_{e_i} = y\left(1 - \frac{\delta_i}{r}\right) \tag{A110}$$

$$z_{e_i} = z\left(1 - \frac{\delta_i}{r}\right) \tag{A111}$$

$$\dot{y}_{e_i} = \dot{y} + \frac{\delta_i}{r}\dot{\theta} z \tag{A112}$$

$$\dot{z}_{e_i} = \dot{z} - \frac{\delta_i}{r}\dot{\theta} y \tag{A113}$$

With these defined, the force components can be written directly for each range of displacement. For $r < \delta_0$,

$$F_y = 0 \tag{A114}$$

$$F_z = 0 \tag{A115}$$

For $\delta_0 < r < \delta_1$,

$$F_y = -k_{y_0} y_{e_0} - c_{y_0} \dot{y}_{e_0} \tag{A116}$$

$$F_z = -k_{z_0} z_{e_0} - c_{z_0} \dot{z}_{e_0} \tag{A117}$$

For $\delta_1 < r < \delta_2$,

$$F_y = -(k_{y_1} - k_{y_0}) y_{e_1} - (c_{y_1} - c_{y_0}) \dot{y}_{e_1} - k_{y_0} y_{e_0} - c_{y_0} \dot{y}_{e_0} \tag{A118}$$

$$F_z = -(k_{z_1} - k_{z_0}) z_{e_1} - (c_{z_1} - c_{z_0}) \dot{z}_{e_1} - k_{z_0} z_{e_0} - c_{z_0} \dot{z}_{e_0} \tag{A119}$$

For $\delta_2 < r$,

$$\begin{aligned} F_y = &-(k_{y_2} - k_{y_1}) y_{e_2} - (c_{y_2} - c_{y_1}) \dot{y}_{e_2} - (k_{y_1} - k_{y_0}) y_{e_1} \\ &- (c_{y_1} - c_{y_0}) \dot{y}_{e_1} - k_{y_0} y_{e_0} - c_{y_0} \dot{y}_{e_0} \end{aligned} \tag{A120}$$

$$\begin{aligned} F_z = &-(k_{z_2} - k_{z_1}) z_{e_2} - (c_{z_2} - c_{z_1}) \dot{z}_{e_2} - (k_{z_1} - k_{z_0}) z_{e_1} \\ &- (c_{z_1} - c_{z_0}) \dot{z}_{e_1} - k_{z_0} z_{e_0} - c_{z_0} \dot{z}_{e_0} \end{aligned} \tag{A121}$$

Substituting equations (A110) - (A113) for each range of displacement into equations (A116) - (A121) and simplifying yields the following: For $\delta_0 < r < \delta_1$,

$$F_y = -k_{y_0} \left(1 - \frac{\delta_0}{r}\right) y - c_{y_0} \left(\dot{y} + \frac{\delta_0}{r} \dot{\theta} z\right) \tag{A122}$$

$$F_z = -k_{z_0} \left(1 - \frac{\delta_0}{r}\right) z - c_{z_0} \left(\dot{z} - \frac{\delta_0}{r} \dot{\theta} y\right) \tag{A123}$$

For $\delta_1 < r < \delta_2$,

$$F_y = -k_{y_1} \left[1 - \frac{\delta_1}{r}\left(1 - \frac{k_{y_0}}{k_{y_1}} \frac{\delta_1 - \delta_0}{\delta_1}\right)\right] y - c_{y_1} \left[\dot{y} + \frac{\delta_1}{r}\left(1 - \frac{c_{y_0}}{c_{y_1}} \frac{\delta_1 - \delta_0}{\delta_1}\right) \dot{\theta} z\right] \tag{A124}$$

$$F_z = -k_{z_1}\Big[1 - \frac{\delta_1}{r}\big(1 - \frac{k_{z_0}}{k_{z_1}}\frac{\delta_1 - \delta_0}{\delta_1}\big)\Big]z - c_{z_1}\Big[\dot{z} - \frac{\delta_1}{r}\big(1 - \frac{c_{z_0}}{c_{z_1}}\frac{\delta_1 - \delta_0}{\delta_1}\big)\dot{\theta}y\Big] \tag{A125}$$

For $\delta_2 < r$,

$$\begin{aligned} F_y = &-k_{y_2}\Big[1 - \frac{\delta_2}{r}\big(1 - \frac{k_{y_1}}{k_{y_2}}\frac{\delta_2 - \delta_1}{\delta_2} - \frac{k_{y_0}}{k_{y_2}}\frac{\delta_1 - \delta_0}{\delta_2}\big)\Big]y \\ &- c_{y_2}\Big[\dot{y} + \frac{\delta_2}{r}\big(1 - \frac{c_{y_1}}{c_{y_2}}\frac{\delta_2 - \delta_1}{\delta_2} - \frac{c_{y_0}}{c_{y_2}}\frac{\delta_1 - \delta_0}{\delta_2}\big)\dot{\theta}z\Big] \end{aligned} \tag{A126}$$

$$\begin{aligned} F_z = &-k_{z_2}\Big[1 - \frac{\delta_2}{r}\big(1 - \frac{k_{z_1}}{k_{z_2}}\frac{\delta_2 - \delta_1}{\delta_2} - \frac{k_{z_0}}{k_{z_2}}\frac{\delta_1 - \delta_0}{\delta_2}\big)\Big]z \\ &- c_{z_2}\Big[\dot{z} - \frac{\delta_2}{r}\big(1 - \frac{c_{z_1}}{c_{z_2}}\frac{\delta_2 - \delta_1}{\delta_2} - \frac{c_{z_0}}{c_{z_2}}\frac{\delta_1 - \delta_0}{\delta_2}\big)\dot{\theta}y\Big] \end{aligned} \tag{A127}$$

Each of these force expressions is of the form

$$F_y = -k_y\Big(1 - \alpha_y\frac{\delta}{r}\Big)y - c_y\Big(\dot{y} + \beta_y\frac{\delta}{r}\dot{\theta}z\Big) \tag{A128}$$

$$F_z = -k_z\Big(1 - \alpha_z\frac{\delta}{r}\Big)z - c_z\Big(\dot{z} - \beta_z\frac{\delta}{r}\dot{\theta}y\Big) \tag{A129}$$

The stiffness and damping coefficients in these expressions are, in general, functions of speed.

The second type of nonlinear force element that can be represented is rotor-stator rubbing. Rubbing is very similar to bearing clearance in that there is an abrupt stiffness increase when contact is made. The rubbing force element contains the additional effect of friction which produces a force tangential to the contact surface. The rub element can be conceptualized as shown in figure 110. It can be modeled using two different formulations. The first is the more conventional and simpler of the two. First, the radial force is calculated neglecting the effect of the frictional force:

$$F_R = -k_R(|\mathbf{r}| - c) = -k_R|\mathbf{r}|\Big(1 - \frac{c}{|\mathbf{r}|}\Big) \tag{A130}$$

Then the tangential force is determined as the product of the radial force and the coefficient of friction:

$$F_\theta = \mu F_R = -\mu k_R|\mathbf{r}|\Big(1 - \frac{c}{|\mathbf{r}|}\Big) \tag{A131}$$

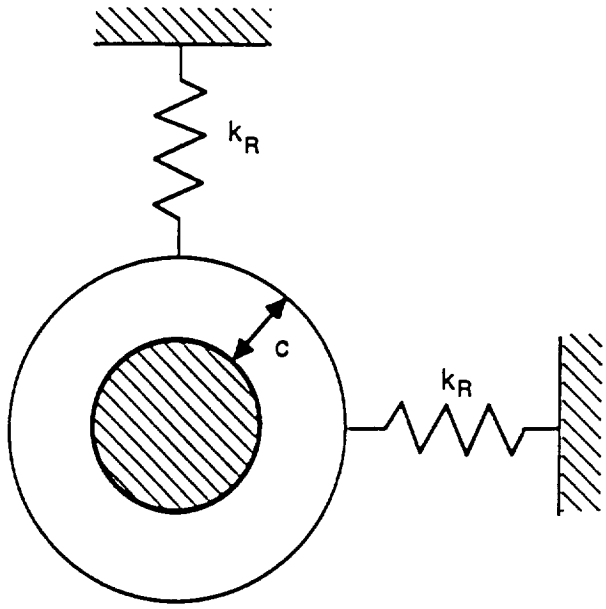

(a)

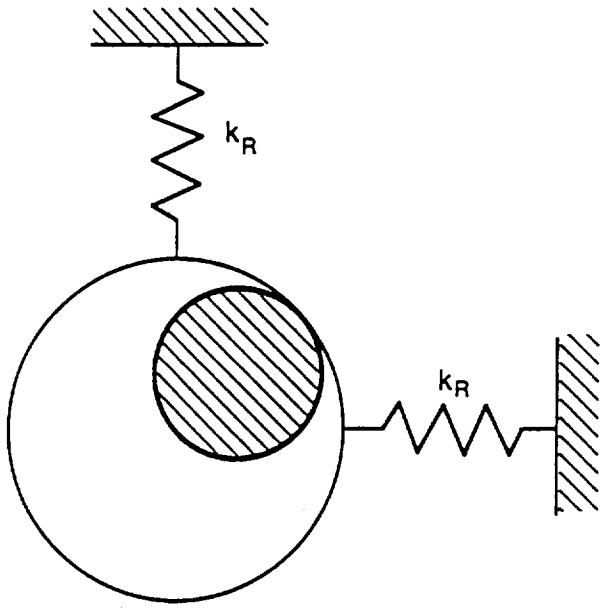

(b)

Figure 110. Conceptual model of rub nonlinear element. (a) Undeflected position. (b) Deflected position.

The assumption is made here that the contact surface normal vector remains collinear with the radial deflection vector. This assumption may be valid for low friction or light contact. In general, however, the contact surface normal will be collinear with the resultant of the radial and tangential forces. This is illustrated graphically in figure 111. A formulation including this effect was developed by von Pragenau [19]. A new vector S has been introduced to define the surface displacement. The total force is equal to the stiffness multiplied by the surface displacement vector

$$\mathbf{F} = -k_R \mathbf{S} \tag{A132}$$

This can be expressed in terms of the contact surface normal and tangential components as

$$\mathbf{F} = -F_N \hat{e}_N - \mu F_N \hat{e}_T \tag{A133}$$

The angle between the force F and the surface contact normal $\hat{e}_N$ is then

$$\gamma = \tan^{-1} \mu \tag{A134}$$

The displacement vectors are redrawn for clarity in figure 112. All three sides and one angle are known, therefore, from elementary trigonometry, we have

$$\frac{|\mathbf{r}|}{\sin(\pi - \gamma)} = \frac{c}{\sin \beta} \tag{A135}$$

from which

$$\sin \beta = \frac{c}{|\mathbf{r}|} \sin(\pi - \gamma) = \frac{c}{|\mathbf{r}|} \sin \gamma \tag{A136}$$

Noting that

$$\sin \gamma = \sin(\tan^{-1} \mu) = \frac{\mu}{\sqrt{1 + \mu^2}} \tag{A137}$$

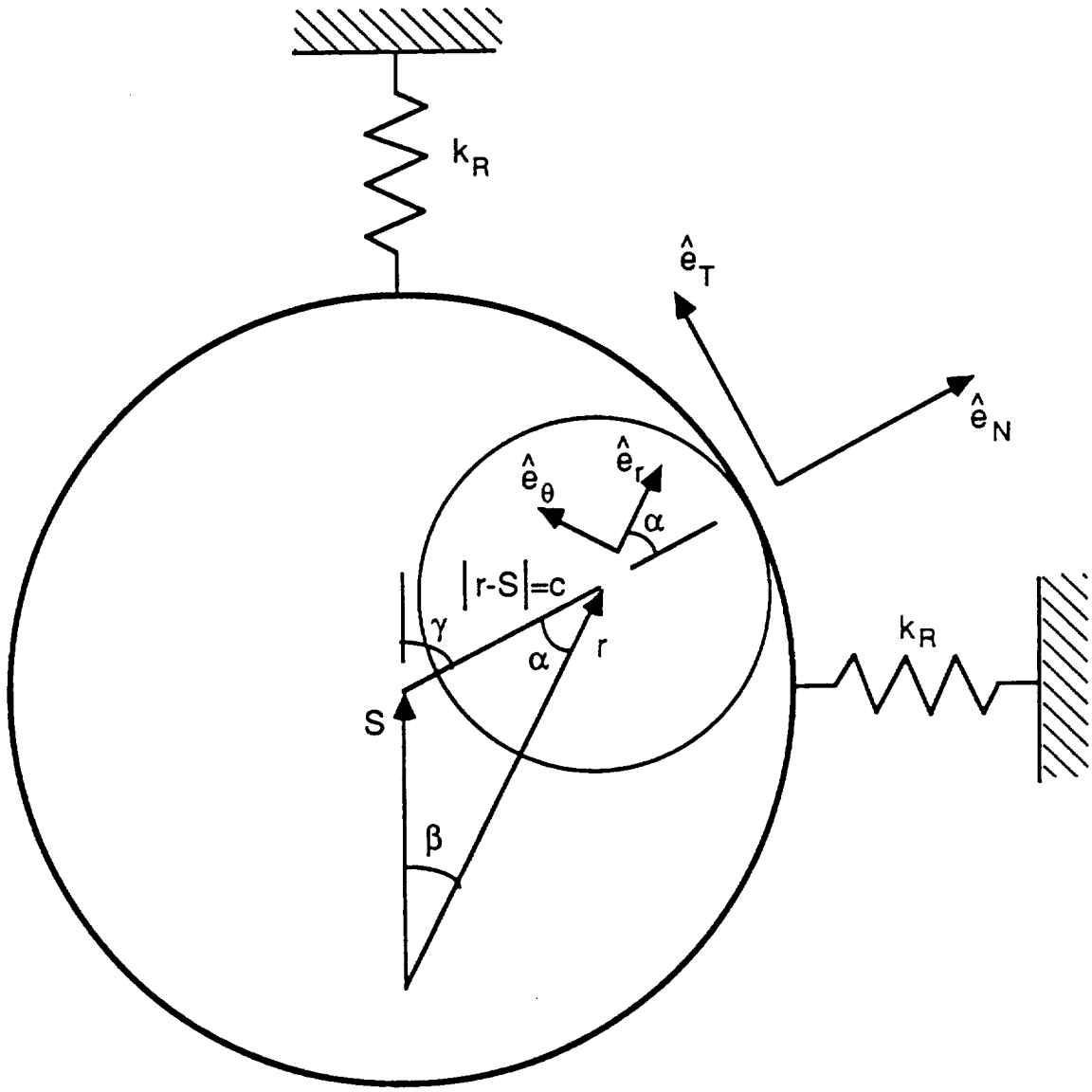

Figure 111. Rub model vector diagram.

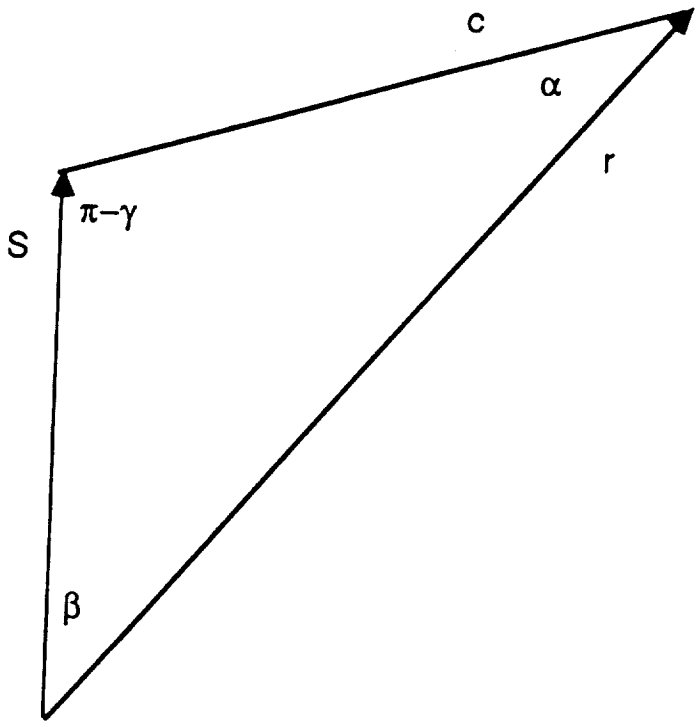

Figure 112. Rub model displacement vector diagram.

and that

$$\alpha = \pi - \beta - (\pi - \gamma) = \gamma - \beta \tag{A138}$$

yields

$$\alpha = \tan^{-1}\mu - \sin^{-1}\left(\frac{c}{|\mathbf{r}|}\frac{\mu}{\sqrt{1+\mu^2}}\right) \tag{A139}$$

The force $\mathbf{F}$ can now be expressed in terms of radial and tangential components.

$$\mathbf{F} = -k_R\mathbf{S} = -k_R(\mathbf{r} - c\hat{e}_N) \tag{A140}$$

but

$$\hat{e}_N = \hat{e}_r \cos\alpha - \hat{e}_\theta \sin\alpha \tag{A141}$$

therefore

$$\mathbf{F} = -k_R\left[(\mathbf{r} - c\cos\alpha)\hat{e}_r + c\sin\alpha\hat{e}_\theta\right] \tag{A142}$$

From equations (A139) and (A136), noting that

$$\cos\beta = \sqrt{1 - \sin^2\beta} \tag{A143}$$

it can be shown that

$$\cos\alpha = \frac{1}{\sqrt{1+\mu^2}}\sqrt{1 - \frac{c^2}{|\mathbf{r}|^2}\frac{\mu^2}{1+\mu^2}} + \frac{c}{|\mathbf{r}|}\frac{\mu^2}{1+\mu^2} \tag{A144}$$

and

$$\sin\alpha = \frac{\mu}{\sqrt{1+\mu^2}}\sqrt{1 - \frac{c^2}{|\mathbf{r}|^2}\frac{\mu^2}{1+\mu^2}} - \frac{c}{|\mathbf{r}|}\frac{\mu}{1+\mu^2} \tag{A145}$$

Substituting (A144) - (A145) into (A142) yields the radial and tangential force components in terms of the radial displacement $\mathbf{r}$

$$\begin{aligned}\mathbf{F} = -k_R|\mathbf{r}|&\left[1 - \frac{c}{|\mathbf{r}|}\frac{1}{\sqrt{1+\mu^2}}\sqrt{1 - \frac{c^2}{|\mathbf{r}|^2}\frac{\mu^2}{1+\mu^2}} - \frac{c^2}{|\mathbf{r}|^2}\frac{\mu^2}{1+\mu^2}\right]\hat{e}_r \\ &- \mu k_R|\mathbf{r}|\left[\frac{c}{|\mathbf{r}|}\frac{1}{\sqrt{1+\mu^2}}\sqrt{1 - \frac{c^2}{|\mathbf{r}|^2}\frac{\mu^2}{1+\mu^2}} - \frac{c^2}{|\mathbf{r}|^2}\frac{1}{1+\mu^2}\right]\hat{e}_\theta\end{aligned} \tag{A146}$$

The third type of nonlinear force element is the floating ring seal. This is a very complex element since it involves an additional mass suspended from the rotor and interacting with the housing through friction. Since this element was not used in any part of this study, the details of its formulation will not be included here.

Eccentricities are geometric offsets from the normal centerline of the housing (stator) or rotor. The are not inherently nonlinear effects, but require the same transformations

(from generalized coordinates to physical coordinates and back) as the nonlinear force calculations; therefore, they are calculated along with the nonlinear forces. Their most pronounced effects occur when nonlinearities are present by altering the deflections required to reach a certain threshold in the nonlinear function (i.e., exceed a seal clearance and rub). Their effects are included by adding the offsets to the relative deflection, velocity, and acceleration expressions as follows:

$$y_{rel} = y_r - y_h + \epsilon_r \cos(\theta + \phi_r) - \epsilon_{h_y} \tag{A147}$$

$$z_{rel} = z_r - z_h + \epsilon_r \sin(\theta + \phi_r) - \epsilon_{h_z} \tag{A148}$$

$$\dot{y}_{rel} = \dot{y}_r - \dot{y}_h - \dot{\theta}\epsilon_r \sin(\theta + \phi_r) \tag{A149}$$

$$\dot{z}_{rel} = \dot{z}_r - \dot{z}_h + \dot{\theta}\epsilon_r \cos(\theta + \phi_r) \tag{A150}$$

$$\ddot{y}_{rel} = \ddot{y}_r - \ddot{y}_h - \ddot{\theta}\epsilon_r \sin(\theta + \phi_r) - \dot{\theta}^2\epsilon_r \cos(\theta + \phi_r) \tag{A151}$$

$$\ddot{z}_{rel} = \ddot{z}_r - \ddot{z}_h + \ddot{\theta}\epsilon_r \cos(\theta + \phi_r) - \dot{\theta}^2\epsilon_r \sin(\theta + \phi_r) \tag{A152}$$

where θ is the angular position of the rotor and for constant speed cases

$$\theta = \omega t \tag{A153}$$

Solution Procedure

The equations of motion for the system have been defined in terms of generalized coordinates associated with the component modes of the rotor and housing. The development assumed that a complete set of component modes would be used to transform from the physical coordinates to the generalized coordinates. If a reduced or truncated set of modes is used (thereby reducing the order of the model), the coordinate transformation (equations (A31) - (A34) for the rotor, and equations (A74) - (A78) for the housing become approximations and error is introduced into the model. If a sufficient number of modes is retained, the magnitude of the error can be made small. The error can be further

reduced for a given number of retained modes by a method known as condensation. This method partially utilizes the modes to be eliminated rather then simply truncating them. The method is developed for this application in reference 20. In order to avoid possible influences on the results, condensation was not used in the numerical investigations of this study.

The equations of motion given by equations (A84) - (A87) are a set of coupled, nonlinear second order differential equations. The nonlinearities in these equations are all contained in the rotor-housing interaction forces. These equations can be linearized in two ways. First, the nonlinear force expressions can be linearized about some operating state as described in chapter III. The state is determined by running the nonlinear transient simulation until a specified time is reached. Second, the nonlinearities can be neglected. For the bearing clearance nonlinearity, this means that the clearance is assumed to be either zero or infinite. The stiffness is then linear and can be handled like the other linear stiffnesses. For the rubbing nonlinearity, the clearance is assumed to be infinite so that rubbing never occurs. The linear set of equations can now be solved using standard techniques.

The stability analysis program obtains the homogeneous solution to the equations of motion (A84):

$$\mathbf{M}\ddot{\eta} + \mathbf{C}\dot{\eta} + \mathbf{K}\eta = \mathbf{0} \tag{A154}$$

where

$$\eta = \begin{Bmatrix} x \\ \mathbf{q_y} \\ \mathbf{q_z} \\ \mathbf{p} \end{Bmatrix} \tag{A155}$$

This can be put into first order form by defining

$$\beta = \begin{Bmatrix} \dot{\eta} \\ \eta \end{Bmatrix} \tag{A156}$$

and writing

$$\begin{bmatrix} 0 & \mathbf{I} \\ \mathbf{M} & \mathbf{C} \end{bmatrix} \dot{\beta} + \begin{bmatrix} -\mathbf{I} & 0 \\ 0 & \mathbf{K} \end{bmatrix} \beta = 0 \tag{A157}$$

Letting

$$\mathbf{P} = \begin{bmatrix} 0 & \mathbf{I} \\ \mathbf{M} & \mathbf{C} \end{bmatrix} \tag{A158}$$

$$\mathbf{R} = \begin{bmatrix} -\mathbf{I} & 0 \\ 0 & \mathbf{K} \end{bmatrix} \tag{A159}$$

and rearranging yields

$$\dot{\beta} = -\mathbf{P}^{-1}\mathbf{R}\beta \tag{A160}$$

Assuming

$$\beta = \mathbf{B}e^{\lambda t} \tag{A161}$$

then

$$\dot{\beta} = \lambda \mathbf{B}e^{\lambda t} \tag{A162}$$

Substituting (A161) and (A162) into (A160) yields a standard eigenvalue problem

$$\lambda \mathbf{B} = -\mathbf{P}^{-1}\mathbf{R}\mathbf{B} \tag{A163}$$

where λ is an eigenvalue and $\mathbf{B}$ is an eigenvector. It should be noted that

$$\mathbf{P}^{-1} = \begin{bmatrix} -\mathbf{M}^{-1}\mathbf{C} & \mathbf{M}^{-1} \\ \mathbf{I} & 0 \end{bmatrix} \tag{A164}$$

so that only $\mathbf{M}$ (whose dimension is half that of $\mathbf{P}$) must be inverted. Many times in practice the interconnection forces defined by equations (A66) and (A67) contain no inertia terms. In these cases $\mathbf{M}$ becomes the identity and the inversion is trivial.

The eigenvalues and eigenvectors are, in general, complex quantities. The eigenvalues provide the natural frequencies and degree of damping for each mode in the system. Damping can be represented as a critical damping ratio for each mode using the relation

$$\zeta_i = \frac{-\lambda_{R_i}}{\sqrt{\lambda_{r_i}^2 + \lambda_{I_i}^2}} \tag{A165}$$

The eigenvectors (or modeshapes) give the relative shape of the deformation that occurs for a given mode. Since they are complex, displaying the vectors in a physically meaningful way is not entirely straightforward. For a given eigenvector $\mathbf{B}$, it can be seen from equation (A156) that the lower half represents the displacement of the generalized coordinate, hence

$$\mathrm{B_i} = \left\{ \begin{array}{c} \dot{\mathrm{N}}_\mathrm{i} \\ \mathrm{N_i} \end{array} \right\} \tag{A166}$$

This part of the eigenvector (N), which is expressed in generalized coordinates, must be transformed back to physical coordinates using the transformations given in equations (A31 - (A34) and (A74) - (A78). Also, if condensation has been performed, the associated transformations must be reversed. This yields a complex eigenvector expressed in physical coordinates with the form

$$\mathrm{W_i} = \left\{ \begin{array}{c} x \\ \mathrm{y} \\ \Theta_\mathrm{z} \\ \mathrm{z} \\ \Theta_\mathrm{y} \\ x_h \\ \mathrm{y_h} \\ \Theta_{\mathrm{z_h}} \\ \mathrm{z_h} \\ \Theta_{\mathrm{y_h}} \end{array} \right\} \tag{A167}$$

The eigenvectors and eigenvalues were used in equation (A101) to separate the variable β into spatial and temporal factors. The transformations performed on β are now performed on $\mathbf{B}$ which, from equation (A161) yields

$$\mathbf{w_i(t)} = \mathbf{W_i} e^{\lambda_i t} \tag{A168}$$

This can be expanded in terms of real and imaginary parts as

$$\begin{aligned}
\mathbf{w_i(t)} &= [\mathbf{W_{R_i}} + j\mathbf{W_{I_i}}] e^{(\lambda_{R_i} + j\lambda_{I_i})t} \\
&= [\mathbf{W_{R_i}} + j\mathbf{W_{I_i}}] e^{\lambda_{R_i} t} [\cos(\lambda_{I_i} t) + j \sin(\lambda_{I_i} t)] \\
&= [\mathbf{W_{R_i}} \cos(\lambda_{I_i} t) - \mathbf{W_{I_i}} \sin(\lambda_{I_i} t)] e^{\lambda_{R_i} t} \\
&\quad + j[\mathbf{W_{R_i}} \sin(\lambda_{I_i} t) + \mathbf{W_{I_i}} \cos(\lambda_{I_i} t)] e^{\lambda_{R_i} t}
\end{aligned} \tag{A169}$$

Since $\mathbf{w(t)}$ must be real, only the real part is needed, so that the motion of the system due to a given mode is

$$\mathbf{w_i(t)} = [\mathbf{W_{R_i}} \cos(\lambda_{I_i} t) - \mathbf{W_{I_i}} \sin(\lambda_{I_i} t)] e^{\lambda_{R_i} t} \tag{A170}$$

The exponential term determines the rate of decay or growth of the motion for the mode. The modeshape characteristics can be displayed by plotting the motion through one period and neglecting the decay term. This will yield a three dimensional figure; however, the lateral motions (y_i, z_i) at particular axial locations are usually of primary interest. For example, the rotor motion at the k^{th} location for the i^{th} mode will be

$$y_k = Y_{R_{k_i}} \cos(\lambda_{I_i} t) - Y_{I_{k_i}} \sin(\lambda_{I_i} t) \tag{A171}$$

$$z_k = Z_{R_{k_i}} \cos(\lambda_{I_i} t) - Z_{I_{k_i}} \sin(\lambda_{I_i} t) \tag{A172}$$

To display these motions, it is necessary to let t vary such that $\lambda_{I_i} t$ covers the range from 0 to 2π. The motions given by equations (A171) and (A172) will trace out an ellipse in the $y - z$ plane. Housing motions and relative motions (rotor minus housing) can be displayed in an identical manner. It should be noted that the display is more than just the eigenvector. It is the transient motion of the vector (without the decay) through one period.

The forced response program obtains the particular solution to the equations of motion. The excitation must be harmonic and can be in one of three forms. The first and most often used form of excitation is due to mass unbalance of the rotor. This excitation is harmonic at a frequency equal to rotational speed. Since the force vector is rotating, the y and z axis components are ± 90 degrees out of phase, depending on the direction of rotation. Since it is inertial, it is applied only to the rotor. The second form of excitation is static (zero frequency) and is due to circumferential pressure variations in the turbopump. It is applied to the rotor with an equal but opposite force applied to the housing. It is also distributed along the length of the rotor. The third form is due to rotating eccentricities in the interconnection elements. The magnitude of the force is equal to the product of the eccentricity and the element's stiffness. For rotor eccentricities, the frequency is equal to rotation speed. For the rolling element bearings, the ball or roller train can become eccentric due to variations in element size and produce an eccentricity rotating at the speed of the rolling element separator (cage). The force is applied to the rotor with an equal but opposite force applied to the housing. The y and z axis components are ± 90 degrees out of phase, depending on the direction of rotation. All three forms of excitation are discretely distributed along the length of the rotor.

The equations of motion can be written for these types of excitation as

$$\mathbf{M}(\Omega)\ddot{\eta} + \mathbf{C}(\Omega)\dot{\eta} + \mathbf{K}(\Omega)\eta = \mathbf{Q}(\omega t) \tag{A173}$$

where the dependency of $\mathbf{M}$, $\mathbf{C}$, and $\mathbf{K}$ on rotational speed (Ω) has been emphasized and

$$\omega = \rho\Omega \tag{A174}$$

Depending on the form of excitation, ρ will be 1, 0, or equal to the rolling element cage speed ratio. Since the equations are linear and a harmonic excitation is applied, the particular solution will be harmonic. The excitation can be written as

$$\mathbf{Q}(t) = \Re[\bar{\mathbf{Q}}e^{j\omega t}] = \Re[(\mathbf{Q_R} + j\mathbf{Q_I})e^{j\omega t}] \tag{A175}$$

where $\Re[\ ]$ denotes the real part. The generalized force vector $\mathbf{Q}$ can be defined by comparison with the right hand side of equation (A84):

$$\mathbf{Q}(t) = \left\{ \begin{array}{c} 0 \\ \mathbf{\Phi}^{\mathbf{T}}\mathbf{F}_{\mathbf{Er_y}}(t) \\ \mathbf{\Phi}^{\mathbf{T}}\mathbf{F}_{\mathbf{Er_z}}(t) \\ -\mathbf{\Phi}_{\mathbf{h_y}}^{\mathbf{T}}\mathbf{F}_{\mathbf{Eh_y}}(t) - \mathbf{\Phi}_{\mathbf{h_z}}^{\mathbf{T}}\mathbf{F}_{\mathbf{Eh_z}}(t) \end{array} \right\} \tag{A176}$$

where $\mathbf{F}_{\mathbf{Er_y}}$, $\mathbf{F}_{\mathbf{Er_z}}$, $\mathbf{F}_{\mathbf{Eh_y}}$, and $\mathbf{F}_{\mathbf{Eh_z}}$, are the excitation forces for the rotor and housing along the y and z axes. For the unbalance excitation

$$F_{Er_y i}(t) = (ma)_i \Omega^2 \cos(\Omega t + \phi_i) \tag{A177}$$

$$F_{Er_z i}(t) = (ma)_i \Omega^2 \sin(\Omega t + \phi_i) \tag{A178}$$

$$F_{Eh_y i}(t) = F_{Eh_z i}(t) = 0. \tag{A179}$$

For the static excitation

$$\mathbf{F}_{\mathbf{Er_y}} = \mathbf{F}_{\mathbf{S_y}} \tag{A180}$$

$$\mathbf{F}_{\mathbf{Er_z}} = \mathbf{F}_{\mathbf{S_z}} \tag{A181}$$

$$\mathbf{F}_{\mathbf{Eh_y}} = \mathbf{F}_{\mathbf{Er_y}} \tag{A182}$$

$$\mathbf{F}_{\mathbf{Eh_z}} = \mathbf{F}_{\mathbf{Er_z}} \tag{A183}$$

For the eccentricity excitation

$$F_{Er_y i}(t) = k_i \epsilon_i \cos(\rho \Omega t + \phi_i) \tag{A184}$$

$$F_{Er_z i}(t) = k_i \epsilon_i \sin(\rho \Omega t + \phi_i) \tag{A185}$$

$$F_{Eh_y i}(t) = F_{Er_y i}(t) \tag{A186}$$

$$F_{Eh_z i}(t) = F_{Er_z i}(t) \tag{A187}$$

From (A175) and (A176)

$$\mathbf{F_E}(t) = \Re\left[(\mathbf{R} + j\mathbf{I})e^{j\rho\Omega t}\right] = \mathbf{R}\cos(\rho\Omega t) - \mathbf{I}\sin(\rho\Omega t) \tag{A188}$$

For unbalance excitation, from equations (A177) - (A178)

$$R_{r_y i} = (ma)_i\Omega^2 \cos\phi_i \tag{A189}$$

$$I_{r_y i} = (ma)_i\Omega^2 \sin\phi_i \tag{A190}$$

$$R_{r_z i} = (ma)_i\Omega^2 \sin\phi_i \tag{A191}$$

$$I_{r_z i} = -(ma)_i\Omega^2 \cos\phi_i \tag{A192}$$

$$R_{h_y} = R_{h_z} = I_{h_y} = I_{h_z} = 0. \tag{A193}$$

For the static excitation, from equations (A180) - (A181)

$$R_{r_y i} = F_{Sy_i} = |F_{S_i}| \cos\left[\tan^{-1}\left(\frac{F_{Sz_i}}{F_{Sy_i}}\right)\right] \tag{A194}$$

$$R_{r_z i} = F_{Sz_i} = |F_{S_i}| \sin\left[\tan^{-1}\left(\frac{F_{Sz_i}}{F_{Sy_i}}\right)\right] \tag{A195}$$

$$R_{h_y i} = R_{r_y i} \tag{A196}$$

$$R_{h_z i} = R_{r_z i} \tag{A197}$$

and I_{r_i} and I_{h_i} are of no consequence since in equation (A188)

$$\sin(\rho\Omega t) = \sin(0t) = 0. \tag{A198}$$

For the eccentricity excitation, from equation (A184) - (A185)

$$R_{r_y i} = k_i \epsilon_i \cos\phi_i \tag{A199}$$

$$I_{r_y i} = k_i \epsilon_i \sin\phi_i \tag{A200}$$

$$R_{r_z i} = k_i \epsilon_i \sin\phi_i \tag{A201}$$

$$I_{r_z i} = -k_i \epsilon_i \cos\phi_i \tag{A202}$$

$$R_{h_y i} = R_{r_y i} \tag{A203}$$

$$I_{h_y i} = I_{r_y i} \tag{A204}$$

$$R_{h_z i} = R_{r_z i} \tag{A205}$$

$$I_{h_z i} = I_{r_z i} \tag{A206}$$

From equations (A175), (A176), and (A188)

$$(\mathbf{Q_R} + j\mathbf{Q_I}) = \begin{Bmatrix} 0 \\ \Phi^{\mathrm{T}}(\mathbf{R_{r_y}} + j\mathbf{I_{r_y}}) \\ \Phi^{\mathrm{T}}(\mathbf{R_{r_z}} + j\mathbf{I_{r_z}}) \\ -\Phi^{\mathrm{T}}_{\mathbf{h_y}}(\mathbf{R_{h_y}} + j\mathbf{I_{h_y}}) - \Phi^{\mathrm{T}}_{\mathbf{h_z}}(\mathbf{R_{h_z}} + j\mathbf{I_{h_z}}) \end{Bmatrix} \tag{A207}$$

where $\mathbf{R}$ and $\mathbf{I}$ are defined using either equations (A189) - (A193), (A194) - (A197), or (A199) - (A206) depending on the form of the excitation. With $\mathbf{Q}$ expressed as in equation (A175), the solution can be assumed to be of a similar form

$$\eta(t) = \Re[\bar{\mathrm{N}} e^{j\omega t}] \tag{A208}$$

so that

$$\dot{\eta}(t) = \Re[j\omega \bar{\mathrm{N}} e^{j\omega t}] \tag{A209}$$

and

$$\ddot{\eta}(t) = \Re[-\omega^2 \bar{\mathrm{N}} e^{j\omega t}] \tag{A210}$$

Substituting (A175) and (A208) - (A210) into (A173) and canceling the $e^{j\omega t}$ term yields

$$[\mathrm{K}(\Omega) - \omega^2 \mathrm{M}(\Omega) + j\omega \mathrm{C}(\Omega)]\bar{\mathrm{N}} = \bar{\mathrm{Q}} \tag{A211}$$

Equating real and imaginary parts of equation (A211) gives

$$(\mathrm{K} - \omega^2 \mathrm{M})\mathrm{N_R} - \omega \mathrm{C}\mathrm{N_I} = \mathrm{Q_R} \tag{A212}$$

$$\omega \mathrm{C}\mathrm{N_R} + (\mathrm{K} - \omega^2 \mathrm{M})\mathrm{N_I} = \mathrm{Q_I} \tag{A213}$$

Equations (A212) and (A213) can be solved simultaneously for $\mathrm{N_R}$ and $\mathrm{N_I}$.

The response vector $\bar{\mathrm{N}}$ defined by equation (A208) can be displayed in exactly the same way as the N defined as the displacement part of the eigenvector in equation (A166). The procedure is exactly the same except that the decay term that is ignored when displaying the eigenvector never appears for the response vector; therefore, the procedure will not be repeated here.

The nonlinear transient simulation obtains the complete solution of equation (A84) with all of the nonlinearities and excitations that have been discussed. Rewriting equation (A84) with the introduction of η as defined by equation (A155) gives

$$\mathrm{M}\ddot{\eta} + \mathrm{C}\dot{\eta} + \mathrm{K}\eta = \mathrm{Q}(t) \tag{A214}$$

This equation can be put into a form that is convenient for numerical solution. First, it can be rearranged as

$$\ddot{\eta} = \mathrm{M}^{-1}[\mathrm{Q}(t) - \mathrm{K}\eta - \mathrm{C}\dot{\eta}] \tag{A215}$$

If the interconnection forces defined by equation (A66) and (A67) contain no inertia terms, then M becomes the identity and inversion is not required. Equation (A215) can

be written with no derivatives on the right hand side by introducing a new variable and corresponding equation

$$\dot{\eta} = \nu \tag{A216}$$

$$\dot{\nu} = \mathbf{M}^{-1}[\mathbf{Q}(t) - \mathbf{K}\eta - \mathbf{C}\nu] \tag{A217}$$

This set of equations is now in the general form of

$$\dot{\mathbf{x}} = \mathbf{f}(\mathbf{x}, t) \tag{A218}$$

These equations will be integrated using the Adams-Moulton predictor-corrector method. The predictor equation for this method is

$$\mathbf{x}^{\mathrm{p}}_{n+1} = \mathbf{x}_n + \frac{h}{24}\left[55\mathbf{f}(\mathbf{x}_n, t_n) - 59\mathbf{f}(\mathbf{x}_{n-1}, t_{n-1}) + 37\mathbf{f}(\mathbf{x}_{n-2}, t_{n-2}) - 9\mathbf{f}(\mathbf{x}_{n-3}, t_{n-3})\right] \tag{A219}$$

The corrector equation is

$$\mathbf{x}_{n+1} = \mathbf{x}_n + \frac{h}{24}\left[9\mathbf{f}(\mathbf{x}^{\mathrm{p}}_{n+1}, t_{n+1}) + 19\mathbf{f}(\mathbf{x}_n, t_n) - 5\mathbf{f}(\mathbf{x}_{n-1}, t_{n-1}) + \mathbf{f}(\mathbf{x}_{n-2}, t_{n-2})\right] \tag{A220}$$

This method requires four starting points which can be obtained by using a simpler method. The method used here is the Euler or tangent line method

$$\mathbf{x}_{n+1} = \mathbf{x}_n + h\mathbf{f}(\mathbf{x}_n, t_n) \tag{A221}$$

The first point needed is the prescribed initial condition vector. Equation (A221) is used three times to obtain enough values to begin using equations (A219) and (A220). An alternate method is built into the simulation as an option. The alternate method was not used in this study and will not be described here.

The numerical integration produces the generalized coordinate motion at the discrete time points

$$t_n = n \cdot h \tag{A222}$$

where n is an integer and varies from zero to the specified maximum. The generalized coordinate motion is transformed back into physical coordinates and these coordinates, along with interaction forces and housing accelerations can be displayed versus time. It is usually necessary to perform certain operations on the results after they have been generated. This post-processing includes such things as filters and Fourier transformations.

The $\mathbf{M}$, $\mathbf{C}$, and $\mathbf{K}$ matrices in equation (A217) are, in general, functions of engine power level. As discussed earlier, due to the relationship between power level and speed, they can be expressed as functions of speed. If speed is a function of time, these matrices (and $\mathbf{M}^{-1}$ if required) must be frequently re-evaluated. It is not necessary to re-evaluate them at each time step, however. The frequency for re-evaluation is specified in terms of a speed increment instead of time. This increment should be made small enough to keep the change in the interconnection coefficients small. This approach allows for more efficient numerical solution of the system equations.

APPENDIX B
HPFTP MODEL NOMINAL DATA

The nominal rotor-housing interconnection coefficient data are shown in figures 113 through 119. These data were provided by the SSME manufacturer with the exception of the pump interstage seal cross-coupled stiffness coefficients. The coefficients provided by the manufacturer were replaced with functions of the form of equation 125 where $\sigma = .6$. The resulting curve closely matched the original data. The damping coefficients for all bearings was a constant of $3.0\frac{\text{lb}\cdot\text{sec}}{\text{in}}$. The frequencies of the nine free-free rotor component modes are shown in table 2. The frequencies of the twenty free interface housing modes are shown in table 3.

Table 2. Frequencies of free-free rotor modes.

Mode 1 - 0.0 Hz.

Mode 2 - 0.0 Hz.

Mode 3 - 634.5 Hz.

Mode 4 - 1350. Hz.

Mode 5 - 1910. Hz.

Mode 6 - 2591. Hz.

Mode 7 - 3216. Hz.

Mode 8 - 3935. Hz.

Mode 9 - 3953. Hz.

156 INTENTIONALLY BLANK

PRECEDING PAGE BLANK NOT FILMED

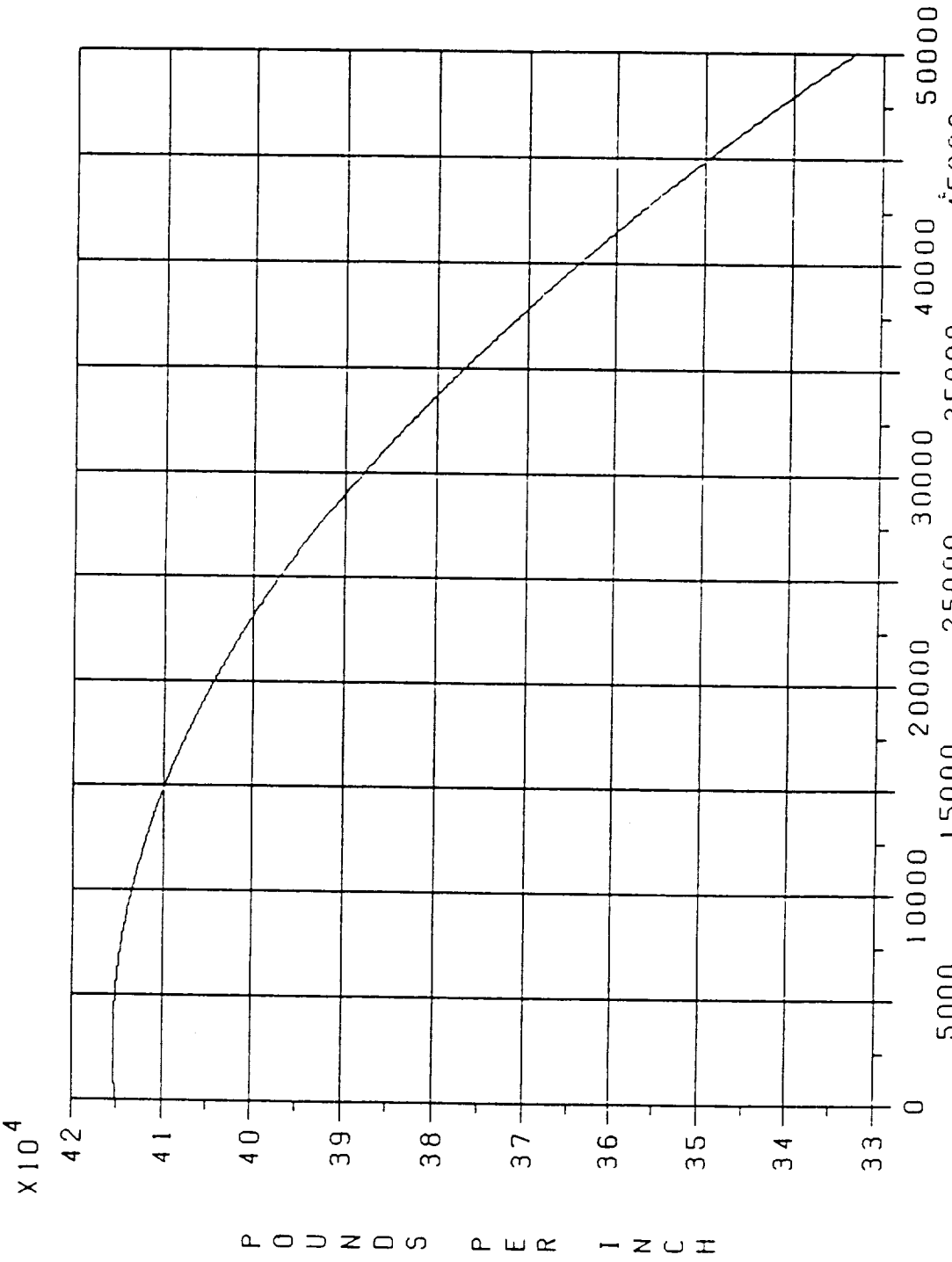

Figure 113. HPFTP bearing stiffness coefficient versus speed.

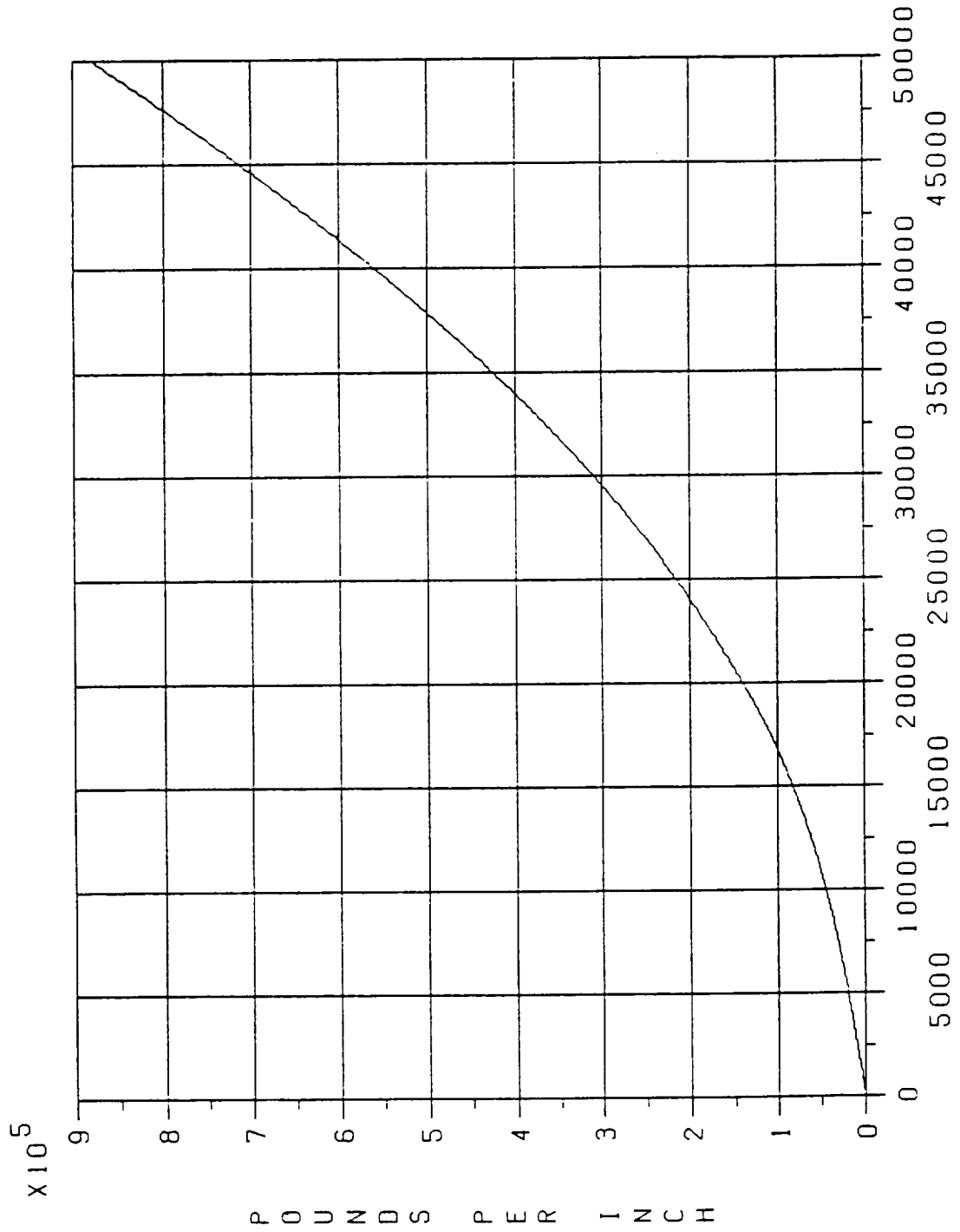

Figure 114. HPFTP pump interstage seal stiffness coefficient versus speed.

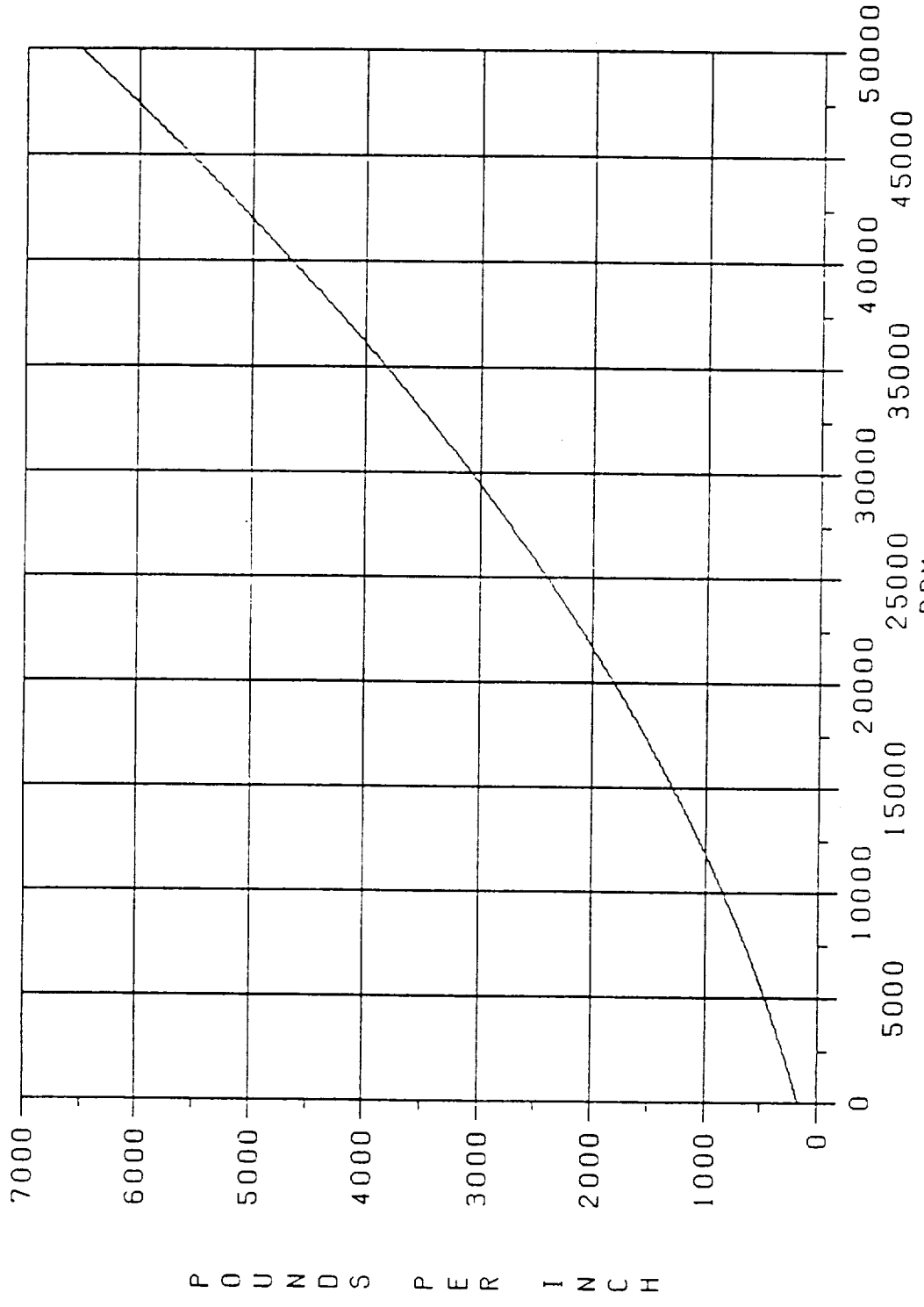

Figure 115. HPFTP turbine interstage seal stiffness coefficient versus speed.

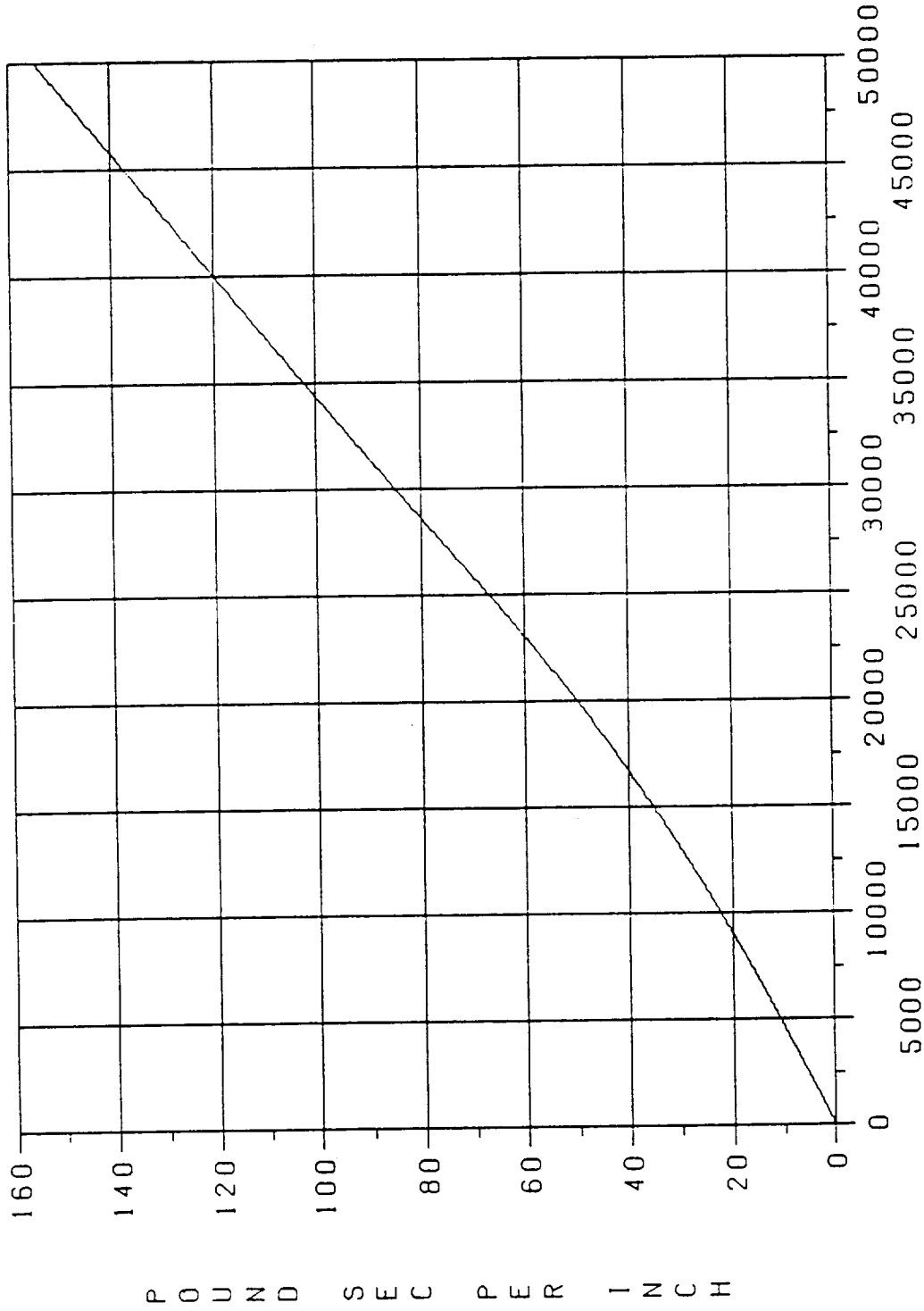

Figure 116. HPFTP pump interstage seal damping coefficient versus speed.

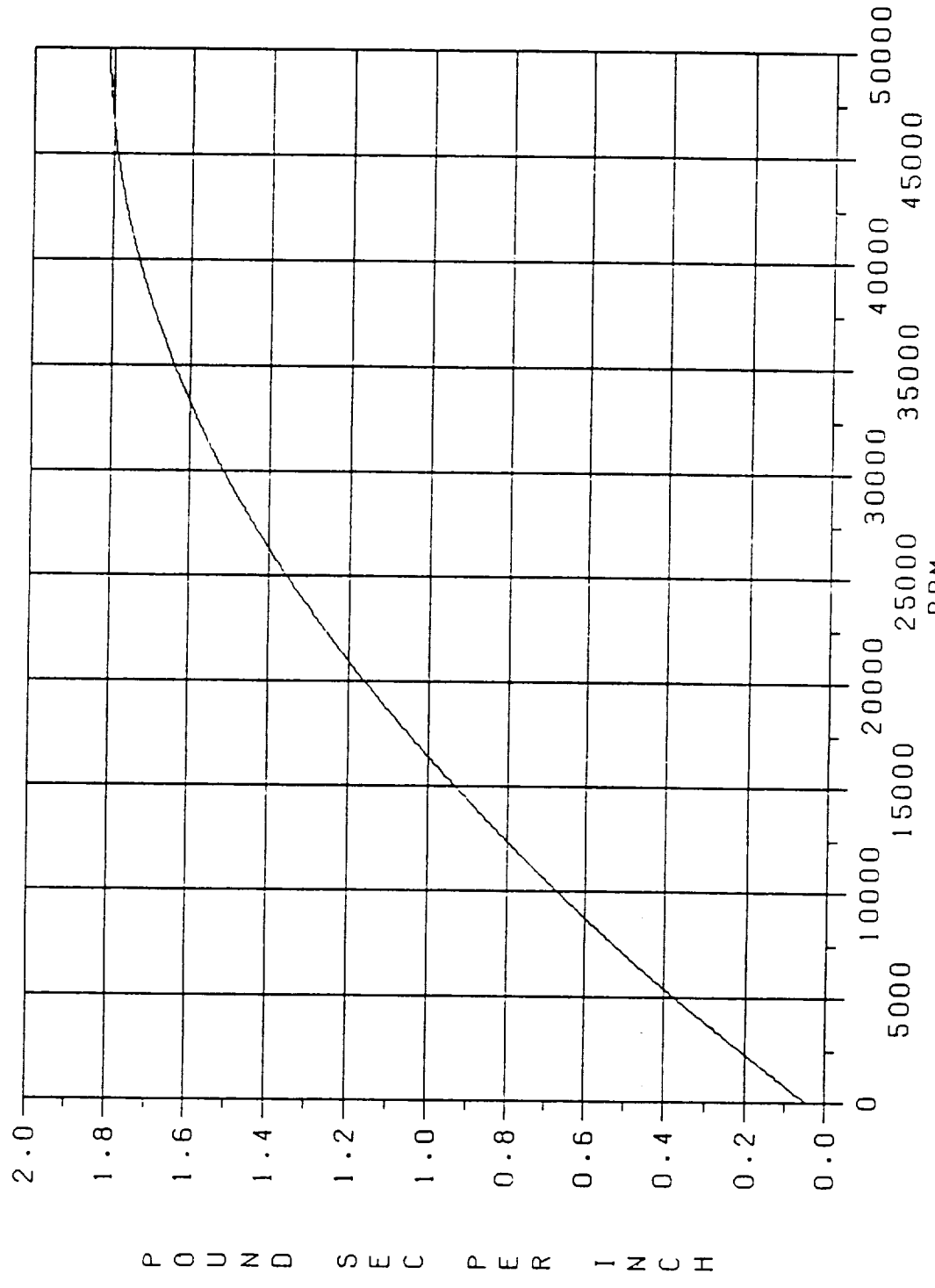

Figure 117. HPFTP turbine interstage seal damping coefficient versus speed.

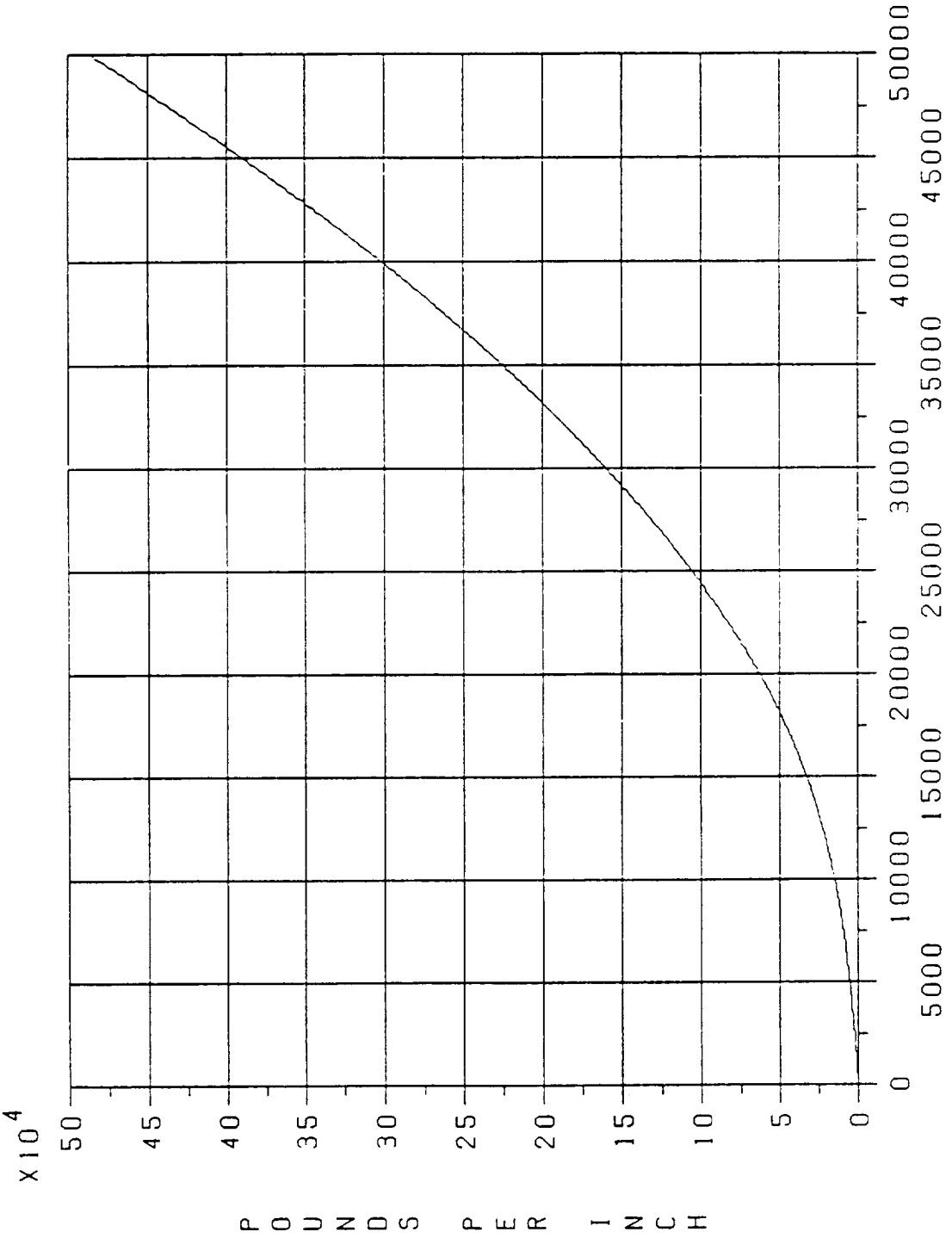

Figure 118. HPFTP pump interstage seal cross-coupled stiffness coefficient versus speed.

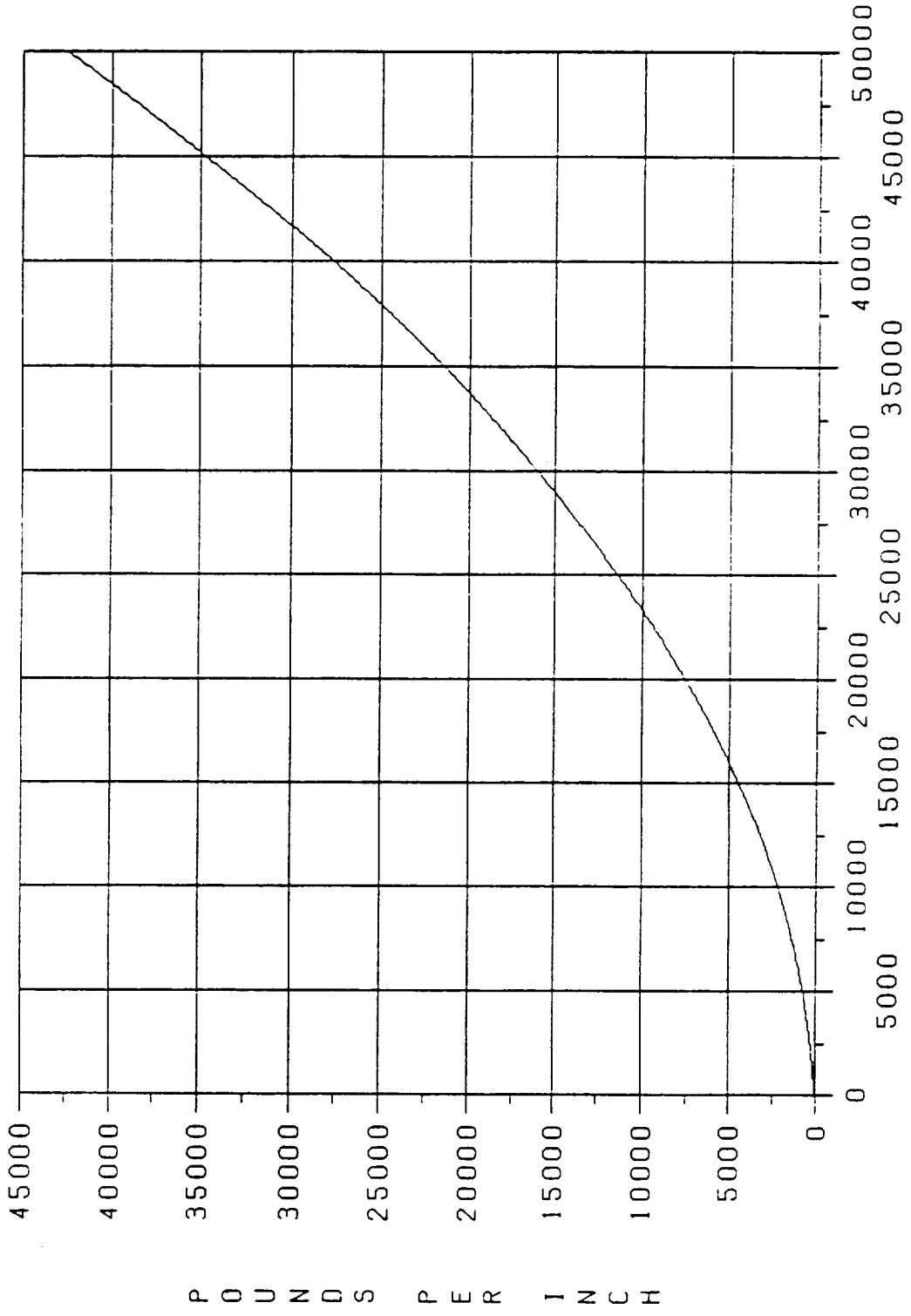

Figure 119. HPFTP turbine interstage seal plus Alford effect cross-coupled stiffness coefficient versus speed.

Table 3. Frequencies of free interface housing modes.

Mode 1 - 50.29 Hz.

Mode 2 - 114.0 Hz.

Mode 3 - 363.9 Hz.

Mode 4 - 417.9 Hz.

Mode 5 - 712.9 Hz.

Mode 6 - 836.3 Hz.

Mode 7 - 920.1 Hz.

Mode 8 - 995.8 Hz.

Mode 9 - 1024. Hz.

Mode 10 -1143. Hz.

Mode 11 -1163. Hz.

Mode 12 -1672. Hz.

Mode 13 -1672. Hz.

Mode 14 -1802. Hz.

Mode 15 -1808. Hz.

Mode 16 -2573. Hz.

Mode 17 -2646. Hz.

Mode 18 -2753. Hz.

Mode 19 -3534. Hz.

Mode 20 -3536. Hz.

REPORT DOCUMENTATION PAGE

Form Approved
OMB No. 0704-0188

Public reporting burden for this collection of information is estimated to average 1 hour per response, including the time for reviewing instructions, searching existing data sources, gathering and maintaining the data needed, and completing and reviewing the collection of information. Send comments regarding this burden estimate or any other aspect of this collection of information, including suggestions for reducing this burden, to Washington Headquarters Services, Directorate for Information Operations and Reports, 1215 Jefferson Davis Highway, Suite 1204, Arlington, VA 22202-4302, and to the Office of Management and Budget, Paperwork Reduction Project (0704-0188), Washington, DC 20503.

1. AGENCY USE ONLY (Leave blank)	2. REPORT DATE	3. REPORT TYPE AND DATES COVERED
	December 1991	Technical Paper

4. TITLE AND SUBTITLE
Limit Cycle Vibrations in Turbomachinery

5. FUNDING NUMBERS

6. AUTHOR(S)
S.G. Ryan

7. PERFORMING ORGANIZATION NAME(S) AND ADDRESS(ES)
George C. Marshall Space Flight Center
Marshall Space Flight Center, Alabama 35812

8. PERFORMING ORGANIZATION REPORT NUMBER
M-676

9. SPONSORING/MONITORING AGENCY NAME(S) AND ADDRESS(ES)
National Aeronautics and Space Administration
Washington, DC 20546

10. SPONSORING/MONITORING AGENCY REPORT NUMBER
NASA TP-3181

11. SUPPLEMENTARY NOTES
Prepared by Structures and Dynamics Laboratory, Science and Engineering Directorate,

12a. DISTRIBUTION/AVAILABILITY STATEMENT
Unclassified – Unlimited

Subject Category: 20

12b. DISTRIBUTION CODE

13. ABSTRACT *(Maximum 200 words)*

High performance turbomachinery is susceptible to a wide variety of vibration problems. Some of these problems are rotor unbalance vibration, dynamic instability, and subharmonic response to unbalance excitation. Understanding these problems is complicated when nonlinearities are present, as they almost always are in actual hardware. For example, dynamic instabilities may manifest themselves as limit cycle vibrations. In some cases the vibration levels are so high that the distinction between a divergent instability and a limit cycle is meaningless. This is because the machinery would be destroyed in either case. In other cases the limit cycle may appear at relatively small levels. These cases may appear to be benign; however, the presence of the limit cycle may be an indication of an impending divergent instability. This matter is complicated by the fact that the frequency of the limit cycle instability is frequently near one-half of the unbalance excitation synchronous frequency. This makes it difficult to distinguish between the limit cycle and a subharmonic response.

The focus of this work is an examination of rotordynamic systems which are simultaneously susceptible to limit cycle instability and subharmonic response. Characteristics of each phenomenon are determined as well as their interrelationship. A normalized, single mass rotor model is examined as well as a complex model of the high pressure fuel turbopump (HPFTP) of the space shuttle main engine (SSME). Entrainment of limit cycle instability by subharmonic response is demonstrated for both models. The nonuniqueness of the solution is also demonstrated.

14. SUBJECT TERMS
rotordynamics, instability, nonlinear, subharmonic, entrainment, limit cycle, turbomachinery

15. NUMBER OF PAGES
188

16. PRICE CODE
A09

17. SECURITY CLASSIFICATION OF REPORT	18. SECURITY CLASSIFICATION OF THIS PAGE	19. SECURITY CLASSIFICATION OF ABSTRACT	20. LIMITATION OF ABSTRACT
Unclassified	Unclassified	Unclassified	Unlimited

NSN 7540-01-280-5500

Standard Form 298 (Rev. 2-89)
Prescribed by ANSI Std. Z39-18
298-102

NASA-Langley, 1991

National Aeronautics and
Space Administration
Code NTT

Washington, D.C.
20546-0001

Official Business
Penalty for Private Use, $300

NASA

National Aeronautics and
Space Administration

Washington, D.C.
20546

Postage an Fees Paid
National Aeronautics and
Space Administration
NASA-451

Official Business
Penalty for Private Use $300

U.S. MAIL

**SPECIAL FOURTH CLASS MAIL
BOOK**

L3 001 TP-3181 911210S090569A
NASA
CENTER FOR AEROSPACE INFORMATION
ACCESSIONING DEPT
P O BOX 8757 BWI ARPRT
BALTIMORE MD 21240

NASA